

## **INFORMATION TO USERS**

**This manuscript has been reproduced from the microfilm master. UMI films the text directly from the original or copy submitted. Thus, some thesis and dissertation copies are in typewriter face, while others may be from any type of computer printer.**

**The quality of this reproduction is dependent upon the quality of the copy submitted. Broken or indistinct print, colored or poor quality illustrations and photographs, print bleedthrough, substandard margins, and improper alignment can adversely affect reproduction.**

**In the unlikely event that the author did not send UMI a complete manuscript and there are missing pages, these will be noted. Also, if unauthorized copyright material had to be removed, a note will indicate the deletion.**

**Oversize materials (e.g., maps, drawings, charts) are reproduced by sectioning the original, beginning at the upper left-hand corner and continuing from left to right in equal sections with small overlaps.**

**Photographs included in the original manuscript have been reproduced xerographically in this copy. Higher quality 6" x 9" black and white photographic prints are available for any photographs or illustrations appearing in this copy for an additional charge. Contact UMI directly to order.**

**Bell & Howell Information and Learning  
300 North Zeeb Road, Ann Arbor, MI 48106-1346 USA**

**UMI<sup>®</sup>**  
**800-521-0600**



## **NOTE TO USERS**

**This reproduction is the best copy available.**

**UMI**



**UNIVERSITY OF OKLAHOMA**

**GRADUATE COLLEGE**

**THE INFLUENCE OF HORIZONTAL VARIATIONS  
IN VERTICAL SHEAR AND LOW-LEVEL MOISTURE ON NUMERICALLY  
SIMULATED CONVECTIVE STORMS**

**A Dissertation**

**SUBMITTED TO THE GRADUATE FACULTY**

**in partial fulfillment of the requirements for the**

**degree of**

**Doctor of Philosophy**

**By**

**YVETTE P. RICHARDSON  
Norman, Oklahoma  
1999**

**UMI Number: 9952416**

**UMI<sup>®</sup>**

---

**UMI Microform9952416**

**Copyright 2000 by Bell & Howell Information and Learning Company.**

**All rights reserved. This microform edition is protected against  
unauthorized copying under Title 17, United States Code.**

---

**Bell & Howell Information and Learning Company  
300 North Zeeb Road  
P.O. Box 1346  
Ann Arbor, MI 48106-1346**

**© Copyright by Yvette Richardson 1999  
All Rights Reserved.**

THE INFLUENCE OF HORIZONTAL VARIATIONS IN VERTICAL SHEAR  
AND LOW-LEVEL MOISTURE ON NUMERICALLY SIMULATED  
CONVECTIVE STORMS

A Dissertation APPROVED FOR THE  
SCHOOL OF METEOROLOGY

BY

  
\_\_\_\_\_  
Dr. [unclear]  
\_\_\_\_\_  
Frederick H. Carr  
\_\_\_\_\_  
Robert James Jones  
\_\_\_\_\_  
John P. Albert  
\_\_\_\_\_  
Dr. [unclear]

## **Acknowledgments**

I find this page one of the most overwhelming to complete because it can never be thorough or generous enough to the many kind souls I am so grateful to have in my life. My husband, Scott, has been with me since the beginning of my college education and much of what I have accomplished I owe to his steadfast encouragement and love. My advisor, Kelvin Droegemeier, has believed in me more than I think I will ever believe in myself and has been indefatigable (he'll like that word!) in his encouragement and support. I am very grateful! I had an amazing committee as well. I feel so fortunate to have had the opportunity to meet regularly with Robert Davies-Jones who is so outstanding in theoretical storm dynamics. I am grateful that I could observe both his brilliance and his kind encouragement. I have learned so much from Douglas Lilly both in his classes and out in the real world at 'tea time' in the afternoons. It was an honor to have him on my committee and to benefit from his insight and clarity. Alan Shapiro has been a constant source of encouragement and intellectual insight. He was just born to be a mentor. Fred Carr was my advisor for my masters degree and I was happy to have him there for my Ph.D. as well. John Albert is one of the best math teachers I ever had and I am very happy he agreed to be part of my committee.

Beyond my committee members, I have benefited greatly from discussions with others, especially scientists in CAPS. I am very grateful to Ming Xue for numerous conversations about modeling issues. He is a very patient and gracious person. Ed Adlerman was also very gracious with his time-height and trajectory code and I appreciate his willingness to share the tools he has developed. I found conversations with other numerical modelers such as Jerry Straka and Morris Weisman also very beneficial.

On a personal level, I feel very fortunate to have had such wonderful friends to support me. You have been so good to me and I am deeply appreciative. Thanks to everyone who brought me food when I was in my office late at night, helped me celebrate after my defense, or offered a word (or shoulder!) of support during the trying times.

I must thank my family (both my natural family and the one I was lucky enough to gain in marriage) for their support, encouragement, and all of those flowers! You have no idea how much it has meant to me.

I have been lucky to be blessed with outstanding teachers my entire life. Each of them played a role in shaping me and I will always owe them. I also owe the staff of the School of Meteorology for their kindness and patience, particularly in the past year as I began teaching. Thanks for your helpfulness and your calming influence!

Finally, I want to thank the students I have taught over the past year. You have been an inspiration to me and helped me remember why I was doing all of this in the first place!

This research was supported by the National Science Foundation under Grant ATM92-22576, by Grant ATM91-20009 to the Center for Analysis and Prediction of Storms, by the University of Oklahoma as a Centennial Research Assistantship and a Patricia Roberts Harris Fellowship, and by the University of Oklahoma School of Meteorology as part of a visiting faculty appointment. The numerical simulations were performed at the Pittsburgh Supercomputing Center, the San Diego Supercomputing Center, and the Environmental Computing Applications System at the University of Oklahoma. The latter is funded by the National Science Foundation under Grant EAR95-12145 and by the University of Oklahoma. Some of the graphics were generated using the ZXPLLOT package developed by Ming Xue at the University of Oklahoma.

## Table of Contents

Chapter 1	Introduction.....	1
Chapter 2	Background.....	7
2.1	Storm Types: General Features, Relationship to Environmental Characteristics.....	7
2.2	Theories of Storm Propagation and Rotation.....	20
Chapter 3	Model Formulation and Validation.....	39
3.1	Model Validation.....	40
3.1.1	Viscous Beltrami Flow Validation.....	41
3.1.2	Scalar Advection Tests.....	45
3.1.3	Test of storm simulations over various shear ranges.....	54
3.2	Model Formulation to Accommodate an Inhomogeneous Base State.....	68
3.2.1	Computational Mixing/Rayleigh Damping.....	69
3.2.2	Radiation (Open) Lateral Boundary Conditions.....	70
3.2.3	Advection at Lateral Boundaries.....	71
3.2.4	Domain Translation.....	75
Chapter 4	Experiments with Inhomogeneous Low Level Moisture.....	81
4.1	Environmental Setup.....	83
4.2	Influence of Variable Moisture in a Weak Shear Environment.....	90
4.3	Influence of Variable Moisture in Strong Shear Environments.....	118
4.3.1	Updraft Continuation in an Unfavorable Moisture Regime.....	119
4.3.1.a	Control Simulation for $q_{vmix}=10$ g/kg with $U_s=30$ m s <sup>-1</sup> .....	119
4.3.1.b	Control Simulation for $q_{vmix}=12$ g/kg with $U_s=30$ m s <sup>-1</sup> .....	119
4.3.1.c	Inhomogeneous Run Starting with $q_{vmix}=12$ g/kg with $U_s=30$ m s <sup>-1</sup> .....	129
4.3.2	Vertical Velocity and Mid-Level Rotation:.....	131
4.3.2.a	Inhomogeneous Run starting with $q_{vmix}=12$ g/kg with $U_s=30$ m s <sup>-1</sup> .....	131
4.3.3	Cell Interactions: Supercell with $U_s=35$ m s <sup>-1</sup> .....	148
4.3.3.a	Control Run Along Centerline ( $q_{vmix}=14$ g/kg).....	148
4.3.3.b	Control Run for Increased Moisture ( $q_{vmix}=16$ g/kg).....	153
4.3.3.c	Inhomogeneous Run Starting with $q_{vmix}=14$ g/kg.....	157
4.3.4	Low-Level Rotation: Supercell with $U_s=30$ m s <sup>-1</sup> .....	160
4.3.4.a	Control Simulation for $q_{vmix}=12$ g/kg with $U_s=30$ m s <sup>-1</sup> .....	160
4.3.4.b	Control Simulation for $q_{vmix}=14$ g/kg with $U_s=30$ m s <sup>-1</sup> .....	162
4.3.4.c	Inhomogeneous Run starting with $q_{vmix}=12$ g kg <sup>-1</sup> with $U_x=30$ m s <sup>-1</sup> .....	162
4.4	Summary.....	165
Chapter 5	Experiments with Inhomogeneous Environmental Shear.....	167

5.1	Analytic Environment Setup.....	167
5.2	Variable Vertical Shear in a Weak Shear Environment.....	175
5.3	Variable Vertical Shear in a Strong Shear Environment .....	185
5.4	Variable Vertical Shear Along the Mean Wind.....	191
Chapter 6	Summary, Conclusions, and Outlook .....	206
References Cited	.....	211
Additional Reading	.....	219
Appendix A	.....	235

## **List of Figures**

Figure 1.1: Squall line simulation by Skamarock et al. (1994a).....	6
Figure 2.1: Browning model of airflow within a severe storm moving to the right of the winds in the middle troposphere. (From Browning, 1964). .....	9
Figure 2.2: Schematic illustrating the pressure and vertical vorticity perturbations arising as an updraft interacts with an environmental wind shear that (a) does not change direction with height and (b) turns clockwise with height (from Klemp, 1987). .....	16
Figure 3.1: Decay of domain maximum u, v, and w for the ARPS versus that for the ideal solution. The model is run for more than two e-folding decay times.....	43
Figure 3.2: Horizontal cross section ( $z=5.5$ m) of the u and v wind components ( $m s^{-1}$ ) for model solution (left) and difference field (right) for the viscous Beltrami test at $t=41$ s. ....	44
Figure 3.3: Model solution for the vertical cross section of perturbation water vapor mixing ratio ( $g kg^{-1}$ ) in a multicell simulation at $t = 3$ hours with regular scalar advection. ....	46
Figure 3.4: Scalar advection test with a 'soup can' of perturbation potential temperature (K) using 4 <sup>th</sup> order default advective scheme in ARPS.....	47
Figure 3.5: Scalar advection test with a 'soup can' of perturbation potential temperature (K) using flux corrected transport (FCT).....	52
Figure 3.6: Vertical cross section of perturbation water vapor mixing ratio ( $g kg^{-1}$ ) in a multicell storm simulation using FCT for the advection of scalars. ....	53
Figure 3.7: Surface potential temperature perturbation (K) with (top) and without (bottom) vertical mixing at the lowest scalar at $t = 4800$ s.....	60
Figure 3.8: Vertical cross section of water vapor mixing ratio for a moist, non- condensing bubble with the WC flux (top) and regular advective (bottom) forms for the advection terms. Horizontal and vertical resolutions are each 500 m. ....	64
Figure 3.9 Vertical cross section of water vapor mixing ratio for a moist, non- condensing bubble with the regular advective (left) and WC flux (right) forms for the advection terms. Horizontal resolution is 2 km and vertical resolution is 500 m.....	65
Figure 3.10: Illustration of a disturbance (circular contours) generated in the interior of the domain that must be allowed to pass through the lateral boundaries. On the left is the homogeneous case, while the right figure shows the inhomogeneous case (slanted contours represent those of the environment). .....	70
Figure 3.11: Schematic illustrating the need to include environmental gradients in the advection terms at the lateral boundaries on inflow.....	72
Figure 3.12: Illustration of a disturbance at the boundary in an inhomogeneous environment. A relaxation term is added to return the boundary value to the environmental value on inflow. ....	73

Figure 3.13 Illustration of grid translation in an inhomogeneous environment. ....	76
Figure 3.14 Contours of the 'u' term in the Bulk Richardson Number at t=0 (top) and t= 4 hours (bottom) as the domain traverses an inhomogeneous environment. ....	79
Figure 3.15: Domain maximum and minimum values as designated in the legend for a domain moving through an inhomogeneous environment. Note the change in grid translation speed. ....	80
Figure 4.1: Weisman and Klemp (1982) thermodynamic profile with qv in the mixed layer equal to 14 g/kg. ....	85
Figure 4.2: Weisman and Klemp (1982) thermodynamic profile with qv in the mixed layer equal to 12 g/kg. ....	87
Figure 4.3: Thermodynamic profile with qv in the mixed layer equal to 12 g/kg and adjusted potential temperature equal to that used with qvmix=16 g/kg. ....	88
Figure 4.4: Weisman and Klemp (1982) thermodynamic profile with qv in the mixed layer equal to 16 g/kg. ....	89
Figure 4.5: Profile of u component of the velocity with height for weak shear case. ....	91
Figure 4.6: Schematic of inhomogeneous domain for CAPE simulations. ....	93
Figure 4.7: Horizontal cross-section of vertical velocity at z=4.6 km at t = 2 hours for weak shear ( $U_s=12 \text{ m s}^{-1}$ ) control run with qvmix=14 g/kg. (Actual computational domain is the southern half of that shown, with a symmetric condition applied at y=96 km.) ....	94
Figure 4.8: Domain maximum vertical velocity versus time for weak shear, inhomogeneous moisture simulation and corresponding homogeneous control runs. Mixed layer mixing ratios (qvmix) are shown in the legend for each homogeneous simulation. The inhomogeneous simulation has 14 g/kg in the initiation location. ....	95
Figure 4.9: Horizontal cross-section of vertical velocity at z=4.6 km at t = 2 hours for weak shear control run with qvmix=13 g/kg. (Actual computational domain is the southern half of that shown, with a symmetric condition applied at y=96 km.) ....	96
Figure 4.10: Horizontal cross-section of vertical velocity at z=4.6 km at t = 2 hours for weak shear ( $U_s=12 \text{ m s}^{-1}$ ) control run with qvmix=16 g/kg. (Actual computational domain is the southern half of that shown, with a symmetric condition applied at y=96 km.) ....	97
Figure 4.11: : Horizontal cross-section of vertical velocity at z=4.6 km at t = 2 hours for weak shear ( $U_s=12 \text{ m s}^{-1}$ ) inhomogeneous moisture simulation with qvmix as shown to right. ....	99
Figure 4.12: Horizontal cross-section of vertical velocity at z=4.6 km at t = 3 hours for weak shear ( $U_s=12 \text{ m s}^{-1}$ ) inhomogeneous CAPE simulation with qvmix as in Figure 4.11. ....	100
Figure 4.13: Horizontal cross-section of vertical velocity at z=4.6 km at t = 2 hours for weak shear ( $U_s=12 \text{ m s}^{-1}$ ) control run with qvmix=18 g/kg. (Actual computational domain is the southern half of that shown, with a symmetric condition applied at y=96 km.) ....	102

Figure 4.14: Domain maximum vertical velocity versus time for inhomogeneous moisture simulation and homogeneous control runs (mixed layer qv shown in legend) for weak shear environment with $U_s=12 \text{ m s}^{-1}$ . Inhomogeneous simulation has $16 \text{ g kg}^{-1}$ at the initiation location. ....	103
Figure 4.15: Horizontal cross-section of vertical velocity ( $\text{m s}^{-1}$ ) at $z=4.6 \text{ km}$ at $t = 4800 \text{ s}$ for weak shear ( $U_s=12 \text{ m s}^{-1}$ ) inhomogeneous moisture simulation with $q_{\text{vmix}} = 16 \text{ g kg}^{-1}$ in initial bubble location. ....	104
Figure 4.16: Horizontal cross-section of vertical velocity at $z=4.6 \text{ km}$ at $t = 2$ hours for weak shear ( $U_s=12 \text{ m s}^{-1}$ ), inhomogeneous moisture simulation with $q_{\text{vmix}}$ as shown to right. ....	105
Figure 4.17: Horizontal cross-section of the perturbation potential temperature at the lowest scalar level for the weak shear ( $U_s = 12 \text{ m s}^{-1}$ ), homogeneous moisture control run with $q_{\text{vmix}} = 16 \text{ g/kg}$ at 2 hours. (Actual computational domain is the southern half of that shown, with a symmetric condition applied at $y=96 \text{ km}$ .) ....	107
Figure 4.18: Horizontal cross-section of the perturbation potential temperature at the lowest scalar level for the weak shear ( $U_s = 12 \text{ m s}^{-1}$ ), inhomogeneous simulation with $q_{\text{v}}$ as shown in Figure 4.16 at 3 hours. ....	108
Figure 4.19: Horizontal cross section of convergence at the lowest scalar level for weak shear ( $U_s=12 \text{ m s}^{-1}$ ), inhomogeneous moisture simulation at 2.5 hours. Environmental mixed-layer mixing ratio as shown in Figure 4.16. ....	109
Figure 4.20: Horizontal cross section of convergence at the lowest scalar level for weak shear ( $U_s=12 \text{ m s}^{-1}$ ), homogeneous moisture control run with $q_{\text{vmix}}=16 \text{ g/kg}$ at 2.5 hours. (Actual computational domain is the southern half of that shown, with a symmetric condition applied at $y=96 \text{ km}$ .) ....	110
Figure 4.21: Processes leading to an asymmetric system in inhomogeneous moisture with weak shear. ....	111
Figure 4.22: Horizontal cross section of perturbation potential temperature at lowest scalar level for weak shear ( $u_s=12 \text{ m s}^{-1}$ ), inhomogeneous moisture simulation at 3 hours. Environmental mixed-layer mixing ratio as shown in Figure 4.16. ....	112
Figure 4.23: Horizontal cross section of perturbation potential temperature at the lowest scalar level for weak shear ( $U_s=12 \text{ m s}^{-1}$ ), homogeneous moisture control run with $q_{\text{vmix}}=16 \text{ g/kg}$ at 3 hours. (Actual computational domain is the southern half of that shown, with a symmetric condition applied at $y=96 \text{ km}$ .) ....	113
Figure 4.24: Horizontal cross section of vertical velocity at 3 hours at $z=4.6 \text{ km}$ for weak shear ( $u_s=12 \text{ m s}^{-1}$ ), homogeneous moisture control run with $q_{\text{vmix}}= 14 \text{ g kg}^{-1}$ . (Actual computational domain is the southern half of that shown, with a symmetric condition applied at $y=96 \text{ km}$ .) ....	114
Figure 4.25: Horizontal cross section of vertical velocity at 3 hours at $z=4.6 \text{ km}$ for weak shear ( $u_s=12 \text{ m s}^{-1}$ ), homogeneous moisture control simulation with $q_{\text{vmix}}=18 \text{ g kg}^{-1}$ . (Actual computational domain is the southern half of that shown, with a symmetric condition applied at $y=96 \text{ km}$ .) ....	115

Figure 4.26: Horizontal cross-section of vertical velocity at $z=4.6$ km at $t = 3$ hours for weak shear ( $U_s=12$ m s <sup>-1</sup> ), inhomogeneous moisture simulation with $qv_{mix}$ as shown in Figure 4.16.....	116
Figure 4.27: Setup for inhomogeneous moisture experiments with strong shear. Green disks represent a split pair of storms. Domain motion is shown with the solid arrow.....	120
Figure 4.28: Profile of east-west wind component with height for strong shear, variable moisture simulations.....	121
Figure 4.29: Domain maximum values for $w$ , $qr$ , and $qc$ for strong shear ( $U_s=30$ m s <sup>-1</sup> ), homogeneous control run with $qv_{mix}=10$ g kg <sup>-1</sup> .....	122
Figure 4.30: Domain maximum values of vertical velocity and rainwater mixing ratio for control run with $U_s=30$ m s <sup>-1</sup> and $qv_{mix}=12$ g kg <sup>-1</sup> .....	123
Figure 4.31: Horizontal cross-section of vertical velocity at $z= 4.6$ km at 3 hours for strong shear ( $U_s=30$ m s <sup>-1</sup> ) control run using $qv_{mix}=12$ g kg <sup>-1</sup> . (Actual computational domain is the southern half of that shown, with a symmetric condition applied at $y=96$ km.).....	124
Figure 4.32: Time-height diagram of maximum vertical vorticity (s <sup>-1</sup> , multiplied by 1000) for strong shear ( $U_s=30$ m s <sup>-1</sup> ) control simulation with mixed layer $qv = 12$ g kg <sup>-1</sup> .....	125
Figure 4.33: Horizontal cross-section of vertical velocity at $z=4.6$ km for strong shear ( $U_s=30$ m s <sup>-1</sup> ), inhomogeneous moisture experiment at 3 hours. Environmental values of the mixed-layer water vapor mixing ratios are shown to right.....	126
Figure 4.34: Time-height diagram of maximum vertical velocity (m s <sup>-1</sup> ) for northern cell in inhomogeneous moisture simulation with $U_s=30$ m s <sup>-1</sup> and $qv=12$ g kg <sup>-1</sup> initially, with the variation in $qv$ as shown in Figure 4.33. (Height is with respect to the lowest scalar level.).....	127
Figure 4.35: Horizontal cross section of vertical velocity at $z=4.6$ km for strong shear ( $U_s=30$ m s <sup>-1</sup> ), inhomogeneous moisture simulation at 3.5 hours. Environmental values of mixed-layer water vapor mixing ratio are shown to right.....	128
Figure 4.36: Domain maximum vertical velocity vs. time for using mixed layer mixing ratio of 10 g kg <sup>-1</sup> in both homogeneous and inhomogeneous moisture environments with $u_s= 30$ m s <sup>-1</sup> .....	130
Figure 4.37: Time-height diagram of maximum vertical vorticity (s <sup>-1</sup> , multiplied by 1000) for northern cell in inhomogeneous moisture case with $U_s=30$ m s <sup>-1</sup> and mixed layer $qv=12$ g kg <sup>-1</sup> initially, with the variation as shown in Figure 4.35.....	132
Figure 4.38: Setup for inhomogeneous moisture simulations for splitting supercells. Control runs are performed using soundings from points A, B, and C.....	133
Figure 4.39: Domain maximum values of vertical velocity for strong shear ( $U_s=30$ m s <sup>-1</sup> ) inhomogeneous moisture case and homogeneous control runs. Inhomogeneous case is initialized in a region of $qv=12$ g kg <sup>-1</sup> , with $qv$ variation as shown in Figure 4.38.....	134

Figure 4.40: Time-height diagram of maximum vertical velocity ( $\text{m s}^{-1}$ ) for southern half of strong shear ( $u_s=30 \text{ m s}^{-1}$ ) control run with mixed layer $qv = 12 \text{ g kg}^{-1}$ . (Height is with respect to the lowest scalar level). .....	135
Figure 4.41: Time-height diagram of maximum vertical velocity ( $\text{m s}^{-1}$ ) for southern half of strong shear ( $u_s=30 \text{ m/s}$ ) control run with mixed layer $qv = 14 \text{ g kg}^{-1}$ . (Height is with respect to the lowest scalar level). .....	136
Figure 4.42: Time-height diagram of maximum vertical velocity ( $\text{m s}^{-1}$ ) in southern half of domain for strong shear ( $U_s=30 \text{ m s}^{-1}$ ), inhomogeneous moisture simulation, with environmental $qv$ varying as indicated following the location of the dominant cell. (Height is with respect to the lowest scalar level). .....	137
Figure 4.43: Horizontal cross section of vertical velocity at $z=4.6 \text{ km}$ at $t=2.5$ hours for inhomogeneous moisture simulation with $U_s=30 \text{ m s}^{-1}$ and initial $qv=12 \text{ g kg}^{-1}$ . Thick line indicates the cross section used in the following figures. Only the southern half of the computational domain is shown. ....	139
Figure 4.44: Vertical ( $x$ - $z$ ) cross section at $t=9000 \text{ s}$ along line shown in Figure 4.43 for inhomogeneous moisture case with $U_s=30 \text{ m s}^{-1}$ and initial $qv=12 \text{ g kg}^{-1}$ (as in Figure 4.38). Contours indicate vertical velocity ( $\text{m s}^{-1}$ ). Domain-relative two-dimensional wind vectors are also shown. ....	140
Figure 4.45: Perturbation pressure (Pa) at $t = 9000 \text{ s}$ along line shown in Figure 4.43 for inhomogeneous simulation with $U_s=30 \text{ m s}^{-1}$ and initial $qv = 12 \text{ g kg}^{-1}$ (as in Figure 4.38). .....	141
Figure 4.46: Vertical velocity at $z=4.6 \text{ km}$ at $t=9900 \text{ s}$ for inhomogeneous simulation with $U_s=30 \text{ m s}^{-1}$ and initial $qv=12 \text{ g kg}^{-1}$ . Thick black line indicates the cross-section used in the following figures.....	142
Figure 4.47: Horizontal cross section of vertical velocity ( $\text{m s}^{-1}$ ) at $t=2.5$ hours at $z=4.6 \text{ km}$ for $13 \text{ g kg}^{-1}$ homogeneous control simulation with $U_s = 30 \text{ m s}^{-1}$ . Symmetric condition is applied at northern boundary.....	143
Figure 4.48: Perturbation pressure (Pa) at $t = 9900 \text{ s}$ along line shown in Figure 4.46 for inhomogeneous simulation with $U_s=30 \text{ m s}^{-1}$ and initial $qv = 12 \text{ g kg}^{-1}$ (as in Figure 4.38). .....	144
Figure 4.49: Vertical ( $x$ - $z$ ) cross section at $t=9900 \text{ s}$ along line shown in Figure 4.43 for inhomogeneous moisture case with $U_s=30 \text{ m s}^{-1}$ and initial $qv=12 \text{ g kg}^{-1}$ (as in Figure 4.38). Contours indicate vertical velocity ( $\text{m s}^{-1}$ ). Domain-relative two-dimensional ( $u$ - $w$ ) wind vectors are also shown (note the change in vector length compared to the previous figure). .....	145
Figure 4.50: Time-height diagram of maximum vertical vorticity in $\text{s}^{-1}$ multiplied by 1000 for southern half of strong shear ( $U_s=30 \text{ m/s}$ ), inhomogeneous moisture simulation with environmental mixed-layer $qv$ varying as shown following the dominant cell. ....	146
Figure 4.51: Time-height diagram of maximum perturbation potential temperature (K) for strong shear ( $U_s=30 \text{ m/s}$ ) control run with $qv_{\text{mix}}=12 \text{ g kg}^{-1}$ . .....	149
Figure 4.52: Time-height diagram of maximum potential temperature perturbation (K) for southern half of strong shear ( $U_s=30 \text{ m/s}$ ), inhomogeneous moisture simulation with environmental mixed-layer $qv$ as shown in Figure 4.38. ....	150

Figure 4.53: Time-height diagram of maximum vertical vorticity ( $s^{-1}$ ) times 1000 for strong shear ( $U_s=35 m s^{-1}$ ) control run with mixed-layer $qv=14 g kg^{-1}$ .....	152
Figure 4.54: Time-height diagram of maximum vertical vorticity ( $s^{-1}$ , multiplied by 1000) for strong shear ( $U_s=35 m s^{-1}$ ) control run with $qv=16 g kg^{-1}$ .....	154
Figure 4.55: Time-height diagram of maximum vertical vorticity ( $s^{-1}$ ) times 1000 for strong shear ( $U_s=35 m s^{-1}$ ) control run with $qv=17 g kg^{-1}$ .....	156
Figure 4.56: Time-height diagram of maximum vertical vorticity ( $s^{-1}$ ) multiplied by 1000 for strong shear ( $U_s=35 m s^{-1}$ ) inhomogeneous simulation with initial $qv=14 g kg^{-1}$ .....	159
Figure 4.57: Time-height diagram of maximum vertical vorticity ( $s^{-1}$ , multiplied by 1000) for strong shear ( $U_s=30 m s^{-1}$ ) control simulation with mixed layer $qv = 12 g kg^{-1}$ .....	161
Figure 4.58: Time-height diagram of maximum vertical vorticity ( $s^{-1}$ , multiplied by 1000) for strong shear ( $U_s=30m/s$ ) control run with $qvmix=14 g kg^{-1}$ .....	163
Figure 4.59: Time-height diagram of maximum vertical vorticity ( $s^{-1}$ ) times 1000 for strong shear ( $U_s=30 m s^{-1}$ ) control run with mixed layer $qv=13 g kg^{-1}$ .....	164
Figure 5.1: Setup for inhomogeneous environment for unidirectional shear simulations. Thin lines indicate shear contours on an x-y cross section of the domain.....	171
Figure 5.2: Sounding used in inhomogeneous shear simulations. (based on Weisman and Klemp 1982).....	177
Figure 5.3: Profile of east-west velocity component for inhomogeneous, unidirectional, weak shear experiments. The middle line represents the profile at the domain center, while the other two lines represent profiles at a distance 75 km to the north and south of the domain center.....	178
Figure 5.4: Horizontal cross section of vertical velocity ( $m s^{-1}$ ) at $z=4.6 km$ at $t=4200 s$ for weak, unidirectional, inhomogeneous shear as in Figure 5.3.	180
Figure 5.5: Horizontal cross section of vertical velocity at $z=4.6 km$ at $t=7200 s$ for weak ( $U_s=12 m s^{-1}$ ), unidirectional, inhomogeneous shear as in Figure 5.3.....	181
Figure 5.6: Horizontal cross section of vertical velocity at $z=4.6 km$ at $t=9000 s$ for weak, unidirectional, inhomogeneous shear as in Figure 5.3.....	182
Figure 5.7: Surface divergence (negative values dashed) at 9000 for weak, unidirectional, inhomogeneous shear as in Figure 5.3. Thick solid line indicates location of cross section shown in the following figure.....	183
Figure 5.8: Vertical (y-z) cross section of potential temperature for weak, unidirectional, inhomogeneous shear as in Figure 5.3.....	184
Figure 5.9: Profile of east-west velocity component for inhomogeneous, unidirectional, strong shear experiments. Middle line corresponds to the profile at the domain center, while the other two lines represent profiles at locations 75 km to the north and south of the domain center.....	186
Figure 5.10: : Vertical velocity at $z=4.6 km$ and $t=2 hours$ for strong shear ( $U_s=22 m s^{-1}$ ), unidirectional shear case as in Figure 5.9.....	188
Figure 5.11 Vertical vorticity ( $s^{-1}$ ) multiplied by $10^5$ at $z=4.6 km$ and $t=2 hours$ for strong ( $U_s=22 m s^{-1}$ ), inhomogeneous, unidirectional shear case as in Figure 5.9.....	189

Figure 5.12 Vertical velocity at $z=4.6$ km and $t=3$ hours for strong ( $U_s=22$ m s <sup>-1</sup> ), unidirectional shear case as in Figure 5.9. (Note the aspect ratio is exaggerated in this plot).....	190
Figure 5.13: Variation of the $u$ term in the Bulk Richardson Number for the environment in which shear varies along the mean wind. Computational domain location at 0, 2.5, 3.5, and 4 hours is shown.....	194
Figure 5.14: Hodographs for domain locations as shown in Figure 5.13.....	195
Figure 5.15: Horizontal cross-section of vertical velocity at $z=4.6$ km for weak shear (profile A in Figure 5.14) homogeneous control run at $t = 2.5$ hours. ....	197
Figure 5.16: Horizontal cross-section of vertical velocity at $z=4.6$ km at $t=4$ hours for homogeneous control run using sounding from initiation location in inhomogeneous domain (profile A in Figure 5.14.).....	198
Figure 5.17: Horizontal cross section of vertical velocity (m s <sup>-1</sup> ) at $z=4.6$ km at $t=2.5$ hours for homogeneous control run using sounding from the location B (297.6, 296.4) in the inhomogeneous environment shown in Figure 5.13. ....	199
Figure 5.18: Horizontal cross-section of vertical velocity at $z=4.6$ km at $t= 2.5$ hours for inhomogeneous simulation with shear varying along the mean wind as in Figure 5.13.....	200
Figure 5.19: Horizontal cross-section of vertical vorticity multiplied by $10^5$ at $z=4.6$ km at $t=2.5$ hours for homogeneous control run using profile A in Figure 5.14.....	202
Figure 5.20: Horizontal cross-section of vertical vorticity at $z=4.6$ km at $t=2.5$ hours for inhomogeneous shear simulation with shear varying along the mean wind as in Figure 5.13. (Note the change in contour interval).....	203
Figure 5.21: : Horizontal cross-section of vertical velocity at $z=4.6$ km at $t=11100$ s (3:05 hours) for inhomogeneous shear simulation with shear varying along the mean wind as in Figure 5.13.....	204
Figure 5.22: Horizontal cross-section of vertical velocity at $z=4.6$ km at 4 hours for inhomogeneous shear simulation with shear varying along the mean wind as in Figure 5.13.....	205

## **Abstract**

Severe storms are typically simulated assuming either an idealized, horizontally homogeneous environment or an observed inhomogeneous environment. These represent opposite ends of the spectrum, and both have limitations with regard to our understanding of severe storms. Conclusions drawn from the former are difficult to generalize because real storms often move through environments that exhibit considerable spatial variation. Real data experiments, on the other hand, include these variations but are so inherently complex that meaningful conclusions about basic storm responses to any one factor in the environment are difficult to construct.

In this study, horizontal variations in vertical shear and low-level moisture are specified in an idealized, controlled manner so that their influence can readily be diagnosed. Simulations are performed using the Advanced Regional Prediction System (ARPS) with significant modification to accommodate the inhomogeneous, but idealized, environmental fields. Development of appropriate boundary conditions for these experiments was particularly challenging and is described herein.

Inhomogeneous environments that remain steady are optimal for interpretation and for proper boundary conditions but are difficult to devise. However, we present several that retain a good degree of realism and are scientifically interesting. In all of the results to be presented, simulations in the inhomogeneous domain are compared to control simulations of storms in homogeneous environments using soundings taken from different locations in the inhomogeneous domain.

We show results in which the low-level moisture varies meridionally in an environment with westerly shear. The resultant propagation of the storm system toward the higher moisture region and the differences between high and low shear cases are examined.

It is found that storms in weak, unidirectional shear environments propagate toward the higher moisture region in time. Initially, this results from favored cell development in this region due to a lower level of free convection and reduced convective inhibition. The cells produced in the high moisture region are generally more intense, produce more rain, and lead to colder temperatures in the cold pool in the higher moisture region, thus enhancing the convergence on that side. This represents a feedback mechanism that causes the cells to be further favored on the high moisture flank.

In environments with strong, unidirectional shear and inhomogeneous low level moisture, a split pair of storms forms, with the left-moving (right-moving) storm encountering lower (higher) values of moisture over its lifetime. Examination of the left-moving storm reveals that *an existing cell can continue to survive even when it moves into an environment with moisture that is insufficient to generate and sustain a storm*. The cell, though weakened, continues to exist for over an hour. On the other hand, the right-moving storm updraft increases in strength and mid-level rotation until it interferes destructively with a redevelopment cell. The influence of low-level moisture on low-level vorticity is more ambiguous due to the interactions among cells.

Simulations in which the vertical shear varies spatially without moisture variations also are presented. It is found that multicell storm systems with a gradient of shear across them experience preferred cell development on the flank with higher shear. When the average shear is higher (i.e., in the borderline multicell/supercell regime), however, cell development is enhanced on the low shear flank while cell organization is enhanced on the strong shear side. In the most interesting case, an idealized environment is constructed such that a multicell storm system moves into a region of much stronger shear over its lifetime. In this case, the multicell system develops a bow echo structure in time.

Thus, storms in both strong and weak shear environments are found to respond to changes in their environment, but the nature of the response is different. The response of key storm attributes, such as updraft strength and mid and low level vorticity, to the prescribed changes is presented.

## **Chapter 1 Introduction**

Severe convective storms represent one of the most important and challenging problems for forecasters. For this reason, great effort has been devoted to studying storm initiation and evolution, as well as the environmental factors governing overall storm structure, through the use of observations, theoretical analyses, and numerical simulations. In particular, a large body of research has focused on the classification of storms into particular types according to rotational characteristics, intensity, and longevity, with the goal of determining environmental indices that uniquely predict those types. Although results from these studies have been extremely useful to forecasters, several important questions remain unanswered (see below).

Our knowledge of severe storms has increased greatly through theoretical and modeling studies. In order to keep the problem tractable, however, all of these studies include certain assumptions about the storm and/or its environment. Theoretical analyses generally assume an isolated, symmetric updraft in an unchanging and horizontally homogeneous, inviscid, and Boussinesq environment. These studies are useful primarily for studying the origin of rotation in severe thunderstorms and, therefore, generally concentrate on supercells. However, they do not provide us with an understanding of a storm's response when its environment changes as it moves. They also do not tell us if a storm will become preferentially biased toward one side or will significantly change its motion when it is in an inhomogeneous environment.

Computer simulations make possible the study of deep convective storm evolution for a wide variety of idealized environmental conditions. Indices relating specific environmental characteristics such as buoyancy and shear were devised and proved to be very useful discriminators of storm type (e.g., Weisman and Klemp 1982, 1984). Once again, however, the focus was generally on a storm evolving from an initial, isolated bubble in an *unchanging, horizontally homogeneous environment, even when the simulated storm traveled several hundred kilometers* (Skamarock et al. 1994a; Figure 1.1). Because horizontal variations on the mesoscale are common, storms can be expected to encounter significant variations over their lifetime. Forecasters have recognized this and often address this possibility in their outlook statements, but have not been given the tools to predict the influence of inhomogeneities on storm dynamics.

Predictions based on observed environments also offer little to increase our understanding because of the concomitant variations in important environmental characteristics. For example, vertical shear and convective available potential energy (CAPE) often vary at the same time, making it difficult to deduce the influence of either one with any certainty. In addition, prediction models, by necessity, include surface features such as terrain, soil properties, and radiative fluxes. Given the complex, uncontrolled variations in almost every aspect of the observed environment, real-data predictions make virtually impossible the assessment of basic storm responses to environmental variations. Similarly, idealized inhomogeneous environments based on geostrophic balance of the environment are also highly complex and do little to further our

understanding of fundamental storm responses to these inhomogeneities (e.g., Skamarock et al., 1994b).

Thus, the literature reveals that the field of meteorology has moved from simple 3-D simulations of isolated storms in *horizontally uniform* environments to full storm-scale predictions (Droegemeier, 1997) or idealized, but highly complex, inhomogeneous environments, and has neglected the area in-between -- an area which is essential if the latter are to be properly interpreted. *This study seeks to bridge this gap in understanding by conducting carefully designed numerical simulations of storms in idealized but horizontally inhomogeneous environments. The simulations are designed to provide clear responses to variations in one particular characteristic at a time in order to aid the interpretation of results.* The motivation for this study comes from well-documented *and ubiquitous* observations showing large environmental variability in environmental characteristics. The variations addressed in this study are in the form of constant gradients at the meso- $\alpha$  scale rather than discontinuities (boundaries) at much smaller scales.

In particular, we examine the influence of variations in vertical shear and low-level moisture because previous studies (e.g., Weisman and Klemp, 1982, 1984) have shown these to have a significant influence on storm morphology. It is reasonable to assume that changes in these quantities over the lifetime of a storm will also be important. For example, if a storm is initiated in a region with moisture and shear values that support storm formation, but then travels into a region that would not support a storm from initiation, will the well-developed

storm be able to persist? If a storm has low-level rotation but moves into a region that does not produce low-level rotation for storms developing in that environment, will the rotating storm continue to rotate? If a storm system develops in an environment with shear values that support only ordinary cells, will it develop into a more organized system if the environmental shear increases over its lifetime?

It is also reasonable to expect that inhomogeneities in vertical shear and low-level moisture could significantly alter the spatial development or propagation of storm systems. For example, will a system composed of ordinary cells develop preferentially toward regions of higher moisture or more favorable vertical shear? Will a supercell's motion deviate toward higher moisture regions? In all cases, how are the responses to inhomogeneities different for ordinary cells versus supercells?

Many of the theories devised to explain the onset of rotation in a developing updraft rely on linear theory; after a storm is fully-developed, nonlinear effects also are significant so that simple extensions of linear theory are not justified. Theories which *do* take into account nonlinearities in the flow (using Ertel's theorem to examine the relation between vortex lines and isentropic surfaces with time) are not as straightforward when the environment does not begin as a horizontally homogeneous base state. Also, ALL of the theories for the onset of rotation in a sheared environment consider only one updraft (or a split pair). In the case of a multicell, several updrafts may be present and may interact with one another (Shapiro and Kogan, 1994) as they move into a region of more

favorable vertical shear. This interference/enhancement may cause completely different results than would be expected for an isolated 'bubble' in the new environment. In addition, spatial variations in moisture may change the timing and location of redevelopments, altering the nature of cell interactions.

*The forecasting challenge posed by these situations makes this a problem of considerable practical significance, and the previous emphasis almost exclusively on storms in either homogeneous or highly complex environments makes this study unique. As stated by Rotunno (1993), 'I believe we are at the point where the modeler can start looking upscale, to understand how these thunderstorms behave in horizontally inhomogeneous, time-dependent environments,' and by Klemp (1987), '...the storm-initiation processes and the interactions between storms and with the larger-scale environment greatly complicate the prospects for forecasting the precise time and location of tornadoes with a significant lead time. Further research in these areas will be necessary in order to improve this outlook substantially.'*



**Figure 1.1: Squall line simulation by Skamarock et al. (1994a).**

## **Chapter 2 Background**

Before discussing the details of the proposed study and the preliminary results, it is instructive to review previous research that has a direct bearing on this project. Because the research to be performed concentrates on the evolution of storms in variable environments, it is crucial to grasp the current understanding of the relationship between storm morphology and the environment, particularly currently accepted theories of storm propagation and rotation. An appreciation of the historical evolution of this understanding also is important.

### **2.1 Storm Types: General Features, Relationship to Environmental Characteristics**

Thunderstorms have long fascinated the human imagination, and theories for their existence have long been sought in order to increase our predictive ability. Observations, theoretical analyses, and computer simulations form the basis of our current understanding.

Early on, it was recognized that a variety of storms exist, and that storms which produce large tornadoes, destructive winds, and/or hail generally move with velocities different than the mean wind in the convective layer (Newton and Newton, 1959; Hirschfeld, 1960) and have net updraft rotation. Although these storms form in the presence of strong environmental shear, they are able to remain nearly erect in their core region, with displacement of cloud and precipitation

material in the downstream direction occurring predominantly at upper levels in the anvil (Hitschfeld, 1960).

Browning and Ludlam (1962) performed a careful analysis of the Wokingham severe storm and recognized that a storm could persist only if the updraft and downdraft are separated so as to avoid interference. This finding was in sharp contrast to characteristics of the ordinary 'airmass' thunderstorm, in which precipitation forms and descends within the updraft core, resulting in a built-in self-destruct mechanism. They also verified radar features associated with especially severe storms, including the forward overhang, the vault, and the 'wall' (similar to the 'hook' (Browning and Donaldson, 1963)).

Browning (1962) clarified the distinction among storms of varying severity by examining the behavior of other storms also present on the day of the Wokingham storm. The motion of each echo-mass consisted of two parts: the translational velocity of the individual cells composing the storm, as well as the position of formation and dissipation of cells (i.e., discrete propagation). Weak storms showed little organization and simply consisted of an irregular cluster of weak cells, each moving approximately in the direction of the mean wind in the convective layer. The more severe storms, however, showed significant organization with new development occurring on the right flank. As individual cells formed there, moved with the mean wind, and dissipated on the left flank, the overall storm motion was to the right of the mean wind. The highest level of organization in Browning's study occurred when the cells of one of these organized storms 'amalgamated' to form a 'supercell', a 'single large cell with

horizontal dimensions of the order of 10 mi'. From this point on, storms consisting of multiple irregular cells were termed 'multicells', those showing a degree of organization due to preferred growth of new cells on one flank were termed 'organized multicells', and the quasi-steady single cell of greater horizontal extent and long duration, generally associated with the most severe weather, was given Browning's original name, the supercell.

The overall airflow pattern proposed by Browning and Ludlam was

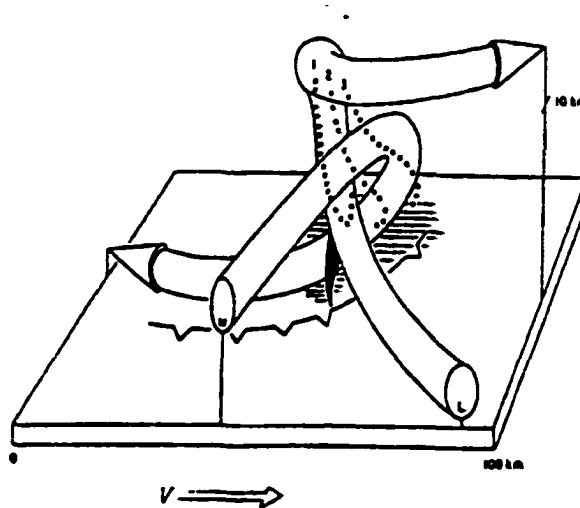


**Figure 2. 1: Browning model of airflow within a severe storm moving to the right of the winds in the middle troposphere. (From Browning, 1964).**

extended (Browning, 1964) to the particular case of supercells moving to the right of the mean wind in an environment characterized by significant shear with winds veering strongly with height (Fig. 2.1), a motion that allows mid-level air to enter the storm from the right flank and curve around the updraft to the forward flank, where falling precipitation causes evaporational cooling and a downdraft. This inflow of mid-level air was not possible in the original Wokingham 2-D model of airflow. The 3-D model is more consistent with the development of an intense downdraft as well as with precipitation trajectories, and later computer simulations (Klemp et al., 1981) have shown it to be amazingly accurate, especially when one considers that it was inferred without the help of numerical simulations or Doppler radar. (Klemp et al. (1981) did, however, show that trajectories through a modeled supercell turn anticyclonically with height.)

The premise that all cells within multicell storms move with the mean environmental wind was challenged by Marwitz' (1972b) observations. In his study, cells were observed to move to the right of the mean winds in one storm and to the left in another while discrete propagation occurred on the right flank for both, resulting in storm motions to the right of the mean winds and parallel to the mean winds, respectively.

Marwitz (1972a,b,c) also sought to describe the environments characterizing particular storm types. He noted that supercell environments contain strong thermal instability, subcloud winds  $> 10 \text{ m s}^{-1}$  which veer by  $> 60^\circ$  from the mean environmental winds, and environmental wind shear through the cloud layer with values between  $2.5 \times 10^{-3} \text{ s}^{-1}$  and  $4.5 \times 10^{-3} \text{ s}^{-1}$ . Conversely, light

winds in the subcloud layer are the distinguishing feature of a multicell environment.

Observations also indicated the phenomena in which an initial cell 'splits' into two, counter-rotating cells (Fujita and Grandoso, 1968; Browning, 1968). (The mechanisms governing this split are intimately related to the rotational dynamics of the storm, as will be discussed in section 2b.)

With the advent of computer technology, it became possible to study the evolution of storms in specified environments. The first realistic simulations were done in 2 dimensions (e.g., Wilhelmson and Ogura, 1972) but were shown to have fundamental limitations when compared with those in three dimensions (e.g., Wilhelmson, 1974; Schlesinger, 1984) or in axisymmetric (Soong and Ogura, 1973) domains. In particular, 2-D updrafts were substantially weaker than their 3-D counterparts owing to an exaggerated adverse vertical pressure gradient, and compensatory dry downflow was stronger relative to the updraft speed. It also became clear that only 3-D simulations could properly simulate the interaction between a circularly symmetric updraft and the environmental shear (Cotton and Tripoli, 1978), and properly characterize the turbulent transfer of energy (Lilly, 1982, 1986).

Tapp and White (1976) presented a 3-D, non-hydrostatic, compressible mesoscale model and models of this type soon became the standard. Klemp and Wilhelmson (1978a) designed a cloud model which was fully compressible yet computationally feasible due to a unique method of integration that handled the time-intensive sound wave terms in a separate step from the less-restrictive

advective terms. This unique method of 'time-splitting' made it possible to perform long integrations of the equations governing deep convection.

Some of the first 3-D simulations studied storm splitting and were carried out by Wilhelmson and Klemp (1978; 1981), Klemp and Wilhelmson (1978a,b), Thorpe and Miller (1978), Schlesinger (1980) and Clark (1979). The dynamics governing the splitting phenomenon will be considered in the next section, while here we focus on the characteristics of environments which promote splitting.

Both Thorpe and Miller (1978) and Wilhelmson and Klemp (1978) noted the fundamental importance of strong storm-relative winds at low levels to inhibit gust front propagation away from the updraft. Thorpe and Miller surmised that the environment conducive to splitting cells has a storm-relative wind field such that the upper and lower wind vectors are in opposition and there is substantial relative inflow. Conversely, the multicell was surmised to develop in environments with weak inflow incapable of preventing the cold outflow from moving away from the updraft center. As we will see below, these wind profiles adhere to the currently accepted theories, although they are a subset of the more general criteria.

The series of studies by Wilhelmson and Klemp were more extensive, involving several shear profiles in order to determine the critical factors for cell splitting. They showed that strong shear at and just above cloud base is important for the splitting process. In their simulations with a unidirectional hodograph, a split occurred as precipitation formed in the initial updraft, resulting in a right-

moving cyclonically-rotating storm and a mirror-image left-moving anticyclonically-rotating cell.

Clark's (1979) multicell simulations resembled those of Klemp and Wilhelmson, although he claimed the splitting process was *not* due to precipitation effects, but rather was caused by entrainment at the front of the updraft due to the vortex pair created through tilting of environmental vorticity by the axisymmetric updraft. He asserted that this vortex pair necessary for entrainment and subsequent splitting was a direct result of the initialization process, partially explaining the differing results of Thorpe and Miller who used a localized heat source/sink in their initialization (Miller and Pearce, 1974).

Klemp and Wilhelmson (1978b) also examined the influence of microphysics and found that a split did not occur if conversion of cloud water to precipitation was forbidden, but did occur if precipitation formation was allowed but evaporative cooling was forbidden. Experiments including the Coriolis force showed substantial enhancement of the cyclonic vorticity in the right-moving storm leading to the formation of a hook echo, but little difference in updraft intensity or rain production. This ruled out the Coriolis force as the cause for the predominance of cyclonic, right-moving storms in the Northern hemisphere. Instead, they showed that this bias occurs when the hodograph turns clockwise with height. Klemp and Wilhelmson (1978b) attributed this enhancement of the right-mover over the left-mover to increased mid-level inflow hypothesized to strengthen the downdraft and subsequent convergence. However, in later studies (Wilhelmson and Klemp, 1981; Klemp et al., 1981), they attributed the slower

development of the left-moving storm in an environment with a clockwise hodograph to an unfavorable low-level vertical pressure gradient. An outline of this mechanism was provided in the appendix of Klemp et al. (1981) with further development given by Rotunno and Klemp (1982) using a simplified model to study the linear and nonlinear effects of vertical wind shear on storm rotation and propagation (see next subsection).

Various observations (Marwitz, 1972a,b,c) as well as theoretical studies (e.g., Moncrieff and Green, 1972) and the numerical simulations cited above suggested a relationship between storm type and the buoyancy and shear of the environment. This relationship was clarified by Weisman and Klemp (1982) using the Wilhelmson-Klemp model to examine over 80 combinations of buoyancy and shear. These simulations used analytic thermodynamic and moisture profiles with the mixed-layer mixing ratio altered to provide varying values of parcel buoyancy. The buoyancy values used were consistent with those typical of severe storm environments ( $1000-3500 \text{ J kg}^{-1}$ ), while the humidity profile was admittedly untypically moist in midlevels. Vertical shear ( $0-0.008 \text{ s}^{-1}$ ) was confined to the lowest 5 km and was unidirectional. *In all simulations, convection was initiated with a thermal perturbation and the environment was horizontally homogeneous. Thus, these simulations predict the evolution of storms that remain in the same environment in which they were initiated. The results do not necessarily extend to cases where a storm system moves into a*

*different environment or has significant variation across it. The current study is designed to address these situations.*

Storm structure was found to be separated into two distinct modes - secondary redevelopment similar to multicells, and splitting cells representing supercells. These two types were found to depend upon the bulk Richardson number (BRN) of the environment, defined by

$$\text{BRN} = \frac{\text{CAPE}}{\frac{1}{2}\bar{u}^2}$$

where  $\bar{u}$  is the difference between a density-weighted mean wind speed taken over the lowest 6 km of the profile and an average surface wind speed taken over the lowest 500 m of the profile, and the convective available potential energy (CAPE) is defined by

$$\text{CAPE} = g \int_{\text{LFC}}^{\text{EL}} \frac{\theta_p(z) - \bar{\theta}(z)}{\bar{\theta}(z)} dz.$$

Here EL refers to the parcel equilibrium level, LFC is the level of free convection,  $\theta_p$  denotes the potential temperature characterizing moist adiabatic ascent of a surface parcel based on a 500 m mean temperature and moisture value,  $g$  is gravity, and  $\bar{\theta}$  is the environmental potential temperature. (In the present study, we also use the virtual potential temperature in the determination of CAPE as it provides a better representation of the true buoyancy (Doswell and Rasmussen, 1994).)

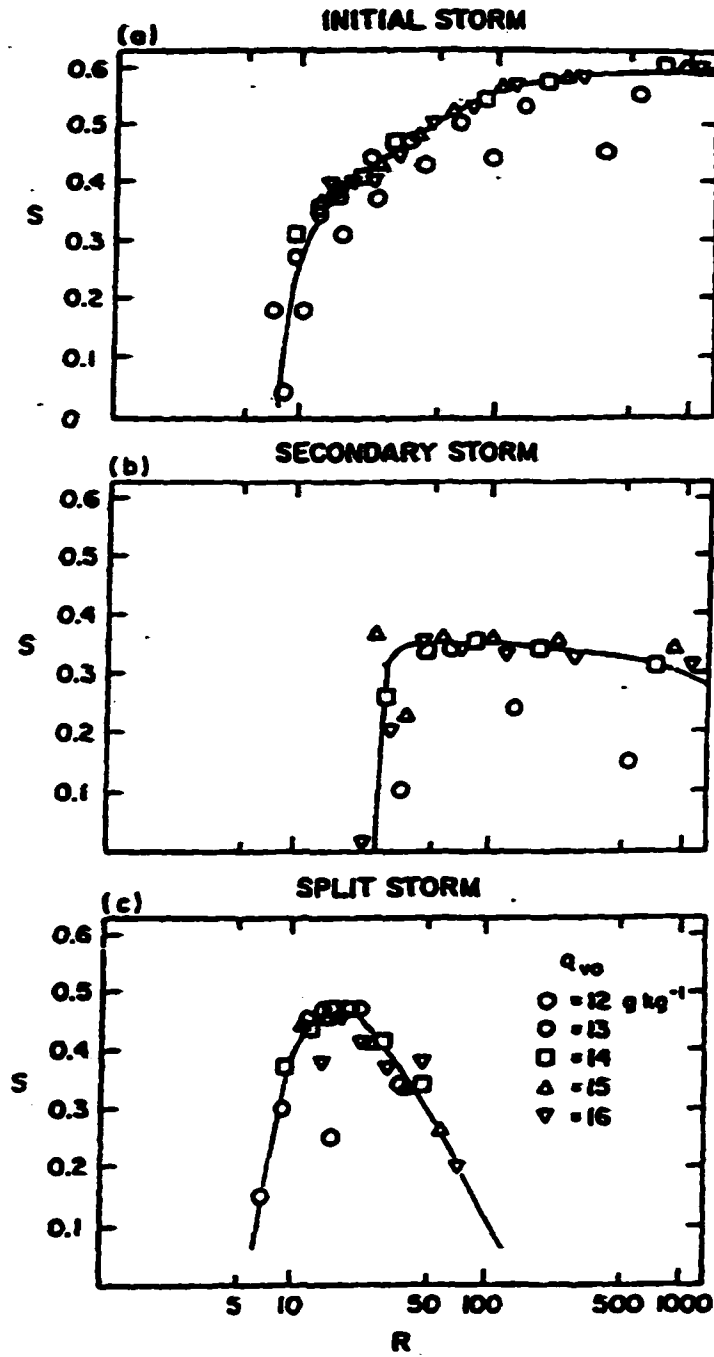


**Figure 2. 2: Storm strength [ $S=(w_{max})/(2CAPE)^{1/2}$ ] versus BRN for (a) initial storms, (b) secondary storms, and (c) split storms. (from Weisman and Klemp, 1982)**

The results of Weisman and Klemp (1982) are shown in Figure 2.2, and indicate a predominance of split storms (supercells) for  $BRN < 50$  and a predominance of secondary (multicell) storms for  $BRN > 35$ . With a constant value of CAPE, increased shear was found to decrease the strength of the initial buoyant plume due to increased entrainment, but to aid later redevelopments.

In the secondary redevelopment case, which occurred for low to moderate wind shear, distinct new cells developed along the boundary of the storm-induced outflow near the surface, and their updrafts had no preferred rotation. These new cells tended to form downstream from the initial updraft, in the region where the outflow directly opposed the shear-induced inflow. Thus, convergence along the gust front was the dominant mechanism for initiating subsequent cells. This initiation depended on weak stability of the low-level environment such that lifting by the gust front enabled air to reach its LFC, and also on the sufficiently slow speed of the gust front such that inflow could be supplied to the new updraft for a significant time.

The second regime, referred to as storm splitting, occurred for higher values of shear for the same value of CAPE, and produced two equal, self-sustaining storms which propagated continuously to the right and left of the mean shear vector for a unidirectional hodograph. The updraft of the rightward moving storm rotated cyclonically, while that of the leftward moving storm rotated anticyclonically. From these results, Weisman and Klemp concluded that a necessary condition for the development of steady, split storms is storm-relative

inflow strong enough to keep the outflow from propagating away from the updraft.

One of their interpretations of this dependence of cell redevelopment on buoyancy and shear depends on the assumption that CAPE magnitude is related to downdraft strength, i.e., that as CAPE increases, the strength of the downdraft outflow also increases, presumably due to the increased rain production and evaporative cooling. Thus, the theory would suggest that for larger CAPE a more intense downdraft is produced and larger shear is needed to prevent the gust front from traveling away from the updraft too quickly.

Weisman and Klemp interpret the denominator of the BRN (referred to as BRNshear) as a measure of both the low-level wind shear and the inflow kinetic energy made available to the storm by the vertical wind shear. The latter interpretation assumes that the storm moves roughly with the mean 0-6 km wind, so that  $\bar{u}$  represents the storm-relative surface inflow. BRNshear also indicates the degree to which rotational properties will be important due to the tilting term in the vorticity equation (see the following section).

Thus, by combining bulk measures of shear and buoyancy, Weisman and Klemp produced simulations which agreed quite well with the observed severe storm behavior. *These results are limited, however, to storms forming in a homogeneous environment, and it is unclear how storms evolve when moving in environments with variable BRN, which is one focus of our present study. For example, if a storm begins in a high BRN environment and develops as a*

*multicell, how will it adjust if it moves into a region of greater shear (lower BRN)?*

Weisman and Klemp (1984) extended their study to include the effect of directionally varying wind shear and found the updraft intensity and the correlation between vertical velocity and vertical vorticity for the right-moving storm were enhanced compared to the left flank storm for a clockwise-curved hodograph. They explained their results with the help of Rotunno and Klemp's (1982) model for the interaction of an updraft with the environmental shear, to be described in the next section.

Skamarock et al. (1994b) simulated a squall line in an inhomogeneous environment in thermal wind balance such that vertical shear was accompanied by horizontal variations in temperature. They then varied both the shear and the moisture along the line to show that 'the evolution of a linear, symmetric MCS into an asymmetric MCS is not dependent on the existence of horizontal inhomogeneities in the convective environment.' They found that 'the along-line variability in convective potential serves to enhance or repress convective development on the northern or southern flanks of the system and hence modify system propagation'. However, because the simulations included the Coriolis force and because the variations in moisture were accompanied by variations in temperature and shear, it is unclear what determined the system propagation. Also, because the moisture was varied independent of the pressure and temperature, it is unclear that their environment was steady.

## **2.2 Theories of Storm Propagation and Rotation**

A theory for anomalous storm propagation (i.e., motion differing from pure advection by the mean winds, such as Browning's model of the right-moving storm) was put forth by Newton and Newton (1959), who treated the updraft as an obstacle in the environmental flow and calculated perturbation pressures associated with this 'blocking' due to momentum transport within the cloud. They concluded that hydrodynamic pressure fields induced by the obstacle (updraft) can produce vertical accelerations independent of and comparable in strength to ordinary buoyancy forces, enabling negatively-buoyant air to be lifted to its level of free convection. For a clockwise-turning environmental wind vector, these pressure perturbations correspond to an enhancement of upward vertical motion in the right-hand portion of the storm with respect to the mean environmental winds. This explanation for updraft motion was generally accepted for many years. However, it is incomplete for several reasons.

For example, it does not consider the rotation of the updraft, which will affect the pressure perturbations. Additionally, although an updraft moving at a speed slower than that of the mean wind does exert a stress on the environmental winds due to eddy momentum transport within the storm, the environmental air is not completely blocked. In fact, later three-dimensional numerical simulations (e.g., Klemp et al, 1981) show that, while stagnation points do exist at many levels, true obstacle flow is approximately valid only at upper levels. Finally, the proposed pressure distribution does not agree with the analytical solution for a Beltrami flow (Davies-Jones, 1985).

Other theories for storm propagation stemmed from the observation of storm splitting (Hitschfeld, 1960; Browning, 1964). The first of these was by Fujita and Grandoso (1968), who surmised that low-level outflow produced new cells downstream from a circular updraft in the same region as existing counter-rotating vortices formed by the diversion of environmental flow around the initial updraft. Assuming that horizontal slices of these counter-rotating updrafts could be approximated by a circular, rotating undiluted disk of subcloud air acted on by an ambient pressure gradient force, Coriolis force, a drag force (parallel to the oncoming stream, due to the difference between the translation of the updraft and the speed of the ambient winds), and a lift source (perpendicular to the oncoming stream, due to the 'Magnus effect' of a rotating cylinder), they predicted diverging cell motions such that the cyclonic storm moved to the right and the anticyclonic storm moved to the left. While the resulting motions agreed with observations, they were later replaced by theories based on results from fully three-dimensional simulations which did not rely on obstacle flow theory and did not require a discrete redevelopment process. The Fujita-Grandoso theorem is conceptually flawed since the pressure gradient force acts on individual air parcels, not on rotating solid disks of air. The theory does not explain dynamically how an internal fluid surface (e.g., cylindrical updraft) comes to behave like an impermeable (i.e., solid) surface.

Rotunno and Klemp (1982) explained the enhancement of the right-moving member of the split pair in the case of a veering shear vector using a model consisting of the following shallow, inviscid, anelastic equations

$$\frac{\partial \vec{v}}{\partial t} + \vec{v} \cdot \nabla \vec{v} = -\nabla \pi + B \hat{k} \quad (2.1)$$

$$\frac{\partial B}{\partial t} + \vec{v} \cdot \nabla B = -N^2 w \quad (2.2)$$

$$\nabla \cdot \vec{v} = 0 \quad (2.3)$$

where  $\vec{v}$  is the 3-D velocity vector,  $B = g\theta'/\theta_0$  is the buoyancy,  $N$  is the Brunt-Väisälä frequency, and  $\pi = [c_p \theta_0 (p/p_0)^\kappa - c_p \theta_0 (\bar{p}/p_0)^\kappa]$  where  $p$ ,  $p_0$ ,  $R$ , and  $c_p$  are the pressure, ground pressure, universal dry air gas constant and the specific heat at constant pressure, respectively, and  $\bar{p}$  is the environmental, hydrostatic pressure. The potential temperature is given by  $\theta = \theta_0 + \bar{\theta}(z) + \theta'(\vec{x}, t)$ . The initial conditions are

$$B(\vec{x}, 0) = B_0(\vec{x}) \quad (2.4)$$

$$\vec{v}(\vec{x}, 0) = U(z) \hat{i} + V(z) \hat{j} + v_0(\vec{x}) \quad (2.5)$$

where  $B_0(\vec{x})$  and  $v_0(\vec{x})$  were chosen to be axisymmetric with respect to the vertical axis. The linearized versions of (2.1)-(2.3) about an environmental wind vector  $\vec{V} = (U(z), V(z), 0)$  are then

$$\frac{D\vec{v}'}{Dt} + w' \cdot \frac{d\vec{V}}{dz} = -\nabla \pi' + B' \hat{k} \quad (2.6)$$

$$\frac{DB'}{Dt} = -N^2 w' \quad (2.7)$$

$$\nabla \cdot \vec{v}' = 0 \quad (2.8)$$

where the primed quantities represent deviations from the environmental values

$$\text{and } \frac{D}{Dt} = \frac{\partial}{\partial t} + \vec{V} \cdot \nabla.$$

Ignoring the influence of buoyancy (i.e.,  $B=0$ ), an equation for  $\pi$  is found by taking the divergence of (2.6) and using (2.8) to yield

$$\nabla^2 \pi' = -2 \frac{d\bar{V}}{dz} \cdot \nabla w' \quad (2.9)$$

Rotunno and Klemp simplified the above relationship by assuming that  $\pi$  consisted of a narrow band of Fourier components, so that, *away from boundaries* (Davies-Jones, 1996),

$$\pi' \propto \frac{d\bar{V}}{dz} \cdot \nabla w' \quad (2.10)$$

indicating that high pressure forms on the upshear flank of the updraft with low pressure on the downshear flank. From this, they concluded that *at any given height (away from boundaries) a negative horizontal pressure gradient forms across the updraft in the direction of the environmental wind shear vector*. For a straight hodograph with constant shear, the pressure perturbations would be vertically stacked but would vary in magnitude according to  $\nabla w'$  so that the greatest magnitude is near the level of the maximum updraft. Thus, below the level of  $w_{\max}$  the vertical pressure gradient force will be upward on the downshear side of the updraft and downward on the upshear side.

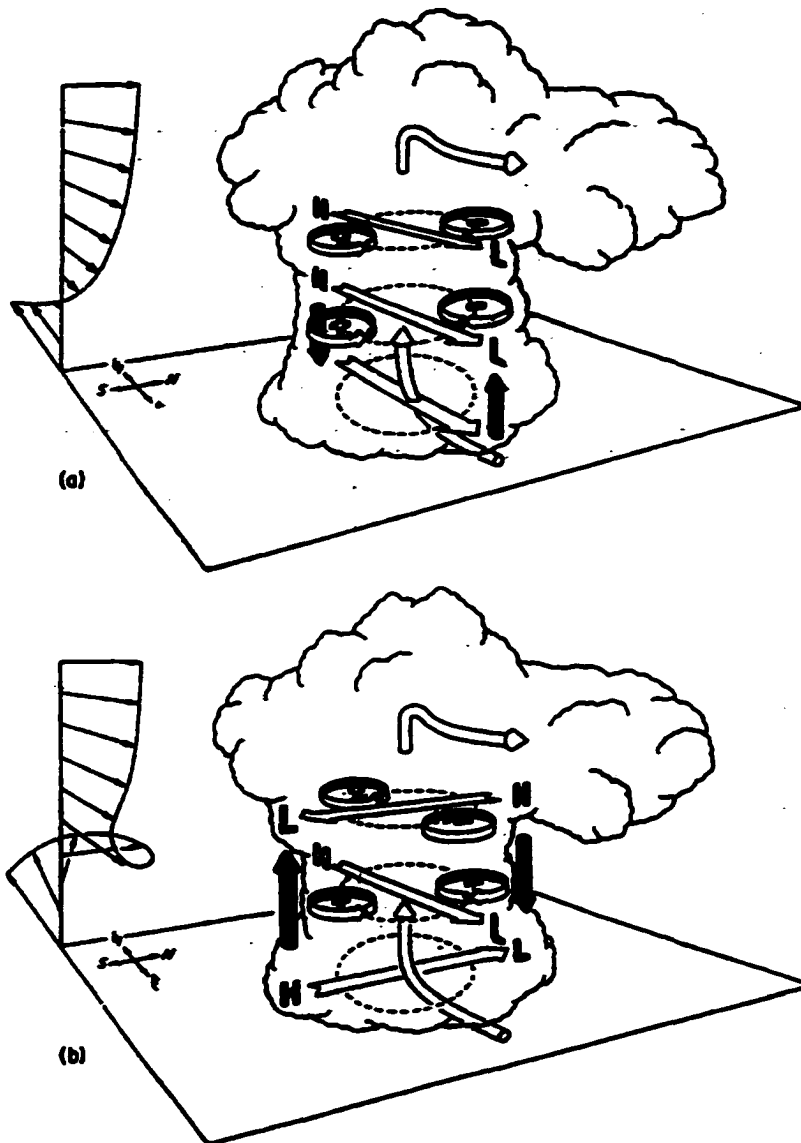


**Figure 2.3: Schematic illustrating the pressure and vertical vorticity perturbations arising as an updraft interacts with an environmental wind shear that (a) does not change direction with height and (b) turns clockwise with height (from Klemp, 1987).**

The opposite is true above the level of  $w_{\max}$ . Thus, the pressure perturbations promote propagation in the direction of the shear vector at low levels and opposite to the shear vector at upper levels; this helps to keep the updraft erect in the presence of the strong shear. When the hodograph veers with height, the pressure perturbation on the right side of the updraft (looking down the shear vector) will be lower at mid-levels than at low levels, causing an upward pressure gradient force on the right side (Figure 2.3). Conversely, the left side will be characterized by higher pressure at mid-levels and a downward pressure gradient force. It is in this manner that linear theory predicts enhancement of the right side of an updraft over the left side when the hodograph veers with height, signifying updraft propagation to the right of the shear vector.

They verified this result using a fully-nonlinear, simplified model of dry, buoyant convection setting  $N^2 = -N_w^2$  for  $w > 0$  and  $N^2 = N_d^2$  for  $w < 0$ , where  $N_w^2 = 5 \times 10^{-6} \text{ s}^{-2}$  and  $N_d^2 = 5 \times 10^{-5} \text{ s}^{-2}$ . The splitting process and enhancement of the right-moving storm could then be investigated by taking the divergence of (2.1) and using (2.3) to yield

$$\begin{aligned}
 -\nabla^2 \pi = & \left( \frac{\partial u}{\partial x} \right)^2 + \left( \frac{\partial v}{\partial y} \right)^2 + \left( \frac{\partial w}{\partial z} \right)^2 + 2 \frac{\partial u}{\partial y} \frac{\partial v}{\partial x} \\
 & + 2 \frac{\partial u}{\partial z} \frac{\partial w}{\partial x} + 2 \frac{\partial v}{\partial z} \frac{\partial w}{\partial y} - \frac{\partial B}{\partial z}
 \end{aligned} \tag{2.11}$$

The forcing terms were clarified by decomposing the perturbation pressure into its linear, nonlinear, and buoyancy-driven parts such that

$$\pi = \pi_L + \pi_{NL} + \pi_B \tag{2.12}$$

where

$$\nabla^2 \pi_L = -2 \left[ \frac{\partial U}{\partial z} \frac{\partial w}{\partial x} + \frac{\partial V}{\partial z} \frac{\partial w}{\partial y} \right] \quad (2.13)$$

$$\begin{aligned} \nabla^2 \pi_{NL} = & - \left( \frac{\partial u}{\partial x} \right)^2 - \left( \frac{\partial v}{\partial y} \right)^2 - \left( \frac{\partial w}{\partial z} \right)^2 - 2 \frac{\partial u}{\partial y} \frac{\partial v}{\partial x} \\ & - 2 \frac{\partial u}{\partial z} \frac{\partial w}{\partial x} - 2 \frac{\partial v}{\partial z} \frac{\partial w}{\partial y} \end{aligned} \quad (2.14)$$

$$\nabla^2 \pi_B = \frac{\partial B}{\partial z} \quad (2.15)$$

There are four forcing mechanisms for local change in the vertical velocity (vertical component of 2.1):  $-\partial\pi_L/\partial z$  due to the linear terms in the momentum equation,  $-\partial\pi_{NL}/\partial z$  due to the nonlinear terms in the momentum equation,  $(-\partial\pi_B/\partial z + B)$  due to the buoyancy forcing, and  $\bar{v} \cdot \nabla w$ , representing advection.

The results of the numerical integration and the decomposition of pressure show that linear forcing similar to that predicted by (2.10) does occur and is responsible for the enhancement of the right flank of an updraft in an environment with a veering wind shear vector (no other forcings show a rightward bias). Nonlinear forcing, on the other hand, is symmetric about the shear vector and is responsible for splitting.

Examining the nonlinear portion of the pressure perturbation forcing (2.14), we notice that the first three terms are related to fluid extension, while the last three terms are related to fluid shear. In particular,  $2u_y v_x = -0.5\zeta^2$  (where  $\zeta$  is

the vertical component of vorticity) for a wind field in pure rotation (i.e.,  $2u = -\zeta y$ ,  $2v = \zeta x$ ). Thus, to the extent that tilting results in pure rotation and not just equal amounts of rotation and deformation, low pressure will be created at midlevels on the flanks of the updraft. This creates upward pressure gradient forces between low and mid levels on each flank and therefore promotes splitting of the original updraft.

Weisman and Klemp (1984) extended their 1982 results to include the effect of a directionally varying wind shear and verified the results of Rotunno and Klemp (1982). They found that right flank storms were favored over left flank storms for clockwise-curved, half-circle hodographs. By decomposing the pressure into its dynamic and buoyancy driven components in a manner similar to Rotunno and Klemp, they showed that the dominant dynamic pressure feature for the right flank storms in moderately- to strongly-sheared environments with clockwise-curved hodographs is a low pressure region at low and mid levels on the right flank. The surface low pressure (mesolow) accelerates flow into the storm, helps hold back the gust front (Brooks et al., 1993a), and suppresses convection in the inflow region ahead of the storm. The dynamically-induced midlevel mesolow promotes updraft growth on the right flank. As the shear increases, the importance of the dynamic component of the pressure increases such that for high shears it becomes greater than the buoyant component over the depth of the updraft. This right flank cell also has a positive correlation between vertical velocity and vorticity as it moves to the right of the mean wind.

Conversely, for the left flank storms, the dominant dynamic pressure feature is a surface high pressure region associated with strong convergence at the gust front. Thus, for these storms, dynamic contributions due to extension terms play an important role in lifting the parcels through the lower portion of the updraft, while buoyancy accelerations dominate above 3 km. These storms also show no appreciable correlation between vertical velocity and vorticity.

Rotunno and Klemp (1985) examined the shear and extension terms in detail using the Klemp-Wilhelmson model to simulate the right-moving member of a split pair in unidirectional shear. They determined that the (negative) shear terms were indeed responsible for rightward enhancement. Recognizing that these terms are associated with rotation implies that the supercell propagates to the south mainly as a consequence of the midlevel updraft rotation that produces low pressure at midlevels on the flanks. To test the importance of midlevel rotation versus precipitation loading in promoting storm splitting, they performed a simulation in which condensation and latent heat release were permitted, but no precipitation formation from cloud droplets was allowed. In this test, the initial splitting is slowed but does occur, in contrast to the similar test by Klemp and Wilhelmson (1978b) in weaker shear. Thus rightward storm propagation is driven by rotation generated on the storm's right flank. An equal left-moving, anticyclonically-rotating storm is also produced given a straight hodograph environment. Although it is anticyclonic, its rotation still produces a low pressure at midlevels since the pressure perturbation depends on  $\zeta^2$ , not  $\zeta$  itself.

Based on these findings, Weisman and Klemp introduced a dynamical distinction between supercells and ordinary cells (of which multicells are comprised), such that a supercell is defined by the existence of dynamically induced mesolows and vertical pressure gradients to enhance the updraft, as well as significant correlation between vertical velocity and vorticity. This allows storms which go through a cyclic behavior to have individual updrafts at a given time classified as supercells. The debate concerning the distinction between multicells and supercells (e.g., Doswell, 1996) as well as the subdivision within the supercell regime itself (e.g., Doswell and Burgess, 1993) still rages, but the characteristics of deep and persistent rotation well-correlated with a persistent updraft occur in most supercell definitions. Storms with behaviors intermediate to these two extremes have been observed (e.g., Foote and Frank, 1983; Miller and Fankhauser, 1983; Nelson and Knight, 1987) and modeled (Jahn, 1995; Richardson and Droegemeier, 1996). *If the dynamical distinctions described are the key differences between supercells and ordinary cells, then one might suspect that the two types of cells will have different responses to inhomogeneities in their environment.*

In the Weisman and Klemp (1982) straight-line simulations noted previously, the southern updraft of a split storm becomes preferentially aligned with the cyclonic member of the original vortex couplet, while the northern updraft becomes preferentially aligned with the anticyclonic element of the couplet. However, in the case of secondary redevelopment, new updrafts merely produced new vortex couplets. Rotunno (1981) used semilinear theory (ignoring

all nonlinear terms except the convergence term in the vertical vorticity equation) and a prescribed vertical velocity field representative of a splitting storm to determine that the origin of initial midlevel rotation was tilting of the environmental vortex lines to form a vortex couplet straddling the updraft. As precipitation forms on the centerline of the updraft, converting it to a downdraft, the vortex tubes are tilted downward so that two vortex pairs exist. As the southern updraft travels to the right of the mean wind, it becomes colocated with the positive vorticity center at mid levels.

Lilly (1982) more clearly showed the origin of midlevel rotation under certain conditions by examining the linearized vertical vorticity equation in natural coordinates, given by

$$\frac{\partial \zeta'}{\partial t} + \bar{V}_H \frac{\partial \zeta'}{\partial s} = \frac{\partial w'}{\partial n} \frac{d\bar{V}_H}{dz} - \frac{\partial w'}{\partial s} \bar{V}_H \frac{d\bar{\psi}}{dz} + f \frac{\partial w'}{\partial z} \quad (2.16)$$

where  $V_H$  is the horizontal velocity amplitude,  $s$  and  $n$  are the coordinates along and orthogonal to the local horizontal wind vector, and  $\psi$  is the wind direction increasing counterclockwise. Lilly investigated two extremes - one given by rectilinear shear such that  $dV_H/dz$  is constant, and  $d\psi/dz=0$ . If the Coriolis force is ignored and we consider the case where  $\bar{V}_H t$  is much less than the length scale of the updraft (i.e., for times near initiation or for critical levels), the advection term on the left may be ignored and the resulting integral yields

$$\zeta' = \int \frac{\partial w'}{\partial n} \frac{d\bar{V}_H}{dz} dt \quad (2.17)$$

resulting in a vortex pair with positive vorticity to the right of the updraft center looking downshear. This would correspond to the expected behavior given an updraft growing in a unidirectionally sheared environment.

The second case is a curved mean hodograph for which  $\bar{V}_H$  and  $\frac{d\bar{\psi}}{dz}$  are constant. In this case, the advective terms are expected to dominate in time everywhere because no critical layer exists (i.e., propagation is off the hodograph). Integration of the steady-state version of (2.16) then yields

$$\zeta' = -w' \frac{d\bar{\psi}}{dz} \quad (2.18)$$

so that vertical velocity and vorticity are proportional.

The nature of this correlation between vertical vorticity and vertical velocity for storm-relative winds which veer with height was determined by Davies-Jones (1984) using linear theory of shallow, inviscid, isentropic convection in a dry, horizontally uniform, unstably stratified, nonrotating atmosphere applied to an isolated, convective storm. By introducing a new parameter, the vertical displacement of air parcels from their original level, he was able to produce a theory for rotation based on the configuration of isentropic surfaces associated with a developing updraft. Based on conservation of potential vorticity for isentropic, inviscid flow,  $\bar{\omega} \bullet \nabla\theta$  is conserved; since it is zero initially (vortex lines and isentropic surfaces are initially horizontal) it is zero for all time, so that each vortex line is constrained to remain within its original isentropic surface. Thus, the displacement of an isentropic surface corresponds to the displacement of vortex lines and can be used to directly deduce the vorticity

field. (This is in contrast to deducing the vorticity field based on the locations of greatest vorticity production which, due to advection, may not be coincident with the greatest vorticity.) Cyclonic (anticyclonic) vorticity is located on slopes of the isentropic surfaces that face toward (away from) the mean vorticity vector.

The vertical velocity field is given by the material derivative of vertical displacement and therefore has two components, one due to the growth of the displacement with time and one due to flow relative to the displacement. An updraft/downdraft pair is thus represented by a peak in the displacement field. The presence of mean flow with respect to the displacement shifts the location of maximum vertical velocity (similar to flow over a mountain) to the upstream portion of a displacement peak. Thus, when the flow has a component along the mean vorticity vector, the maximum vertical velocity and vertical vorticity will be positively correlated.

Dividing the vorticity into components parallel to the storm-relative mean wind (the  $p$  direction) and perpendicular to the storm-relative mean wind (the  $q$  direction), we obtain

$$\bar{\omega} = -\left[\bar{v} - \bar{c}\right] \frac{d\psi}{dz} \hat{p} + \frac{d\left[\bar{v} - \bar{c}\right]}{dz} \hat{q} = \omega_s \hat{p} + \omega_c \hat{q} \quad (2.19)$$

where  $\omega_s$  is referred to as the streamwise vorticity and  $\omega_c$  is referred to as the crosswise vorticity. We see that the streamwise vorticity is related to the storm-relative wind speed as well as the rate at which the storm-relative winds veer with height, while the crosswise vorticity is related to the storm-relative speed shear. When we assume the displacement peak is axisymmetric, the correlation

coefficient between vertical velocity and vertical vorticity is predicted by linear theory to be

$$r \approx \frac{\omega_s}{\omega} (P^2 + 1)^{-1/2} \quad (2.20)$$

where  $P$  is given by

$$P = \sigma D / |\bar{v} - \bar{c}|. \quad (2.21)$$

Here  $\sigma$  is the growth rate of the displacement and  $D$  is a typical length scale for horizontal gradients of buoyancy. Thus, there will be larger correlation between vertical velocity and vertical vorticity when the storm-relative winds are strong or the growth rate of the disturbance is small (small  $P$ ), and the vorticity is mostly streamwise. This result is physically reasonable because large storm-relative flow displaces the region of maximum vertical velocity upstream from the displacement peak, which is the same location as the vertical vorticity in the purely streamwise case. When the growth of the displacement field is large, the correlation decreases as a component of positive vertical velocity is generated in regions of both positive and negative vorticity. Note that this is consistent with (2.17) where it was assumed that storm-relative advection terms are small ( $P \gg 1$ ).

Rotunno and Klemp (1985) used similar reasoning based on conservation of equivalent potential vorticity  $\frac{1}{\rho} [\bar{\omega} \cdot \nabla \theta_e]$ , where  $\theta_e$  is the equivalent potential temperature. Assuming that  $\theta_e$  is nearly conserved, that there is a near one-to-one correspondence between  $\theta_e$  and buoyancy, and that diffusion is not important, equivalent potential vorticity is approximately conserved. In their simulation of a

right-moving storm, they showed that vortex lines are indeed tilted along with the isentropic surfaces, producing cyclonic vorticity to the right of the updraft and anticyclonic to the left. They claim that as the updraft propagates to the south due to the midlevel rotation, the vertical velocity and vorticity tend to come into phase.

Thus, mid-level rotation is caused primarily by tilting of environmental vortex lines as isentropic surfaces are deformed by the updrafts and downdrafts. The correlation between the vertical velocity and vertical vorticity depends on the magnitude of the storm-relative winds and the change in direction of the storm-relative winds with height. A measure of this change in direction, is given by the storm-relative environmental helicity (SREH),

$$\text{SREH}(\bar{c}) = \int_0^h (\bar{v} - \bar{c}) \cdot \bar{\omega} dz = - \int_0^h \hat{k} \cdot (\bar{v} - \bar{c}) \times \frac{\partial \bar{v}}{\partial z} dz \quad (2.22)$$

where  $\bar{c}$  is the storm motion vector,  $\bar{v}(z)$  is the environmental wind profile, and  $\hat{k}$  is the unit vector in the vertical. Geometrically, this quantity represents minus twice the area swept out by the storm-relative velocity vector between 0 and h on a hodograph. Davies-Jones et al. (1990) found that the storm-relative helicity through 3 km shows promise as a tornado forecasting tool, with values of SREH greater than  $150 \text{ m}^2 \text{ s}^{-2}$  associated with tornado formation.

Storm-relative environmental helicity was shown to be a better predictor of net updraft rotation than the BRN by Droegemeier et al. (1993) who suggest using BRN to predict storm type for a given environment and SREH to

characterize the rotational properties of storms once their motions can be established. Brooks and Wilhelmson (1993) also showed that peak updrafts in simulated storms are greater for larger values of environmental helicity. This was attributed to an upward pressure gradient force dependent on the magnitude of the storm-relative winds and the rate at which wind direction increases with height using a simple Beltrami flow solution. This conclusion is in agreement with Lilly (1986), who showed that the transfer of energy from the rotational to the overturning components is maximized when the updraft and vortex coincide. However, Jahn and Droegemeier (1996) showed that SREH was a worse predictor of both storm type and mesocyclone intensity than BRN in their simulated storms in which SREH and BRN were allowed to vary independently.

Thus far we have primarily considered midlevel rotation; however, slightly different reasoning is required to explain low-level rotation. Klemp and Rotunno (1983) surmised in their simulation of a tornadic supercell that low-level rotation, in contrast to midlevel rotation, is strongly influenced by the generation of horizontal vorticity owing to horizontal gradients of potential temperature in the inflowing air. Changes in vertical and horizontal vorticity with time, given a Boussinesq assumption, are governed by the following equations:

$$\frac{d\zeta}{dt} = \bar{\omega}_H \cdot \nabla_H \mathbf{w} + \zeta \frac{\partial \mathbf{w}}{\partial z} + F'_\zeta \quad (2.23)$$

and

$$\frac{d\bar{\omega}_H}{dt} = \bar{\omega} \cdot \nabla \bar{\mathbf{v}}_H + \nabla \times (\mathbf{B}\hat{\mathbf{k}}) + F'_H \quad (2.24)$$

where the  $F$  terms represent the effects of mixing. Thus, as rain-cooled air spreads out in the downdraft, air moving toward the updraft flows nearly parallel to the isotherms and acquires vorticity comparable to that of the environmental flow. As this air approaches the updraft, the horizontal vorticity is tilted according to the first term on the righthand side of (2.23) and subsequently stretched according to the second term. However, Davies-Jones and Brooks (1993) pointed out the difficulty in generating vertical vorticity very near the ground through tilting by the updraft alone. For example, in a Beltrami model the vortex lines are coincident with streamlines and therefore generation of vertical vorticity very near the ground by tilting would require abrupt upward turning of the streamlines and large vertical velocities near the ground. Instead, they suggest that cyclonic vorticity develops as a parcel descends in the downdraft. During this descent, the barotropic portion of the vorticity is coincident with the trajectories, while the baroclinic component of the vorticity is horizontal. Thus, as air descends 'feet first' (with stronger velocities nearer the ground) the baroclinic portion of the vorticity is tilted into the vertical such that when the air arrives at the ground it already has a significant vertical component of vorticity which is then stretched as the air enters the updraft. In this manner, significant low-level vorticity can be produced very near the ground. Davies-Jones (1996) derived an analytic expression for the baroclinic component of vorticity generated over a specific time based on the Cauchy equation for isentropic flow with the extension to equivalent isentropic flow. By assuming the downdraft could be represented by

a descending isentropic surface, he showed that cyclonic rotation develops in the left side of the downdraft.

Rotunno and Klemp (1985) explained the development of low-level rotation by considering the circulation around a fluid circuit as it approached the updraft along the temperature gradient of the gust front. The circulation around a closed material curve, subject to the inviscid, Boussinesq approximation, is given by

$$\frac{dC}{dt} = \frac{d}{dt} \oint \bar{\mathbf{v}} \cdot d\bar{\ell} = \oint B \hat{\mathbf{k}} \cdot d\bar{\ell} \quad (2.25)$$

By selecting a curve around the updraft at low-levels and tracing its trajectory back in time, they deduced the development of circulation around this material curve. It became clear that the air entering the updraft is composed of a stream of air originating at low levels along with a stream of air originating from higher levels. The creation of positive circulation occurs predominantly along the portion of the curve where  $B$  is negative and  $dz$  is negative. Since this circulation is related to the vorticity contained in the area surrounded by the curve, positive circulation implies positive vertical vorticity when the curve reaches its final, horizontal state. These results are consistent with the interpretation of Davies-Jones and Brooks (1993) for production of positive vertical vorticity in the descending air.

Brooks et al. (1994a) and Brooks et al. (1994b) have discussed the importance of a balance between the strength of storm-relative midlevel winds and the intensity of the midlevel mesocyclone for the development of low-level

mesocyclones. The storm-relative midlevel winds influence the low-level mesocyclone through their influence on the precipitation distribution with rain falling further from the updraft for higher midlevel storm-relative winds. With weaker winds, rain falls very close to the updraft as it is wrapped around by the midlevel mesocyclone and low-level mesocyclogenesis commences quickly. However, the outflow from the cold air eventually undercuts the inflow to the storm in this case. As the midlevel storm-relative winds increase, the rain falls further away from the updraft and mesocyclogenesis is slowed, although after developing, the mesocyclone is more persistent due to the weaker outflow winds.

Thus, low-level mesocyclogenesis depends on the environment even though it is produced primarily due to processes internal to the storm (i.e., the production of streamwise vorticity in the baroclinic regions of the storm rather than the tilting of environmental vortex lines). *Our understanding of the balance needed to produce a sustained low-level mesocyclone has progressed dramatically in the past ten years, but only in cases where the environment is horizontally homogeneous. Because the establishment of this balance appears to involve storm motion, storm rotation, mid-level wind strength, and low-level humidity (for the production of sufficient rain), the process by which this balance gets established or is maintained when a storm moves into a less or more favorable environment is totally unclear.*

### **Chapter 3 Model Formulation and Validation**

The model used in the experiments described herein is the Advanced Regional Prediction System (ARPS), developed by the Center for Analysis and Prediction of Storms (CAPS) at the University of Oklahoma (Xue et al., 1995). While the ARPS is a full-physics prediction and data assimilation system, it is used here as a three-dimensional, non-hydrostatic cloud model in the spirit of the Klemp and Wilhelmson (1978a) model. All experiments incorporate Kessler warm rain microphysics and flux-corrected transport (FCT) (Zalesak, 1979) for advection of perturbation potential temperature and total water variables. Fourth-order horizontal and 2<sup>nd</sup>-order vertical advection is used for momentum, turbulent diffusivities for momentum and heat ( $K_m$  and  $K_h$ ), and base state potential temperature. The model is modified to accommodate an inhomogeneous environment by altering the lateral boundary radiation condition, the computational mixing, and the lateral boundary advection. Details of these modifications are described in this chapter. There is no mixing in the normal direction at the boundaries. The horizontal resolution is 1.5 km and the vertical resolution is 350 m throughout the troposphere with stretching up to 1200 m applied in the stratosphere. Storms are initiated using a thermal perturbation of 2 K with a horizontal radius of 10 km and a vertical radius of 1400 m, along with a moisture perturbation as described in section 3.1.2. The subgrid closure is a 1.5-order scheme based on turbulent kinetic energy (TKE) with a predicted Prandtl number, an anisotropic, stability-dependent mixing length following Deardorff (1980), and

mixing coefficients following Moeng (1984) and Moeng and Wyngaard (1988).

Details of all model settings are listed in Appendix A.

### **3.1 Model Validation**

Before a model is used, its accuracy should be validated, preferably via comparison with analytic solutions to the equations of motion. These solutions are, therefore, invaluable and, unfortunately, relatively rare and limited to specific flow configurations. Analytic solutions capable of testing all aspects of a fully compressible cloud model do not exist. However, coding and formulation errors can often be uncovered through comparison with other, similar models. Solutions that diverge significantly between models are then suspect and the source for this difference can be determined and corrected if necessary. In this way, reproducibility of results is fostered and comparisons can be made between simulations made with different models. Because this study relates most directly to that of Weisman and Klemp (1982, 1984), the Klemp–Wilhelmson model is used for comparisons.

The ARPS model was first validated using an analytic solution for a viscous Beltrami flow (Shapiro, 1993) to verify nonlinear momentum and pressure advection, mixing with a constant viscosity, pressure gradient formulations, and computational mixing. It is not a test of the moisture, microphysics, or turbulence closure schemes; these were evaluated by comparison with the Klemp–Wilhelmson model over a range of environmental vertical shear values. Scalar advection tests used an analytic solution for advection of a soup can-shaped, passive perturbation in a velocity field. These tests showed large errors using 4<sup>th</sup>-order horizontal and 2<sup>nd</sup>-order vertical

advection, leading to the inclusion of the flux-corrected transport scheme. Each of these validation tests is described below.

### 3.1.1 Viscous Beltrami Flow Validation

A Beltrami flow is one in which the vorticity and velocity vectors are parallel everywhere. Because of this unique flow configuration, the governing equations are simplified considerably and an analytic solution is possible in which the pressure is related to the velocity and height through a diagnostic equation.

The viscous Beltrami flow is an excellent model test case because it is one of the few exact solutions for a viscous flow that retains nonlinearity in the momentum advection term, providing a test of the momentum and pressure advection, mixing, and pressure gradient formulations. This test was originally performed by Shapiro (1993) using the ARPS but is repeated here due to subsequent model changes.

Beginning with the Navier-Stokes equations with constant density, and considering the case of a Beltrami flow, in which case velocity and vorticity are proportional, exact solutions for the velocity components are given by:

$$u = -\frac{A}{k^2 + l^2} \left[ \begin{array}{l} \lambda l \cos(kx) \sin(ly) \sin(mz) \\ + mk \sin(kx) \cos(ly) \cos(mz) \end{array} \right] \exp(-v\lambda^2 t), \quad (3.1)$$

$$v = \frac{A}{k^2 + l^2} \left[ \begin{array}{l} \lambda k \sin(kx) \cos(ly) \sin(mz) \\ - ml \cos(kx) \sin(ly) \cos(mz) \end{array} \right] \exp(-v\lambda^2 t), \quad (3.2)$$

and

$$w = A[\cos(kx)\cos(ly)\sin(mz)]\exp(-v\lambda^2 t), \quad (3.3)$$

where

$$\lambda^2 = k^2 + l^2 + m^2, \quad (3.4)$$

$k$ ,  $l$ , and  $m$  are wavenumbers in the  $x$ ,  $y$ , and  $z$  directions, respectively,  $v$  is the viscosity, and  $A$  is the amplitude of the vertical velocity at  $t=0$ .

The pressure is given by

$$p = p_s - \rho \left( \frac{u^2 + v^2 + w^2}{2} \right) - \rho g z \quad (3.5)$$

where  $p_s$  is a function of time and represents the stagnation pressure at ground level.

The model is tested by inserting an initial condition consistent with (3.1)-(3.5) and running the model forward in time, comparing the final model solution with the exact solution. The domain used is  $92 \times 67 \times 47$  gridpoints with  $dx=3$  m,  $dy=2$  m,  $dz=1$  m. The large timestep is 0.19 s and the small timestep is 0.002 s as in Shapiro (1993). The model is initialized using an isentropic base state with  $\theta = 300$  K, resulting in a slight variation of the density with height such that a perfect match with the exact solution is not expected. The base state pressure consists of the first and third terms of (3.5), so the perturbation pressure is equal to the middle term of (3.5). The amplitude ( $A$ ) is set to  $2.0 \text{ m s}^{-1}$ , and  $k$ ,  $m$ , and  $l$  are set such that there are 2, 1, and 1 wavelengths in the  $x$ ,  $y$ , and  $z$  directions, respectively. The viscosity is  $1 \text{ m}^2 \text{ s}^{-1}$ .

The exact solution consists of a pattern of vortices whose amplitude decays in time, as shown in Figure 3.1, where the model and exact solutions for  $u$ ,  $v$ , and  $w$  are given as indicated. The model solution matches the exact solution very well as the exact and model solution curves are virtually indistinguishable. Very slight discrepancies in  $w$  were apparent when the standard ARPS initialization was used,

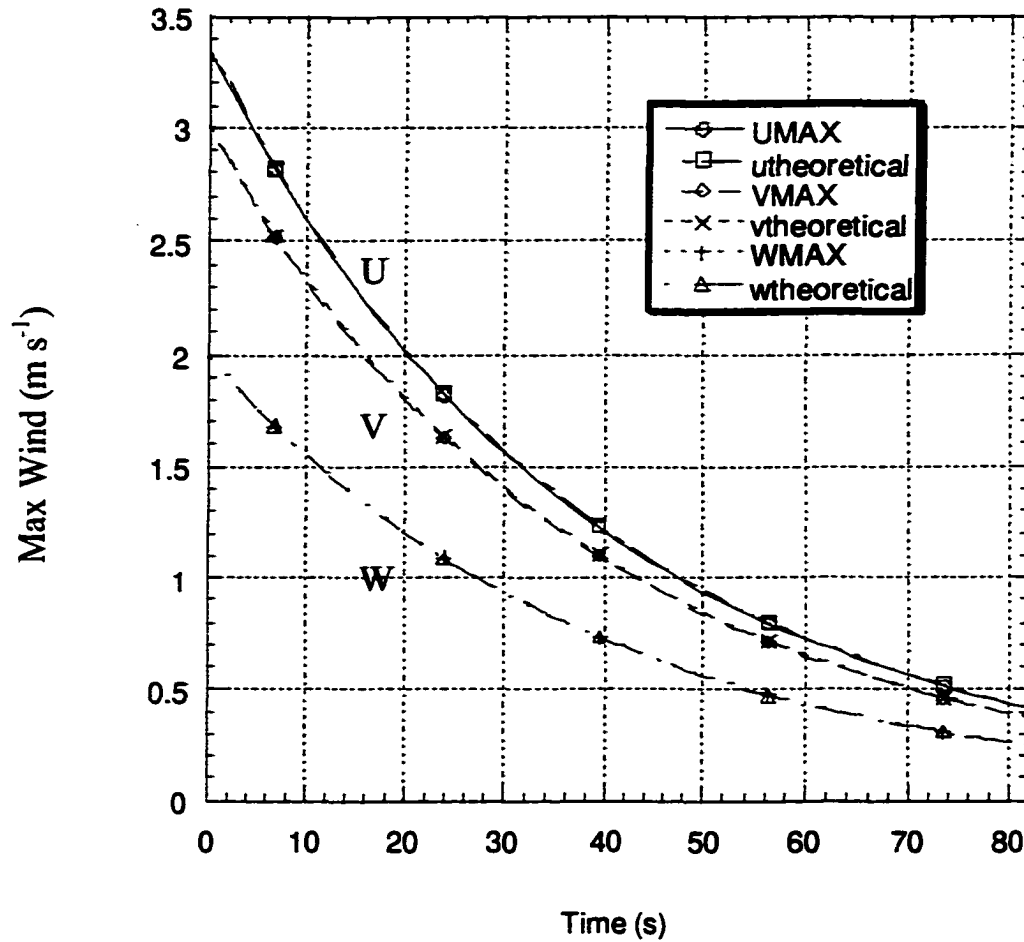


**Figure 3.1: Decay of domain maximum  $u$ ,  $v$ , and  $w$  for the ARPS versus that for the ideal solution. The model is run for more than two e-folding decay times.**

due to the variation of the density with height in the model. When the initial state is forced to have constant density and constant potential temperature with hydrostatic pressure, contrary to the ideal gas law but not inconsistent with the exact solution, the model solution for  $w$  agrees with the exact solution as shown. The potential temperature, rather than the density as in the analytic solution, is constant throughout the run.

The model pressure shows significant disagreement with the exact solution, but this is not surprising since the analytic solution is only unique to within a constant at each time step. For example, when a constant value of pressure (approximately 2.5

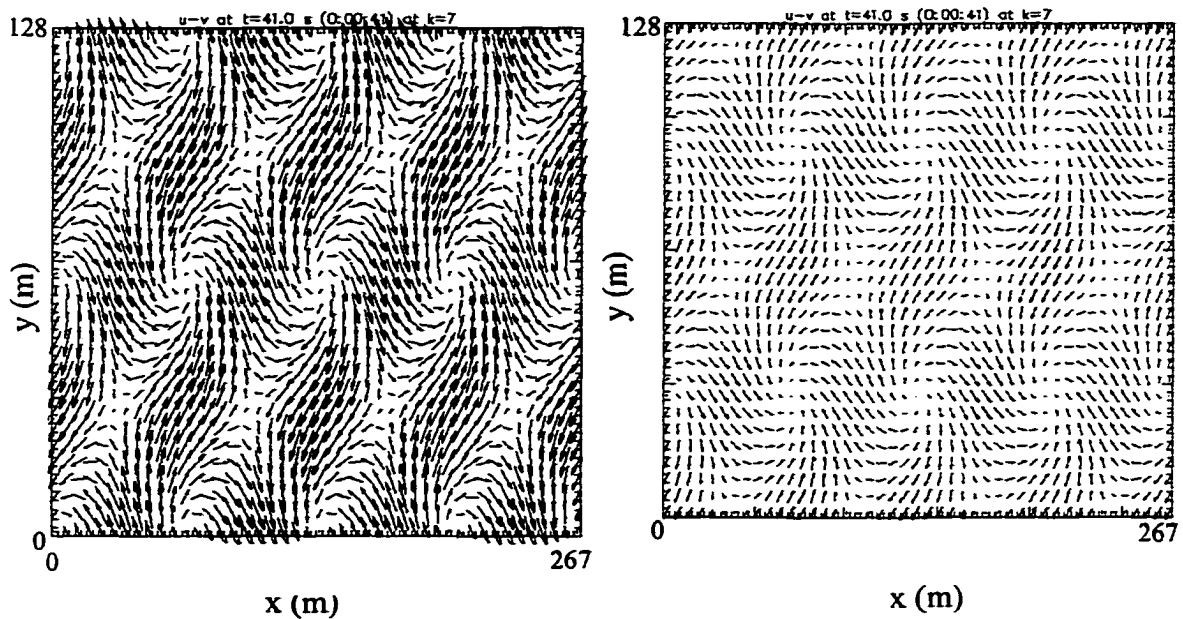


**Figure 3.2: Horizontal cross section ( $z=5.5$  m) of the  $u$  and  $v$  wind components ( $\text{m s}^{-1}$ ) for model solution (left) and difference field (right) for the viscous Beltrami test at  $t=41$  s. (Maximum value of  $u$  on left (right) is  $0.83$  ( $0.06$ )  $\text{m s}^{-1}$ . Maximum value of  $v$  on left (right) is  $0.75$  ( $0.04$ )  $\text{m s}^{-1}$ .)**

Pa) is removed over the entire model domain at  $t = 41$  s, the pressures of the exact and model solutions differ by only approximately 0.02 Pa.

The exact solution for the horizontal winds at 41 s at 5.5 m, along with the difference field between the model and exact solutions, is shown in Figure 3.2, where we note the small magnitude of the differences, again indicating an acceptable solution, particularly considering the discrepancy in the two systems of equations. Fields at other levels showed similar agreement.

### **3.1.2 Scalar Advection Tests**

Early multicell storm simulations using simple 4<sup>th</sup>-order horizontal and 2<sup>nd</sup>-order vertical scalar advection showed that the model solution was sensitive to changes in domain motion, particularly when the domain motion was changed during a simulation. In this particular case, sharp gradients associated with the cloud region could be advected backward in the domain, leading to dispersion errors on the inflow side of the storm (Figure 3.3). These errors took the form of waves, leading to the development of spurious cells on the inflow side that strongly influenced the solution.

To understand the reason for this behavior, I performed an advection test of a scalar perturbation with a sharp gradient in the form of a cylinder (soup can) of perturbation potential temperature with magnitude  $-10$  K. (The buoyancy force was neglected in these simulations so that potential temperature was a passive scalar.)

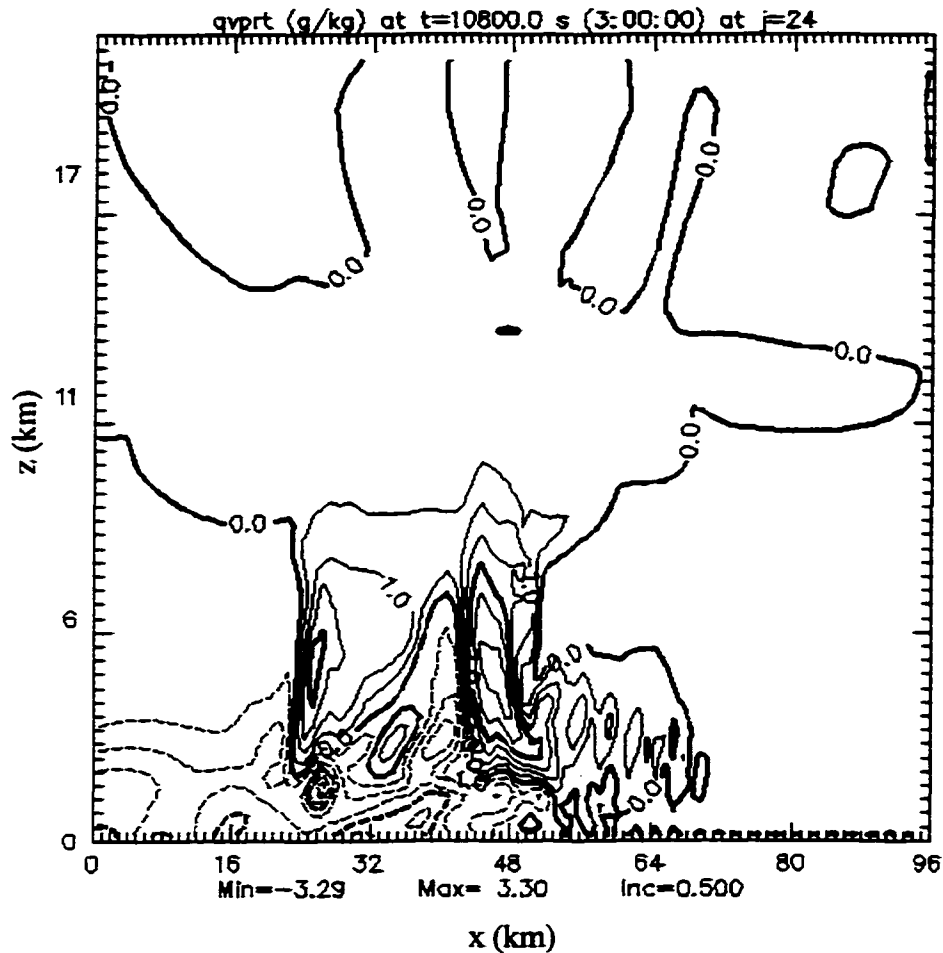


**Figure 3.3: Model solution for the vertical cross section of perturbation water vapor mixing ratio ( $\text{g kg}^{-1}$ ) in a multicell simulation at  $t = 3$  hours with regular scalar advection.**

A vertical slice of perturbation potential temperature after 900 seconds using 4<sup>th</sup>-order horizontal and 2<sup>nd</sup>-order centered vertical advection is shown in Figure 3.4. In this figure, the cylinder is being advected toward the right, and large perturbations in the trailing region are evident.

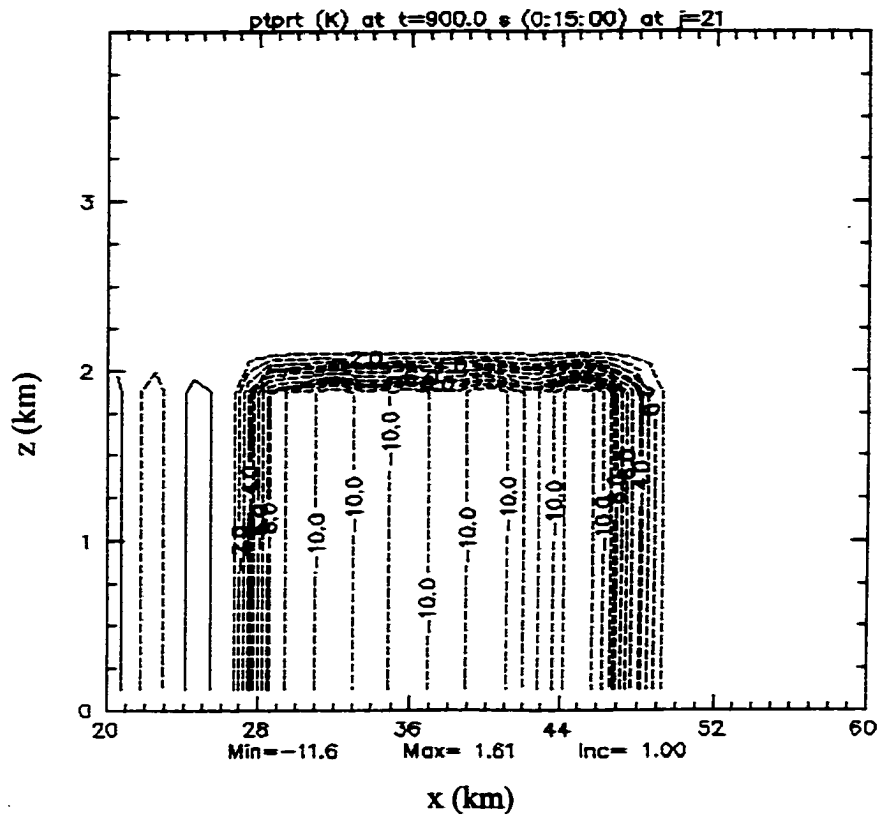


**Figure 3.4: Scalar advection test with a 'soup can' of perturbation potential temperature (K) using 4<sup>th</sup> order default advective scheme in ARPS.**

Clearly, this is a poor solution, producing perturbations of up to 16% in the trailing region. This may not lead to significant problems for a storm simulation in a strongly sheared environment where small perturbations will have a difficult time growing. However, for the simulations in this study, some of which involve low shear environments, these spurious perturbations can lead to new cells that

significantly influence subsequent storm morphology. Thus, a better form of advection was desired.

Based on the storm simulation results with a moving domain, as well as the above test, dispersion errors were believed to be the main culprit; thus, a monotonic scheme was sought. The ARPS included an untested version of the flux-corrected transport (FCT) (Zalesak, 1979) advection scheme which ensures a monotonic solution by combining a monotonic low-order scheme with a more accurate higher-order scheme. The process is as follows:

Consider the following system of equations

$$\theta_t + f_x = 0 \quad (3.6)$$

where  $\theta$  and  $f$  are vector functions of independent variables  $x$  and  $t$ . We may write this equation as

$$\theta_i^{n+1} = \theta_i^n - \Delta x_i^{-1} [F_{i+(1/2)} - F_{i-(1/2)}] \quad (3.7)$$

where  $F$  is the transportive flux that depends on  $f$  at one or more time levels. The functional dependence of  $F$  on  $f$  and  $\Delta t$  defines the integration scheme (Zalesak, 1979) in each step of the procedure.

The solution algorithm is as follows:

- 1) Compute  $F_{i+1/2}^L$ , the transportive flux given by some low order scheme guaranteed to give monotonic (ripple-free) results for the problem at hand.

- 2) Compute  $F_{i+1/2}^H$ , the transportive flux given by some high order scheme
- 3) Define the “antidiffusive flux”:

$$A_{i+1/2} \equiv F_{i+1/2}^H - F_{i+1/2}^L \quad (3.8)$$

- 4) Compute the updated low order solution:

$$\theta_i^{ud} = \theta_i^n - \Delta x_i^{-1} [F_{i+1/2}^L - F_{i-1/2}^L] \quad (3.9)$$

- 5) Limit the  $A_{i+1/2}$  in a manner such that  $\theta^{n+1}$  as computed in step 6 below is free of extrema not found in  $\theta^{ud}$  or  $\theta^n$ :

$$A_{i+1/2}^C = C_{i+1/2} A_{i+1/2}, \quad 0 \leq C_{i+1/2} \leq 1 \quad (3.10)$$

- 6) Apply the limited antidiffusive fluxes:

$$\theta_i^{n+1} = \theta_i^{ud} - \Delta x^{-1} [A_{i+1/2}^C - A_{i-1/2}^C] \quad (3.11)$$

The critical step is step 5. In the absence of the flux limiting step,  $\theta^{n+1}$  would simply be the time-advanced high order solution (Zalesak, 1979). In the ARPS, the low order solution is found using the first-order donor cell (upstream) algorithm that is naturally monotonic. The higher-order solution is determined using a trapezoidal method in which a leapfrog step is applied from time  $n-1$  to  $n+1$ . This solution is combined with the field at time  $n$  to compute a flux valid at  $n+1/2$  that is used to obtain the final field at  $n+1$ . The flux limiting compares this new value with the maximum (minimum) values from the low-order solution as well as from the previous

timestep at all points surrounding the point under consideration. This determines the positive (negative) fluxes allowed for a given cell.

This algorithm was applied to the soup can advection test. Tests using FCT as originally formulated in the ARPS model showed errors similar to those with regular advection. I determined these errors to be due, in an indirect way, to the flux form implemented. In ARPS, the potential temperature equation is given by

$$\frac{\partial(\rho^* \theta')}{\partial t} = - \left[ u \rho^* \frac{\partial \theta'}{\partial \xi} + v \rho^* \frac{\partial \theta'}{\partial \eta} + w^c \rho^* \frac{\partial \theta'}{\partial \zeta} \right] + \dots \quad (3.12)$$

where  $\rho^*$  is the base state density multiplied by the three dimensional transformation Jacobian ( $\sqrt{G}$ ),  $w^c$  is the contravariant vertical velocity component, and  $\xi$ ,  $\eta$ , and  $\zeta$  are the computational grid coordinates. To cast the advection in flux form we add and subtract the term

$$\theta' \left( \frac{\partial(u\rho^*)}{\partial x} + \frac{\partial(v\rho^*)}{\partial y} + \frac{\partial(w^c\rho^*)}{\partial z} \right)$$

from the right side of (3.12). We can then write (3.12) as

$$\begin{aligned} \frac{\partial(\rho^* \theta')}{\partial t} = & - \left[ \frac{\partial(u\rho^* \theta')}{\partial \xi} + \frac{\partial(v\rho^* \theta')}{\partial \eta} + \frac{\partial(w^c\rho^* \theta')}{\partial \zeta} \right] \\ & + \theta' \left( \frac{\partial(u\rho^*)}{\partial x} + \frac{\partial(v\rho^*)}{\partial y} + \frac{\partial(w^c\rho^*)}{\partial z} \right) + \dots \end{aligned} \quad (3.13)$$

Comparing (13) and (6), it is clear that, for the ARPS,  $\vec{f} = \rho \bar{v} \theta$ . The FCT advection scheme applied to the first term on the right side of (13) would give a result representing the full advection term in (12) exactly if the fluid were anelastic.

Because ARPS is a fully compressible model, however, the small correction term  $[\theta \nabla \cdot (\rho \bar{v})]$  must also be included. The flux ( $\bar{f}$ ) includes density in order that the correction term be as small as possible since it can introduce non-monotonicity in the solution.

Subtle errors, such as the timestep used in the forward integration, were found in the untested code and were corrected. A significant error was found in the low order solution that included a diffusion term as in Zalesak (1979), presumably to ensure monotonicity. However, this term was found to be both in error and unnecessary and was thus removed.

It also became clear that care must be taken in step 5, where the limiting is performed, such that the value of the variable itself is used in the comparison of maximum (minimum) values, not the value of the variable multiplied by  $\rho$ . Otherwise, as was apparent in the ARPS, overshoots in the variable could be allowed based on the stratification of  $\rho$ . In other words, the maximum value of a variable would be allowed to grow due to advection provided that its value multiplied by  $\rho$  remained less than the value of  $\rho\theta$  at surrounding points. Clearly this is not the desired result. Thus, I modified the scheme to ensure that  $\theta$  is compared only to itself in the comparison step. Zalesak (1979), who used constant density in his tests, did not address stratification or compressibility issues. I believe I addressed these complications in an appropriate manner. With these changes, the solution shown in Figure 3.5 is obtained for advection of a potential temperature perturbation of  $-10$  K.

Clearly this solution is superior to that obtained with 4<sup>th</sup>-order horizontal and 2<sup>nd</sup>-order vertical advection (compare to Figure 3.4:). This test was repeated for perturbations in  $qv$ , and  $qc$  and was done in all three directions with similar, very favorable results.

Another issue arises due to the vertical stratification of the variable being transported. For example, potential temperature advection can be thought of as advection of the base state plus advection of the perturbation. Consider a potential temperature perturbation being advected horizontally in a highly stratified environment. Clearly the perturbation should not grow in time, but it will be allowed

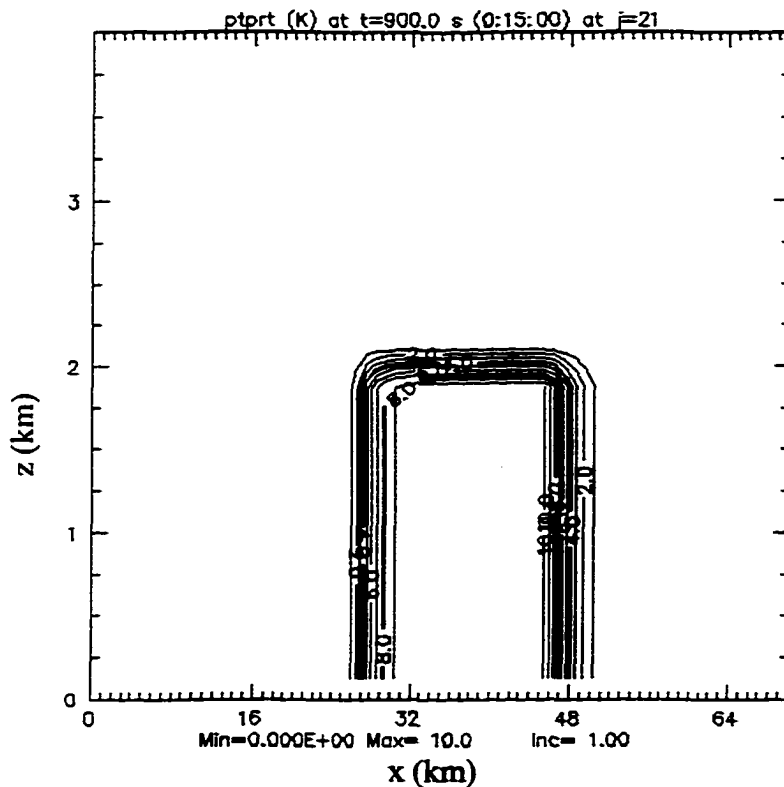


**Figure 3.5: Scalar advection test with a 'soup can' of perturbation potential temperature (K) using flux corrected transport (FCT).**

to grow if the comparison in the FCT flux limiter is done using total potential temperature at neighboring points. For this reason, the advection of perturbation potential temperature alone is done using the FCT scheme, while the (vertical) advection of base state potential temperature is added as a separate term.

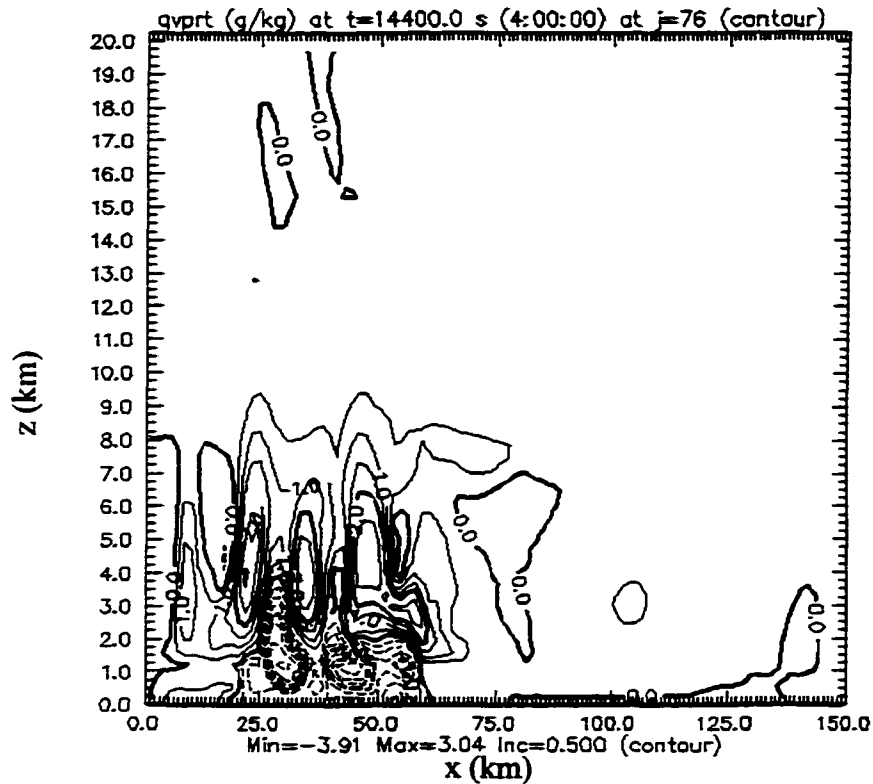


**Figure 3.6: Vertical cross section of perturbation water vapor mixing ratio ( $\text{g kg}^{-1}$ ) in a multicell storm simulation using FCT for the advection of scalars.**

Although water vapor also is stratified, the predicted variable is total water vapor so the FCT scheme was applied to this quantity. The perturbation and base state advection terms could have been handled separately, but it was felt that conserving water vapor was the most important requirement and using FCT for the total quantity was, therefore, preferable. In order to prevent horizontal advection

from creating spurious maxima that were allowed due to this stratification, I performed the flux limiter in each direction separately before applying it to the entire grid cell. For example, for advection in the x-direction, only the surrounding points in the x-direction were used in the comparison. Only vertical advection could then incorrectly generate new maxima due to the stratification. This method appears to have eliminated the spurious cells apparent in earlier runs and also made the solution much less sensitive to changes in domain translation. Figure 3.6 shows a vertical cross-section of  $qv$  for a domain whose speed was increased after 2 hours and no wave patterns on inflow are apparent.

Finally, lateral boundary relaxation terms are added to nudge the solution toward the base state value on inflow. This assumes that disturbances at the boundary have a limited extent beyond the boundary such that after inflow persists for some time, the boundary values relax to those of the environment. The assumed extent of the disturbances is governed by a specified relaxation coefficient. Advection at all points is first calculated assuming zero gradient conditions in the direction normal to the boundary on inflow. The relaxation terms are then added to this solution.

### **3.1.3 Test of storm simulations over various shear ranges**

The previous tests showed that the ARPS solutions were sufficiently accurate in terms of advection of momentum and scalars as well as the formulation of the pressure gradient and buoyancy forces. However, they did not verify the microphysics or turbulence closure. Before using the ARPS model, it was necessary to verify these aspects of the model for storm simulations spanning a range of environmental shears, encompassing both multicell and supercell storms. Weisman

and Klemp (1982) (hereafter WK82) produced one of the classic simulation studies spanning this range of shears. Because my results build upon theirs, I sought to reproduce their results and verify sufficient performance of the ARPS to ensure comparability with previous simulation studies utilizing the Klemp-Wilhelmson (KW) model.

The first verification attempts based on the information available in WK82 showed large differences between the solutions produced by the two models, with initial storms much weaker (by 10-12 m/s) in the ARPS compared to their WK82 counterparts and possessing differing evolutions (i.e., splitting versus non-splitting storms) for weak-moderate shear environments. While it is unreasonable to expect different models to produce identical results, the reasons for any egregious differences must be understood in order to rule out incorrect formulations or coding errors in either model.

The KW model was obtained and used to reproduce the results in WK82 in order to insure our knowledge of the model settings used in their study. Through trial and error, it became clear that the model formulations employed to obtain those results were a combination of those reported in Klemp and Wilhelmson (1978a) and Wilhelmson and Chen (WC) (1982). In particular, the advection schemes of WC were used, but turbulent mixing was applied to the total state, as in KW, rather than to the perturbations. With this knowledge, the ARPS settings and formulations could be altered systematically to match those of KW in order to determine which model formulations caused the differing results.

Due to the large differences in storm strength, I suspected that either the physical or computational mixing was too strong in the ARPS. Simply eliminating the most obvious differences in model settings regarding turbulent mixing (e.g., the proportionality constant ( $C_m$ ) relating the mixing coefficient ( $K_m$ ) and the turbulent kinetic energy, as well as the dissipation constant ( $C_\epsilon$ ) in the turbulence parameterization) did not result in satisfactory agreement between the simulations. Because it was clear that a highly non-linear storm simulation was an imperfect venue for determining important model differences, more simplified tests were performed to determine the origin of the disagreement.

The first simplified test simulated a dry, buoyant bubble in a neutral environment. This test showed slight differences between the two models in the vertical velocity and potential temperature perturbation fields after only 1800 s. Because there were very few factors influencing this test, it was fairly easy to determine that these differences were due to the computational mixing settings. I discovered an error in the formulation of vertical computational mixing in the ARPS model. The ARPS formulation was

$$\phi_{t,mix} = c \frac{\partial^2}{\partial z^2} (\bar{\rho} \phi) \quad (3.14)$$

where  $\phi$  is a perturbation quantity. This formulation incorrectly changes  $\phi$  in time in a stratified environment even when  $\phi$  has no gradients. The correct formulation for the mixing term should be

$$\phi_{t,mix} = c \frac{\partial}{\partial z} \bar{\rho} \frac{\partial}{\partial z} (\phi) \quad (3.15)$$

This change was used in all further simulations.

I also discovered that the KW model divides the horizontal computational mixing coefficient in half after the first timestep. After determining the correct computational mixing value to use in the ARPS, the dry bubble maximum vertical velocity and potential temperature perturbation matched quite well with the KW solution. However, striking differences persisted in the vertical profiles of the potential temperature perturbations and mixing coefficient (Km).

In particular, as the bubble rose, the ARPS solution tended toward nearly constant  $\theta'$  in the vertical at the lowest few levels, while the KW solution tended toward a stable solution at low levels. In a neutral environment, the only processes acting on potential temperature at low levels are the mixing and advection of the initial bubble. Advection of potential temperature at the lowest scalar level was formulated identically in the two models, so the difference had to be due to the assumptions for mixing at the lower boundary. The vertical mixing was a more likely suspect than the horizontal mixing, which had similar formulations in both models and also would be small compared to vertical mixing for the initial bubble, given the bubble geometry.

To compute vertical mixing in the ARPS, an artificial scalar level is defined one-half grid space below the lower boundary (k=1) and values at this level are set equal to those of the scalars one-half grid space above the boundary (k=2). This results in mixing at k=2 if a gradient exists between k=2 and k=3. In the KW model,

there is no mixing in the vertical direction for the lowest scalar level (one-half grid space above the lower boundary), essentially assuming zero second derivative of the scalar at this point. This assumed boundary condition affects both the turbulent (physical) mixing and the computational mixing.

In the case of the warm bubble in a neutral environment, the potential temperature within the lowest grid box is unchanged by mixing in the KW model. In the ARPS, on the other hand, the zero gradient condition at the lower boundary leads to an increase of potential temperature due to the temperature gradient within the bubble. The net result is increased stability beneath the bubble in the KW model and, thus, physical mixing is not activated as it is in the ARPS, where the solution is nearly neutral beneath the bubble.

The proper way to handle turbulent mixing at the lower boundary is to prescribe a turbulent heat or momentum flux based on specified or computed surface temperature and velocity, but this will only be necessary for real predictions or studies in which surface physics effects are deemed important. They are neglected here, but one must still consider turbulent mixing. In the present simulations for either model, surface physics parameterizations would not have been well represented given the coarse vertical resolution. Turbulent mixing, instead, was performed based on the assumed gradient between the surface and the first scalar level above the surface, as described above.

The ARPS assumption of zero gradient seeks to prevent spurious sources or sinks at the lower boundary. The KW assumption of zero second derivative was originally used so that 'vertical gradients in the mean state profiles are not distorted

due to eddy mixing near the boundaries. This undesirable smoothing does occur with the so called “free slip” condition which requires the normal first derivatives to become zero at the boundaries.’ (Klemp and Wilhelmson, 1978a) It is my belief that the assumption of zero second derivative in the vertical at the lowest scalar level above the ground is more justifiable than the assumption of zero gradient between the lowest scalar and the ground when the vertical grid resolution is relatively coarse. Thus, vertical mixing at the lowest scalar was not applied in my simulations. This led to an almost perfect match between the two models for the dry bubble solutions, and an improved match between the models for a storm simulation with weak shear.

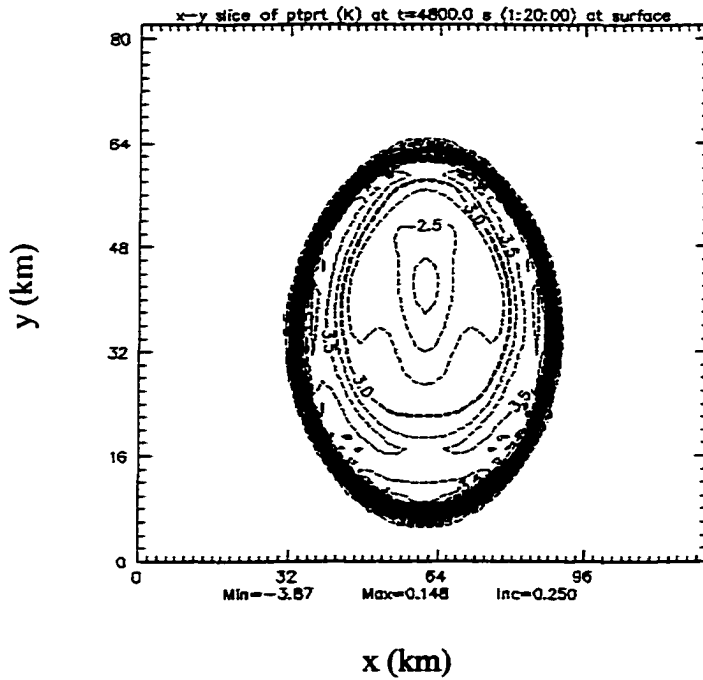
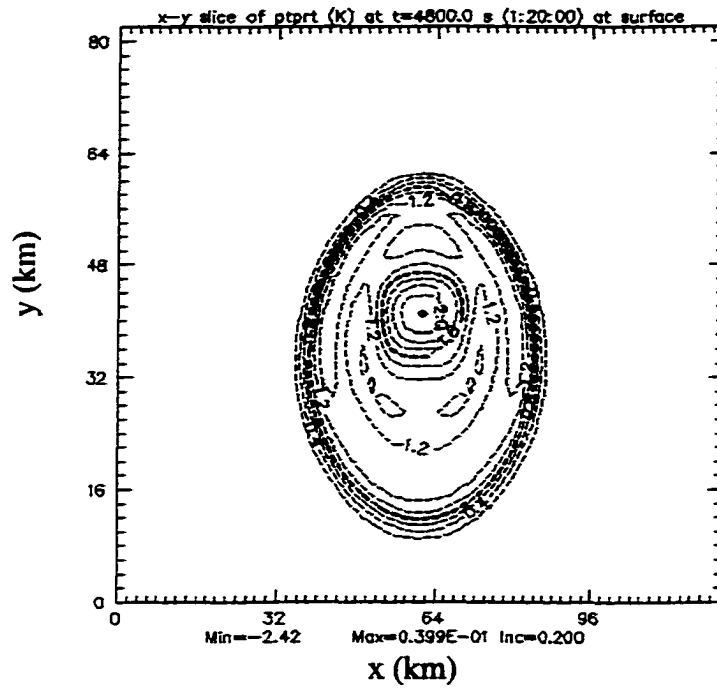


**Figure 3.7: Surface potential temperature perturbation (K) with (top) and without (bottom) vertical mixing at the lowest scalar at  $t = 4800$  s.**

With the removal of vertical mixing at the  $k=2$  scalar level, the storm simulation is altered, particularly with respect to the advance of the gust front. In Figure 3.7, for storm simulations using the ARPS model, it is clear that without mixing the gust front moves much farther from the initial storm and is more intense. This affects the strength of the initial storm as well as subsequent redevelopments along the gust front which depend on a sensitive balance between the gust front strength and the vertical shear of the environment (Rotunno et al., 1988). The solution without mixing is likely the more realistic solution, since it is unlikely the air between the ground and 350 m is neutrally stratified as the original ARPS boundary condition would suggest. It is much more likely to be stably stratified, such that a zero second derivative assumption is an improvement.

Thus, the first significant change in the storm strength came from the change in the horizontal computational mixing coefficient, and the second significant change in the storm strength and evolution came from the removal of vertical mixing at the lowest scalar level.

The dry bubble experiments also pointed out a problem in the ARPS initialization procedure. The usual procedure for specifying a neutral environment in the ARPS uses a two-level sounding (e.g., 0 and 30 km) with potential temperature set to the same value at both levels. The ARPS performs a hydrostatic integration at these levels, interpolates to an evenly-spaced intermediate grid, and then finally interpolates to the model grid (which may be stretched). This is the same procedure used for any single sounding run. The error in this procedure is the hydrostatic integration on the original sounding levels rather than the model levels, particularly if

the levels are spaced far apart, as in the neutral sounding. The pressures are correct at the two levels of the sounding, but the linear interpolation to the intermediate grid makes pressure linear between them (in my case causing a *linear* pressure profile from 0 to 13 km!). A better procedure is to perform the hydrostatic integration directly on the model grid after interpolating the input variables to those levels. This change is incorporated in the remainder of tests and simulations presented.

The dry bubble experiment verified the advection of scalars, the computational mixing, and the formulation of  $K_m$  for a dry environment, at least in comparison to the results of KW. The next test examined a moist bubble in an environment with neutral potential temperature and stratified base state water vapor ( $q_{vbar}$ ), with no microphysics employed. This test initially resulted in overturning of the base state in the ARPS but not in KW, leading to the recognition that KW does not include the effect of water vapor stratification in their buoyancy production term for TKE. With this change in the ARPS, the overturning disappeared and the results matched KW much better. However, even though vertical velocity matched to within  $1 \text{ m s}^{-1}$ , there were noticeable differences in the surface water vapor field. The only obvious source for this discrepancy was the difference in formulation of the advective terms for  $q_v$  between the two models.

The version of the KW model used by WK82 incorporated the flux form introduced by Wilhelmson and Chen (1982), rather than the advective form used by the original KW model and by the ARPS. To test the influence of the different advection schemes, I changed the KW  $q_v$  equation from flux form to advective form and the agreement with the ARPS was dramatically improved, resulting in nearly

identical surface water vapor fields. This result is somewhat puzzling because the only difference between the two forms of the  $qv$  equation is a term which should be nearly zero for flows with a velocity much less than the speed of sound -- an appropriate approximation for these simulations.

The advection terms for velocities and for mixing ratios of water vapor, cloud water and rainwater (on a grid with constant  $\Delta z$ ) were written by Wilhelmson and Chen (1982) as

$$\phi_t = -(\mathbf{u}\phi)_x - (\mathbf{v}\phi)_y - (\bar{\rho}w\phi)_z \bar{\rho}^{-1} + \phi(u_x + v_y + \bar{\rho}^{-1}(\bar{\rho}w)_z) \quad (3.16)$$

The final term in the equality would be zero for perfectly anelastic flow. This term was assumed to be zero by WC because their desired solution was the anelastic one. Evidently this term either is significantly non-zero or the above equality does not hold in the finite-difference solution because there are large differences between solutions obtained with the two schemes. This discrepancy is larger when the flow is less well-resolved, i.e., when coarser resolution is used.

To test the differences between the advection schemes, I added the flux form for advection of  $qv$  to the KW model and ran it with a moist, non-condensing bubble in an environment neutral to both  $\theta$  and  $qv$ . I turned off condensation in these simulations and used both forms of advection with varying horizontal resolutions. Although the environment is unrealistic due to the supersaturation that would occur at upper levels given a constant  $qv$ , it is a good test case because it clearly shows the effects of the advective formulation without the complications of microphysics or excessive mixing as the moist bubble rises.

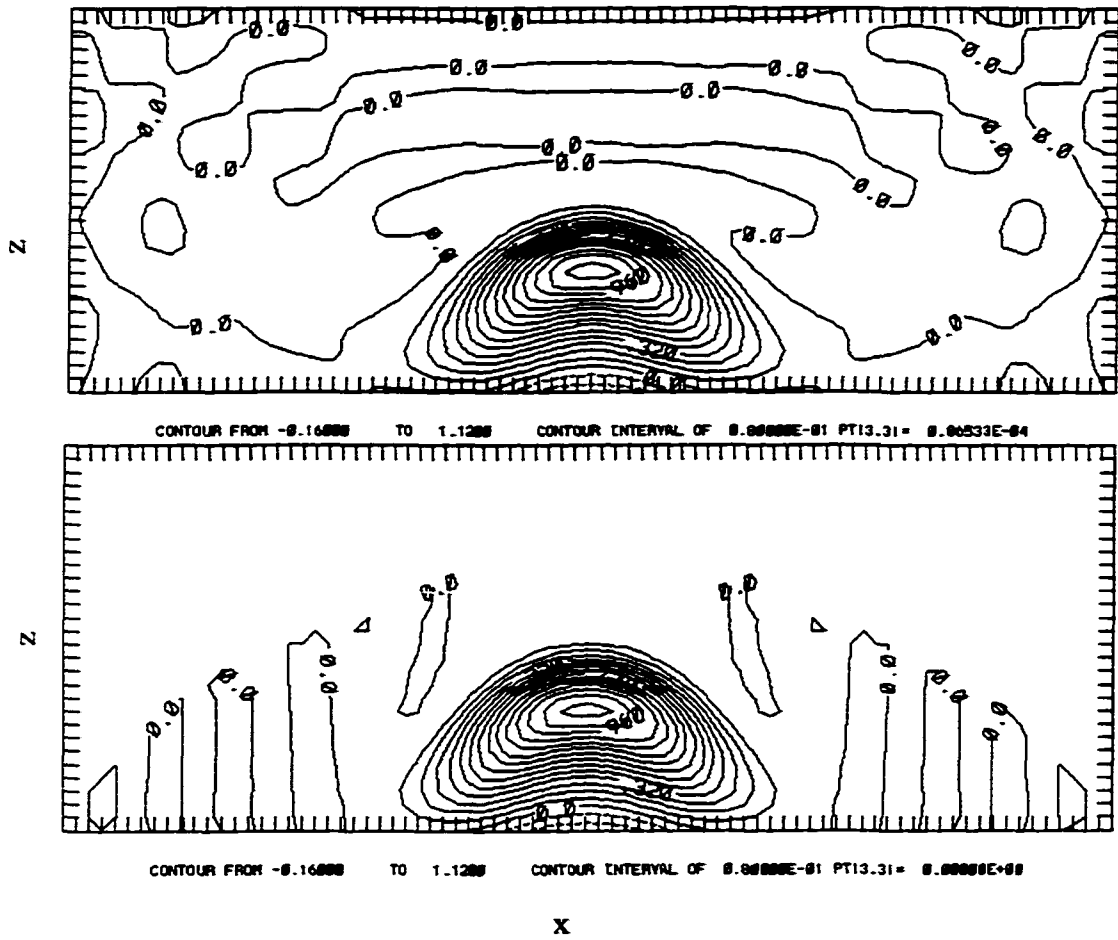


**Figure 3.8: Vertical cross section of water vapor mixing ratio for a moist, non-condensing bubble with the WC flux (top) and regular advective (bottom) forms for the advection terms. Horizontal and vertical resolutions are each 500 m.**

The surface water vapor fields for 500m and 2 km horizontal resolutions are shown in Figure 3.8 and Figure 3.9 for the two schemes, and it is clear that the advective form retains the same basic pattern for both resolutions while the flux form varies considerably. The vertical resolution is 500 m in both cases.

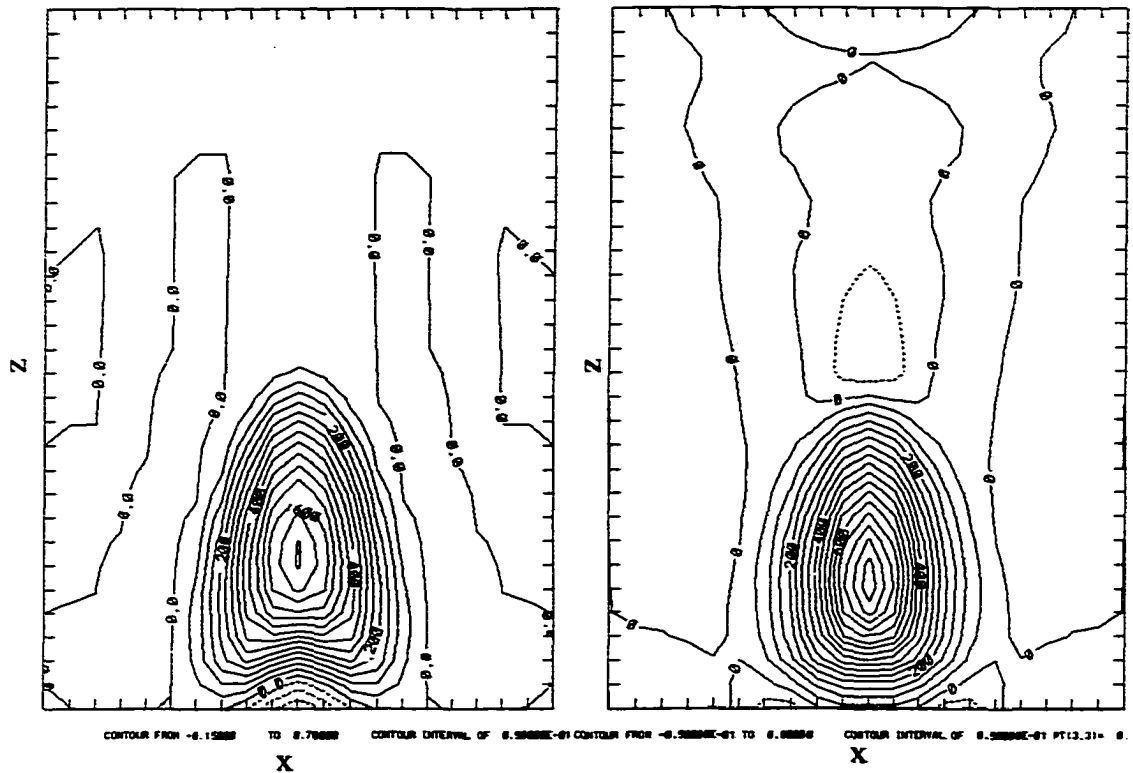


**Figure 3.9 Vertical cross section of water vapor mixing ratio for a moist, non-condensing bubble with the regular advective (left) and WC flux (right) forms for the advection terms. Horizontal resolution is 2 km and vertical resolution is 500 m.**

Looking at the 500 m resolution case, a y-z slice of  $qv'$  through the maximum updraft shows a clear difference in the advection of  $qv'$  for the two schemes. In the advective form, the  $qv'$  field advances in a symmetric, orderly manner like a 'front' of  $qv'$  rising in time. This is the anticipated solution, because  $qv'$  is neutral in the surrounding environment and, thus, velocity perturbations caused by acoustic modes throughout the domain should not result in any  $qv'$  perturbations. The perturbations outside the main  $qv'$  region are most likely due to aliasing (note the  $2-4\Delta x$  structure). The influence of the acoustic modes is clear in the flux form of the equations where  $qv'$  perturbations are spread throughout the domain. This is a result of neglecting the elastic correction term and, thus, wherever the elastic divergence is nonzero a perturbation will be created in  $qv'$ , even if  $qv'$  itself has no gradients! This is clearly undesirable, but should have a small effect as long as the solution is nearly anelastic.

Skamarock and Klemp (1992) showed that unstable acoustic modes can be excited by the KW time-split scheme but can be effectively controlled using a divergence damping term added to the momentum equations or by using the Robert-Asselin (Asselin, 1972) time filter. The divergence damping method is generally preferable to using a large time filter coefficient because it is more selective in damping only the acoustic modes. This divergence damping is used in ARPS but not in the version of the KW model used by Weisman and Klemp. Perhaps this had some bearing on the above results.

In summary, the following changes were made to the ARPS model based on comparisons with the Klemp-Wilhelmson model:

- \* Removed mixing in the vertical direction at  $k=2$  (the first scalar point above the ground)
- \* Changed vertical computational mixing to  $\frac{\partial}{\partial z} \left[ \rho^* \frac{\partial s}{\partial z} \right]$  rather than  $\frac{\partial^2}{\partial z^2} [\rho^* s]$ 
  - Multiplied vertical computational mixing coefficient by  $1/Pr$  for scalars
  - Changed buoyancy force computation to match KW
- \* Changed sounding interpolation routine
  - Removed interpolation to an intermediate grid
  - Changed hydrostatic integration of base state to match KW
- \* Added  $qv$  perturbation to bubble (only added if resulting  $qv$  is less than the surface  $qv$  so that  $qv$  doesn't increase with height. If the  $qv$  needed to preserve RH is greater than the surface  $qv$ , the surface  $qv$  is used at that level.)
- \* Added boundary condition call for  $qv$  and theta *after* microphysical computations are performed.
  - Added an option which uses Weisman and Klemp (1982) turbulence specifications
    - ( $C_m=C_e=0.2$ , fixed mixing length, fixed Prandtl number)
  - Removed contribution of  $dqv/dz$  to the dry buoyancy production term for TKE
  - Removed rain contribution to moist buoyancy production term for TKE
  - Set buoyancy production term at lowest scalar equal to the value computed at the next lowest scalar.
- \* Set limit on TKE so that  $K_m$  cannot exceed  $1000 \text{ m}^2/\text{s}$ .
  - Removed factor of 2 in TKE diffusion term.

**Removed computational mixing of TKE.**

**Changed evaporation so that it is limited by the amount needed for saturation**

**Changed the production term due to buoyancy in the turbulent kinetic energy equation to make same approximations as KW**

Most of these differences did not result in significant changes in the storm evolution. Among the most important influences were computational mixing, the turbulence parameters, the mixing at the lowest level, and the Prandtl number. The settings with an asterisk are those which were kept in the simulations to be presented in subsequent chapters.

### **3.2 Model Formulation to Accommodate an Inhomogeneous Base State**

It is perhaps not surprising that little effort has been made to study idealized, inhomogeneous environments; models simply are not designed to accommodate such fields. The proper modeling techniques to use when the environment is homogeneous are fairly well understood. When a model is used in prediction mode, the fields are obviously inhomogeneous, but they are not idealized and, thus, boundary conditions from a larger-scale model can be applied. Proper techniques for handling these fields are also fairly well-understood and are the subject of much research effort. An idealized, but inhomogeneous environment simulation, on the other hand, has been virtually unexplored. The techniques used for a homogeneous simulation must be modified with great care to take into account environmental gradients. A larger scale model is not feasible and also not possible since many of the environments used to

produce reasonable variations across a small domain become absolutely unstable when allowed to extend far past the domain. Thus, in order to accommodate an inhomogeneous, idealized environment, the model had to undergo significant alteration.

### **3.2.1 Computational Mixing/Rayleigh Damping**

One of the main concerns with an inhomogeneous base state is diffusion of the base state horizontal gradients in time due to artificial numerical influences. In particular, computational mixing, which acts to damp out noise of computational origin, can destroy base state gradients over a long time period. These gradients are obviously not of computational origin and should, therefore, not be damped. For this reason, computational mixing in a homogeneous simulation is applied only to deviations from the vertically-stratified base state, though, physically, this assumption is not justifiable. In our case, the computational mixing acts only on deviations from the 3-dimensional base state, requiring an extra array for each variable. It is also eliminated in the normal direction at the lateral boundaries.

Similar mixing of base state gradients can occur within the Rayleigh damping layer at the top of the domain. In this layer, we damp only perturbations from a 3-D base state array rather than the 1-D traditional base state.

The changes to computational mixing are applied to all scalar and momentum variables. Without these changes, inhomogeneities were reduced in time for environments in which velocities varied nonlinearly.

### 3.2.2 Radiation (Open) Lateral Boundary Conditions

Radiation lateral boundary conditions were designed with a homogeneous base state in mind. When the base state is inhomogeneous, the lateral boundary conditions tend to interpret the base state as a gravity wave disturbance and advect the inhomogeneity out through the lateral boundary (Figure 3.10). This eliminates the base state gradients in time and also creates artificial regions of convergence and divergence since this effect is greatest at the boundaries. Therefore, the lateral boundary conditions must be modified when an inhomogeneous environment is used.

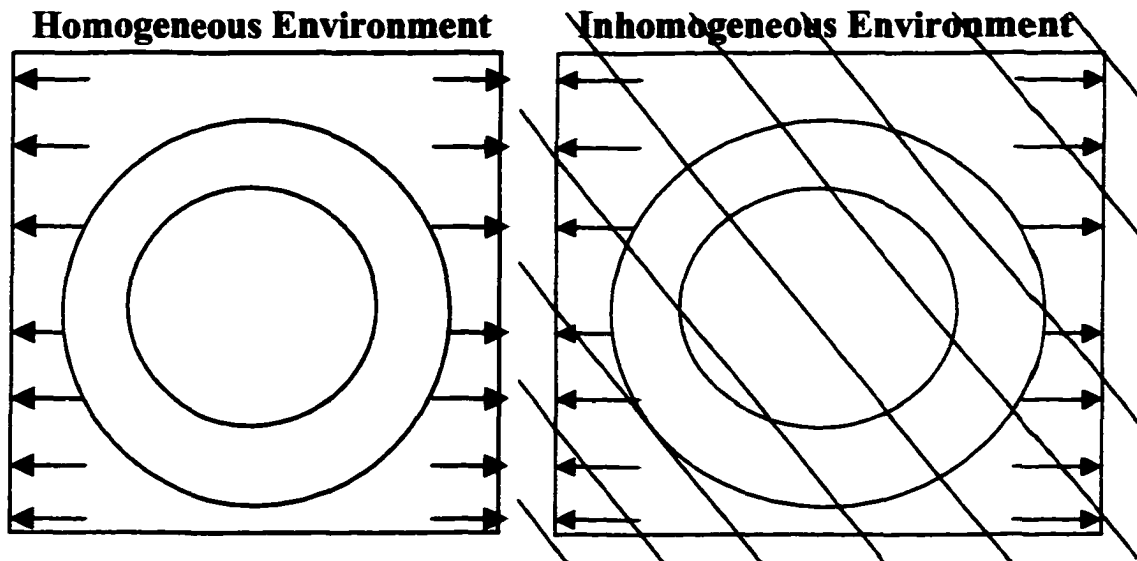


**Figure 3.10: Illustration of a disturbance (circular contours) generated in the interior of the domain that must be allowed to pass through the lateral boundaries. On the left is the homogeneous case, while the right figure shows the inhomogeneous case (slanted contours represent those of the environment).**

In essence, the lateral boundary condition is applied to perturbations from the inhomogeneous state since these are the modes associated with gravity wave disturbances. The modified lateral boundary condition is then

$$\frac{\partial\phi}{\partial t} - \frac{\partial\phi}{\partial t_{env}} = -(u + c_x) \left[ \frac{\partial\phi}{\partial x} - \frac{\partial\phi}{\partial x_{env}} \right] \quad (3.17)$$

for a variable at the eastern or western boundary. Using this form, an inhomogeneous environment with no perturbation will remain steady in time and no spurious regions of convergence or divergence develop. Here 'c' is a gravity wave speed that is normally either assumed to have a particular value (Klemp and Wilhelmson, 1978a) or is estimated from the fields (Orlanski, 1976). In our case, the Orlanski method, which requires multiple time levels of  $\phi_{env}$  is very difficult to apply when the domain is moving through the inhomogeneous environment. For this reason, the Klemp-Wilhelmson method is used, with  $c_x = c_y = 45 \text{ m s}^{-1}$ . This boundary condition is applied only to the velocity component normal to the boundary, and only when the phase speed is greater than any inward-directed normal velocity component such that gravity wave propagation would be directed out of the domain. A similar form was suggested by Carpenter (1982).

### 3.2.3 Advection at Lateral Boundaries

When an environment varies spatially, advection at the lateral boundaries must be done with great care so that environmental gradients are accounted for on inflow. When the environment is homogeneous, a zero gradient condition is assumed for

advection when inflow occurs normal to the lateral boundary. Obviously this is a faulty assumption when the environment is inhomogeneous. In that case, the advection must be done using the appropriate environmental gradient. For example, given a prescribed steady state environment with variable shear, the solution for momentum variables will remain steady only if the advection in both horizontal directions is correctly included (Figure 3.11). Thus, the environmental gradient must be prescribed in some manner.

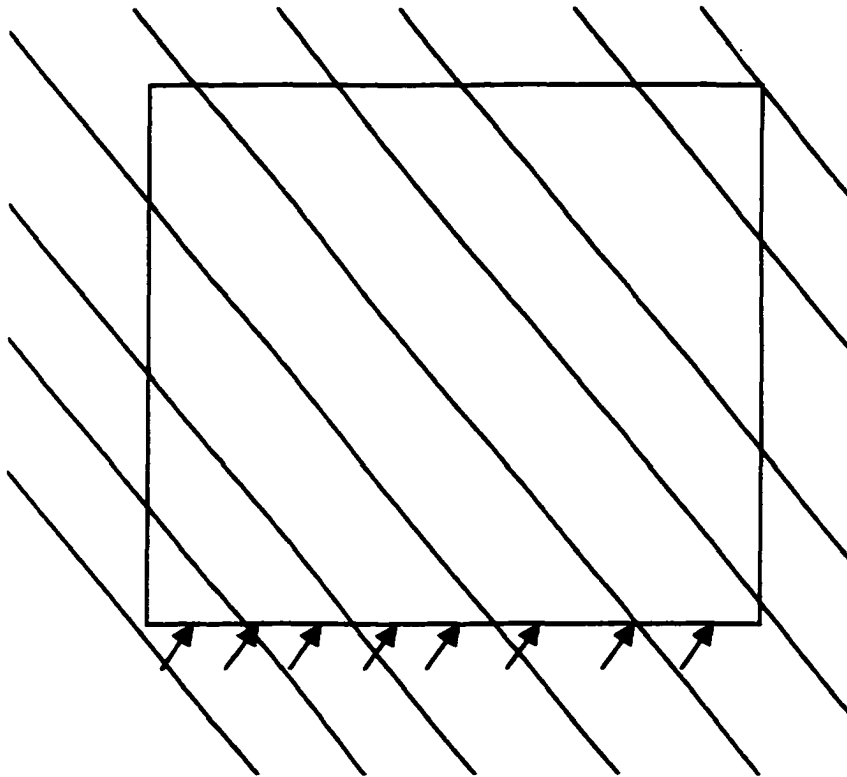


**Figure 3.11: Schematic illustrating the need to include environmental gradients in the advection terms at the lateral boundaries on inflow.**

However, simply specifying a constant gradient can lead to significant errors when the wind changes from outflow to inflow at a boundary or when a large perturbation reaches the boundary. For example, a boundary value that has become higher than the environmental value for that location should be expected to return to the environmental value on inflow after some time. The constant gradient condition could, instead, result in further growth of the perturbation in time, rather than a return to environmental values.

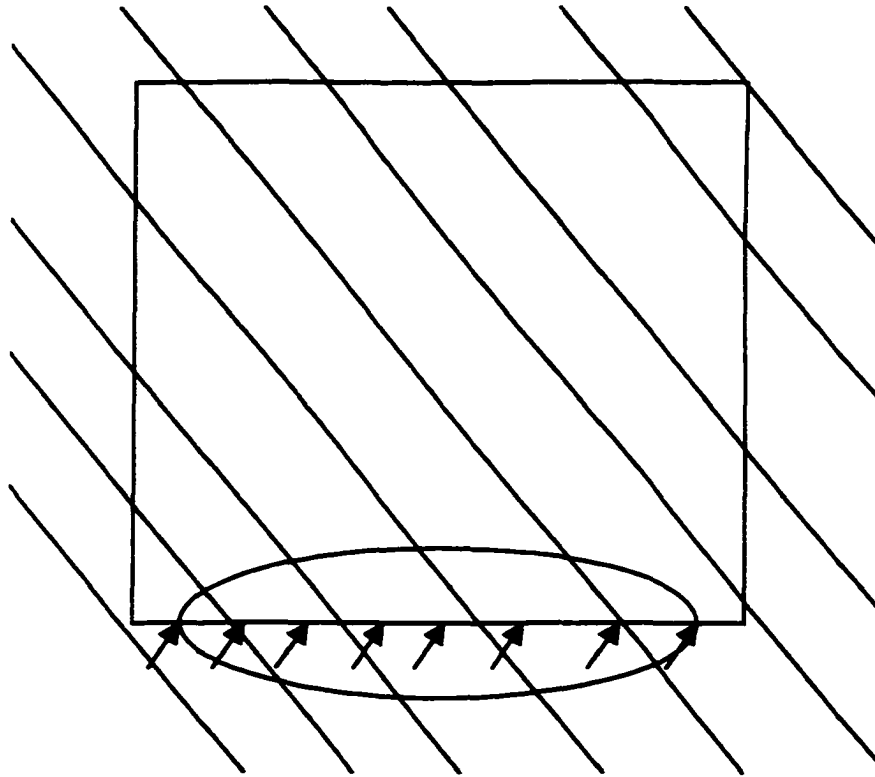


**Figure 3.12: Illustration of a disturbance at the boundary in an inhomogeneous environment. A relaxation term is added to return the boundary value to the environmental value on inflow.**

To facilitate the return to environmental values, a relaxation term is added at the boundary. For example, the advection of  $u$  at the southern boundary on inflow is given by

$$-\frac{\partial u}{\partial t} + v \frac{\partial u}{\partial y} = v \left[ \frac{\partial u}{\partial y} \right]_{env} + r^* |v| [u(tpas) - u_{env}(tpas)] \Delta y^{-1} \quad (3.18)$$

where  $r^*$  is a relaxation coefficient chosen to be 0.5 in our simulations and the relaxation term is lagged in time to maintain linear stability.

In essence, the relaxation term partially cancels the advection by perturbations from the initial state at the inflow boundary. If there is no perturbation, the change of  $u$  in time due to advection will be the sum of the above term plus the advection of  $u$  in the  $x$  direction. Because the environment is designed to be steady-state, the advection terms in the two directions will cancel and  $u$  will be equal to the environmental value at all times; thus, the relaxation will have no effect. If, however, there are disturbance  $u$  and  $v$  values at the boundary, then  $u$  will be relaxed back to its environmental value in time as air flows into the domain. This assumes the advection of the environmental gradient of  $u$  by  $v'$  is small such that, on pure inflow,  $u$  would not depart significantly from its environmental value. Very large environmental gradients, together with very large perturbation  $v$  values on inflow, would invalidate this assumption, but studies suggest it is justified as long as storms remain sufficiently far from the inflow boundary (Weisman et al. 1998).

This boundary specification is somewhat similar to the procedure used by limited domain models whose boundaries are forced by the solution of a larger scale model. Because of the inflow assumptions made here, no conclusions about upscale

influences, i.e. from storm to environment, will be made in this study. An alternative formulation or at least a very large domain would be needed to address this problem. The current study, instead, focuses on the influence of the changing environment on the storm.

### 3.2.4 Domain Translation

Domain translation in a homogeneous environment is relatively straightforward as one simply subtracts the domain speed from the velocity components. When the environment is inhomogeneous, several adjustments must be made to account for domain translation. The rate of change of environmental variables is given by

$$\frac{\partial \phi}{\partial t_{env}} = -c_x \frac{\partial \phi}{\partial x} - c_y \frac{\partial \phi}{\partial y} \quad (3.19)$$

where  $c_x$  and  $c_y$  are the domain translation speeds in the x and y directions, respectively. The computation of the right-hand side is simplified greatly if the changes in the environment are linear with x and y, since this does not require one to keep track of the position of the grid in the larger environment. For this reason, the environments used in our experiments involve linear variations of variables in x and y.

With regard to the normal velocity components, if the environment is steady-state but the domain moves in time, then  $\frac{\partial \phi}{\partial t_{env}}$  is used in the radiation boundary condition to specify the change at the boundary due to domain motion. Similarly, the inhomogeneous background arrays used in the computational mixing and lateral

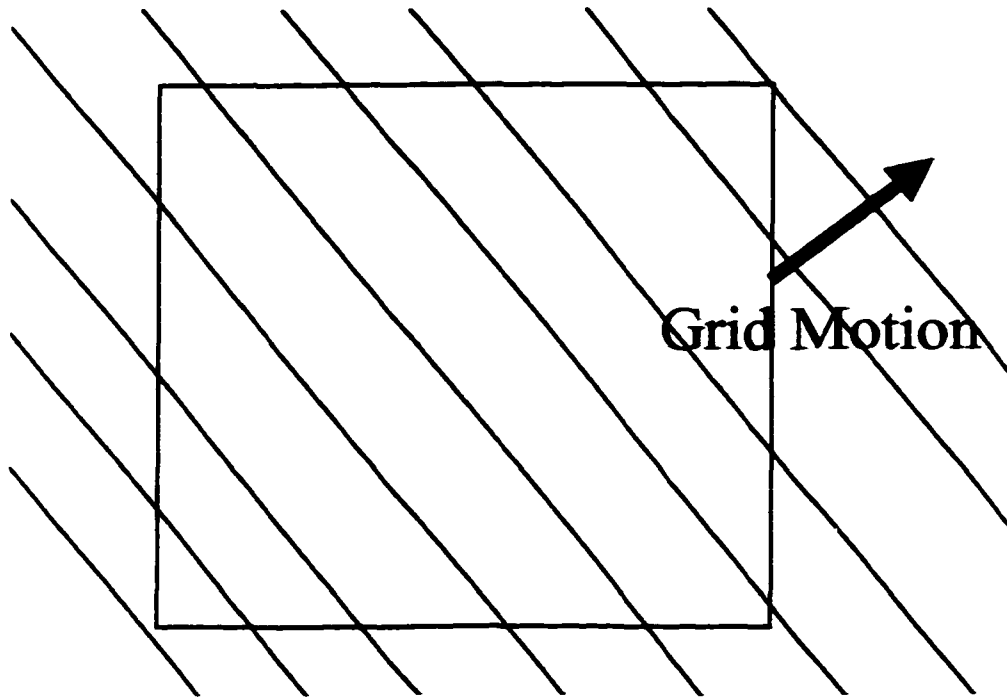


**Figure 3.13 Illustration of grid translation in an inhomogeneous environment.**

boundary relaxation routines for all variables must be adjusted each time step to account for movement through the inhomogeneous domain. This is done by adding a time tendency term at each time step. When all of these changes are included, the domain is able to move through the inhomogeneous environment without producing any perturbations while changing the shear in the appropriate manner. An example of the 'u' term in the Bulk Richardson Shear in a moving domain at 0 and 4 hours is shown in Figure 3.14. Figure 3.15 shows the maximum value of variables during this simulation, and it is clear that no perturbations in  $w$  or scalars is created. At the last timestep of this simulation, a disturbance in the environment ( $w=1 \times 10^{-5} \text{ m s}^{-1}$ ) in the southeast corner was generated due to overturning in the environment as the

Richardson number fell below the stability limit. To avoid those regions where the environment is inherently unstable due to large shear, our results do not extend beyond 4 hours.

If the domain speed is changed during a simulation, as is often necessary, care must be taken to adjust the present and past values of all variables in the leapfrog scheme such that the next time step results in the correct time tendency (i.e., to ensure that the solution remains Galilean invariant) according to

$$\frac{\partial \phi}{\partial t}_{old} = \frac{\partial \phi}{\partial t}_{new} - \Delta u_{move} \frac{\partial \phi}{\partial x} - \Delta v_{move} \frac{\partial \phi}{\partial y} \quad (3.20)$$

where  $\Delta u_{move}$  and  $\Delta v_{move}$  give the changes in the domain motion in the x and y directions and  $\phi$  represents any of the model variables. Thus, the value of a variable at  $tpast$  is adjusted such that

$$\phi(tpast)_{new} = \phi(tpast)_{old} - \Delta t_{big} (\Delta u_{move} \frac{\partial \phi}{\partial x} + \Delta v_{move} \frac{\partial \phi}{\partial y}) \quad (3.21)$$

where the gradients are evaluated as an average of  $tpresent$  and  $tpast$  values. For radiation lateral boundary conditions, a zero gradient is normally assumed when adjusting the boundary point. In our case, the environmental gradient is used for adjusting the boundary points, and domain translation adjustments must also be applied to the base state arrays used for computational mixing.

When all of these changes are made to the model, the environment remains steady in time and no perturbations are created at the boundaries, as evidenced in Figure 3.15, which shows the domain minimum values of  $u$  and  $v$  decreasing at a fixed rate for an initial domain translation speed and at an increased rate when the domain speed is changed. The maximum values of vertical velocity, perturbation potential temperature, cloud water, and perturbation pressure are all within roundoff error for the computer.

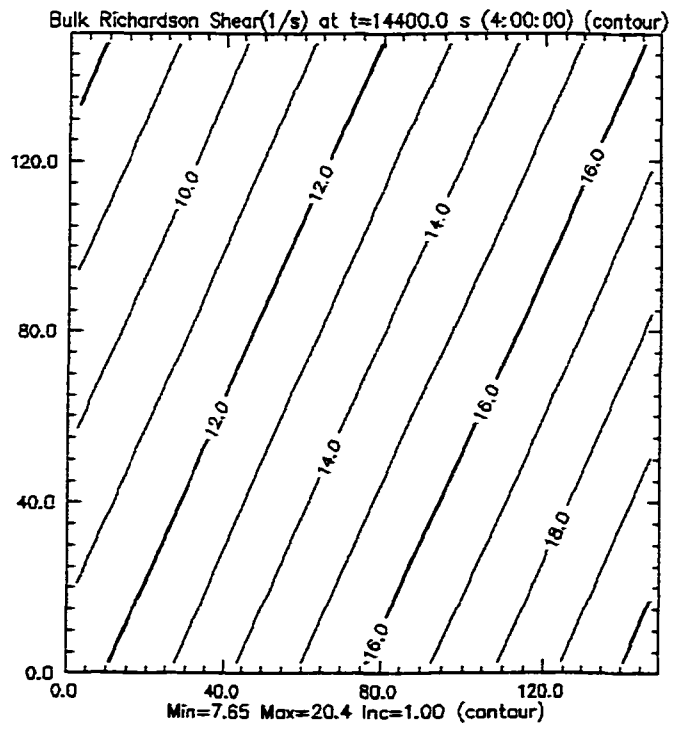
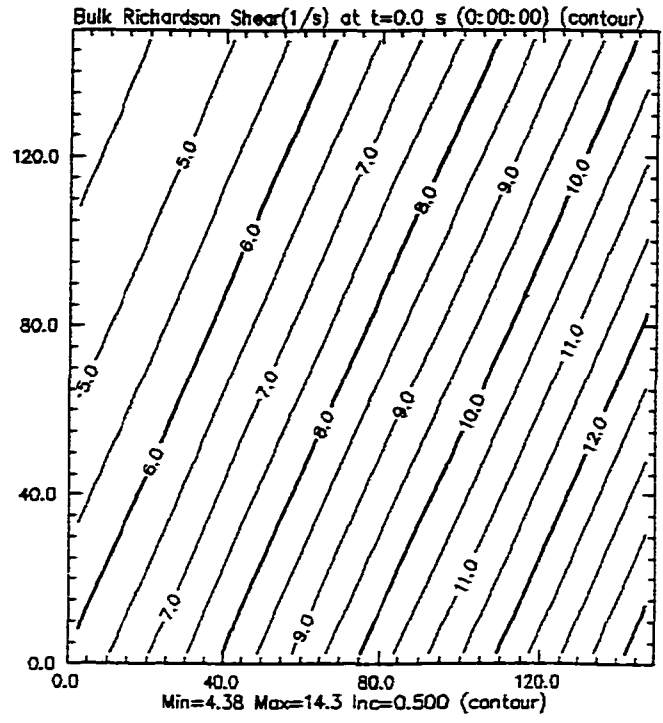


**Figure 3.14 Contours of the 'u' term in the Bulk Richardson Number at t=0 (top) and t= 4 hours (bottom) as the domain traverses an inhomogeneous environment.**

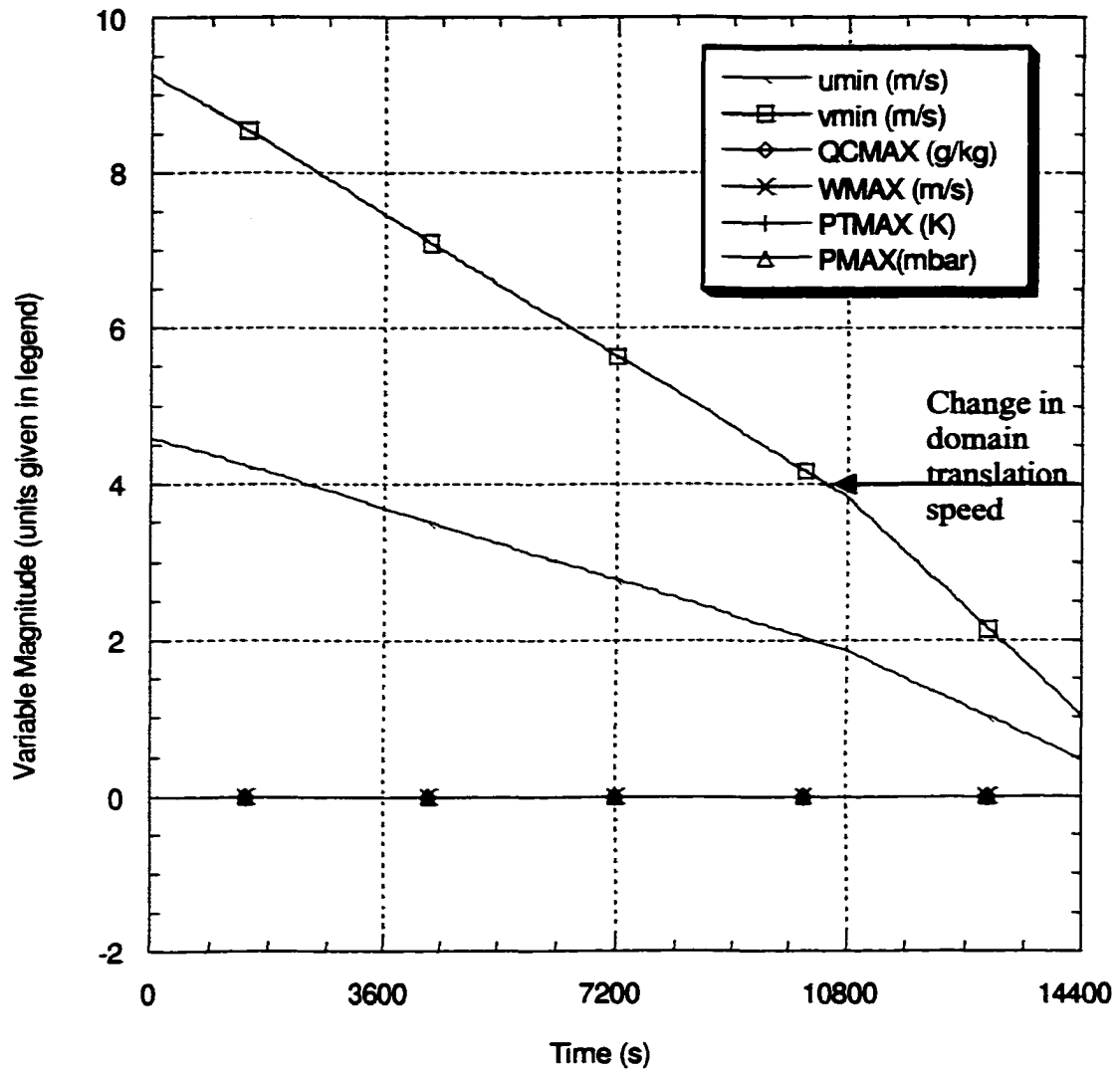


**Figure 3.15: Domain maximum and minimum values as designated in the legend for a domain moving through an inhomogeneous environment. Note the change in grid translation speed.**

## **Chapter 4 Experiments with Inhomogeneous Low Level Moisture**

Storm environments are often characterized by significant variations in moisture and/or temperature, and the effect of these variations is virtually unknown. It is reasonable to believe that a change in the moisture available to a storm will significantly affect its ensuing morphology. Theoretically, the maximum updraft speed realized by a parcel is directly related to the CAPE, which is very sensitive to the low-level moisture. Convective initiation, on the other hand, is quite sensitive to the environmental Convective Inhibition (CIN), which itself is sensitive to low-level moisture. The combination of these facts has led to the widely held belief that 'storms seek out the better moisture', although no specific mechanism for this behavior is generally offered. It is also unclear whether this behavior should be expected both in weak and strong shear conditions. The ability to perform idealized, inhomogeneous environment simulations allows us, for the first time, to address these questions in a systematic and controlled manner and to offer proposed mechanisms for observed storm behavior in various shear regimes. When a single temperature profile is used with varying moisture profiles, both the CAPE and CIN are affected. Such is the case here. Thus, these experiments are best described as variable moisture experiments rather than simply variable CAPE experiments.

CAPE is often used as a predictor of storm strength and the potential for hail and other severe weather. The dependence of storm 'type' (i.e., the updraft rotation and longevity of a storm) on CAPE is a bit more muddled. The classic storm type

predictand, the BRN, uses CAPE in its numerator such that, for the same environmental vertical shear, high CAPE leads to high BRN and, thus, a more multicellular nature to the convection (Weisman and Klemp, 1982). The usual reasoning relates the CAPE to the strength of the downdraft such that high CAPE would indicate a more intense downdraft that is capable of undercutting the updraft, thus leading to a multicell system. However, this presumes that CAPE and downdraft-CAPE (DCAPE) are correlated. In reality, there may not exist a direct relationship between CAPE and storm type when a wide range of hodographs and thermodynamic profiles is considered.

Given identical temperature and shear profiles, we would expect, however, that updraft strength should increase with increased low-level moisture, regardless of storm type. Mid-level rotation, which results from tilting of environmental horizontal vorticity, depends strongly upon gradients in vertical velocity and would, therefore, also be expected to increase as low-level moisture increases. The dependence of low-level rotation on low-level moisture is a bit more complex. Brooks et al. (1994b) suggest that low-level moisture plays an integral role in distinguishing between tornadic and nontornadic storm environments.

If the CIN is too great, it may not be possible to generate a storm for a given initial perturbation. It is unclear, however, whether this same environment could support an *existing* storm which formed in more favorable moisture and then moved into the less favorable environment. *If this is the case, some storms may exist largely because of their history rather than their current surroundings.* A simulation based

on a sounding representative of the ambient environment would therefore result in no deep convection, while one based on a sounding from the location of storm initiation could greatly overestimate storm strength. This dilemma calls into question the popular notion of a 'proximity' sounding.

As a storm system moves into regions of increased low-level moisture, the location and timing of cell redevelopment along the gust front may also be altered, affecting the interactions among cells and influencing the original cell either constructively or destructively. Interactions such as this will be discussed, but it is unclear that general results about storm intensity can be drawn since both positive and negative interactions are possible.

#### **4.1 Environmental Setup**

In order to isolate the effects of variable moisture, it was desirable to construct an environment in which moisture variations are independent of the vertical shear. In order to facilitate interpretation and boundary condition requirements, it is also desirable to have a steady-state environment. The most straightforward scenario meeting these goals is one in which moisture varies such that its advection by the horizontally-homogeneous base state winds is zero, i.e., moisture varies in the direction perpendicular to the base state winds. (A similar setup was used by Skamarock *et al.* (1994b) to study the effect of variable CAPE on a numerically modeled squall line. However, they also allowed the wind shear to vary and, by varying moisture independently of the pressure, it is unclear whether their environment was steady state.)

Simply eliminating the advection of moisture is not sufficient to obtain a steady state. Because the moisture field is related to the hydrostatic pressure field through the virtual temperature, a horizontal variation in the moisture will lead to a concomitant variation in pressure. This pressure gradient will then accelerate the winds and the environment will evolve, making analysis and the provision of robust lateral boundary conditions difficult. One method for remediation is to introduce a small variation in the horizontal winds such that the momentum advection terms compensate for the pressure gradient force, keeping the environment steady. This leads to difficulties in interpretation, however, because both the shear and the CAPE vary. Also, this strategy would require a wind component across the pressure gradient, leading to advection of pressure and moisture, and, thus, a non-steady state.

A more elegant approach is to let the temperature vary slightly, along with the moisture, such that the virtual temperature remains horizontally uniform. In this way, pressure also remains horizontally uniform and the environment will remain steady. This is the approach used in this study, where the adjustment to potential temperature for a given specific humidity variation is given by

$$\theta' = -\frac{\bar{\theta} [(q_v - \bar{q}_v)(1 - \varepsilon)]}{(\varepsilon + \bar{q}_v)(1 + \bar{q}_v)} \quad (4.1)$$

where  $\varepsilon$  is the ratio of the gas constant for dry air ( $R_d$ ) to the gas constant for water vapor ( $R_v$ ) and the barred quantities represent base state values.

Weisman and Klemp (1982) examined the influence of CAPE within homogeneous environments by specifying a particular vertical profile for potential

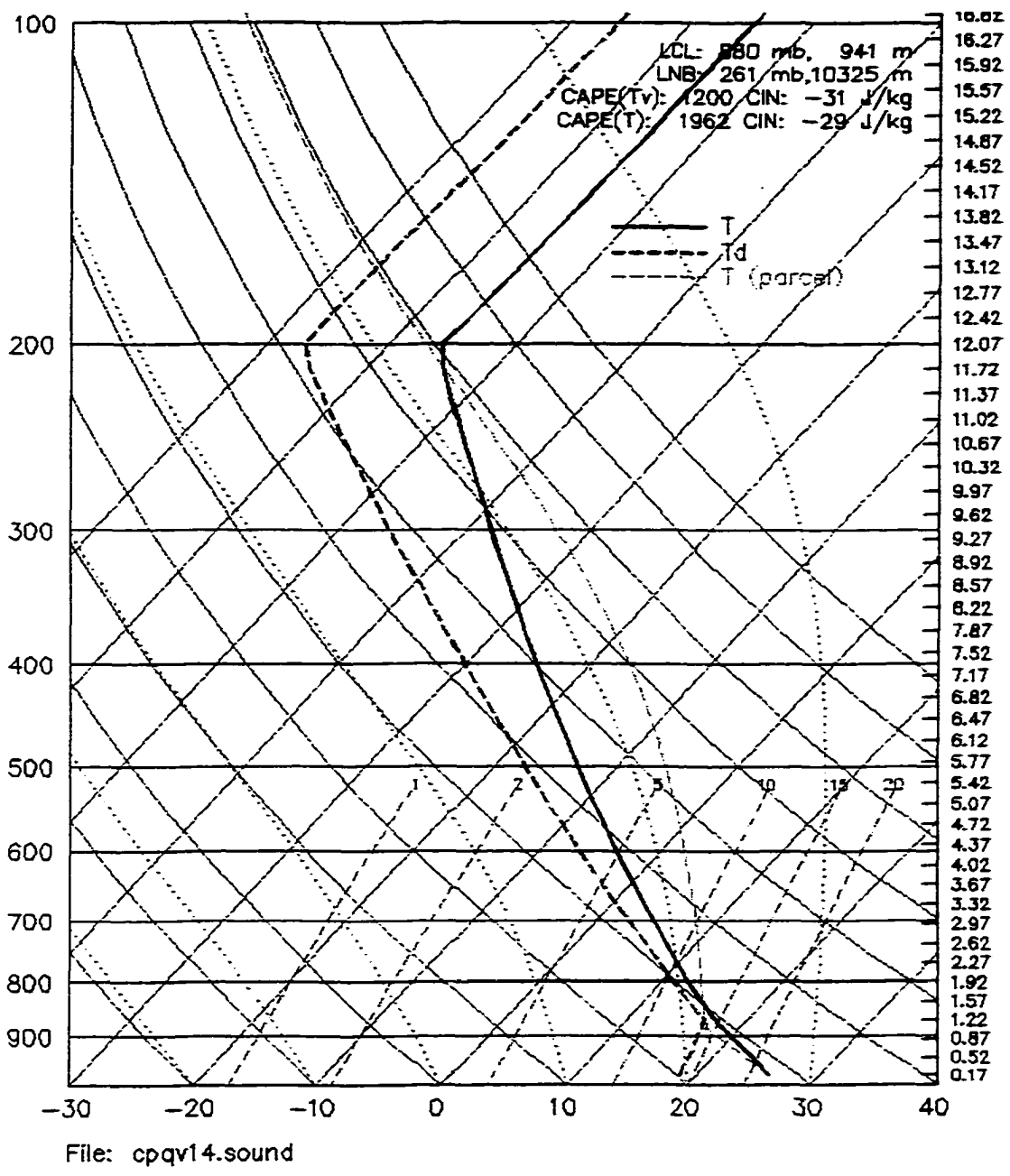
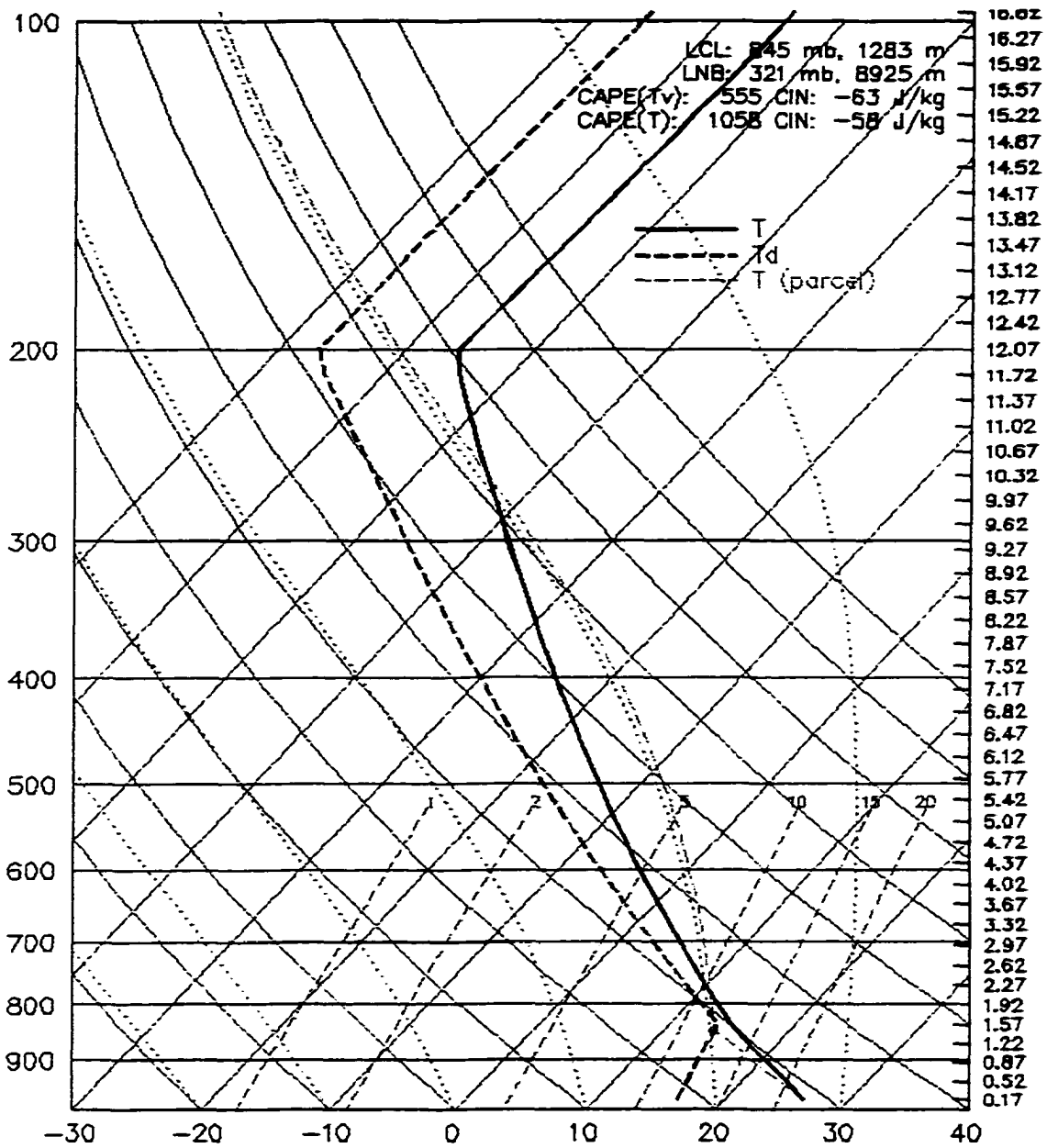


**Figure 4.1: Weisman and Klemp (1982) thermodynamic profile with  $q_v$  in the mixed layer equal to 14 g/kg.**

temperature and relative humidity (Figure 4.1). The CAPE was altered for different experiments by changing the value of the water vapor mixing ratio within the mixed layer. A similar method is used here, but the moisture variation occurs across a single environment. To facilitate comparison with their results, the original Weisman and Klemp sounding is specified in the location of the greatest mixed layer water vapor mixing ratio to be used in the simulation. The mixed layer value of  $q_v$  is then decreased systematically across the domain, with the corresponding change in potential temperature added to maintain constant virtual potential temperature.

Previous studies have suggested that even small variations in low level temperature can influence the initiation of storms (Crook, 1996; Brooks et al., 1993b), particularly when the variations occur at certain levels such that CIN is greatly modified. In our simulations, the temperature perturbations are applied throughout a layer, thereby reducing their influence on CIN. (In Crook (1996) the temperature 'error' was applied only at the surface, while in Brooks et al. (1993b) the temperature 'error' occurred at a higher level, resulting in a markedly different LFC.)

To illustrate the change in the vertical temperature profile in a typical scenario for the present study, Figure 4.2 shows the modified profile of temperature used at the domain location with mixing ratio of 12 g/kg when the base state mixing ratio is 18 g/kg (i.e., the mixed layer mixing ratio has been adjusted by 6 g/kg at this location and (4.1) has been used to determine the temperature adjustment at each level). Figure 4.3 shows the same water vapor profile paired with the modified temperature profile taken from a different portion of the domain (corresponding to a mixing ratio



File: cpqv12.sound

**Figure 4.2: Weisman and Klemp (1982) thermodynamic profile with  $q_v$  in the mixed layer equal to 12 g/kg.**

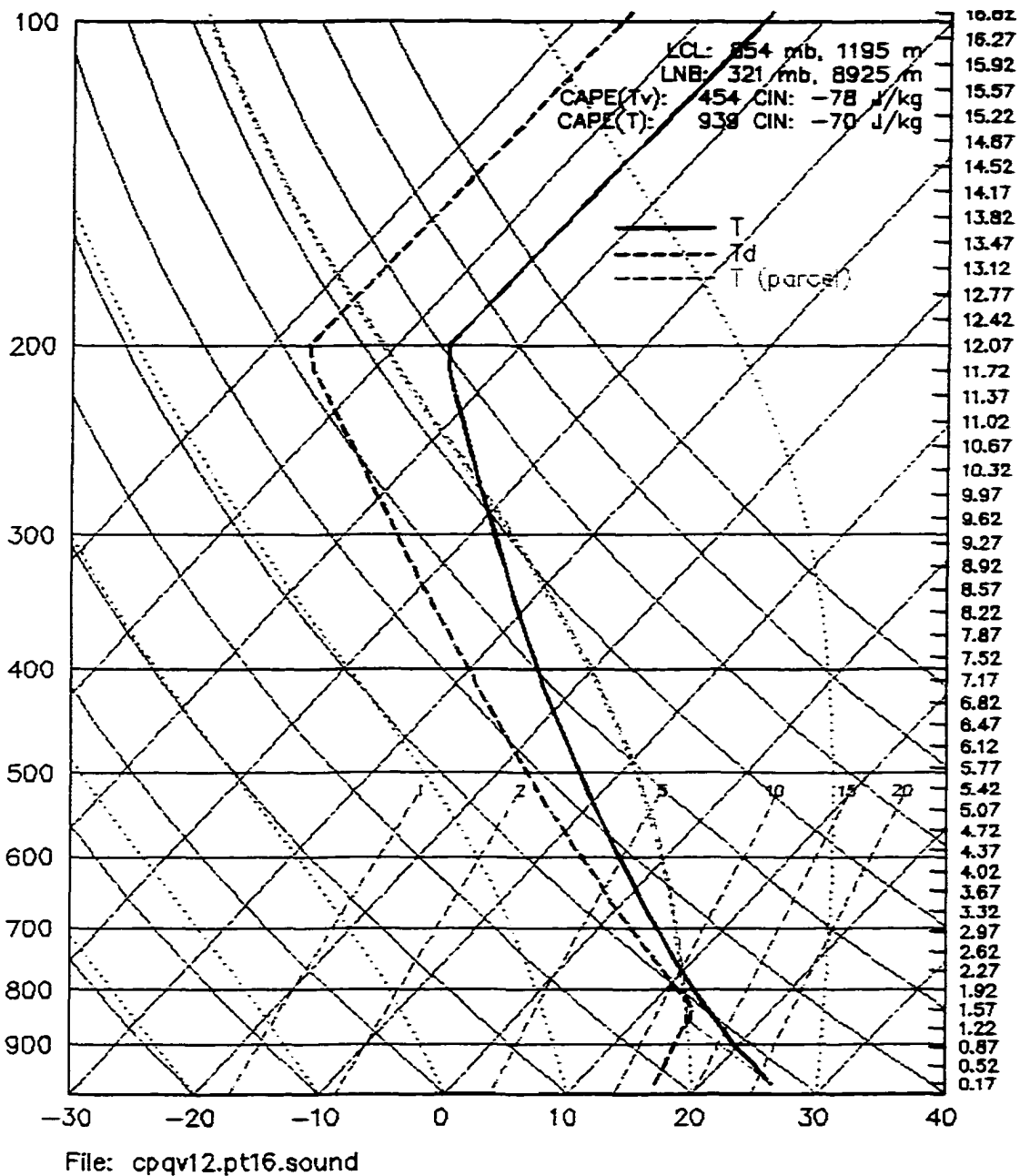


**Figure 4.3: Thermodynamic profile with  $q_v$  in the mixed layer equal to 12 g/kg and adjusted potential temperature equal to that used with  $q_{vmix}=16$  g/kg.**

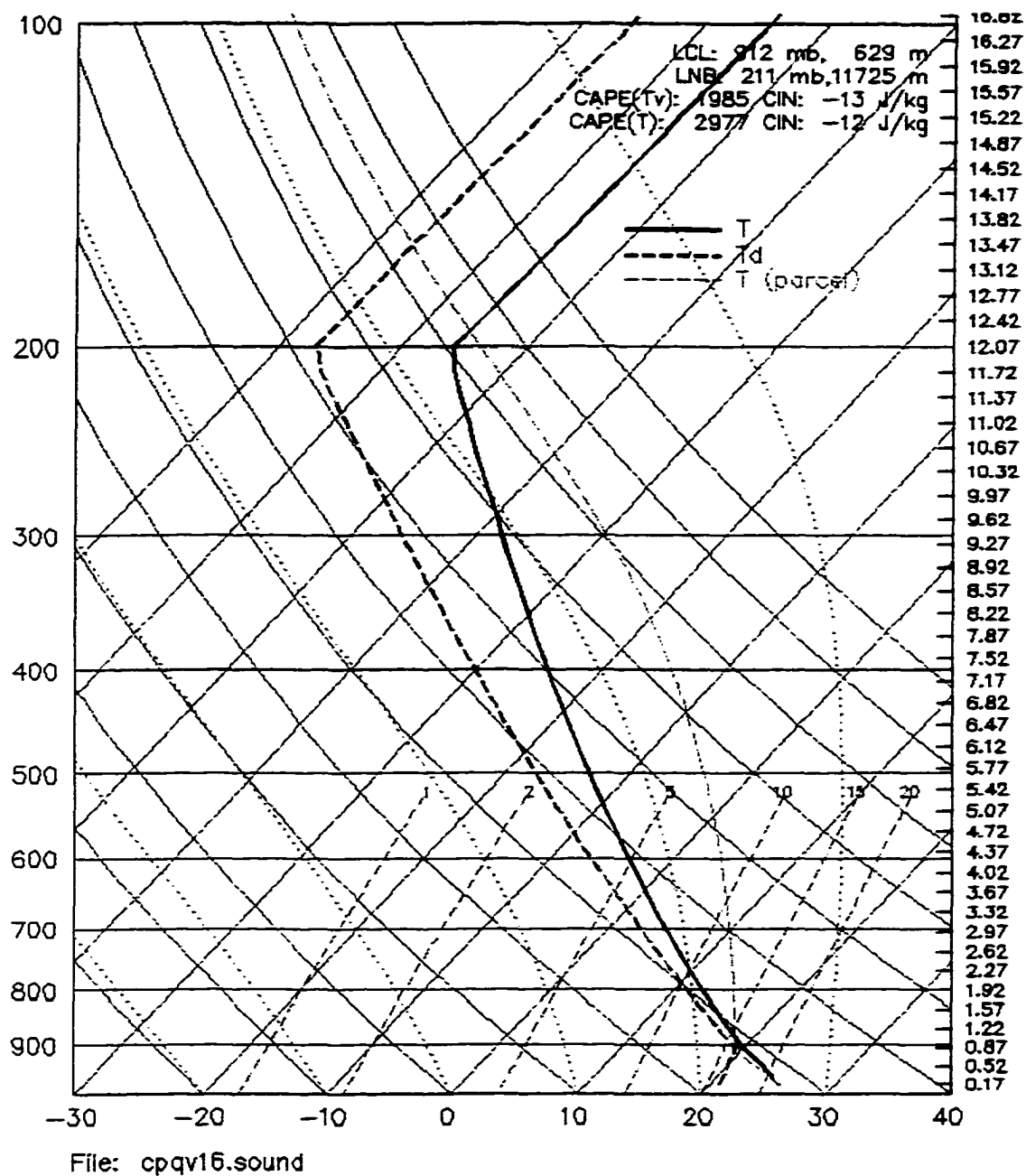


**Figure 4.4: Weisman and Klemp (1982) thermodynamic profile with  $q_v$  in the mixed layer equal to 16 g/kg.**

of 16 g/kg). By comparing these two soundings, with equivalent mixing ratios but with slight modifications to temperature, we see that the CIN is altered very little and the LFC and the LCL are nearly identical. In contrast, we compare Figure 4.3 with Figure 4.4, having the same temperature profile but different mixing ratio values, to see the influence of changes in water vapor alone. In this case, the CAPE, CIN, LFC, and LCL are all dramatically different. It is clear that changes in the mixing ratio have much greater influence on overall sounding properties than do slight changes in temperature. For this reason, our experiments assume that changes in storm behavior are due primarily to the specified moisture variations.

In all variable moisture experiments, the domain is 120x192x20 km<sup>3</sup>, with the initial disturbance centered with respect to x and y. For the control runs, which are symmetric about an east-west plane centered on the disturbance, only half the computational domain is needed in the y direction, with a symmetry condition imposed at y = 96 km.

#### **4.2 Influence of Variable Moisture in a Weak Shear Environment**

The above procedure is used to examine the influence of variable moisture on a simulated storm with an environment characterized by weak vertical shear. The shear is unidirectional in the east-west direction, with the wind magnitude determined by

$$u = U_s \tanh(z/z_s) \tag{4.2}$$

where  $z_s = 3000$  m and  $U_s = 12$  m s<sup>-1</sup>, producing a wind profile as shown in Figure 4.5. The question here is whether or not the multicell system initiated along the

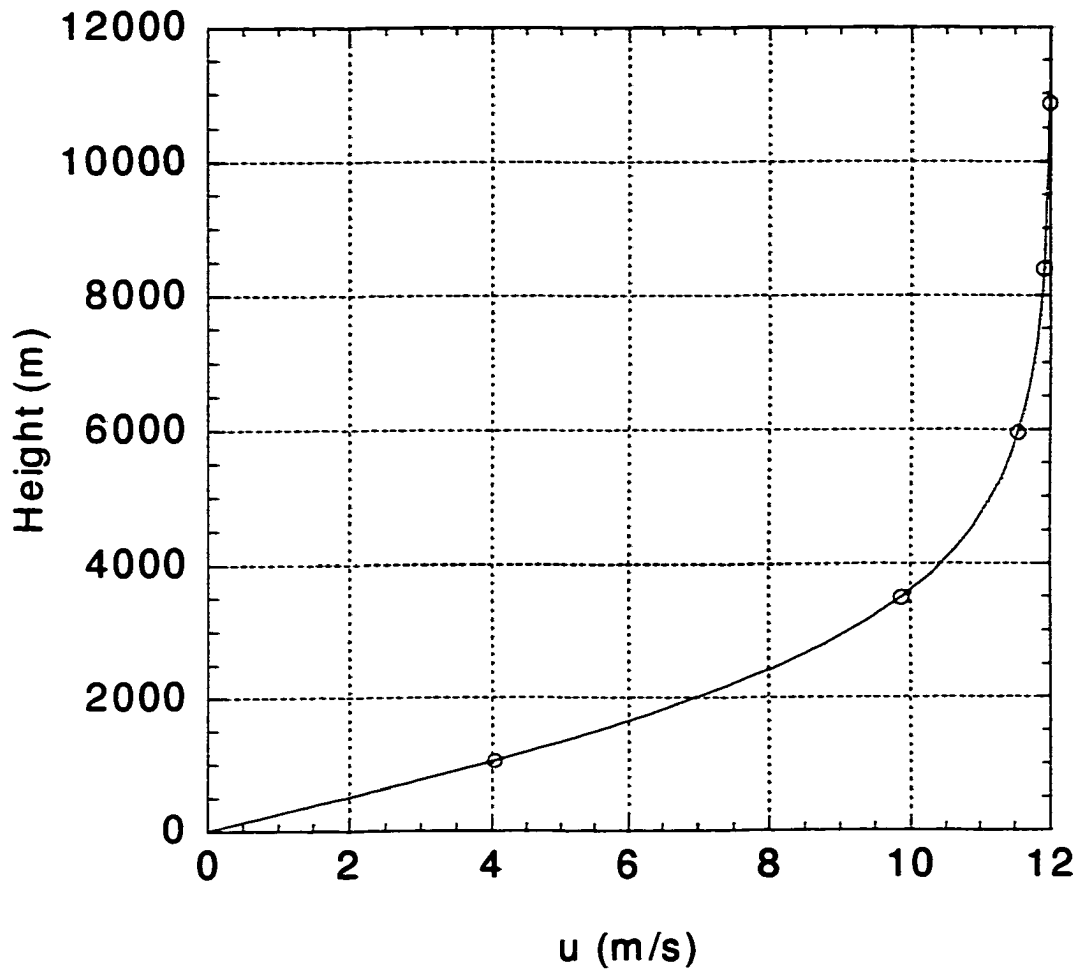


**Figure 4.5: Profile of u component of the velocity with height for weak shear case.**

symmetry axis at  $y=96$  km will develop preferentially toward the flank that extends into greater moisture. We might expect this to be the case because the LFC is lower on this flank, and regeneration of cells should be more easily accomplished. We consider two cases with different initial values of moisture.

In the first inhomogeneous case, the mixed-layer mixing ratio varies as shown in Figure 4.6, with a value of  $14 \text{ g kg}^{-1}$  at the initiation location. A homogeneous control simulation performed using this initial thermodynamic profile develops the multicell storm system shown in Figure 4.7 at 2 hours. Cells form along an arc that is symmetric with respect to the mean shear vector. A time series of the domain maximum value of vertical velocity is shown in Figure 4.8 and indicates typical multicell behavior in which the initial cell is the strongest and is followed by weaker cells at various intervals. Given this control run for the initiation location of the inhomogeneous domain, we would expect the gust front in the inhomogeneous case to spread into mixing ratios of  $12\text{-}13 \text{ g kg}^{-1}$  on the northern side and  $15\text{-}16 \text{ g kg}^{-1}$  on the southern side.

Vertical velocities at  $z=4.6$  km at 2 hours for control runs using  $13 \text{ g kg}^{-1}$  and  $16 \text{ g kg}^{-1}$  are shown in Figure 4.9 and Figure 4.10, respectively. Cell locations are similar in the  $14$  and  $16 \text{ g kg}^{-1}$  simulations, while the lateral spread of cells is greatly reduced in the  $13 \text{ g kg}^{-1}$  case. In all of these simulations, the original cell splits as rain forms on its central axis. New cells form on the downshear side of the cold pool, where rain-induced outflow opposes the low level winds and leads to enhanced convergence. This convergence depends upon the strength of the rain-induced

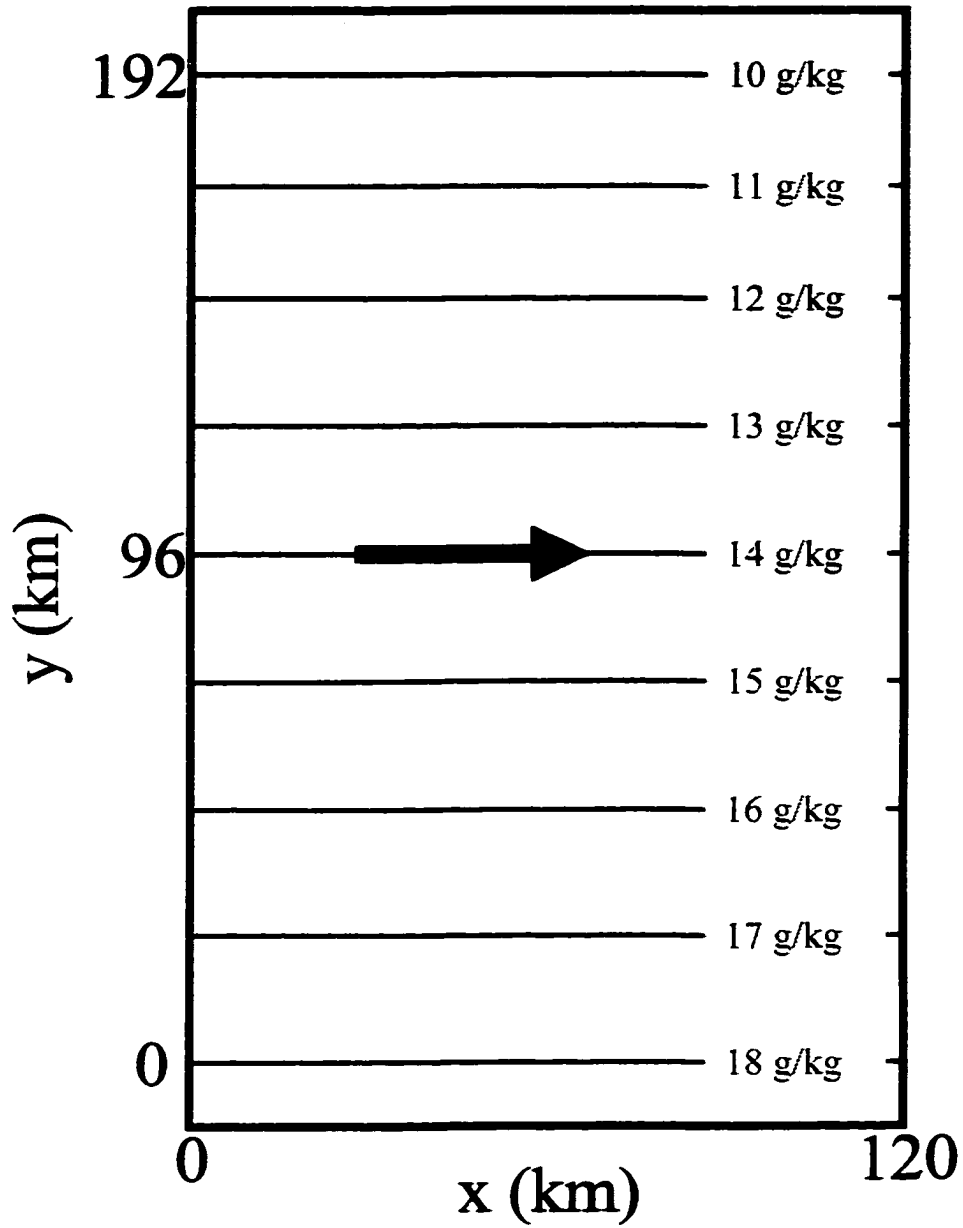
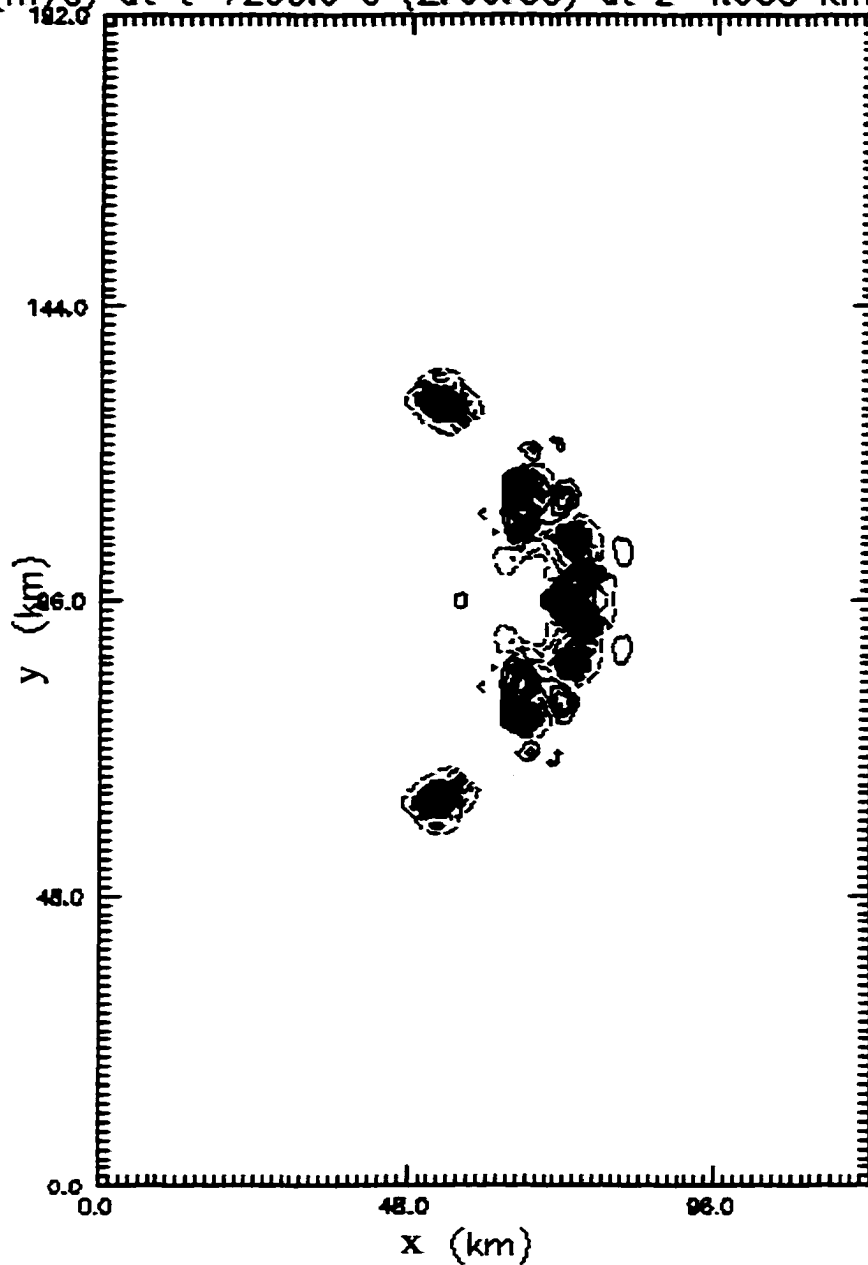


**Figure 4.6: Schematic of inhomogeneous domain for CAPE simulations.**

wprt (m/s) at t=7200.0 s (2:00:00) at z=4.600 km



Min=-4.21 Max=15.5 Inc=1.00 (contour)

**Figure 4.7: Horizontal cross-section of vertical velocity at  $z=4.6$  km at  $t = 2$  hours for weak shear ( $U_s=12$  m s<sup>-1</sup>) control run with  $q_{vmix}=14$  g/kg. (Actual computational domain is the southern half of that shown, with a symmetric condition applied at  $y=96$  km.)**

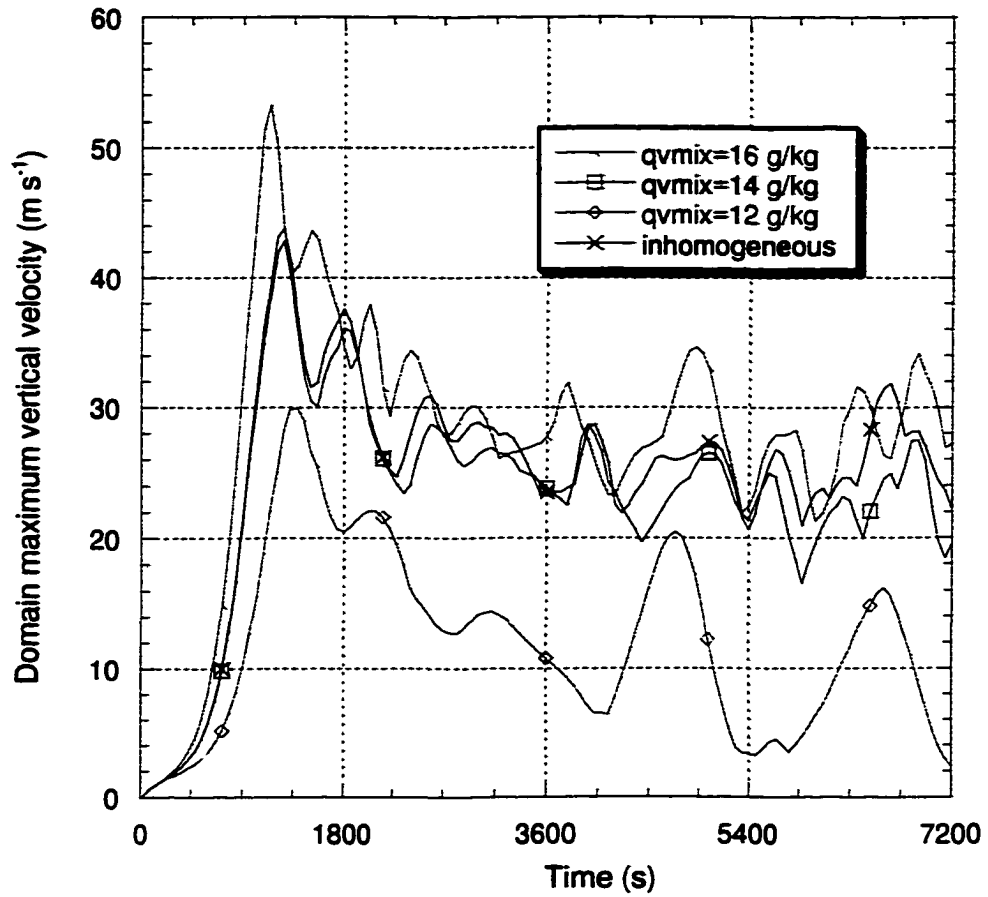
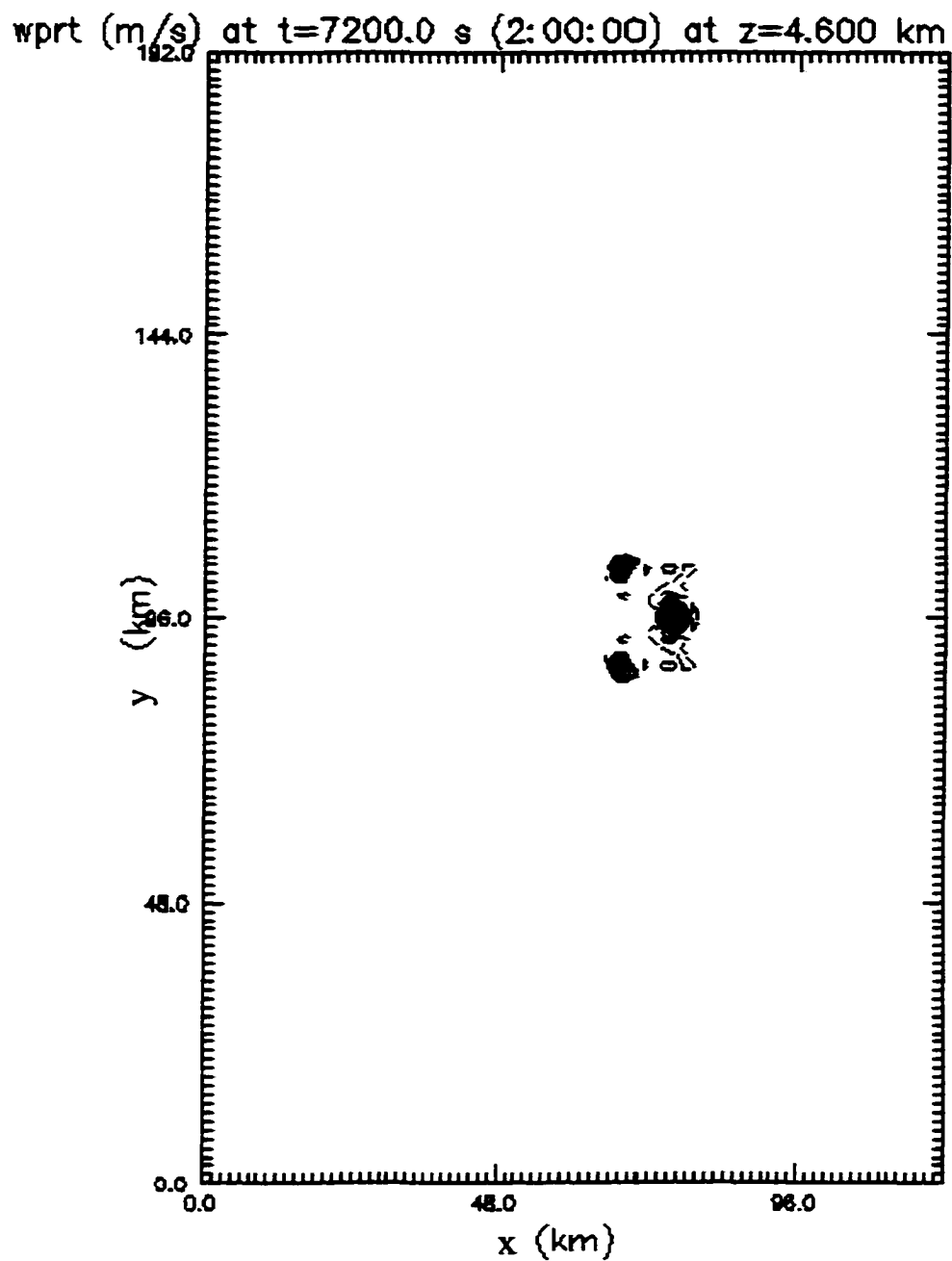


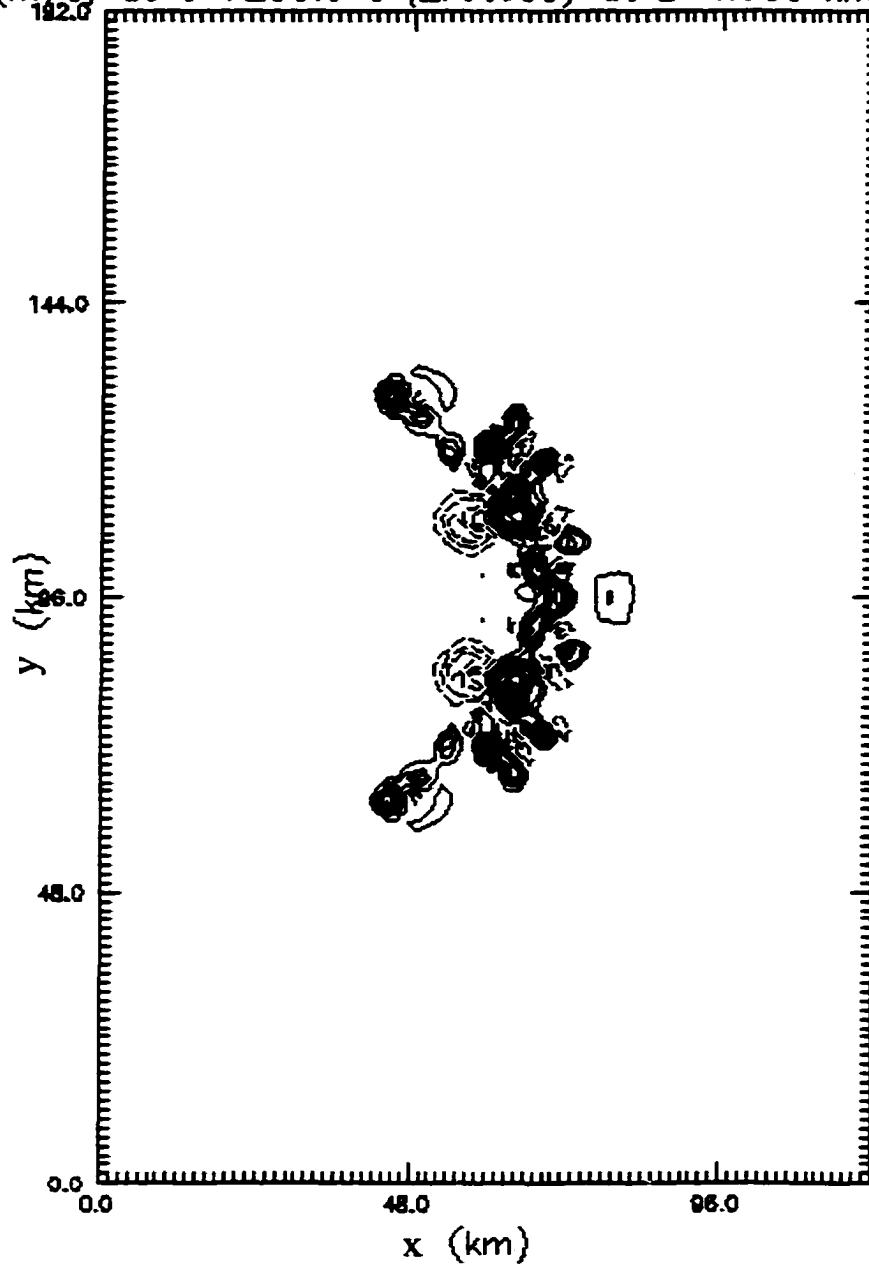
**Figure 4.8: Domain maximum vertical velocity versus time for weak shear, inhomogeneous moisture simulation and corresponding homogeneous control runs. Mixed layer mixing ratios ( $q_{vmix}$ ) are shown in the legend for each homogeneous simulation. The inhomogeneous simulation has 14 g/kg in the initiation location.**



Min=-2.31 Max=15.4 Inc=1.00 (contour)

**Figure 4.9: Horizontal cross-section of vertical velocity at  $z=4.6$  km at  $t = 2$  hours for weak shear control run with  $q_{vmix}=13$  g/kg. (Actual computational domain is the southern half of that shown, with a symmetric condition applied at  $y=96$  km.)**

wprt (m/s) at t=7200.0 s (2:00:00) at z=4.600 km



Min=-7.95 Max=17.7 Inc=2.00 (contour)

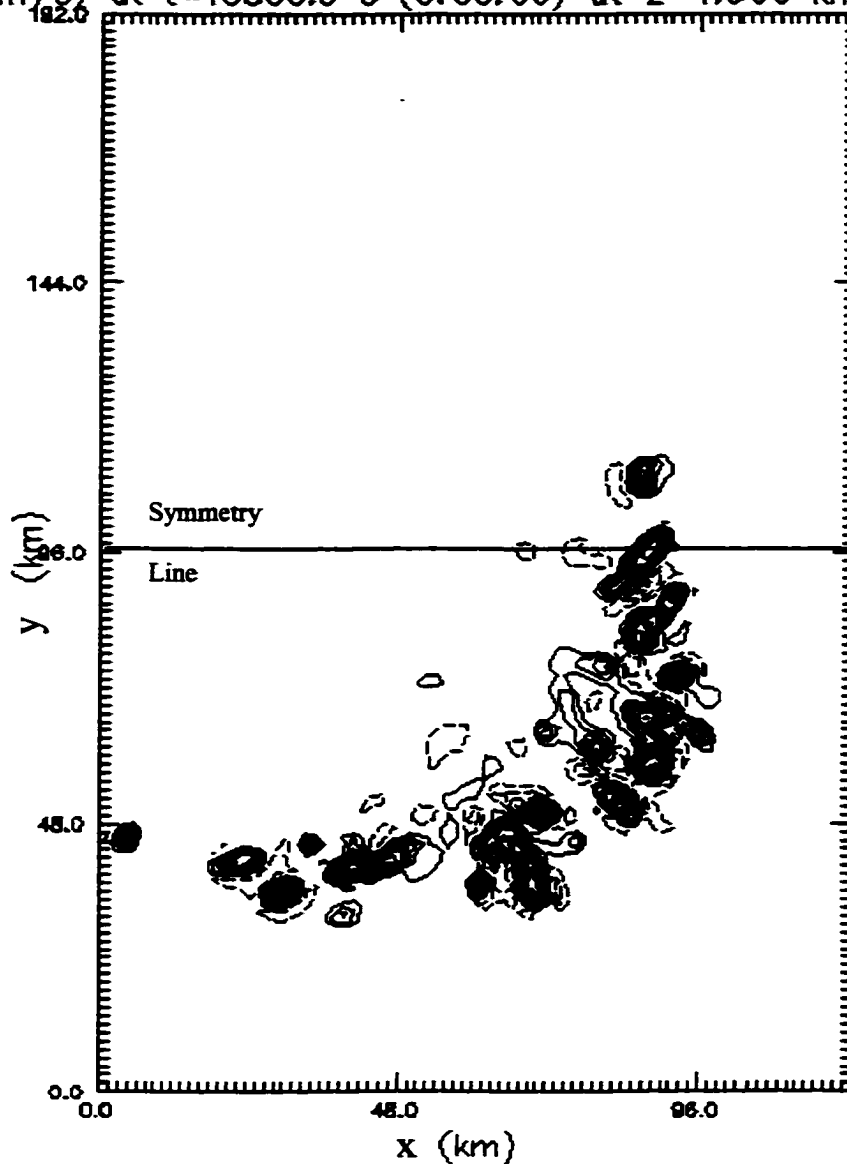
**Figure 4.10: Horizontal cross-section of vertical velocity at  $z=4.6$  km at  $t = 2$  hours for weak shear ( $U_s=12 \text{ m s}^{-1}$ ) control run with  $q_{\text{mix}}=16 \text{ g/kg}$ . (Actual computational domain is the southern half of that shown, with a symmetric condition applied at  $y=96$  km.)**

outflow, which is determined by the amount of rain produced as well as the amount of evaporational cooling. With larger low-level mixing ratios, more rain is produced, leading to a stronger cold pool and enhanced convergence, provided that the environmental sounding is sufficiently subsaturated (Brooks et al. 1994b). In addition, the LFC is much lower and the CIN is less, so that cells form more easily in the higher moisture regions. All of these influences contribute to the differences in new cell development on the flanks of the gust fronts. Although the  $13 \text{ g kg}^{-1}$  control run does not produce new cells on the flanks of its cold pool, it is unclear whether a different cold pool, formed in higher moisture and thus having stronger convergence, would also be unable to generate new cells as it moves into the  $13 \text{ g kg}^{-1}$  air.

In particular, when a cell is initiated in the inhomogeneous environment at the location corresponding to  $q_v=14 \text{ g kg}^{-1}$ , we might expect that cells will develop more easily on its southern side, with weaker cells forming on the northern side. The increased rain production compared to the  $13 \text{ g kg}^{-1}$  case should produce a stronger cold pool that more readily forces parcels to their LFC as it moves into the  $13 \text{ g kg}^{-1}$  air. The domain maximum value of vertical velocity, shown in Figure 4.8, indicates a very strong initial updraft that quickly decreases in intensity and is followed by weaker maxima. The original cell again splits into two as rain falls on the central axis, with the southern updraft significantly stronger. As the cold pool spreads beneath the original updraft, cells are initiated on predominantly the southern side (Figure 4.11), although one weak, short-lived cell does form to the north.



wprt (m/s) at t=10800.0 s (3:00:00) at z=4.600 km



Min=-8.63 Max=21.1 Inc=2.00 (contour)

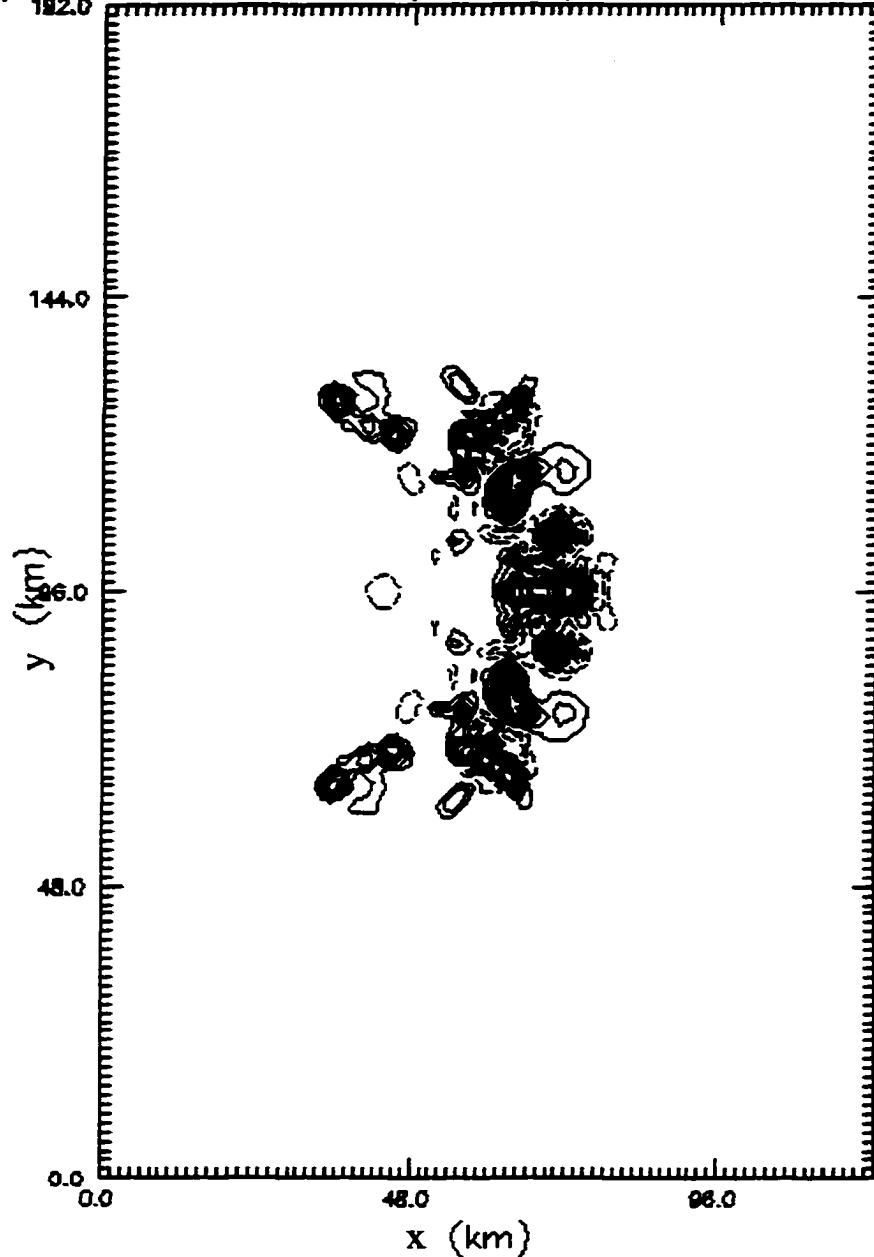
**Figure 4.12: Horizontal cross-section of vertical velocity at  $z=4.6$  km at  $t = 3$  hours for weak shear ( $U_s=12 \text{ m s}^{-1}$ ) inhomogeneous CAPE simulation with qvmix as in Figure 4.11.**

As time progresses, the cells become increasingly skewed toward the side with greater moisture, despite a north-south symmetry in gust front location. At 2 hours, *all* significant cells are located at or south of the original symmetry line (see Figure 4.11) and this pattern continues at 3 hours (Figure 4.12). This result is to be expected given the striking difference in cell development along the flanks in the control simulations. Despite the increased rain production compared to the low moisture control simulation, the cold pool is unable to generate new cells in the drier air to the north. New cells are generated almost exclusively to the south, skewing the system toward this direction in time.

While the above result is interesting, it is somewhat expected since the control runs themselves do not display the same lateral extent of cells in different environments. It is of interest, therefore, to see if this skewing toward higher moisture will occur even when the control runs all show similar lateral development. In that case, the biasing cannot be attributed to a simple inability to generate flank cells but must be due to some other process.

To illustrate, a second inhomogeneous simulation is performed with storm initiation at  $q_v = 16 \text{ g kg}^{-1}$ . Vertical velocities at  $z=4.6 \text{ km}$  and 2 hours for control runs with  $q_v = 14, 16, \text{ and } 18 \text{ g kg}^{-1}$  are shown in Figure 4.7, Figure 4.10, and Figure 4.13, respectively. Each of the control simulations produces cells on the flanks of the gust front. In the inhomogeneous case, initial cell development is very similar to the  $16 \text{ g kg}^{-1}$  control run (Figure 4.14). The original cell splits as rain forms on its central axis, and the system remains quite symmetric throughout the first hour as a new cell

wprt (m/s) at t=7200.0 s (2:00:00) at z=4.600 km



Min=-9.17 Max=24.2 Inc=2.00 (contour)

**Figure 4.13: Horizontal cross-section of vertical velocity at  $z=4.6$  km at  $t = 2$  hours for weak shear ( $U_s=12 \text{ m s}^{-1}$ ) control run with  $q_{\text{mix}}=18 \text{ g/kg}$ . (Actual computational domain is the southern half of that shown, with a symmetric condition applied at  $y=96$  km.)**

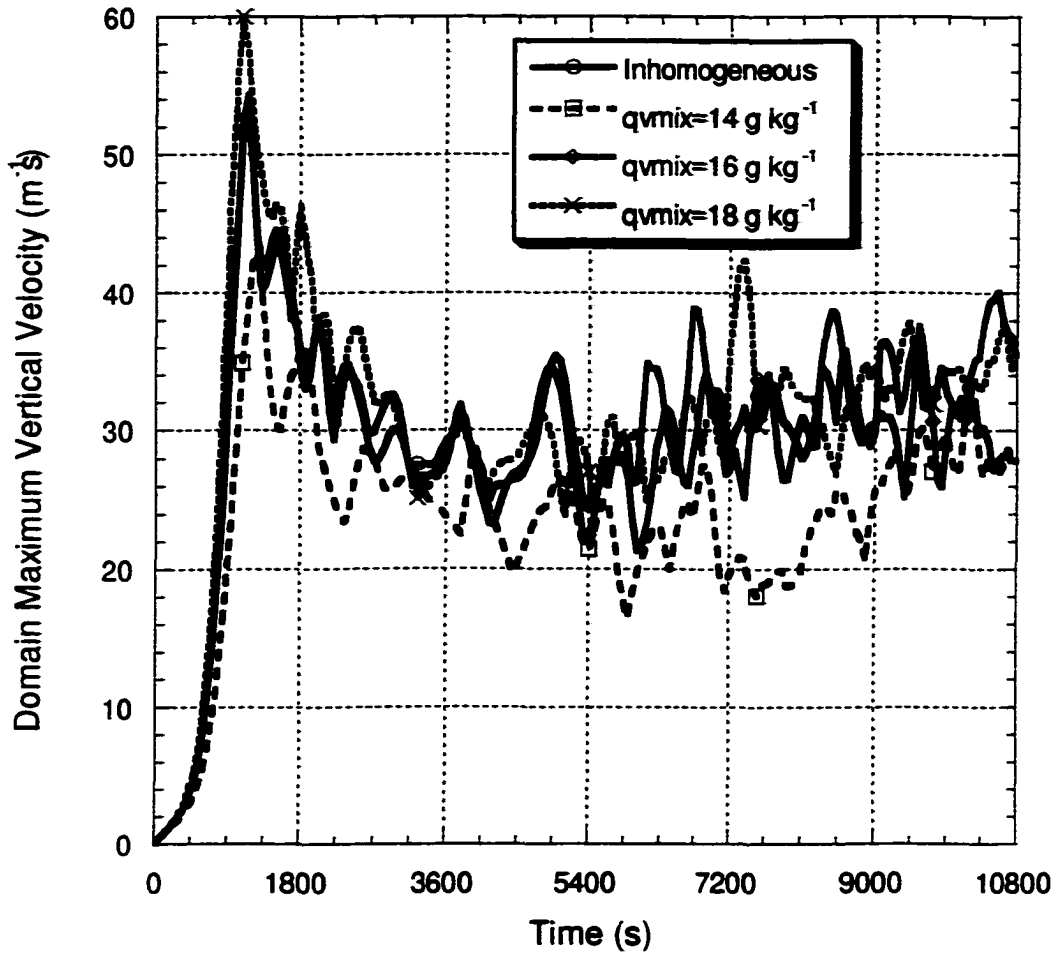
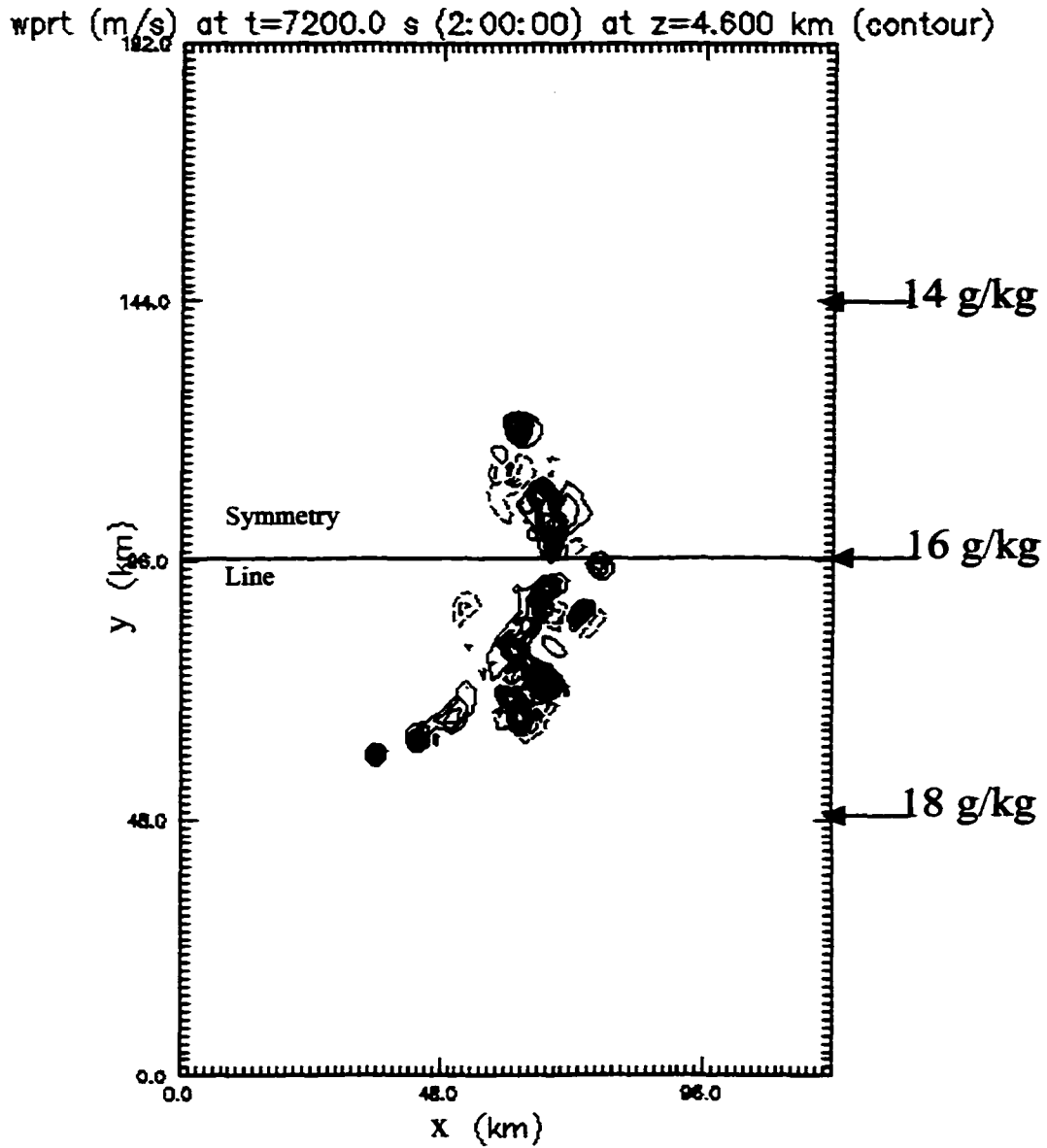


**Figure 4.14: Domain maximum vertical velocity versus time for inhomogeneous moisture simulation and homogeneous control runs (mixed layer  $q_v$  shown in legend) for weak shear environment with  $U_s=12 \text{ m s}^{-1}$ . Inhomogeneous simulation has  $16 \text{ g kg}^{-1}$  at the initiation location.**





Min=-9.36 Max=21.3 Inc=2.50 (contour)

**Figure 4.16: Horizontal cross-section of vertical velocity at  $z=4.6$  km at  $t = 2$  hours for weak shear ( $U_s=12 \text{ m s}^{-1}$ ), inhomogeneous moisture simulation with qvmix as shown to right.**

develops in the downstream direction on the symmetry line (Figure 4.15). The northern and southern cells are roughly equivalent in size and intensity. However, 5 minutes later, new cells form on the southern side of the system; similar development is delayed on the northern side. By two hours (Figure 4.16), the system has become significantly skewed toward the southern flank, with the most intense cells well south of the original symmetry line. Cells do not extend as far to the north as in the control simulations, *suggesting that the forcing which initiated these cells in the control simulation is no longer sufficient in the inhomogeneous case.*

Potential temperature perturbations at 2 hours at the lowest scalar point are shown for the  $16 \text{ g kg}^{-1}$  control simulation as well as the inhomogeneous simulation in Figure 4.17 and Figure 4.18, respectively. The cold pool has clearly become biased toward the southern (high moisture) side in the inhomogeneous case as stronger cells have developed in this region and produced more rain, creating stronger potential temperature gradients and increased outflow. Since the low-level environmental winds are constant across the domain, the increased outflow to the south results in greater convergence, as shown in Figure 4.19 for the inhomogeneous case (compare with Figure 4.20 for the control run). Thus, because cells developed more easily to the south and were stronger than their northern counterparts, the cold pool also became stronger to the south, serving to increase convergence and further aid the development of new cells.

This feedback process is shown in Figure 4.21. At three hours, the perturbation potential temperature at the lowest scalar point is skewed such that

Control run,  $q_{vmix}=16$  g/kg

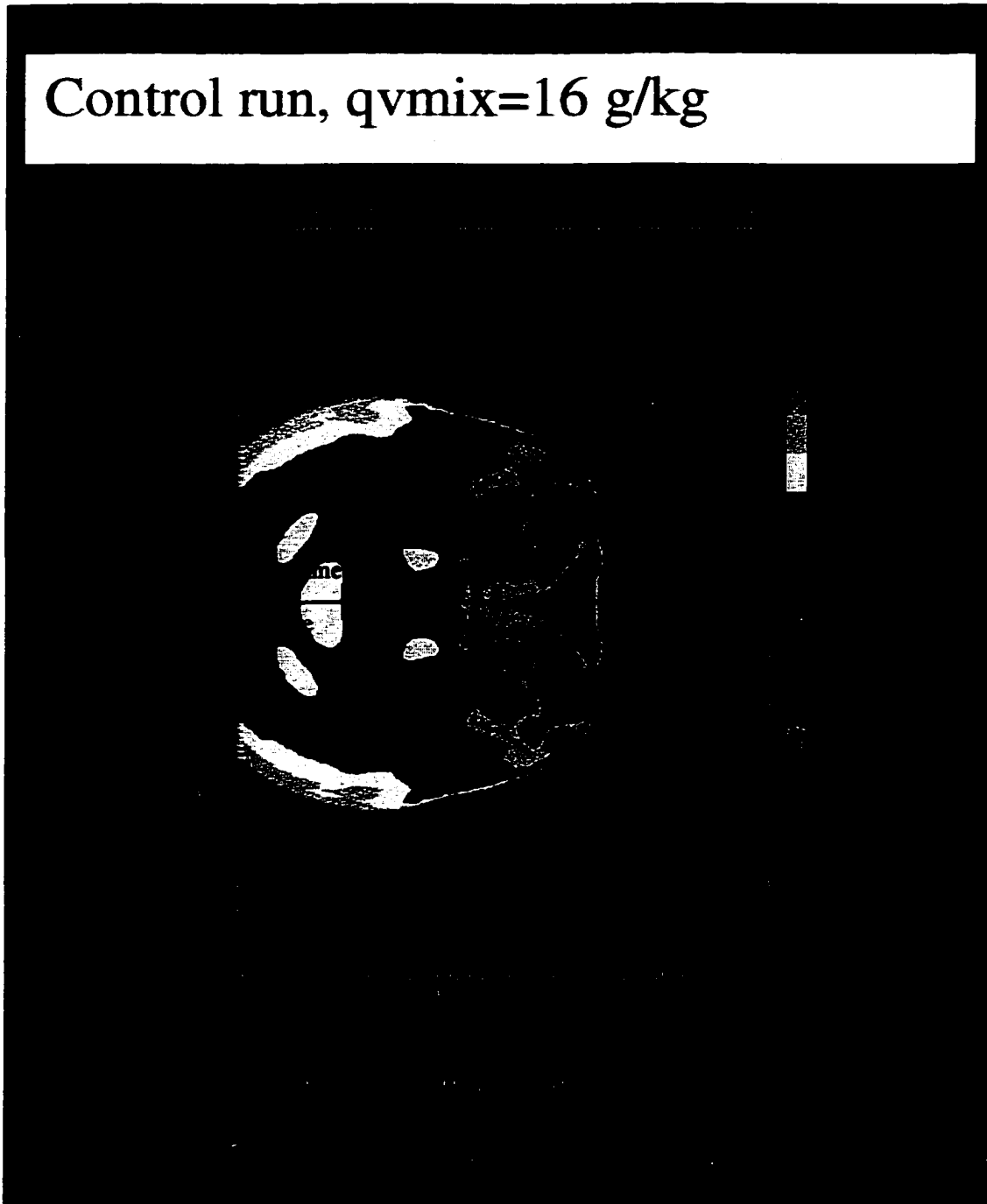


**Figure 4.17:** Horizontal cross-section of the perturbation potential temperature at the lowest scalar level for the weak shear ( $U_s=12$  m s<sup>-1</sup>), homogeneous moisture control run with  $q_{vmix} = 16$  g/kg at 2 hours. (Actual computational domain is the southern half of that shown, with a symmetric condition applied at  $y=96$  km.)

## Inhomogeneous run

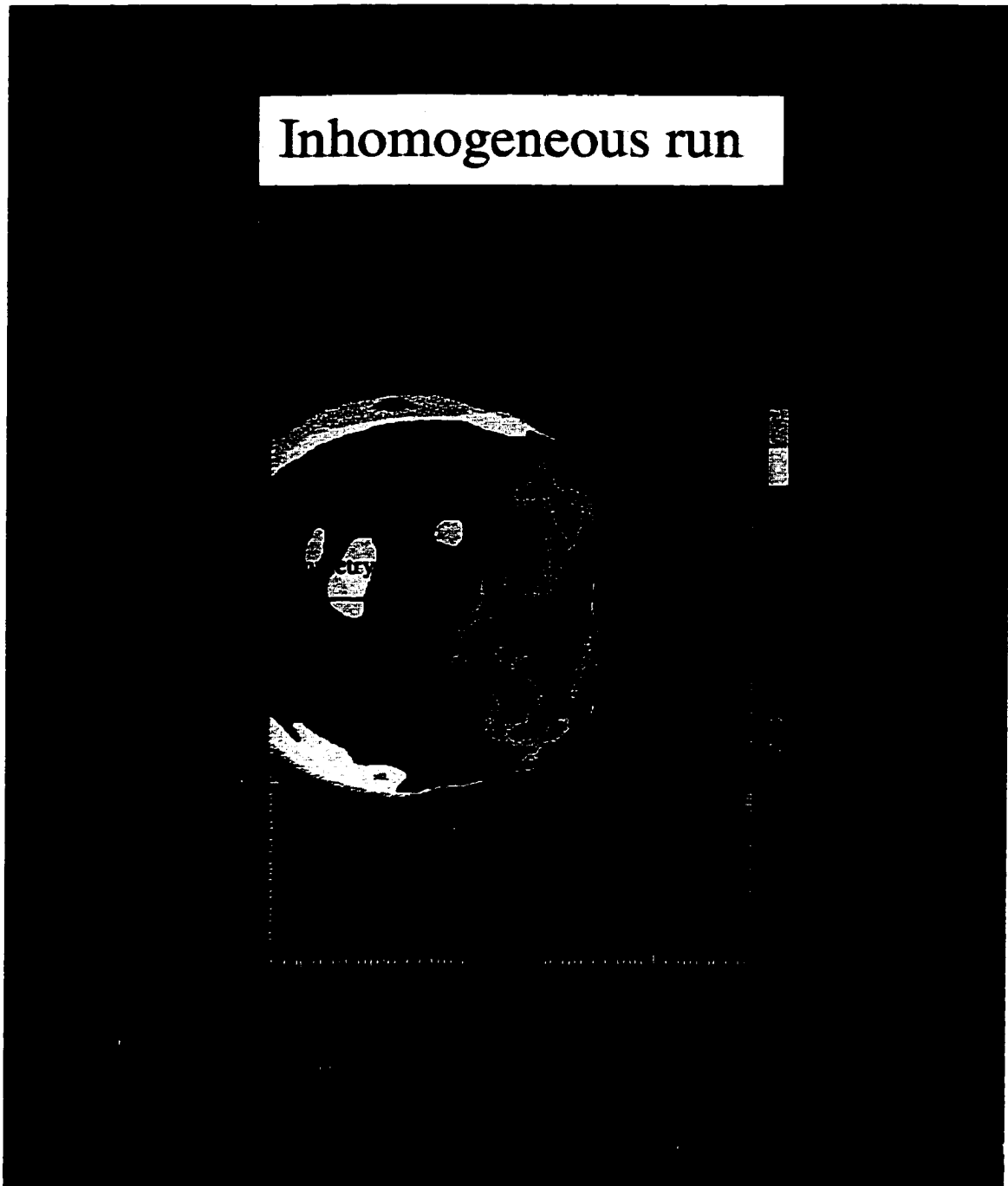


**Figure 4.18: Horizontal cross-section of the perturbation potential temperature at the lowest scalar level for the weak shear ( $U_s = 12 \text{ m s}^{-1}$ ), inhomogeneous simulation with  $qv$  as shown in Figure 4.16 at 3 hours.**



**Figure 4.19: Horizontal cross section of convergence at the lowest scalar level for weak shear ( $U_s=12 \text{ m s}^{-1}$ ), inhomogeneous moisture simulation at 2.5 hours. Environmental mixed-layer mixing ratio as shown in Figure 4.16.**

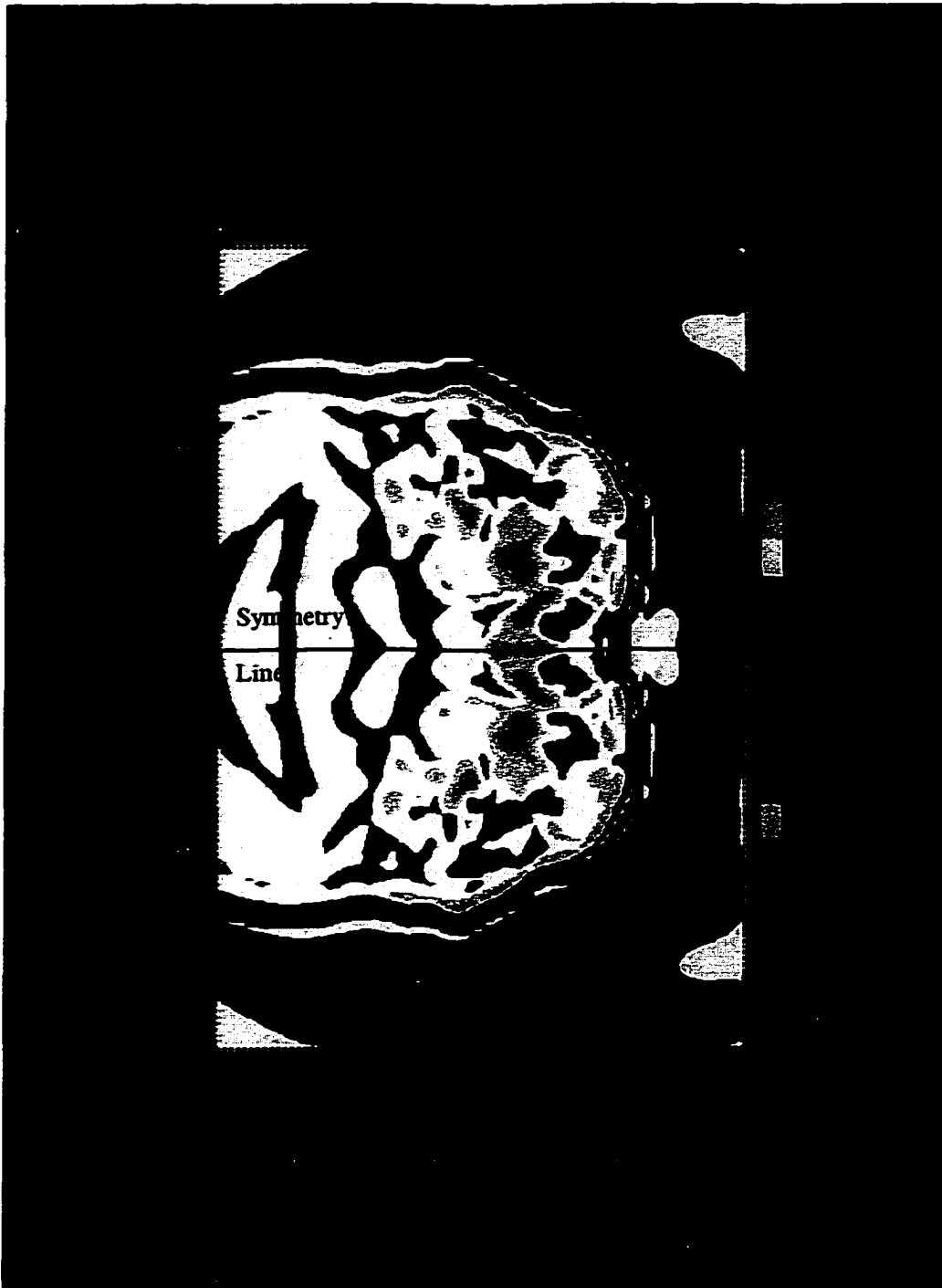


**Figure 4.20: Horizontal cross section of convergence at the lowest scalar level for weak shear ( $U_s=12 \text{ m s}^{-1}$ ), homogeneous moisture control run with  $q_{vmix}=16 \text{ g/kg}$  at 2.5 hours. (Actual computational domain is the southern half of that shown, with a symmetric condition applied at  $y=96 \text{ km}$ .)**

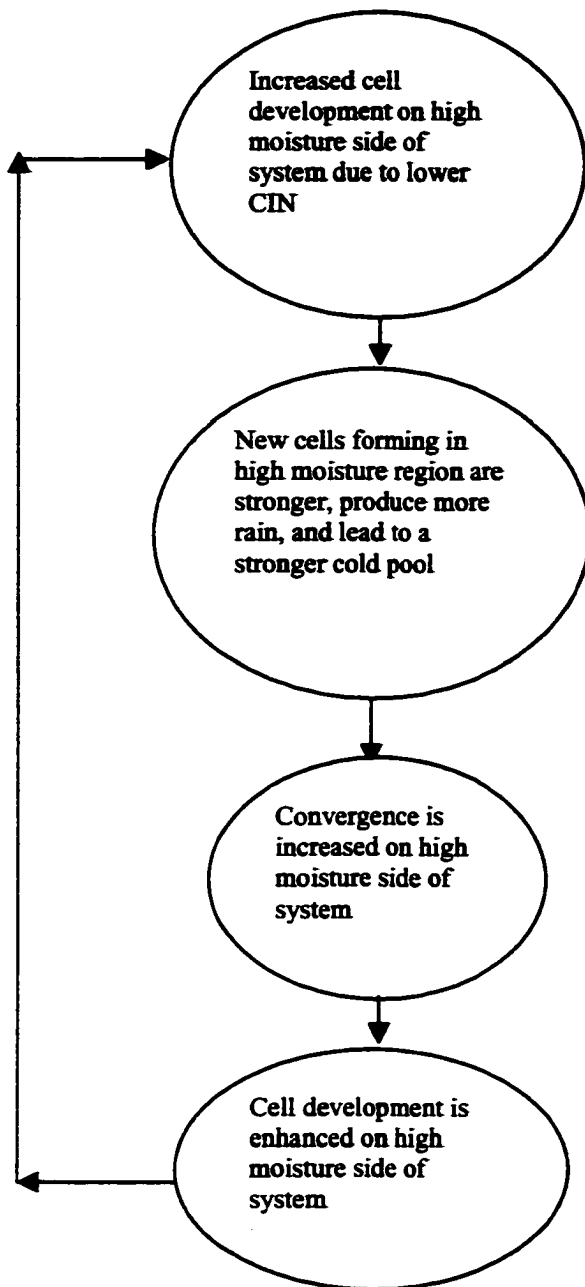


**Figure 4.21: Processes leading to an asymmetric system in inhomogeneous moisture with weak shear.**



**Figure 4.22: Horizontal cross section of perturbation potential temperature at lowest scalar level for weak shear ( $u_s=12 \text{ m s}^{-1}$ ), inhomogeneous moisture simulation at 3 hours. Environmental mixed-layer mixing ratio as shown in Figure 4.16.**

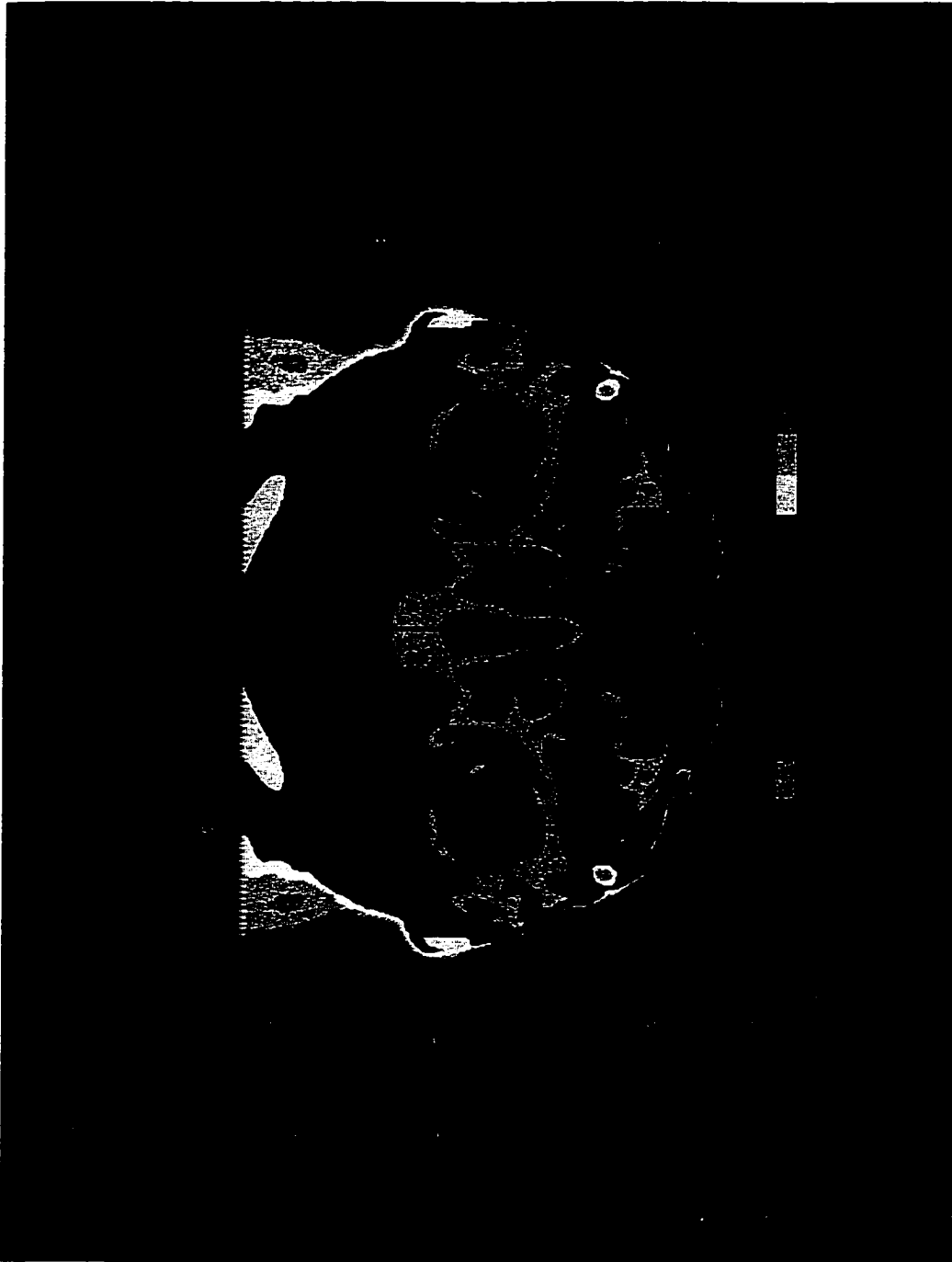
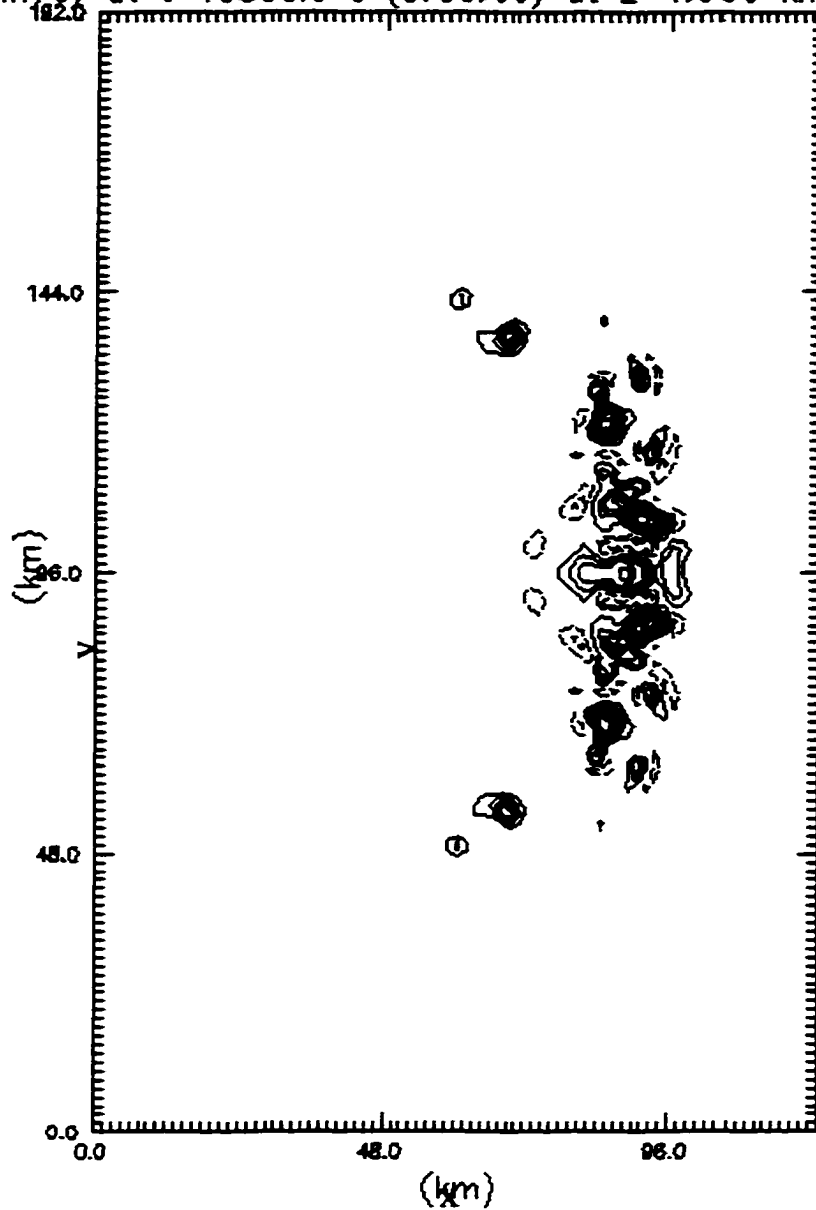


**Figure 4.23: Horizontal cross section of perturbation potential temperature at the lowest scalar level for weak shear ( $U_s=12 \text{ m s}^{-1}$ ), homogeneous moisture control run with  $q_{vmix}=16 \text{ g/kg}$  at 3 hours. (Actual computational domain is the southern half of that shown, with a symmetric condition applied at  $y=96 \text{ km}$ .)**

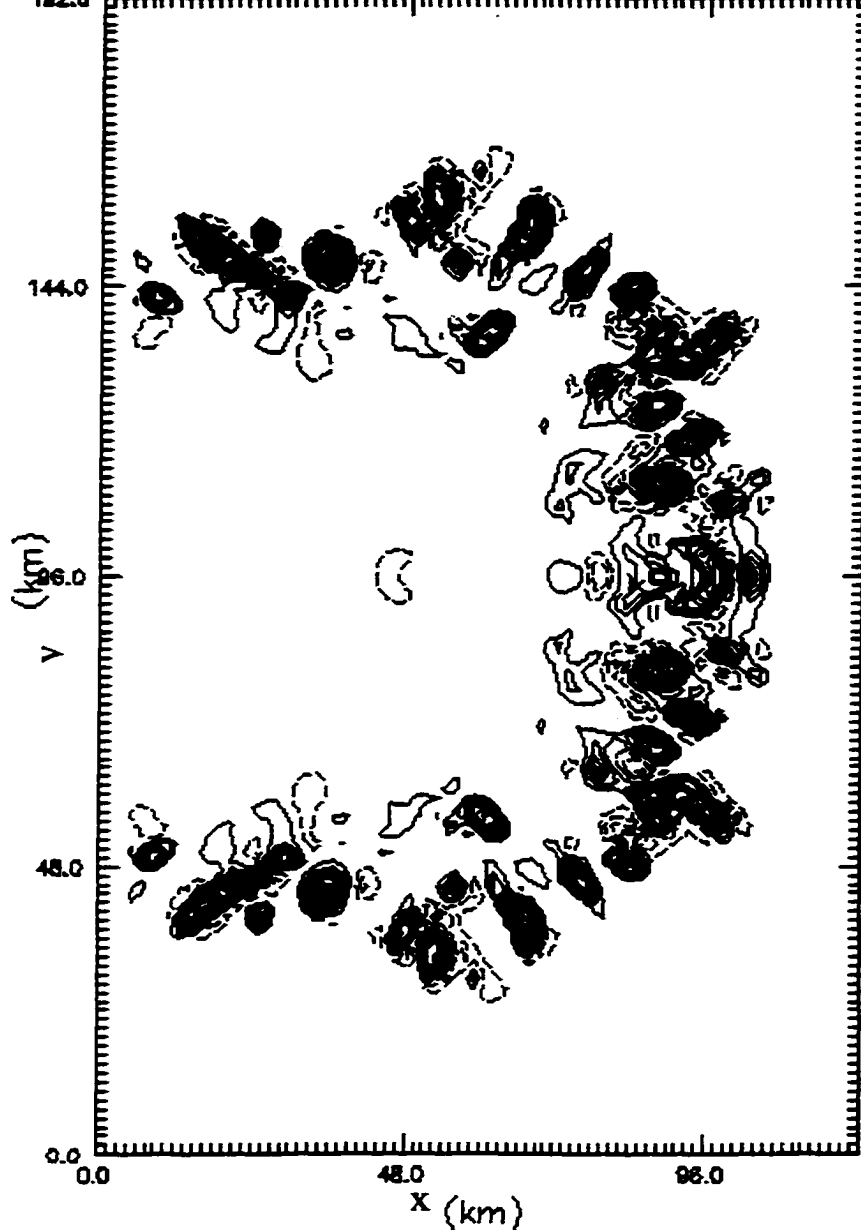
wprt ( $\text{m/s}$ ) at  $t=10800.0$  s (3:00:00) at  $z=4.600$  km



Min=-6.50 Max=19.9 Inc=2.00 (contour)

**Figure 4.24: Horizontal cross section of vertical velocity at 3 hours at  $z=4.6$  km for weak shear ( $u_s=12 \text{ m s}^{-1}$ ), homogeneous moisture control run with  $q_{\text{vmix}}= 14 \text{ g kg}^{-1}$ . (Actual computational domain is the southern half of that shown, with a symmetric condition applied at  $y=96$  km.)**

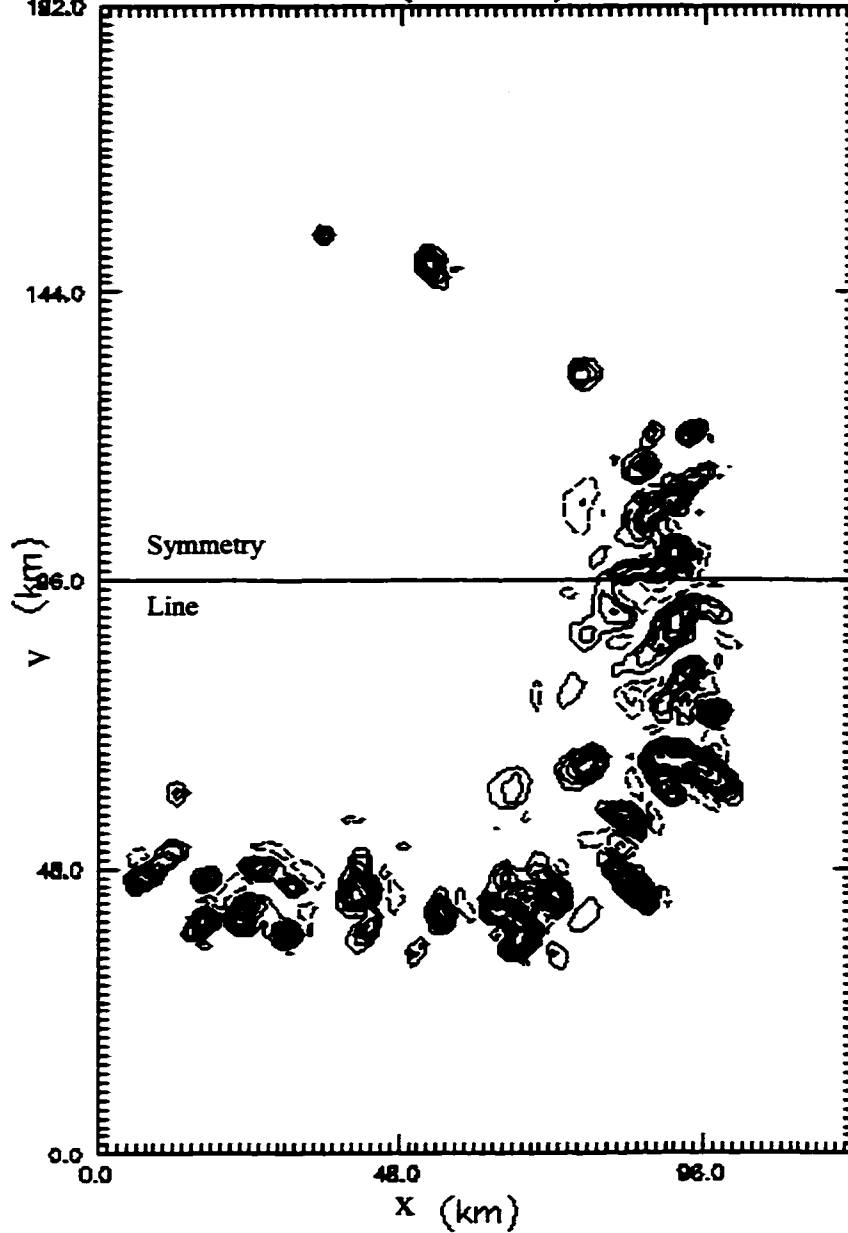
wprt (m/s) at t=10800.0 s (3:00:00) at z=4.600 km



Min=-9.21 Max=26.9 Inc=2.00 (contour)

**Figure 4.25: Horizontal cross section of vertical velocity at 3 hours at  $z=4.6$  km for weak shear ( $u_s=12 \text{ m s}^{-1}$ ), homogeneous moisture control simulation with  $q_{\text{mix}}=18 \text{ g kg}^{-1}$ . (Actual computational domain is the southern half of that shown, with a symmetric condition applied at  $y=96 \text{ km}$ .)**

wprt (m/s) at t=10800.0 s (3:00:00) at z=4.600 km



Min=-13.2 Max=24.2 Inc=2.50 (contour)

**Figure 4.26: Horizontal cross-section of vertical velocity at  $z=4.6$  km at  $t = 3$  hours for weak shear ( $U_s=12 \text{ m s}^{-1}$ ), inhomogeneous moisture simulation with qmix as shown in Figure 4.16.**

nearly all of the coldest air is south of the original symmetry line (compare Figure 4.22 with Figure 4.23). The control runs at this time (Figure 4.24 and Figure 4.25) do show differences in lateral extent as well, so a portion of the asymmetry could be deduced from them. However, the asymmetry at earlier times is not predicted from the control runs, and at three hours (Figure 4.26), the inhomogeneous run shows fewer cells to the north than even the  $14 \text{ g kg}^{-1}$  control run. Thus, we believe the feedback mechanism mentioned above is also contributing to the asymmetry.

From these results, we conclude that systems composed primarily of air-mass thunderstorms become preferentially biased toward regions with higher values of low-level moisture rather than simply continuing a pattern of predominantly downstream redevelopment. When the system is initiated in a region that is borderline for cell development on the flanks, the asymmetries begin very quickly. When the system begins in a moister region, the asymmetries take somewhat longer to develop, but become pronounced even at times when the control runs would not suggest asymmetry.

The propagation of the system is heavily influenced by the gradients in ambient moisture. Whereas individual cell motion continues to follow the mean wind, new cell development is preferentially biased toward the high moisture flank. This combination of cell motion and cell development leads to system propagation in a direction between that predicted by the mean shear vector and that given by the moisture gradient. *If one were to ignore the inhomogeneities in moisture and presume that system propagation is dictated primarily by a dynamical response to the*

*shear, incorrect conclusions regarding storm system motion relative the shear vector could be drawn.*

### **4.3 Influence of Variable Moisture in Strong Shear Environments**

The previous section demonstrates the importance of variations in moisture on the propagation of a system comprising ordinary cells. Given that ordinary cells and supercells are dynamically distinct, it is not clear that the two types of storms will be influenced by moisture variations in a similar manner. To determine the response of supercell storms to moisture variations, simulations in environments characterized by strong values of vertical shear are performed. The following questions are addressed in these simulations:

- 1) How long will a supercell continue to exist when it moves into a region of moisture insufficient to initiate the storm?
- 2) Will the vertical velocity of a supercell respond to changes in low-level moisture as predicted by parcel theory? In what manner will mid-level rotation adjust to the change in moisture?
- 3) Will an updraft without significant low-level rotation be able to develop it upon moving into increased low-level moisture?
- 4) To what extent does cell interaction impede or enhance the development of low-level vorticity? Does an inhomogeneous environment influence this interaction through a change in the timing of redevelopments?

The simulations described below are those which best address the above questions.

### **4.3.1 Updraft Continuation in an Unfavorable Moisture Regime**

To address the question of continued storm existence in an environment that would not support storm initiation, a storm is initiated in an environment favorable to the development of a long-lived storm and allowed to move into an environment with decreased moisture. Figure 4.27 shows the setup for this environment, with  $q_v=12 \text{ g kg}^{-1}$  at the domain center and an east-west wind that is unidirectional with height. The profile of the  $u$  component of the wind with height is shown in Figure 4.28. The initial cell splits (represented by the dots), with the left-moving member of the split pair entering a region that does not support storm initiation. Control runs for locations A, B, and C in Figure 4.27 are described below.

#### **4.3.1.a Control Simulation for $q_{vmix}=10 \text{ g/kg}$ with $U_s=30 \text{ m s}^{-1}$**

When the environmental mixing ratio is only  $10 \text{ g/kg}$ , the initial bubble rises, condensation occurs, and minimal rain is produced. The vertical velocity briefly reaches  $11 \text{ m s}^{-1}$  and then quickly weakens (Figure 4.29). Thus, no sustained storm is able to develop in this environment.

#### **4.3.1.b Control Simulation for $q_{vmix}=12 \text{ g/kg}$ with $U_s=30 \text{ m s}^{-1}$**

With  $q_{vmix} = 12 \text{ g/kg}$ , the initial storm splits into right and left-moving cells that remain dominant throughout the simulation (Figure 4.30 and Figure 4.31) and have significant mid-level rotation greater than  $0.01 \text{ s}^{-1}$  (Figure 4.32). These cells maintain vertical velocities greater than  $25 \text{ m s}^{-1}$  throughout the three hour simulation.

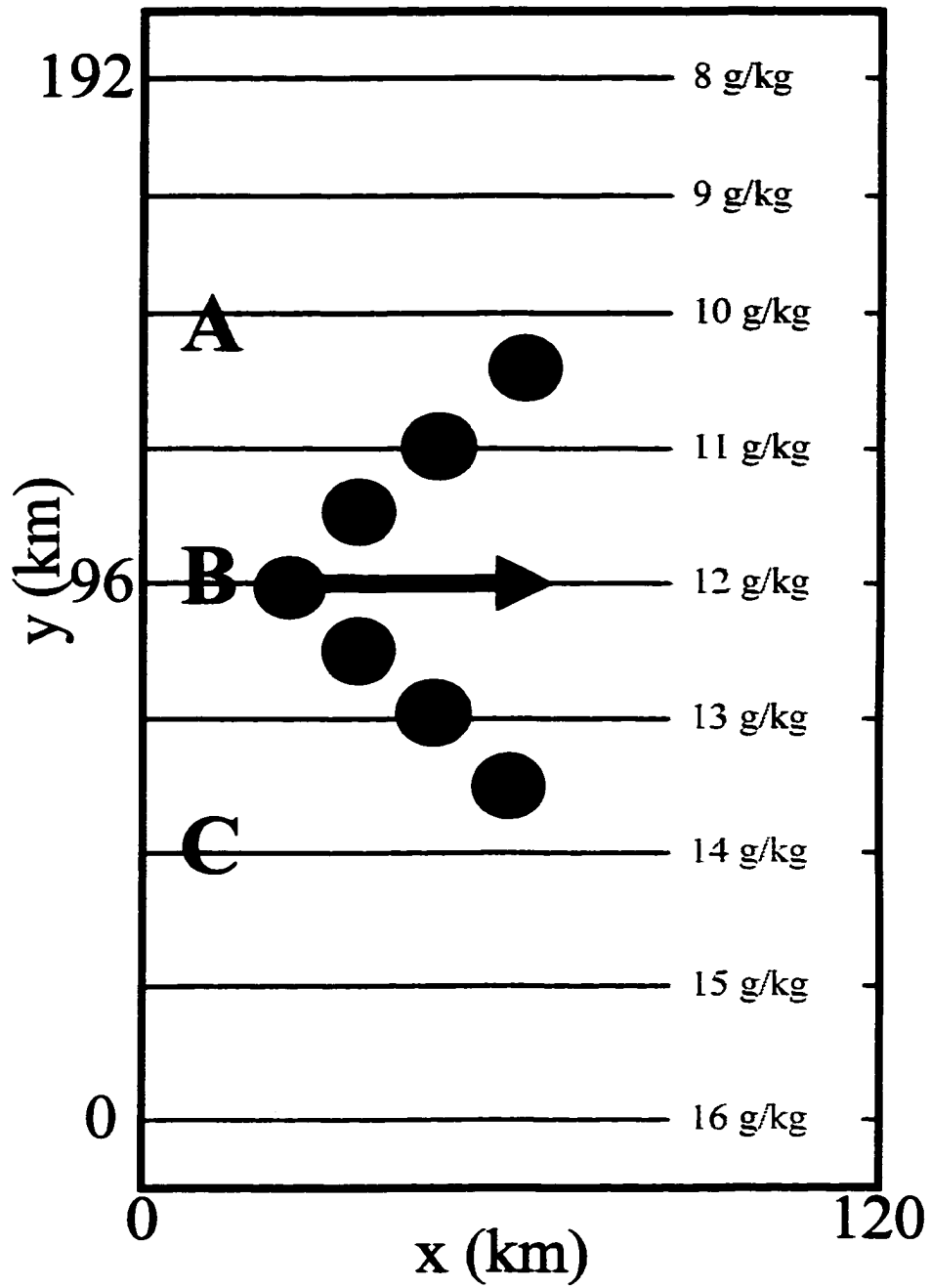


**Figure 4.27: Setup for inhomogeneous moisture experiments with strong shear. Green disks represent a split pair of storms. Domain motion is shown with the solid arrow.**

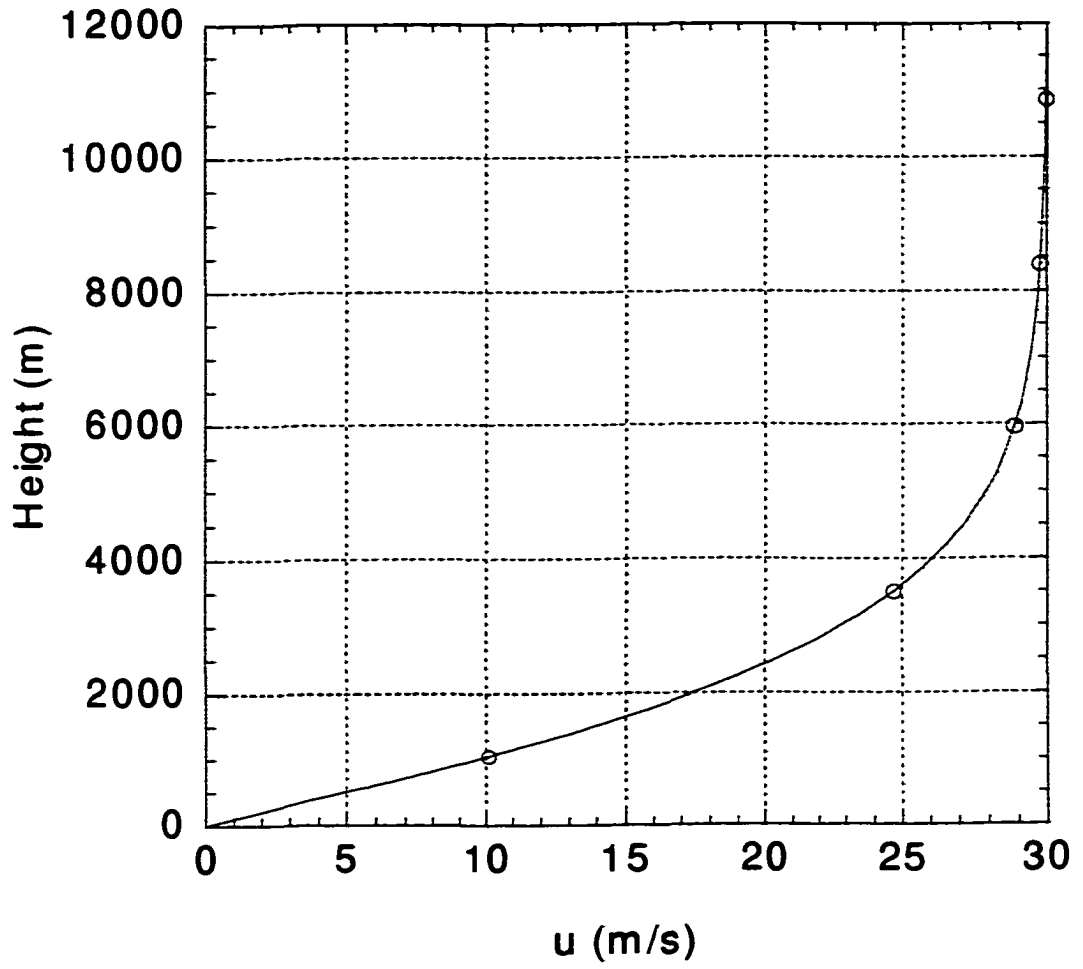


**Figure 4.28: Profile of east-west wind component with height for strong shear, variable moisture simulations.**

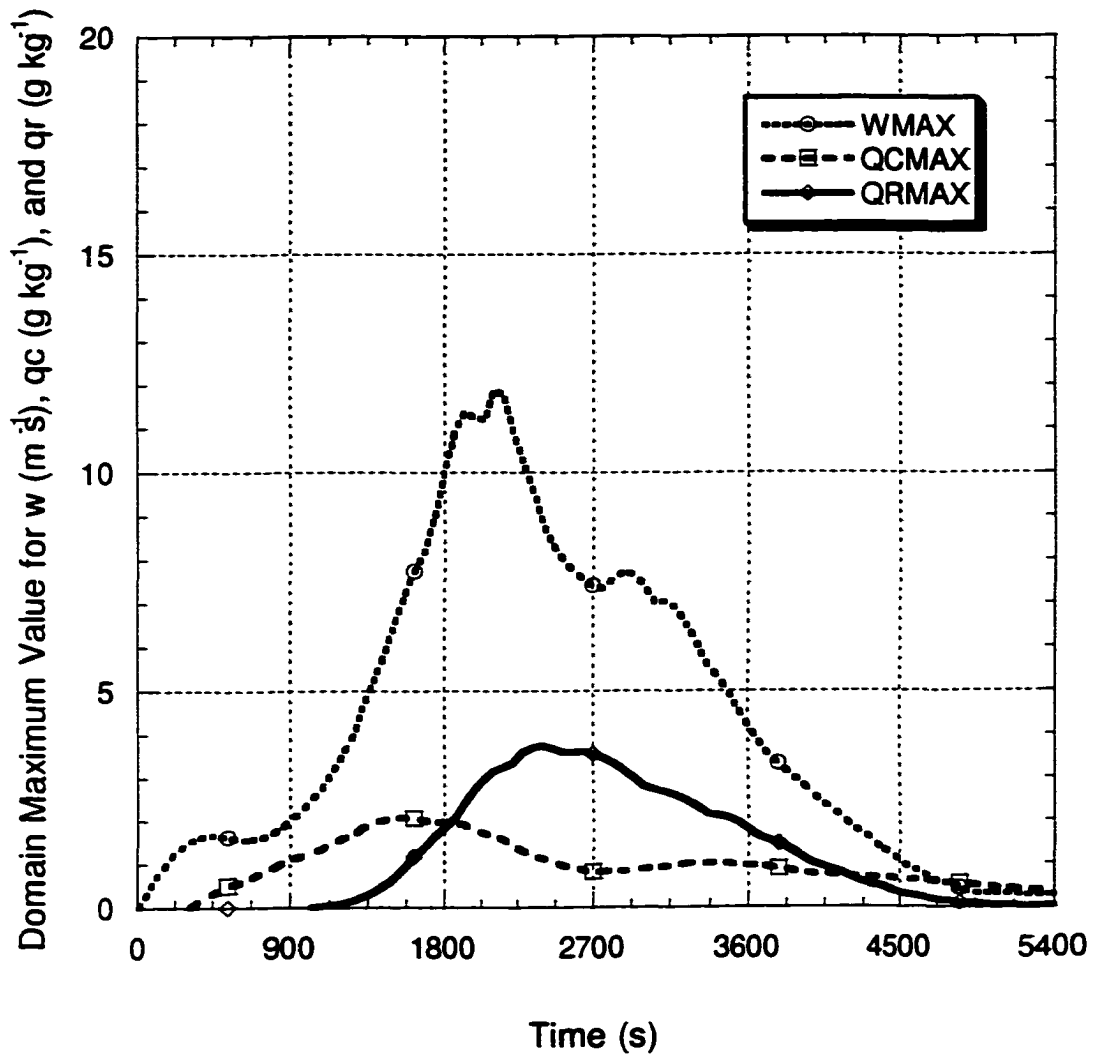


**Figure 4.29: Domain maximum values for  $w$ ,  $qr$ , and  $qc$  for strong shear ( $U_s=30 \text{ m s}^{-1}$ ), homogeneous control run with  $qvmix=10 \text{ g kg}^{-1}$ .**

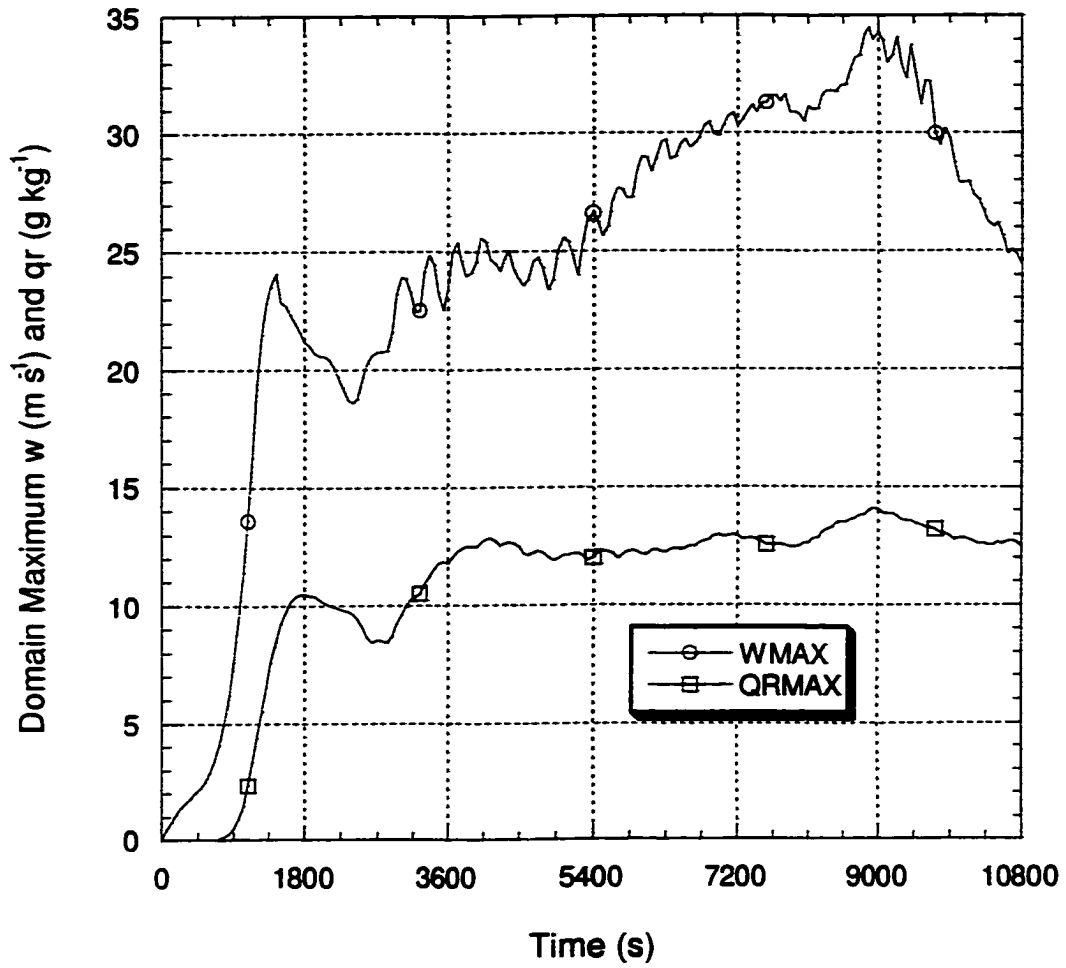
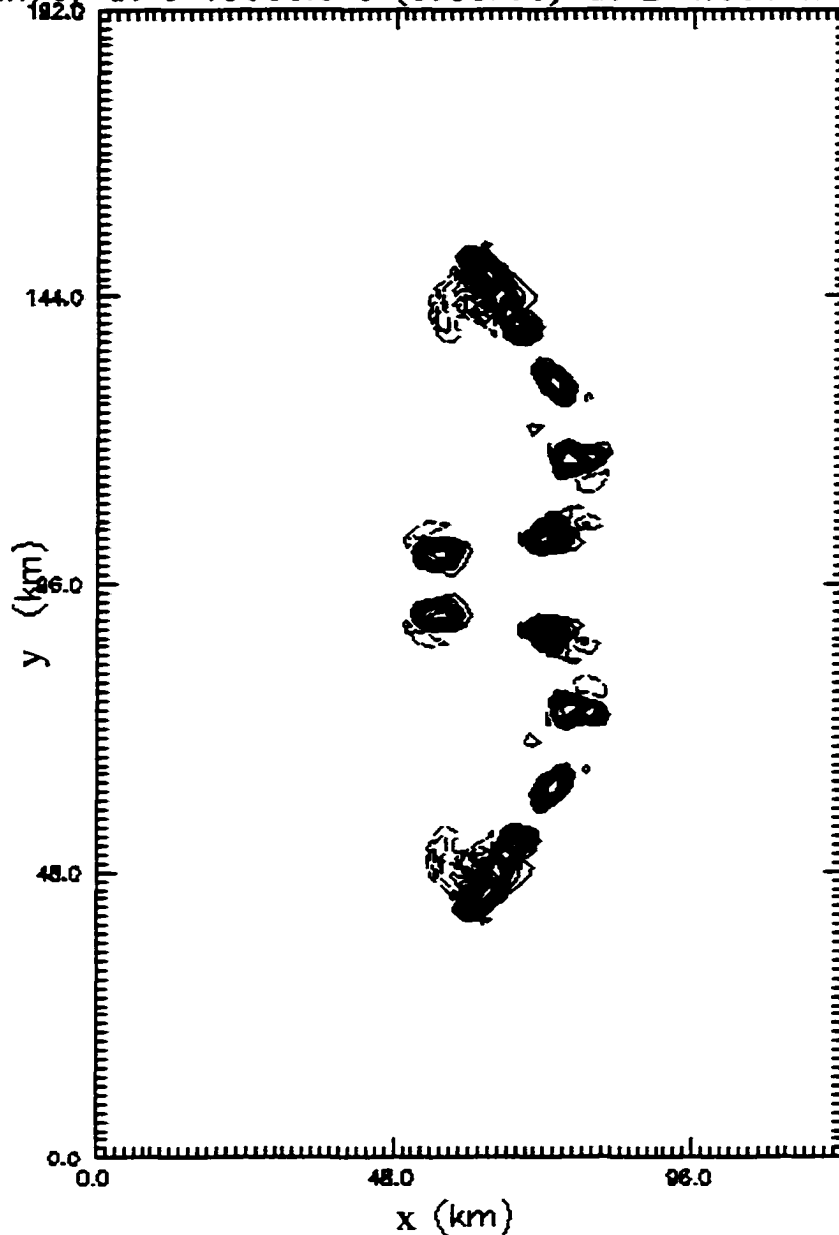


**Figure 4.30: Domain maximum values of vertical velocity and rainwater mixing ratio for control run with  $U_i=30 \text{ m s}^{-1}$  and  $q_{vmix}=12 \text{ g kg}^{-1}$ .**

wprt (m/s) at t=10800.0 s (3:00:00) at z=4.600 km



Min=-8.51 Max=19.0 Inc=2.00 (contour)

**Figure 4.31: Horizontal cross-section of vertical velocity at  $z=4.6$  km at 3 hours for strong shear ( $U_s=30$  m s<sup>-1</sup>) control run using  $qv_{mix}=12$  g kg<sup>-1</sup>. (Actual computational domain is the southern half of that shown, with a symmetric condition applied at  $y=96$  km.)**

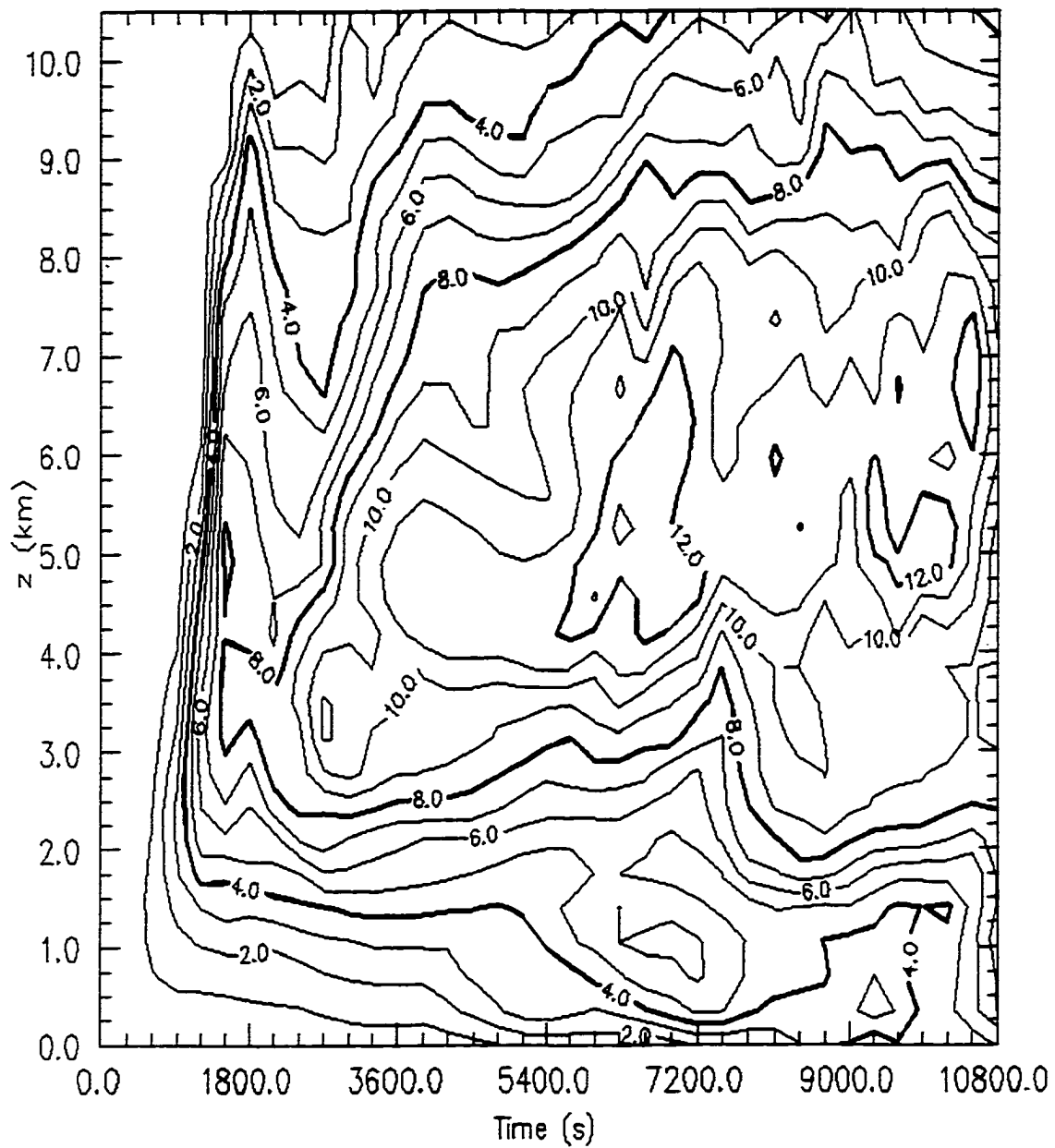
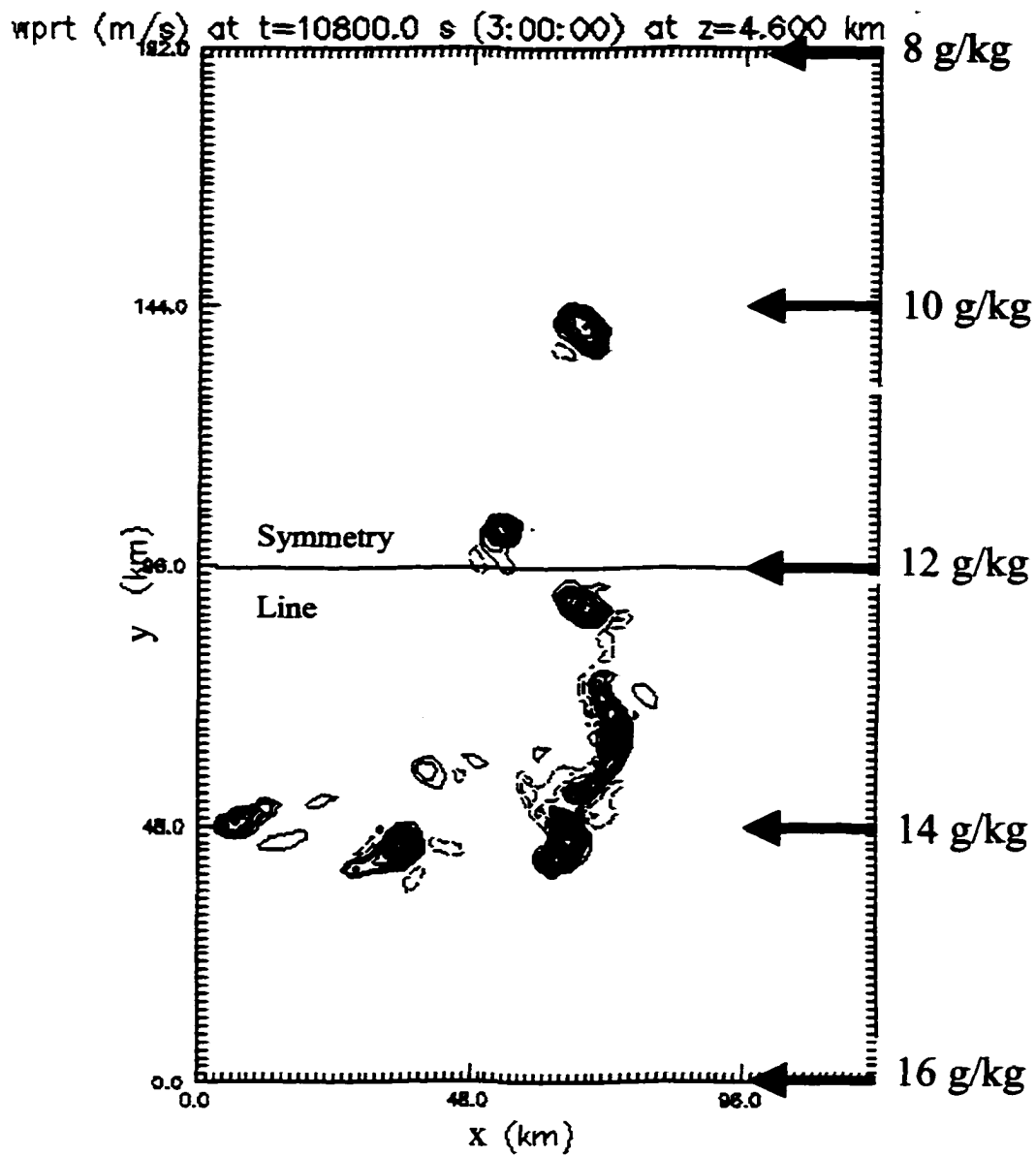


**Figure 4.32: Time-height diagram of maximum vertical vorticity ( $\text{s}^{-1}$ , multiplied by 1000) for strong shear ( $U_x=30 \text{ m s}^{-1}$ ) control simulation with mixed layer  $qv = 12 \text{ g kg}^{-1}$ .**



Min=-7.91 Max=29.7 Inc=2.50 (contour)

**Figure 4.33: Horizontal cross-section of vertical velocity at  $z=4.6$  km for strong shear ( $U_s=30 \text{ m s}^{-1}$ ), inhomogeneous moisture experiment at 3 hours. Environmental values of the mixed-layer water vapor mixing ratios are shown to right.**

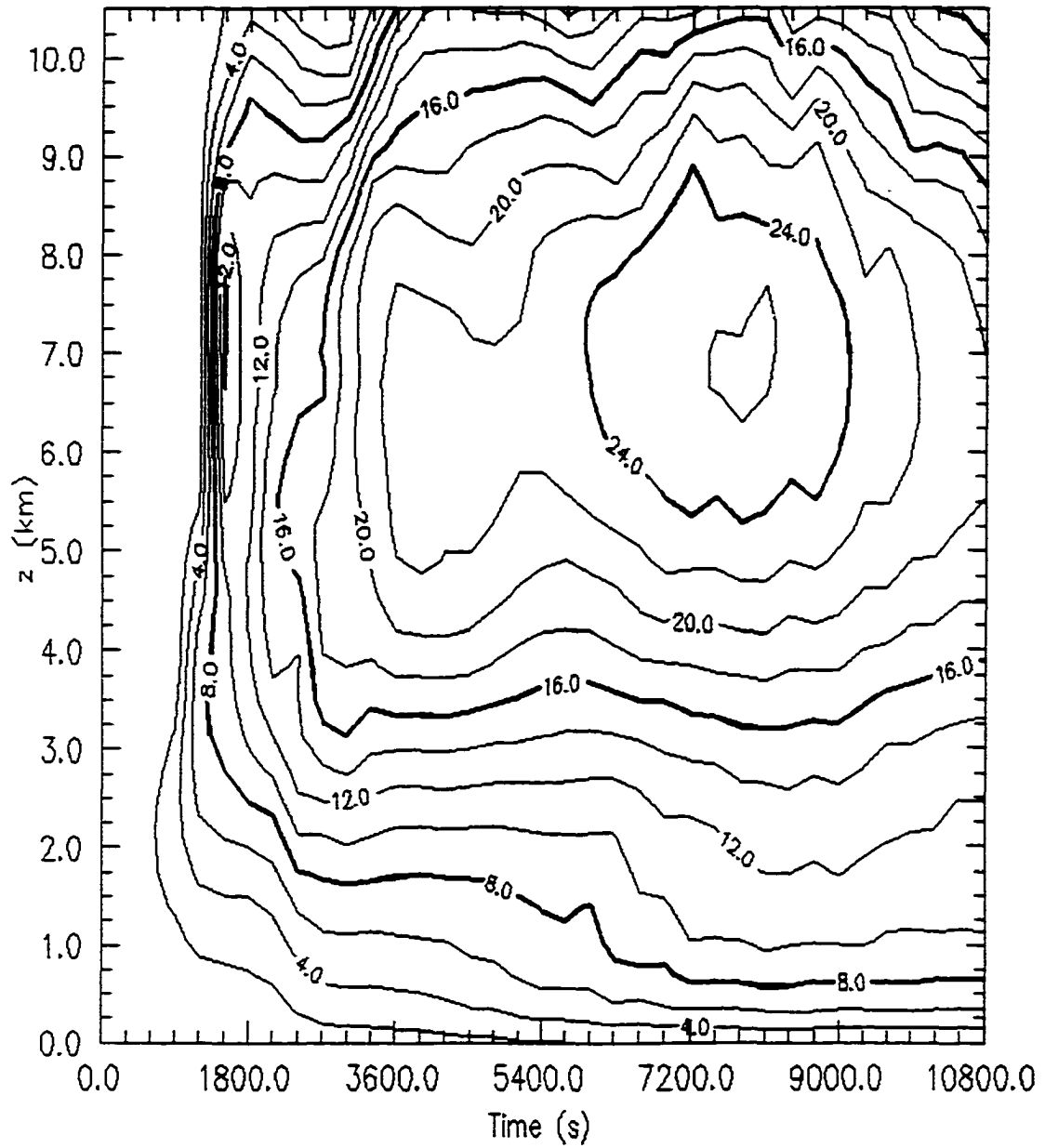
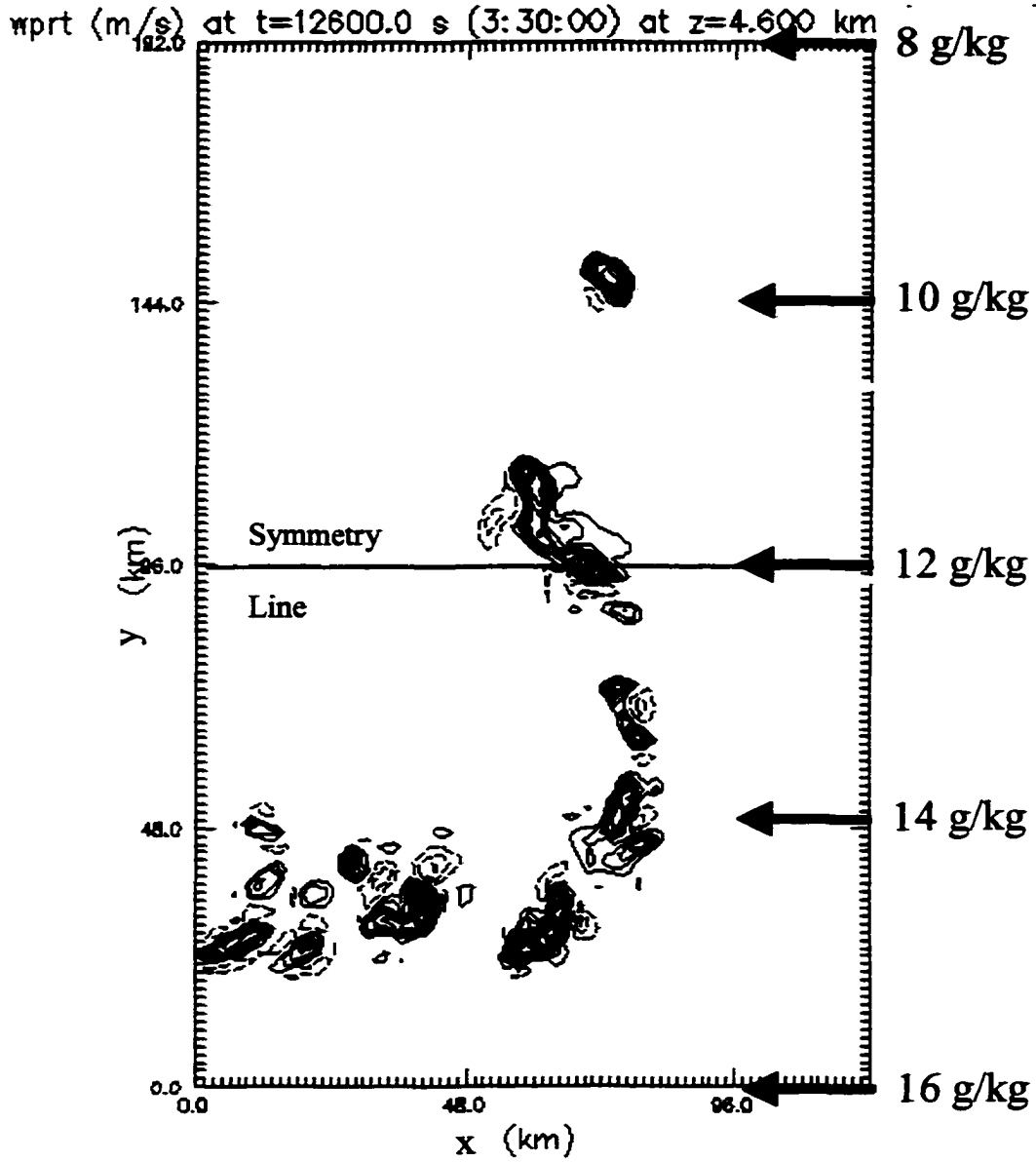


**Figure 4.34: Time-height diagram of maximum vertical velocity ( $\text{m s}^{-1}$ ) for northern cell in inhomogeneous moisture simulation with  $U_c=30 \text{ m s}^{-1}$  and  $q_v=12 \text{ g kg}^{-1}$  initially, with the variation in  $q_v$  as shown in Figure 4.33. (Height is with respect to the lowest scalar level.)**



Min=-8.78 Max=27.8 Inc=2.50 (contour)

**Figure 4.35: Horizontal cross section of vertical velocity at  $z=4.6$  km for strong shear ( $U_s=30 \text{ m s}^{-1}$ ), inhomogeneous moisture simulation at 3.5 hours. Environmental values of mixed-layer water vapor mixing ratio are shown to right.**

#### 4.3.1.c Inhomogeneous Run Starting with $q_{vmix}=12$ g/kg with $U_x=30$ m s<sup>-1</sup>

In this simulation, the initial cell splits as expected. The northern cell moves into decreasing moisture with time (Figure 4.33) and weakens considerably (Figure 4.34), *yet it continues to exist*. At three hours, this storm is located in 10 g/kg air and persists (Figure 4.35) for over another hour (the end of the simulation). Thus, *a cell which forms in strong shear can continue to exist when it moves into air that would not be able to generate a sustained storm given identical initialization. Thus, the only reason the northern cell exists at 4 hours is because of its history.* This result has interesting implications regarding proximity soundings because the inflow to a storm at a particular time may not be the determining factor for its current behavior. Even a very carefully placed inflow sounding may be very misleading.

One might then ask if a storm *initialized* in the *inhomogeneous* environment at the 10 g kg<sup>-1</sup> location would be sustained since it would have somewhat higher moisture to draw upon from its southern side. If this is the case, the inhomogeneity *across the storm* may be the critical factor for existence, rather than the fact that the storm came from a region of higher moisture.

To disprove this theory, an inhomogeneous environment with the same gradient in  $q_v$  but with only 10 g kg<sup>-1</sup> at the initiation location is performed. Figure 4.36 shows the domain maximum vertical velocity for both the homogeneous and the inhomogeneous case (initial bubble located where  $q_v=10$  g kg<sup>-1</sup>). The updraft speed follows a similar course in either domain, reaching a brief maximum and then decreasing back to zero. Thus, a sustained storm would not form in this location,

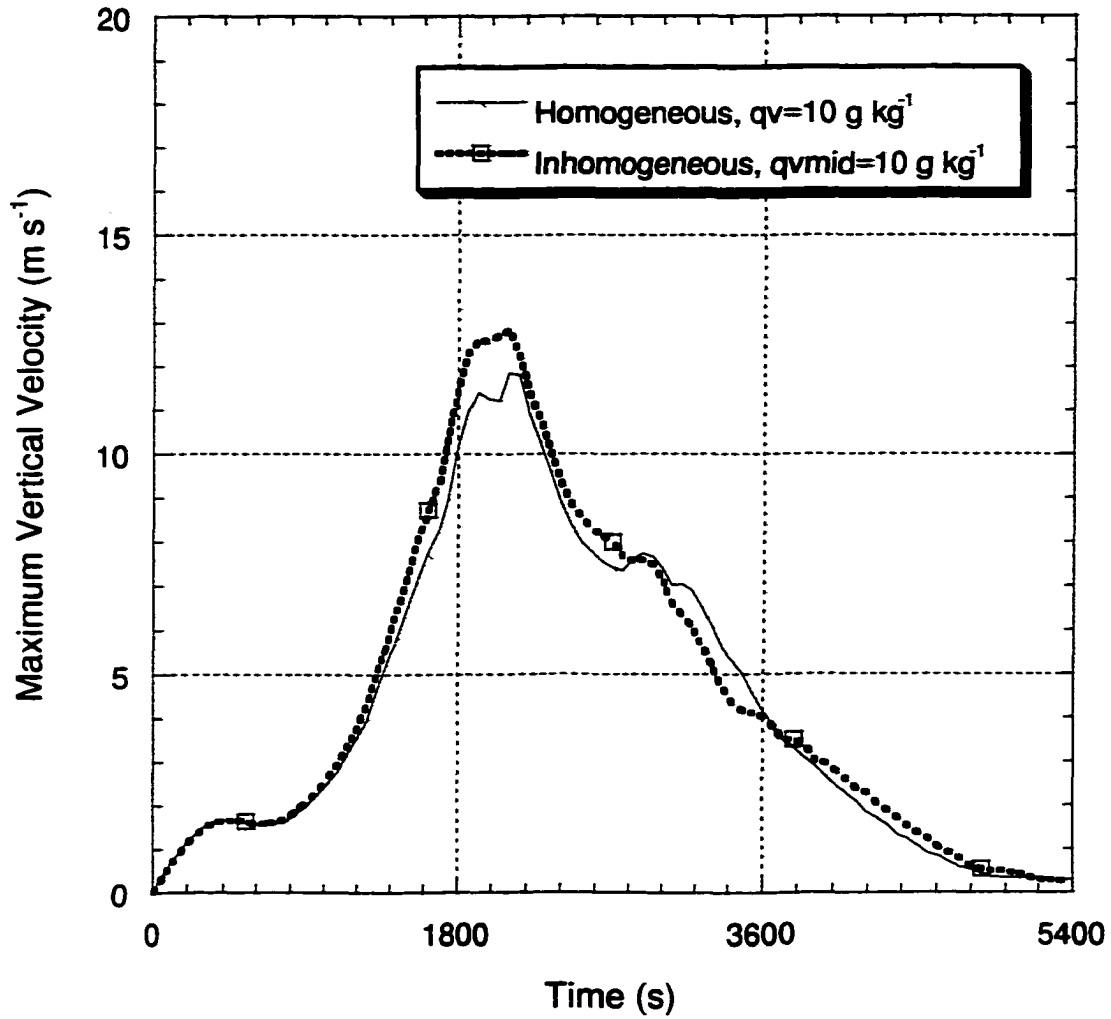


**Figure 4.36: Domain maximum vertical velocity vs. time for using mixed layer mixing ratio of  $10 \text{ g kg}^{-1}$  in both homogeneous and inhomogeneous moisture environments with  $u_t = 30 \text{ m s}^{-1}$ .**

reaffirming that the cell moving into this environment continues to exist, for a length of time much greater than the time for parcels to traverse the updraft, solely because of its history.

#### **4.3.2 Vertical Velocity and Mid-Level Rotation:**

Parcel theory suggests that the vertical acceleration of an air parcel will increase as the CAPE of the environment increases. If parcel theory is approximately valid in the updraft of a severe storm, as updraft soundings suggest (Bluestein et al., 1988; Davies-Jones, 1974; personal experience in VORTEX), then the vertical velocity should show a strong dependence on the amount of low-level moisture present, though perhaps with a time lag. We also expect mid-level rotation to increase as the moisture increases due to its dependence on vertical velocity gradients in the tilting term of the vorticity equation. In the previous example (Section 4.3.1), decreases in moisture were shown to cause significant decreases in updraft strength. These were also associated with decreases in mid-level vertical vorticity (Figure 4.37). We now consider the case of *increasing* moisture over a storm's lifetime. The same setup is used, but we now focus attention on the right-moving member of the split pair.

##### **4.3.2.a Inhomogeneous Run starting with $q_{vmix}=12$ g/kg with $U_s=30$ m s<sup>-1</sup>**

When a cell moves from a region with  $12$  g kg<sup>-1</sup> of water vapor to a region with  $14$  g kg<sup>-1</sup>, we see in Figure 4.39 that the domain maximum vertical velocity does increase slightly. This increase is surprisingly small for this case in light of the fact that, theoretically, the maximum updraft should follow

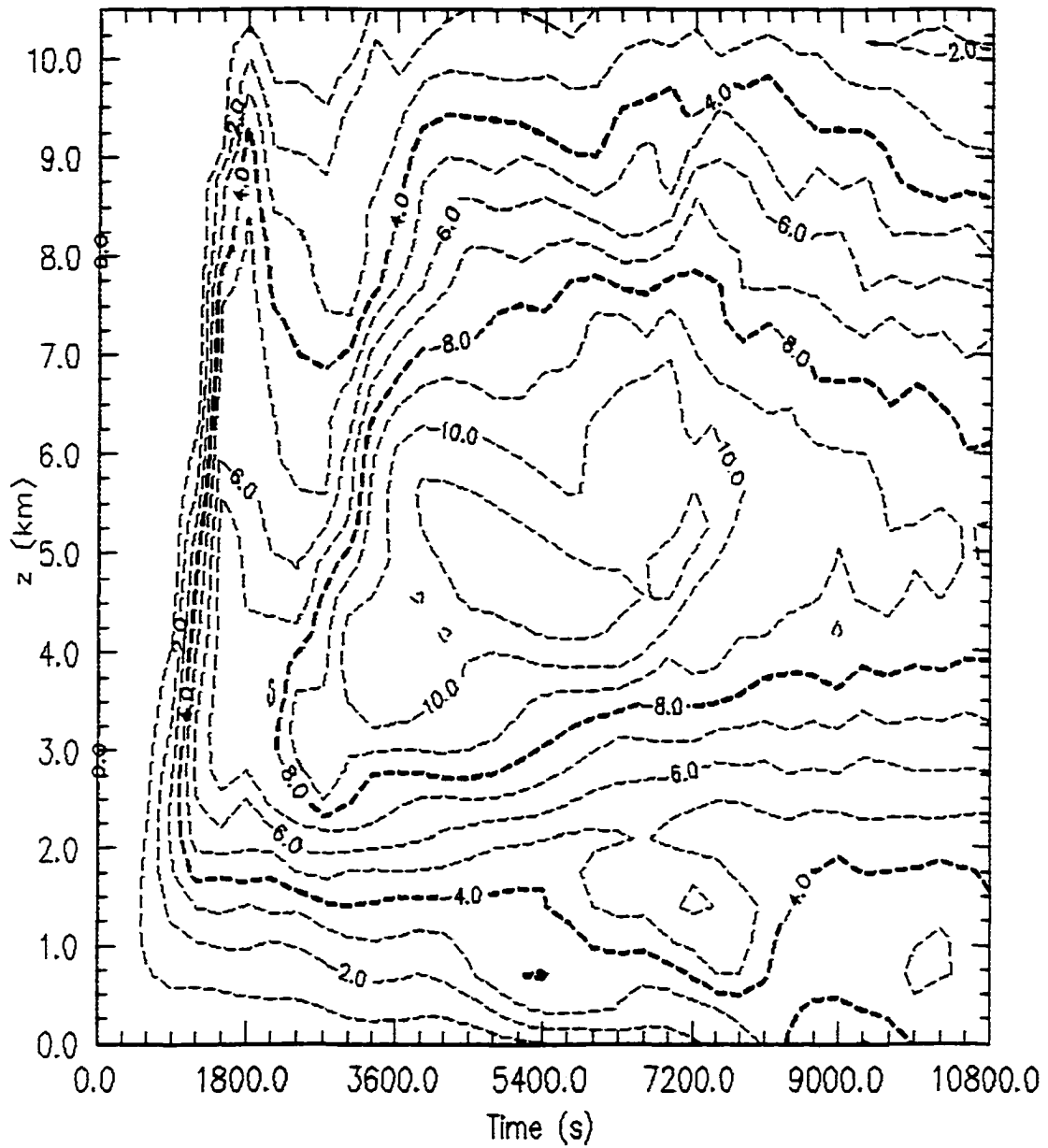


**Figure 4.37: Time-height diagram of maximum vertical vorticity ( $s^{-1}$ , multiplied by 1000) for northern cell in inhomogeneous moisture case with  $U_x=30 \text{ m s}^{-1}$  and mixed layer  $q_v=12 \text{ g kg}^{-1}$  initially, with the variation as shown in Figure 4.35.**

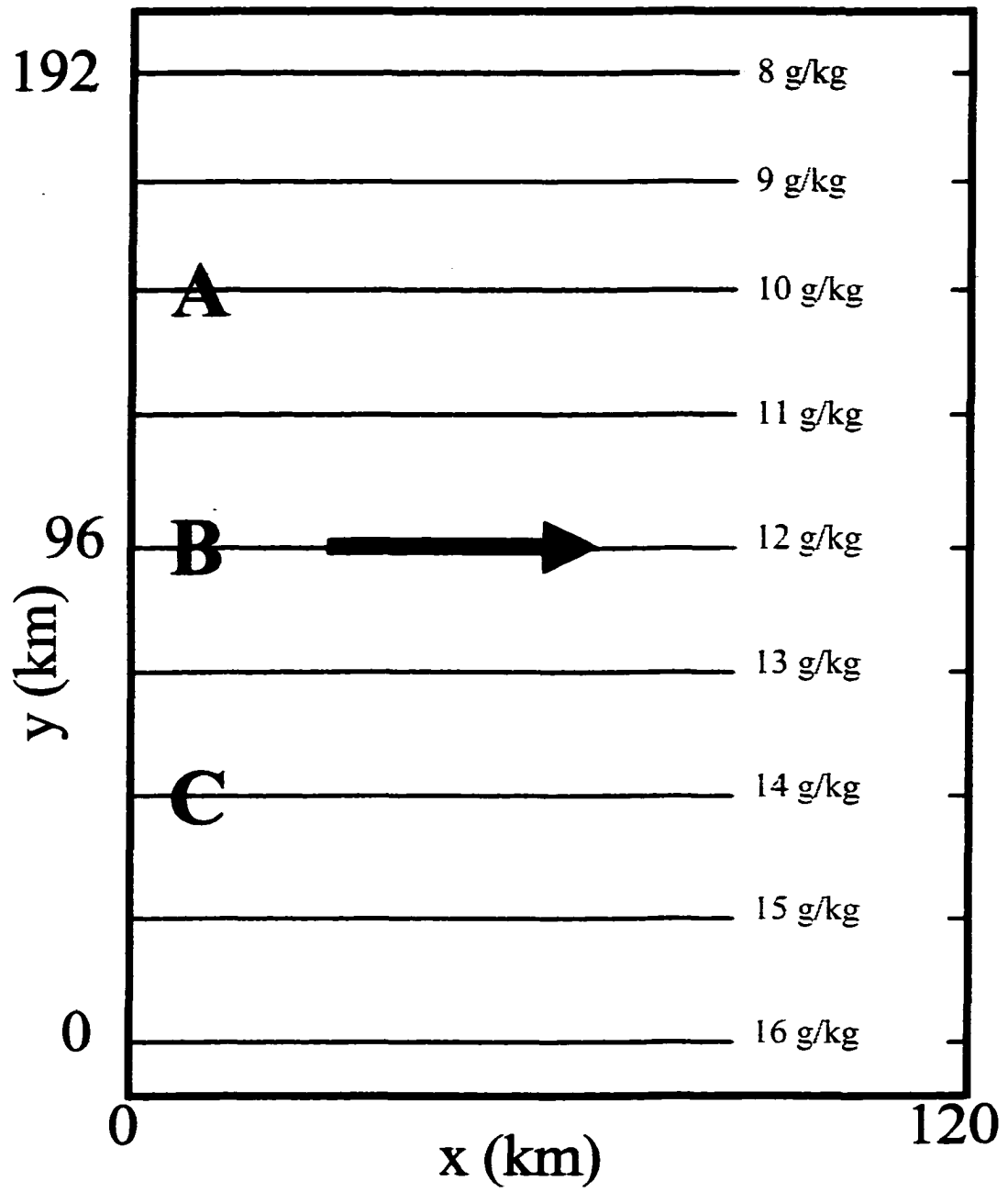


**Figure 4.38: Setup for inhomogeneous moisture simulations for splitting supercells. Control runs are performed using soundings from points A, B, and C.**

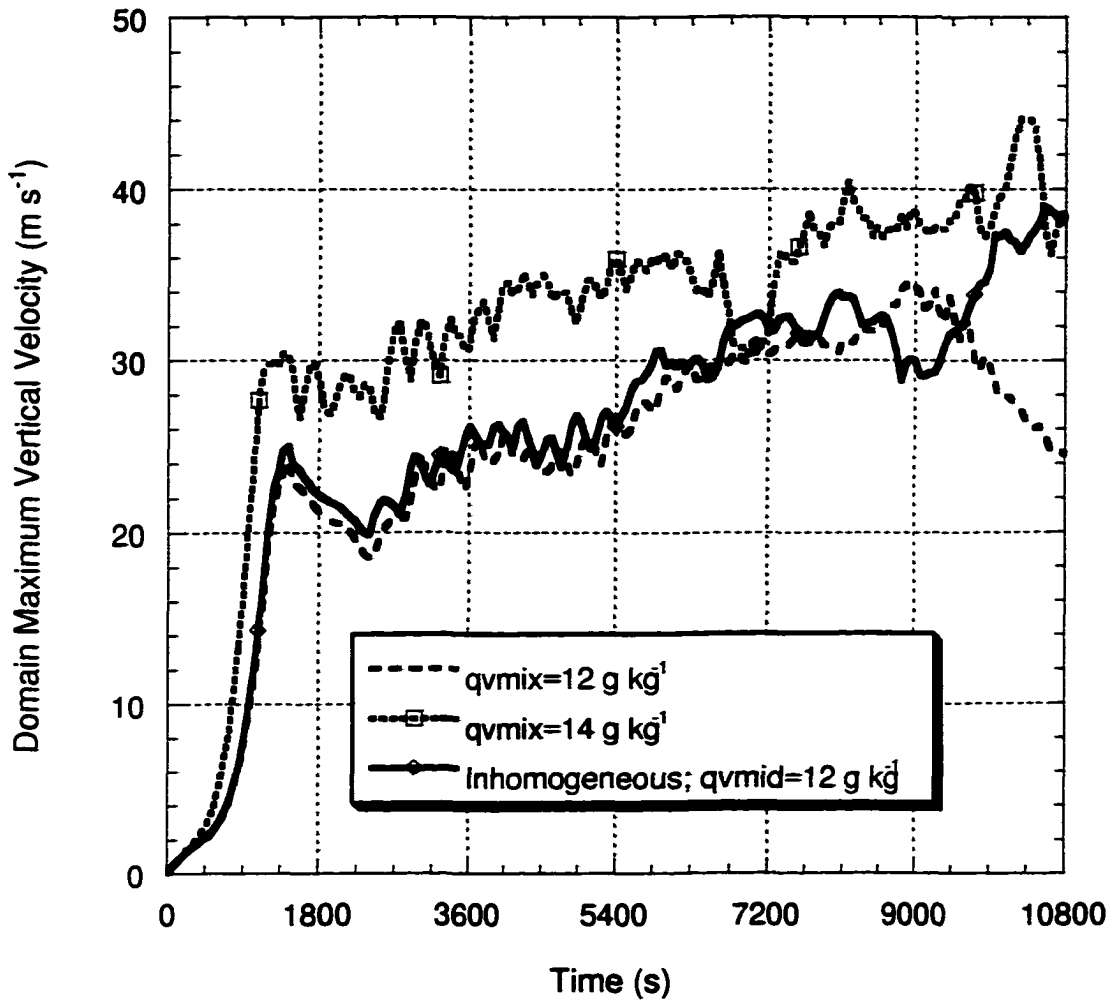


**Figure 4.39: Domain maximum values of vertical velocity for strong shear ( $U_s=30 \text{ m s}^{-1}$ ) inhomogeneous moisture case and homogeneous control runs. Inhomogeneous case is initialized in a region of  $q_v=12 \text{ g kg}^{-1}$ , with  $q_v$  variation as shown in Figure 4.38.**

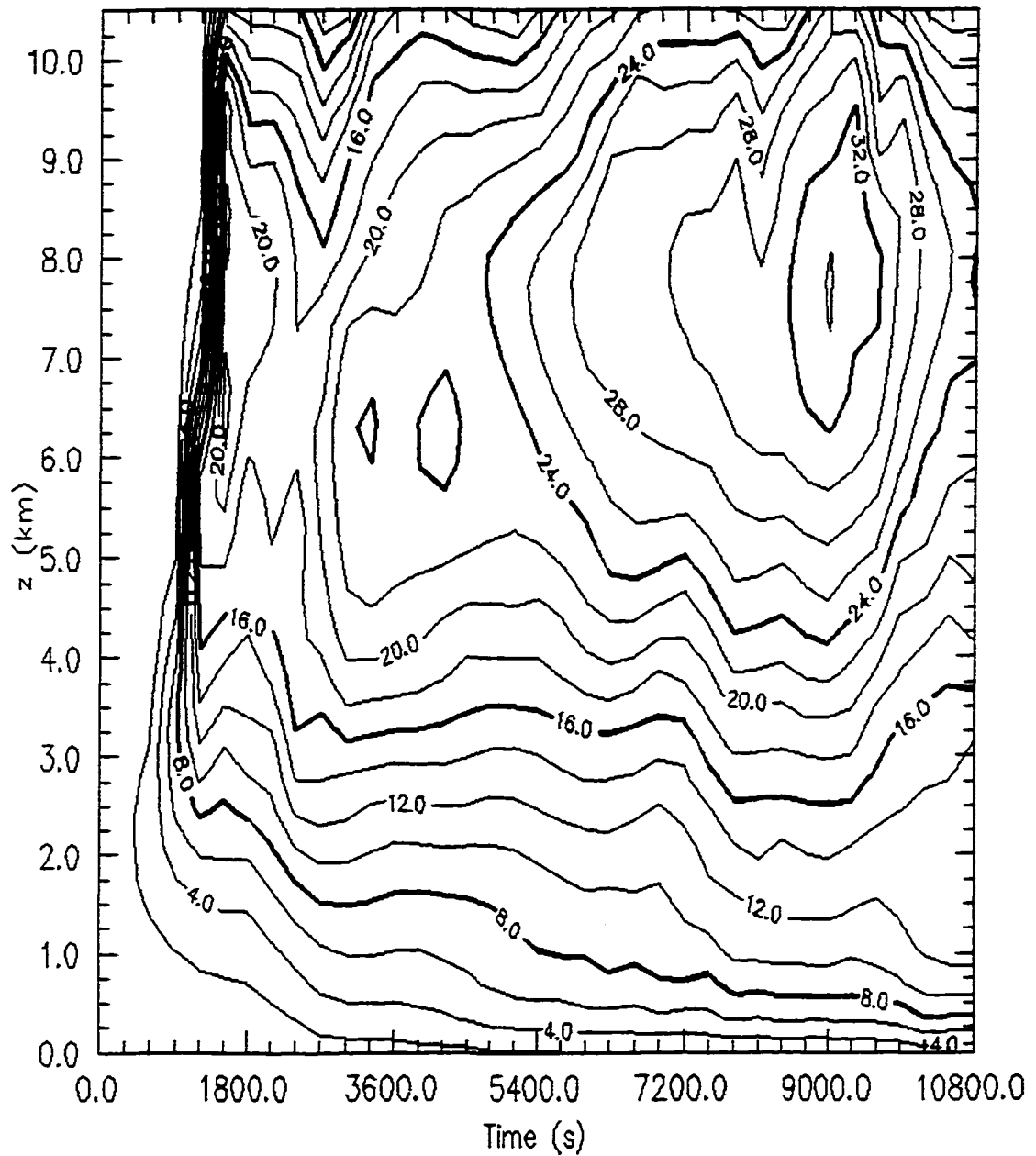


**Figure 4.40: Time-height diagram of maximum vertical velocity ( $\text{m s}^{-1}$ ) for southern half of strong shear ( $u_x=30 \text{ m s}^{-1}$ ) control run with mixed layer  $qv = 12 \text{ g kg}^{-1}$ . (Height is with respect to the lowest scalar level).**

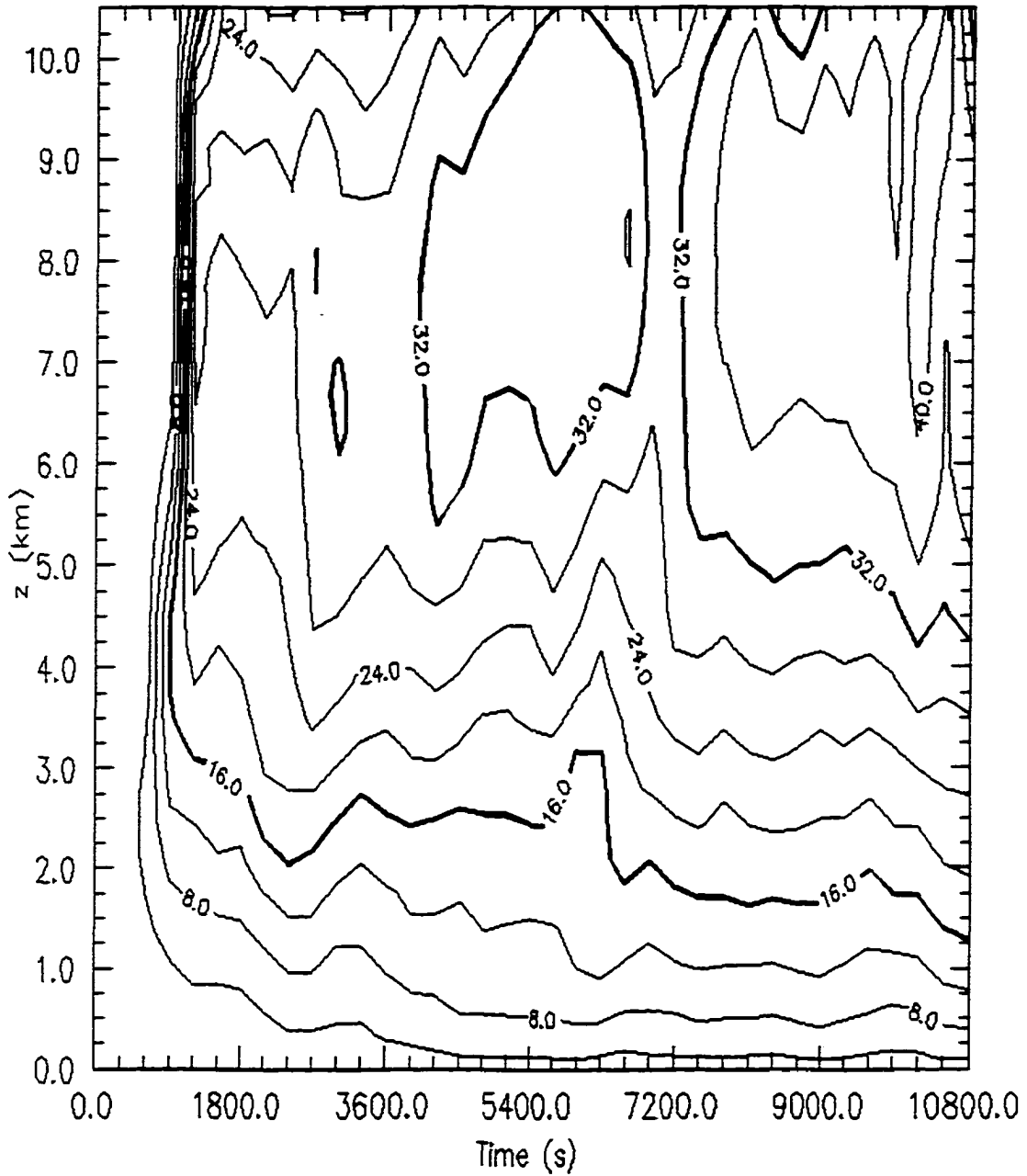


**Figure 4.41: Time-height diagram of maximum vertical velocity ( $\text{m s}^{-1}$ ) for southern half of strong shear ( $u_s=30 \text{ m/s}$ ) control run with mixed layer  $q_v = 14 \text{ g kg}^{-1}$ . (Height is with respect to the lowest scalar level).**

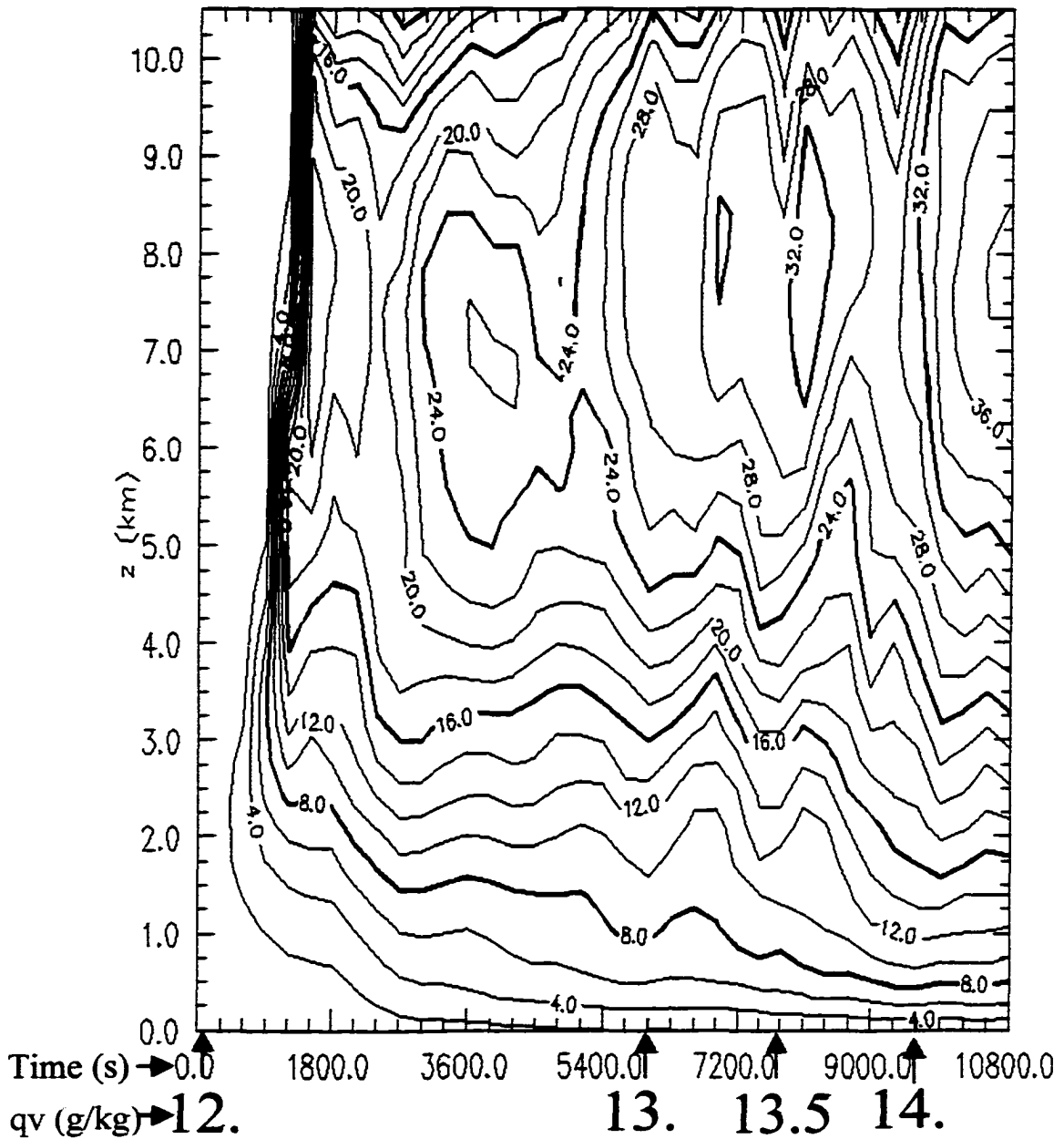


**Figure 4.42: Time-height diagram of maximum vertical velocity ( $\text{m s}^{-1}$ ) in southern half of domain for strong shear ( $U_s=30 \text{ m s}^{-1}$ ), inhomogeneous moisture simulation, with environmental  $q_v$  varying as indicated following the location of the dominant cell. (Height is with respect to the lowest scalar level).**

$$w_{\max} = \sqrt{2 * \text{CAPE}} \quad (4.3)$$

Over the first two hours, the CAPE experienced by the storm increases by a factor of 1.5, so the maximum vertical velocity could be expected to increase by 22.5%. The increase actually experienced is closer to 10%. However, this represents only a point measurement. A time-height diagram of vertical velocity shows that, although the point maximum is only slightly higher, the updraft reaches this value over a much larger depth of the storm, particularly during the first 1.5 hours (compare Figure 4.42, Figure 4.40, and Figure 4.41). At 2.5 hours, contrary to the predictions of parcel theory, the updraft in the inhomogeneous case is *weaker* than the control -- even though it is located in air having a mixing ratio more than  $1.5 \text{ g kg}^{-1}$  greater than the control, and has been ingesting air with a moisture content exceeding that of the control for its entire lifetime. This discrepancy indicates that the assumptions inherent to parcel theory are not justified for this cell at this time. I believe this is due to interference from a nearby cell.

Figure 4.43 shows the vertical velocity at  $z=4.6 \text{ km}$  in the inhomogeneous domain at 2.5 hours. The original right-mover has split into two cells (A and B) and there is considerable interference between them. A vertical cross section through these cells (Figure 4.44) illustrates this interference, with the colliding outflow winds at upper levels creating a downdraft, between the updrafts, extending down to 8 km. The convergence at cloud top is associated with high pressure and an adverse pressure gradient in the upper regions of the updraft (Figure 4.45).

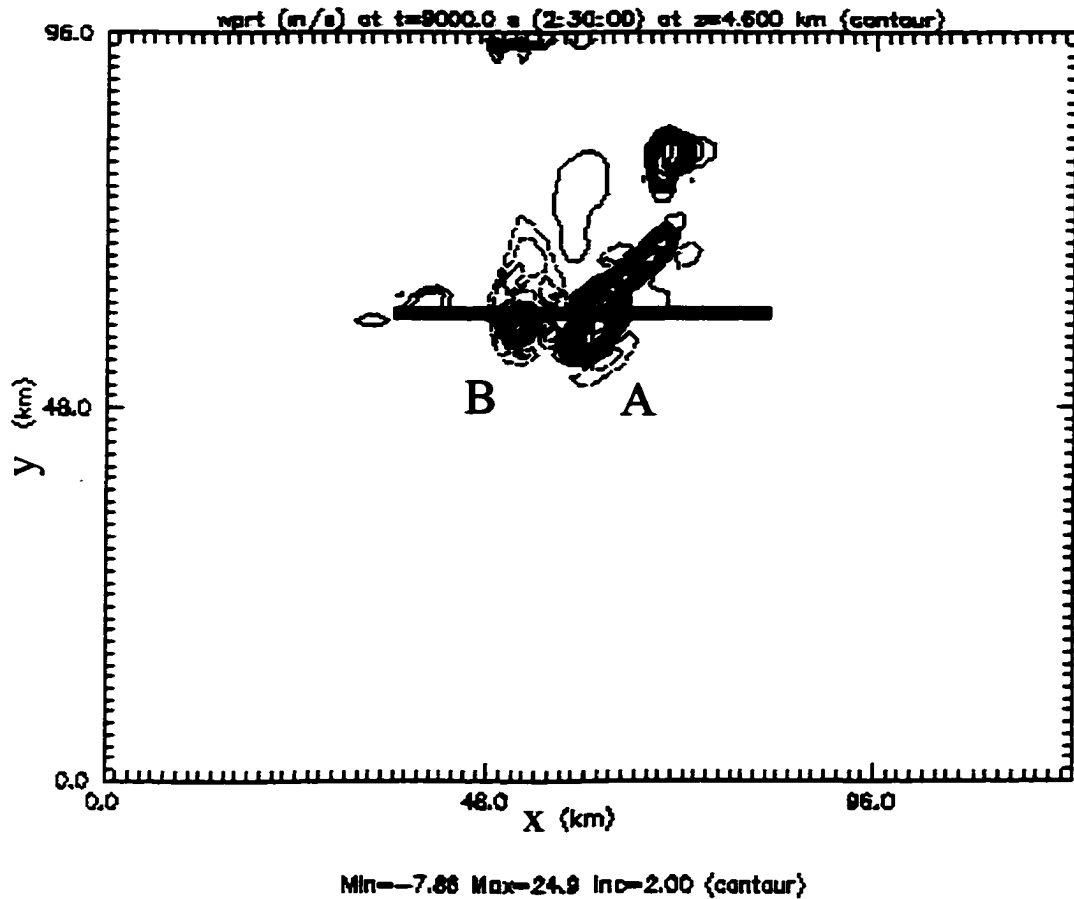


**Figure 4.43: Horizontal cross section of vertical velocity at  $z=4.6$  km at  $t=2.5$  hours for inhomogeneous moisture simulation with  $U_i=30$  m s<sup>-1</sup> and initial  $q_v=12$  g kg<sup>-1</sup>. Thick line indicates the cross section used in the following figures. Only the southern half of the computational domain is shown.**

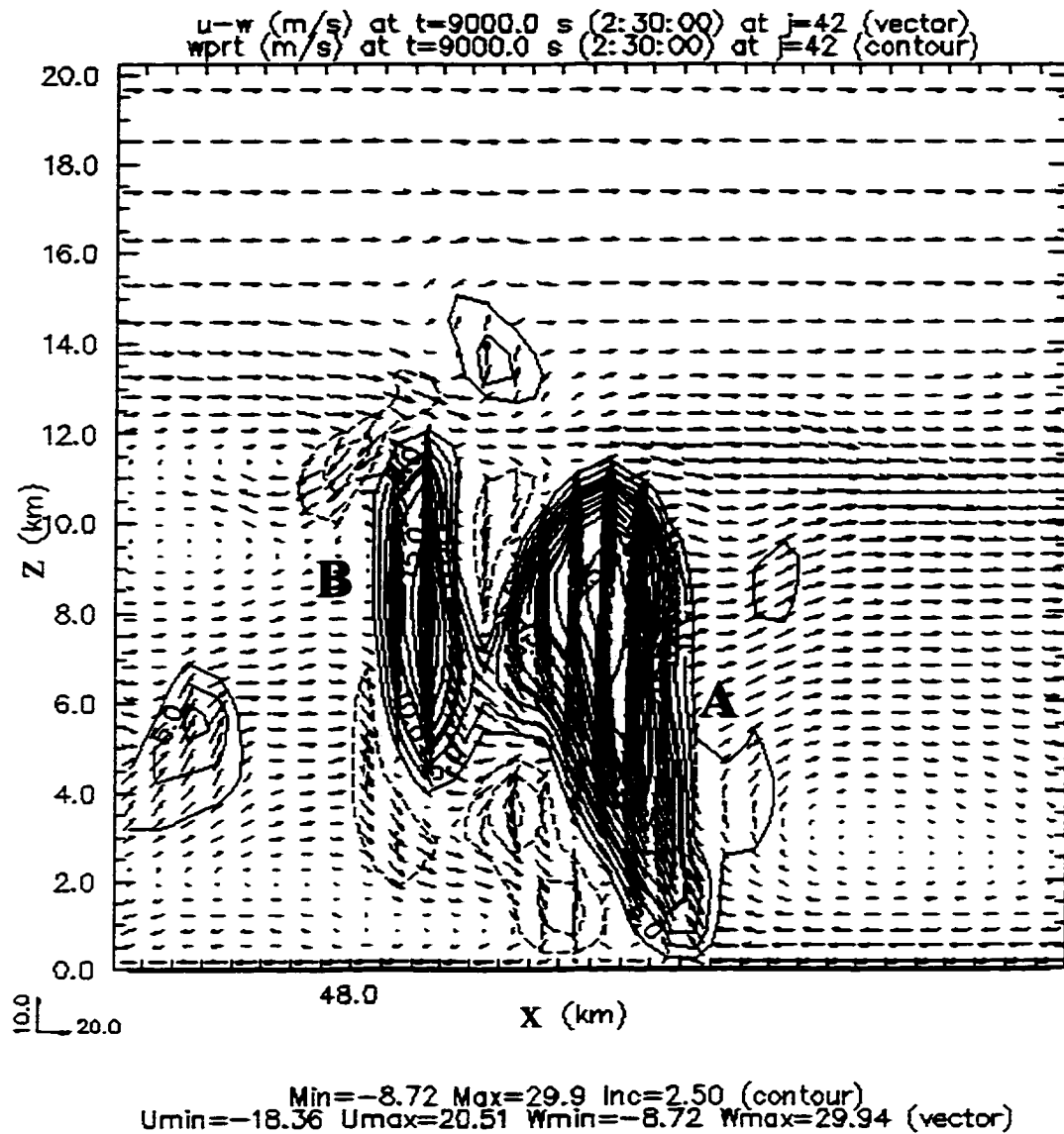


**Figure 4.44: Vertical (x-z) cross section at  $t=9000$  s along line shown in Figure 4.43 for inhomogeneous moisture case with  $U_s=30$  m s<sup>-1</sup> and initial  $qv=12$  g kg<sup>-1</sup> (as in Figure 4.38). Contours indicate vertical velocity (m s<sup>-1</sup>). Domain-relative two-dimensional wind vectors are also shown.**

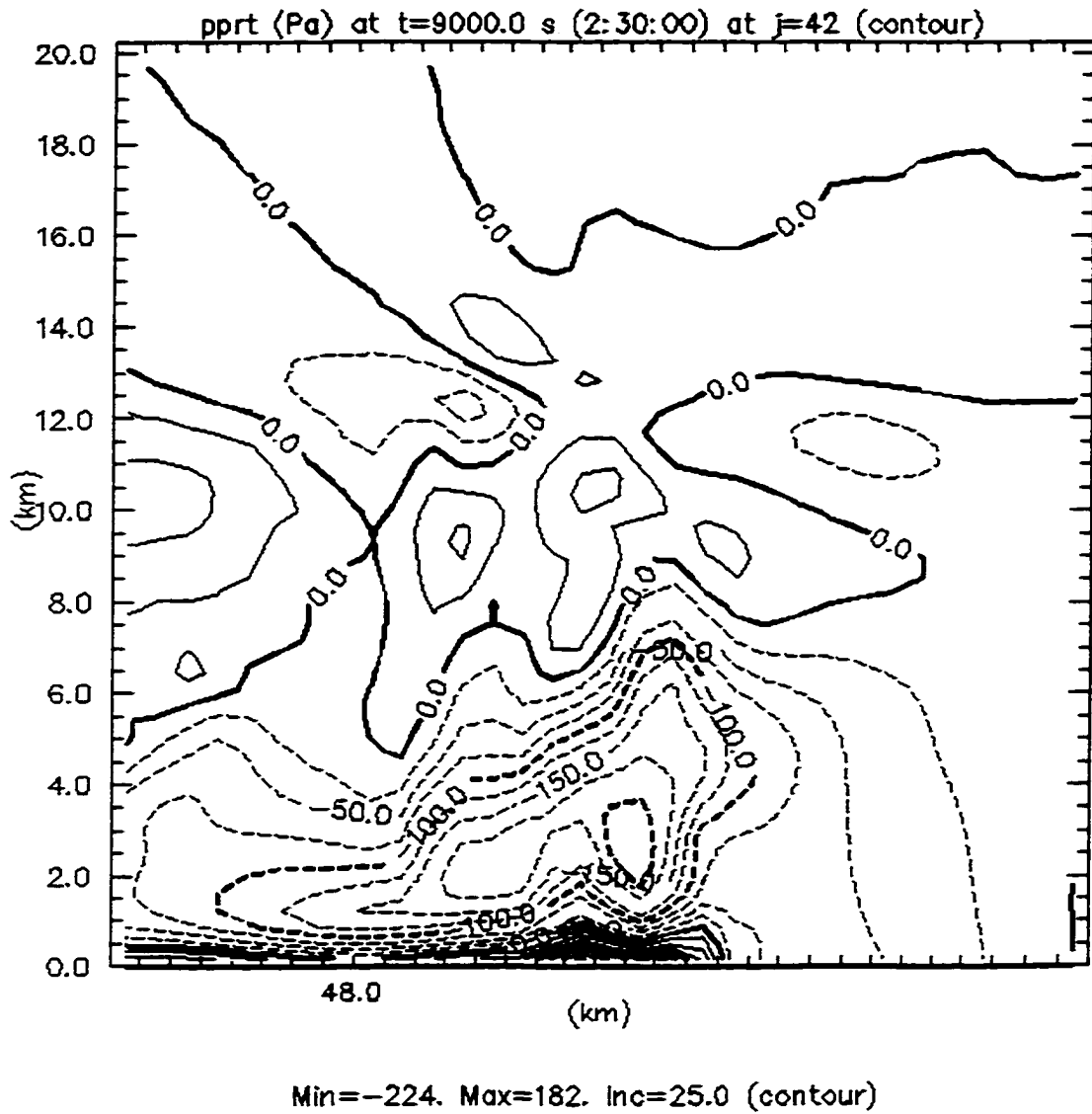


**Figure 4.45: Perturbation pressure (Pa) at  $t = 9000$  s along line shown in Figure 4.43 for inhomogeneous simulation with  $U_r = 30 \text{ m s}^{-1}$  and initial  $q_v = 12 \text{ g kg}^{-1}$  (as in Figure 4.38).**

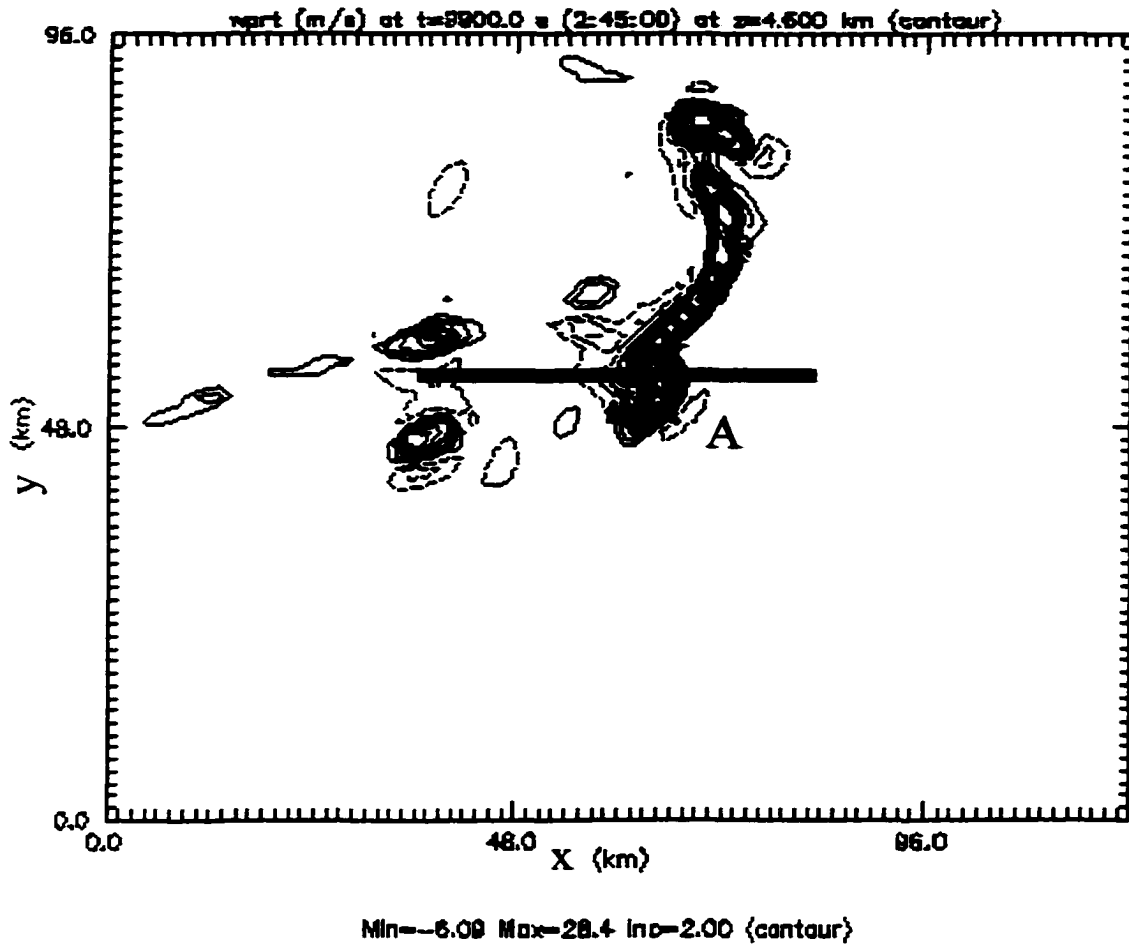


**Figure 4.46: Vertical velocity at  $z=4.6$  km at  $t=9900$  s for inhomogeneous simulation with  $U_i=30$  m s<sup>-1</sup> and initial  $qv=12$  g kg<sup>-1</sup>. Thick black line indicates the cross-section used in the following figures.**

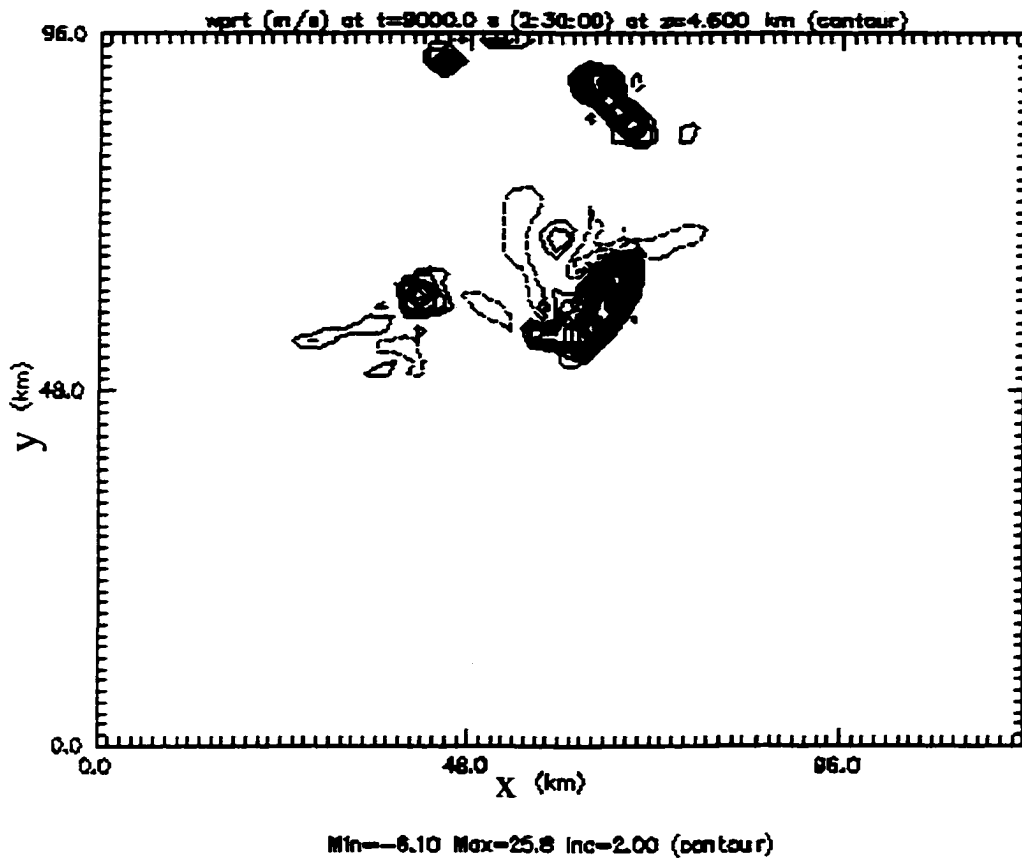
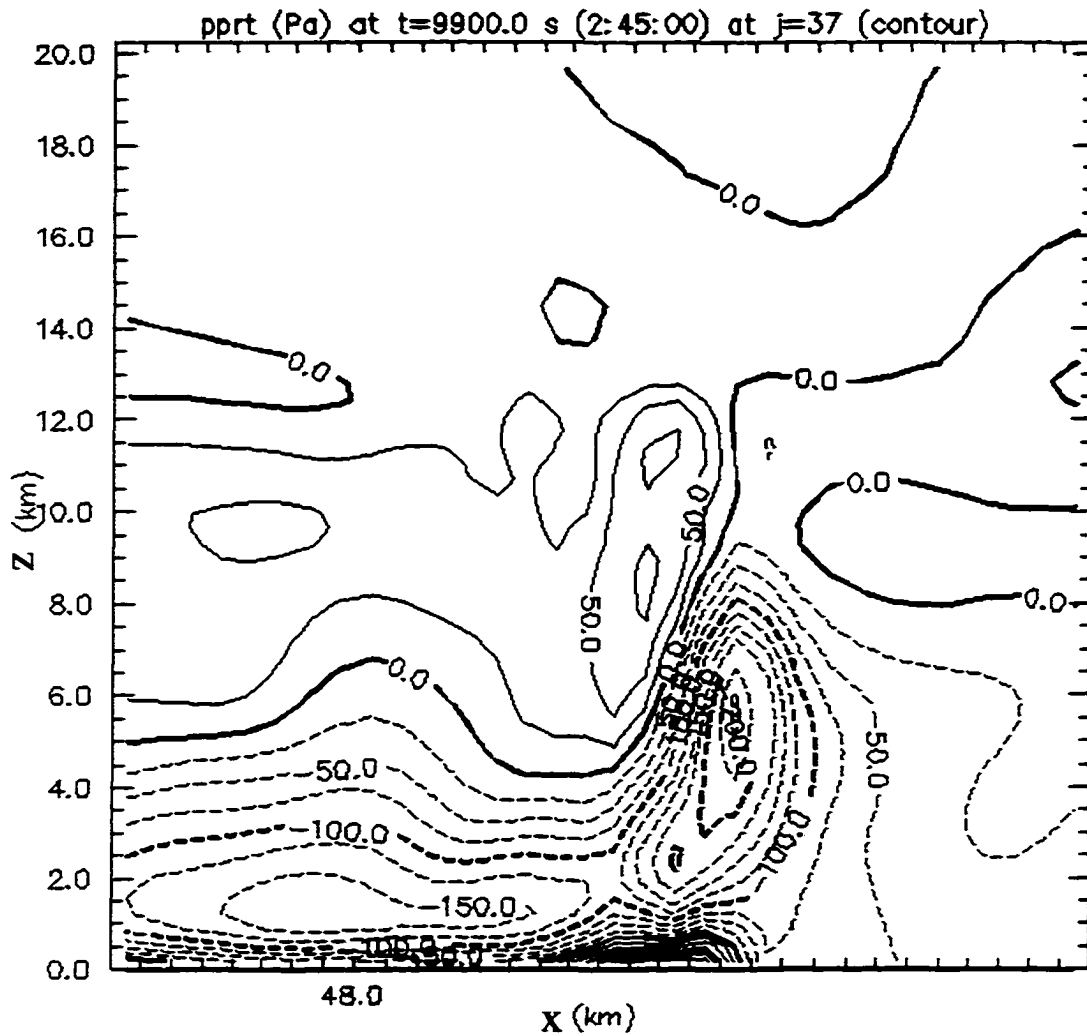


**Figure 4.47: Horizontal cross section of vertical velocity ( $\text{m s}^{-1}$ ) at  $t=2.5$  hours at  $z=4.6$  km for  $13 \text{ g kg}^{-1}$  homogeneous control simulation with  $U_c = 30 \text{ m s}^{-1}$ . Symmetric condition is applied at northern boundary.**



Min=-258. Max=145. Inc=25.0 (contour)

**Figure 4.48: Perturbation pressure (Pa) at  $t = 9900$  s along line shown in Figure 4.46 for inhomogeneous simulation with  $U_i = 30 \text{ m s}^{-1}$  and initial  $qv = 12 \text{ g kg}^{-1}$  (as in Figure 4.38).**

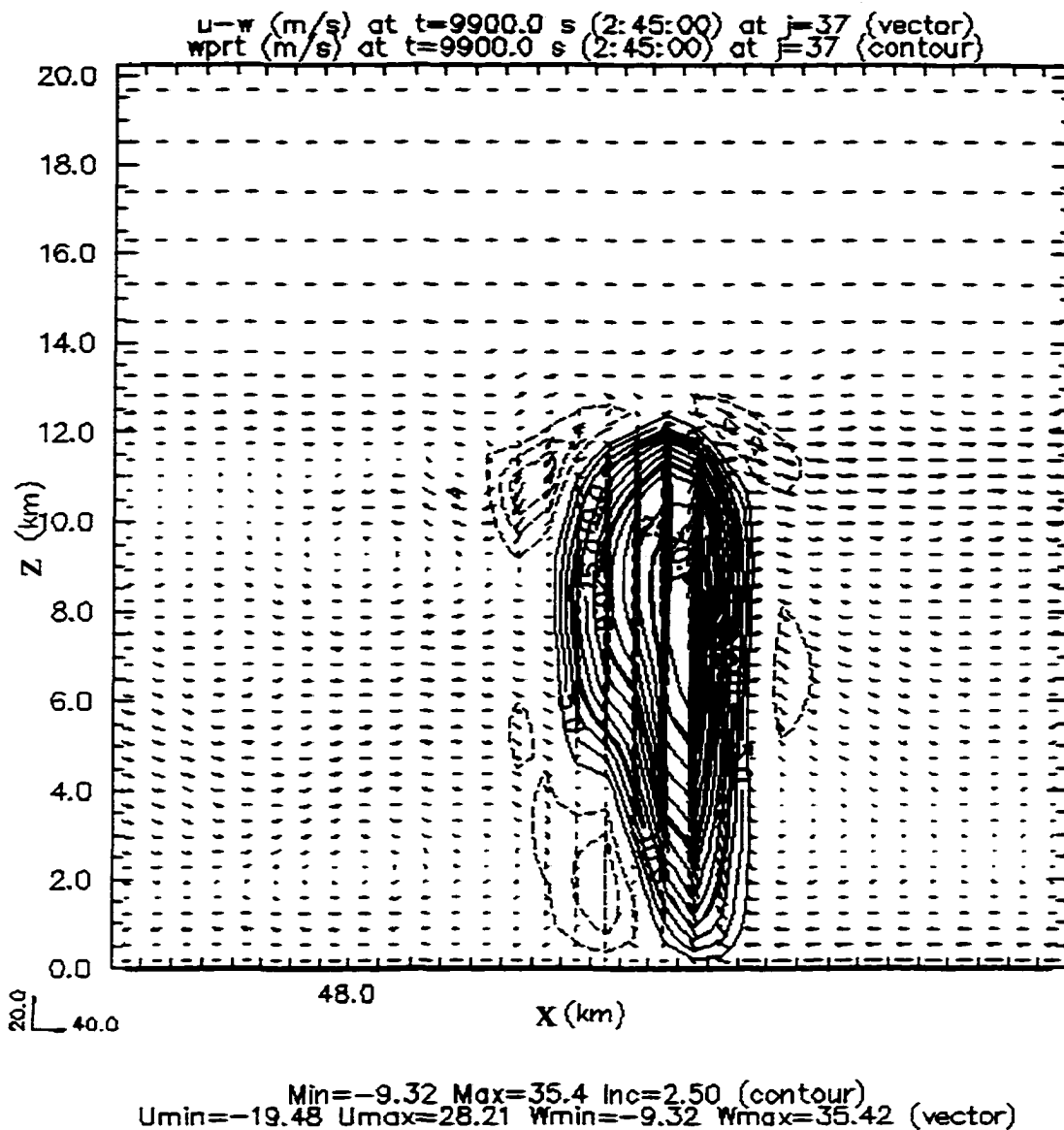


**Figure 4.49: Vertical (x-z) cross section at  $t=9900$  s along line shown in Figure 4.43 for inhomogeneous moisture case with  $U_0=30$  m s<sup>-1</sup> and initial  $q_v=12$  g kg<sup>-1</sup> (as in Figure 4.38). Contours indicate vertical velocity (m s<sup>-1</sup>). Domain-relative two-dimensional (u-w) wind vectors are also shown (note the change in vector length compared to the previous figure).**

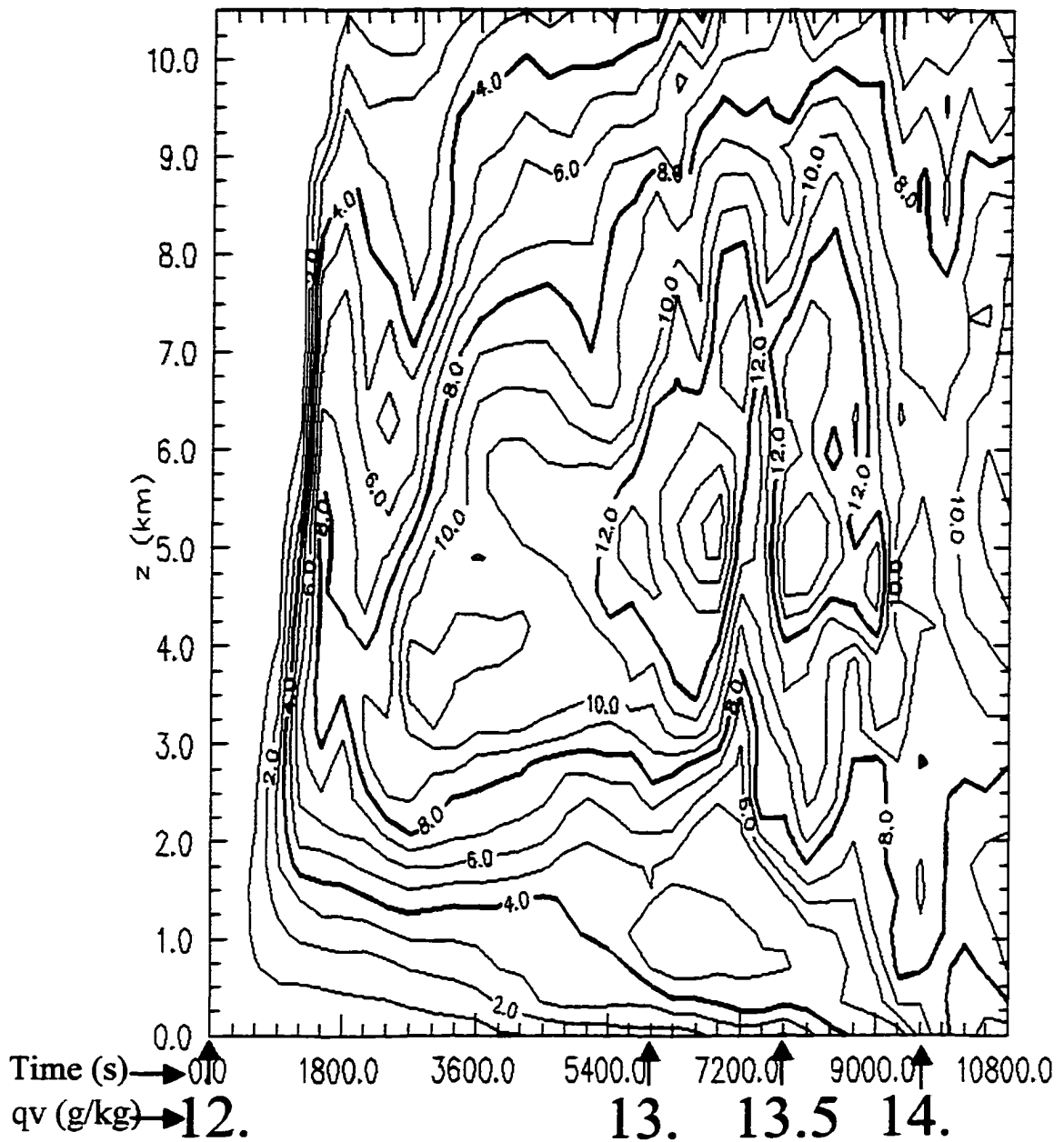


**Figure 4.50: Time-height diagram of maximum vertical vorticity in  $s^{-1}$  multiplied by 1000 for southern half of strong shear ( $U_s=30$  m/s), inhomogeneous moisture simulation with environmental mixed-layer  $q_v$  varying as shown following the dominant cell.**

At 9900 s, cell B is no longer evident and cell A has become the dominant cell on the southern end of a line (Figure 4.46), bearing a somewhat closer resemblance to the dominant cell in the  $13 \text{ g kg}^{-1}$  control run (Figure 4.47). The adverse pressure gradient (Figure 4.48) and the peripheral downdraft (are altered without the interference from cell B (Figure 4.48). At this time, cell A is in a region with  $q_v = 14 \text{ g kg}^{-1}$ , and its updraft speed is much closer to that of the control run (Figure 4.39). Thus, the updraft speed *does* appear to respond to the changes in water vapor when the cell is isolated, but the influence of increased moisture may compete with cell interference when multiple cells are present.

The maximum mid-level vertical vorticity (Figure 4.50) follows the maximum vertical velocity pattern quite closely for the original cell. At three hours, this correlation breaks down as cell B, which is the strongly rotating portion of the original updraft, dissipates. The maximum vertical velocity at this time is associated with cell A, which began as a pulse to the original updraft and contained a vortex couplet. At three hours, this cell is just beginning to achieve significant vertical vorticity at midlevels.

To summarize, moisture will affect the vertical velocity (and mid-level vorticity) of a storm in two different ways: directly, through alteration of buoyancy (compare Figure 4.51 and Figure 4.52, showing maximum potential temperature perturbation in the control and inhomogeneous runs, respectively) and indirectly, by altering the timing and location of other cells.

### 4.3.3 Cell Interactions: Supercell with $U_s=35 \text{ m s}^{-1}$

To further examine cell interaction, we consider a case with a slightly higher mixing ratio at the initiation location. The mixed layer water vapor mixing ratio ( $q_{\text{vmix}}$ ) varies from 10 g/kg at the northern edge of the domain to 18 g/kg at the southern edge, producing a range of CAPE from 500–4000 J kg<sup>-1</sup>. A storm is initiated in the center of the domain where the water vapor mixing ratio within the mixed layer is 14 g/kg. The shear used in the simulation is given by  $u = 35 \tanh(z/z_s) \text{ m s}^{-1}$  where  $z_s$  is 3000 m. This value of shear is chosen in order to produce split cells that move with a component perpendicular to the mean wind such that the cells will experience significant variations in moisture over their lifetime (Figure 4.27).

Control runs are performed in homogeneous environments using soundings taken from four locations in the inhomogeneous domain. These control runs are performed over the same time period and with the same domain motion as the inhomogeneous run. Details for each of the control runs are described below. The focus in this discussion is on the significant role of cell interactions in the development of low-level vorticity.

#### 4.3.3.a Control Run Along Centerline ( $q_{\text{vmix}}=14 \text{ g/kg}$ )

The first control run uses the sounding corresponding to  $q_{\text{vmix}}=14 \text{ g/kg}$  (Figure 4.1). The original cell splits into left and right-moving members that subsequently strengthen, exceeding their original strength until just under 2 hours. At 6600 s, a new cell (cell B) forms northeast (southeast) of the right (left) mover (cell A). During this time, cell A weakens considerably, as expected with cells in close

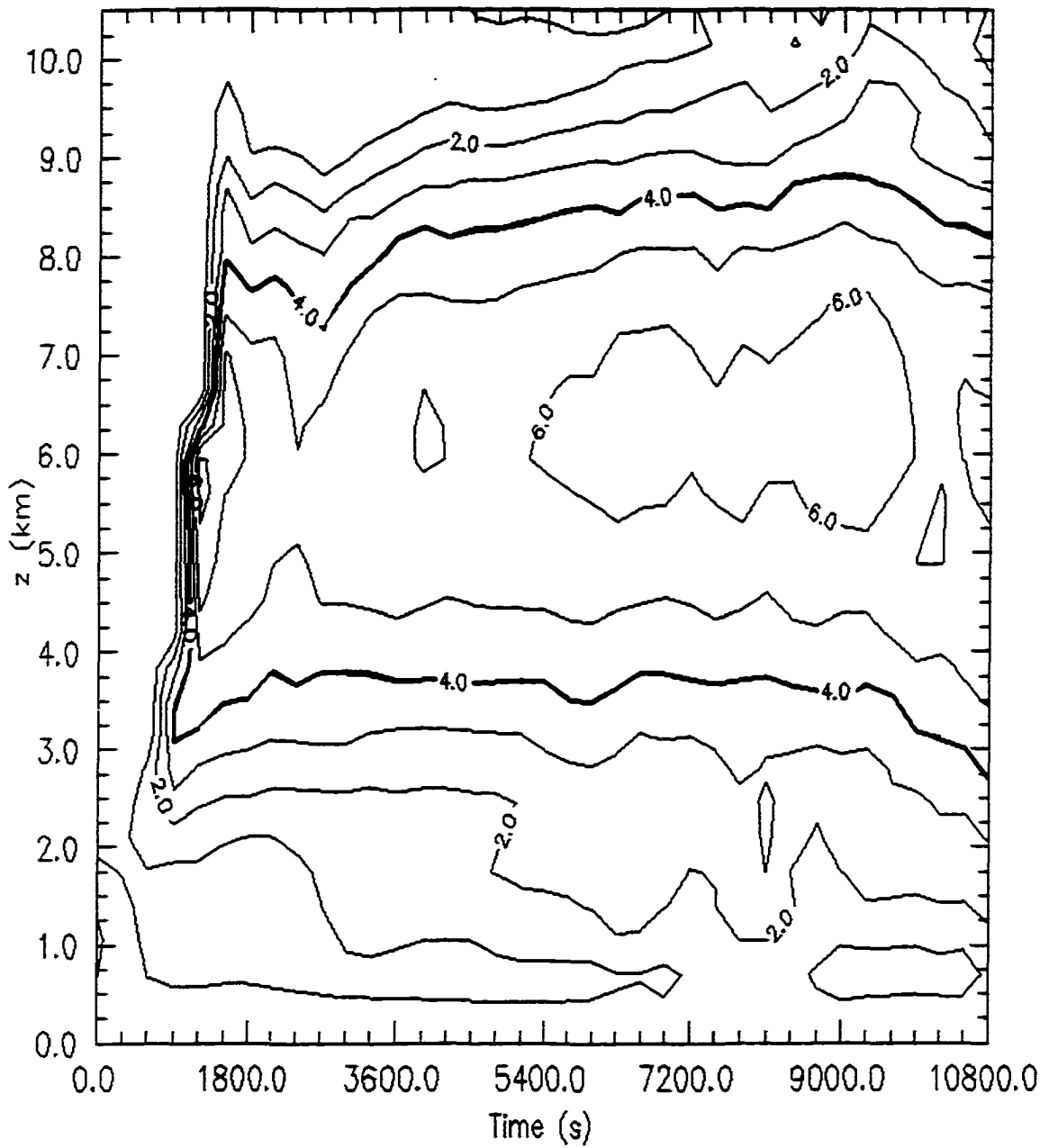


**Figure 4.51: Time-height diagram of maximum perturbation potential temperature (K) for strong shear ( $U_s=30$  m/s) control run with  $q_{vmix}=12$  g  $kg^{-1}$ .**

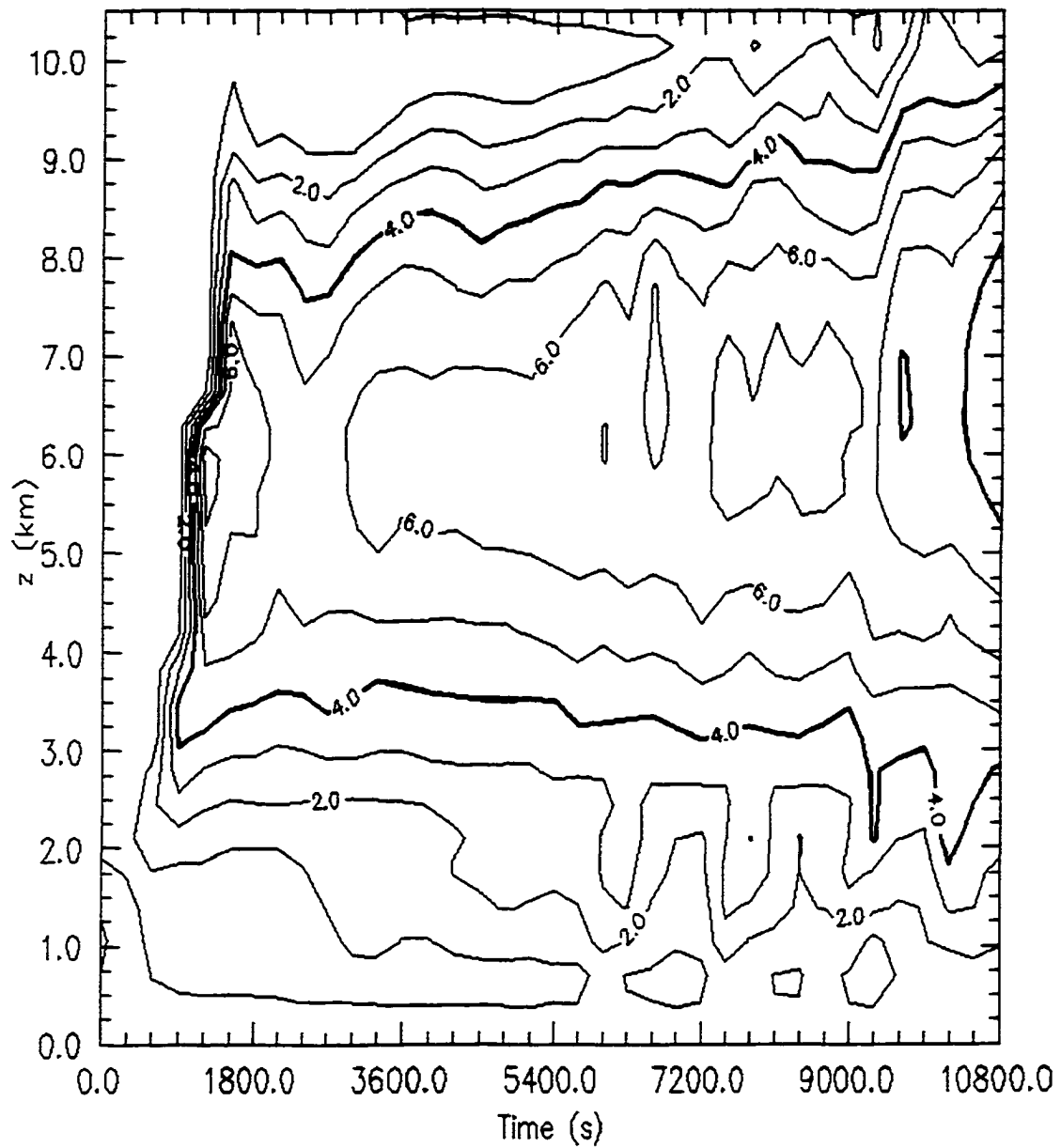


**Figure 4.52: Time-height diagram of maximum potential temperature perturbation (K) for southern half of strong shear ( $U_s=30$  m/s), inhomogeneous moisture simulation with environmental mixed-layer  $qv$  as shown in Figure 4.38.**

proximity to one another. This weakening is generally attributed to the development of downdrafts on the cloud edges due to the competing circulations of adjacent cells (Turpeinen, 1982). Despite this, Cell B intensifies and splits, with its cyclonic member merging with another new cell (cell D) forming between B and A. Cell merger would not necessarily be expected in this case if these were ordinary cumulus clouds because the axis connecting the two cells is perpendicular to the shear vector (Turpeinen, 1982). In this configuration, ordinary cells tend to suppress one another rather than merge. However, this expectation must be modified in our case since the cells under consideration are supercells and are not simply traveling with the mean wind.

The deviate motion caused by the splitting of the northern cell allows its southern half (the right-mover) to merge with the new cell. The cell formed by this merger strengthens considerably and eventually develops significant low level vorticity greater than  $0.012 \text{ s}^{-1}$  (Figure 4.53). Numerous investigators have documented intensification of cumulus updrafts through the merger process (e.g., Westcott, 1984; Miller, 1977; Orville et al., 1980; Turpeinen, 1982), and a few have noted similar behavior associated with the merger of severe storm echoes (e.g., Lemon, 1976; Bluestein, 1998). In our simulation, the merger of a right moving cell with a new cell and the subsequent intensification of low-level vorticity is intriguing and suggests further research on such a mechanism for producing or enhancing low-level vorticity is warranted.

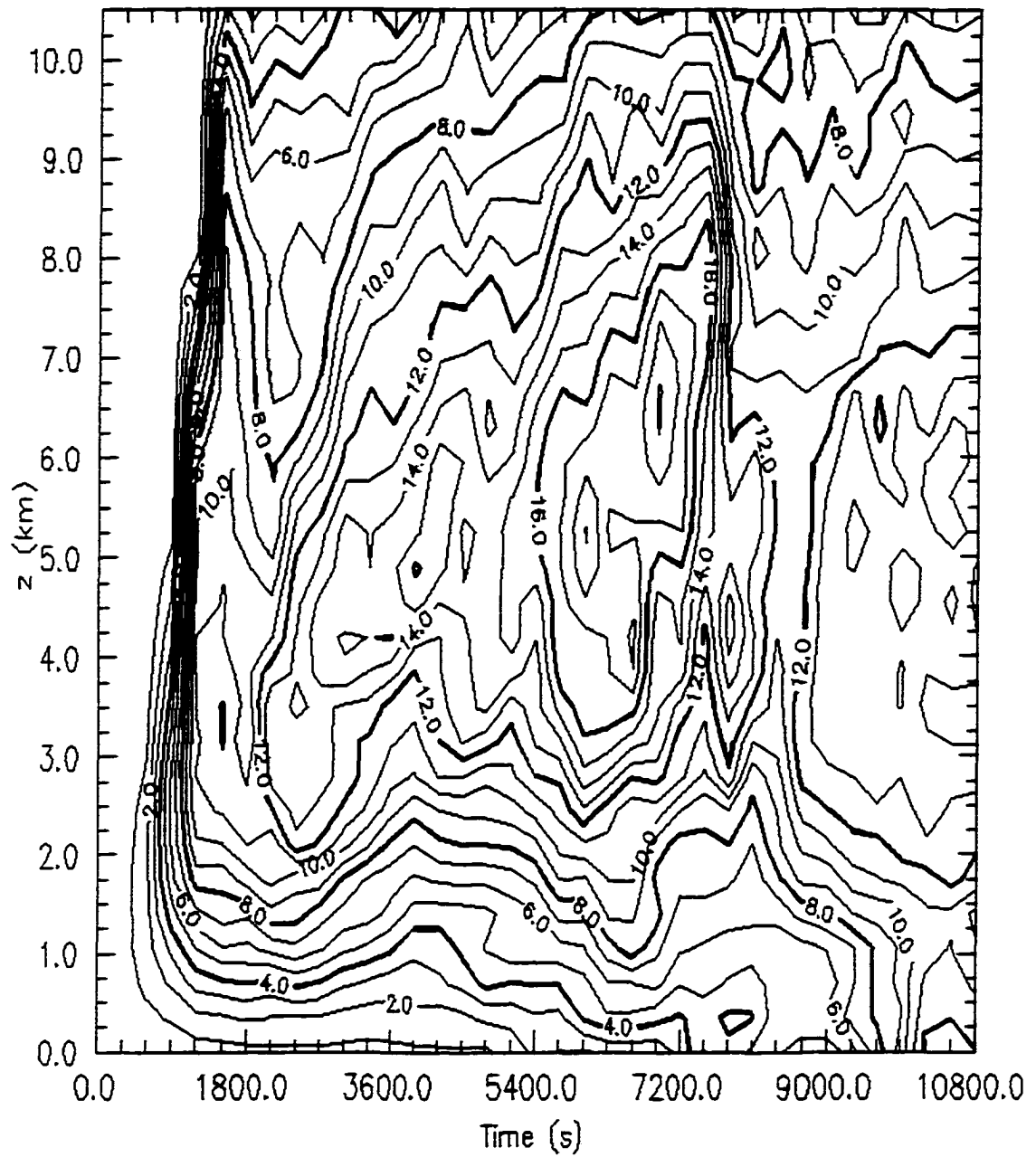


**Figure 4.53: Time-height diagram of maximum vertical vorticity ( $s^{-1}$ ) times 1000 for strong shear ( $U_x=35 \text{ m s}^{-1}$ ) control run with mixed-layer  $qv=14 \text{ g kg}^{-1}$ .**

To summarize, in this simulation the original split cells exhibit significant mid-level rotation but do not develop significant low-level rotation. A low-level mesocyclone does not form until almost three hours into the simulation, and it is associated with a new cell further to the east that formed via the merger of two updrafts.

#### 4.3.3.b Control Run for Increased Moisture ( $q_{vmix}=16 \text{ g/kg}$ )

Increasing the mixed layer mixing ratio to  $16 \text{ g kg}^{-1}$  leads to greatly enhanced buoyancy and larger vertical velocities, resulting in increased tilting of environmental vorticity. Thus, we would expect the simulation with enhanced moisture to have greater values of mid-level vorticity produced primarily through tilting. Examining Figure 4.54 and comparing to Figure 4.53, we see that this is indeed the case, with the  $16 \text{ g kg}^{-1}$  simulation exhibiting larger mid-level vertical vorticity, particularly during the first hour of the simulation.

Increased moisture also should lead to increased rain production and increased evaporation (as long as the environmental sounding is sufficiently subsaturated), thus aiding the formation of large potential temperature gradients in the cold pool. One would expect this to aid in the development of low-level vorticity (Rotunno and Klemp, 1985; Brooks et al., 1994b) if properly positioned relative to the storm inflow. However, in this simulation there is *no* development of significant low-level vertical vorticity. While it is tempting to conclude from this that larger moisture must somehow be detrimental to the production of low-level vorticity, examination of a simulation using  $17 \text{ g/kg}$  in the mixed layer easily disproves this assumption.

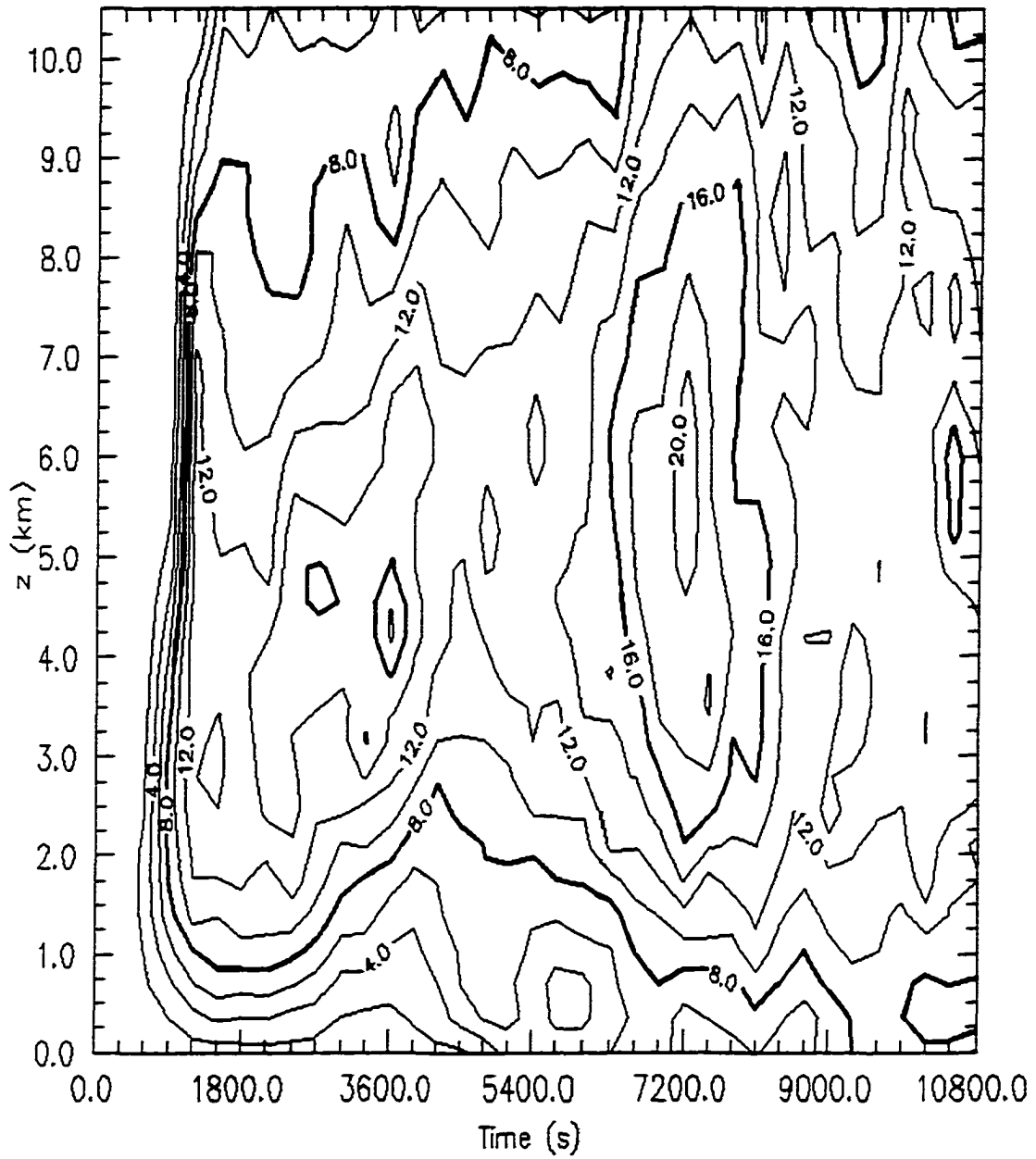


**Figure 4.54: Time-height diagram of maximum vertical vorticity ( $\text{s}^{-1}$ , multiplied by 1000) for strong shear ( $U_1=35 \text{ m s}^{-1}$ ) control run with  $q_v=16 \text{ g kg}^{-1}$ .**

The  $17 \text{ g kg}^{-1}$  case produces very strong ( $> .02 \text{ s}^{-1}$ ) low-level vorticity (Figure 4.55) in the second main cell (cell B) which forms in a manner similar to cell B in the  $14 \text{ g kg}^{-1}$  control run, but with greater intensity. We believe that a similar process for the development of low-level vorticity does not occur in the  $16 \text{ g kg}^{-1}$  case because the interaction between cells is different due to the timing of their development. The cells of the original split pair in all of the control simulations develop strong mid-level vorticity but do not produce significant low-level vorticity. However, subsequent cells that form and split *do* produce low-level vorticity in some cases. We believe this is partially due to their fortuitous development along an existing cold pool rich with baroclinically-generated vorticity, similar to the process associated with cyclic mesocyclogenesis in which secondary updrafts develop mesocyclones much more rapidly than the first (Adlerman et al., 1999). In other words, although the cells of the original split pair never develop the ideal configuration for producing strong low-level vorticity, subsequent cells forming along the gust front do. In the  $16 \text{ g kg}^{-1}$  case, this production is disrupted by the interactions between the numerous cells.

In particular, cell B splits *before* the new cell forms to its south, causing the right mover of cell B to move *in front of* the new cell rather than merging with it as it did in the  $14 \text{ g/kg}$  case. Without this merger, cell B does not intensify and become the dominant cell. Instead, three cells of nearly equal intensity coexist. Although a detailed circulation budget has not been performed, cursory analysis suggests that the production of low-level vorticity is primarily disrupted by surface divergence from a

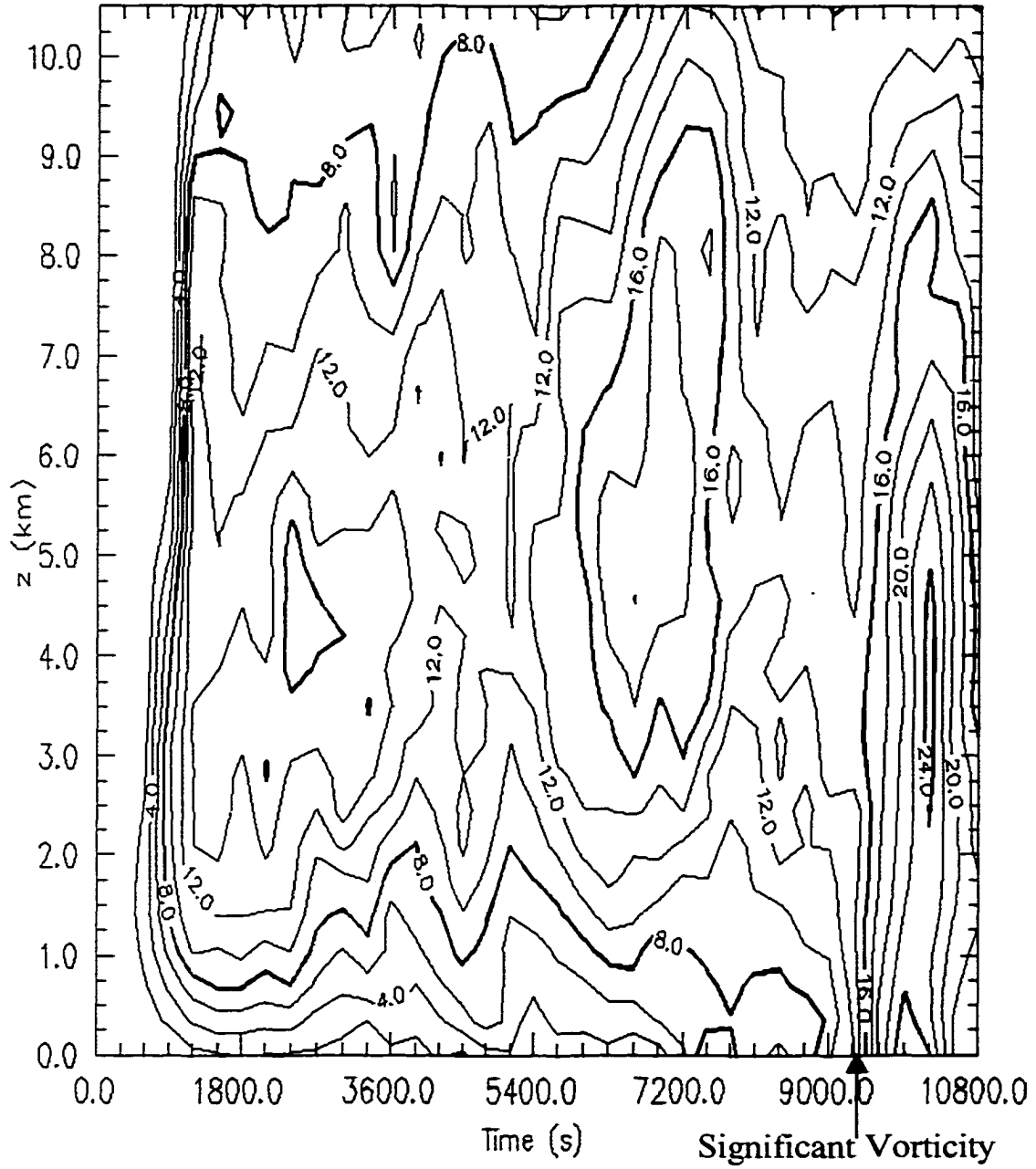


**Figure 4.55: Time-height diagram of maximum vertical vorticity ( $\text{s}^{-1}$ ) times 1000 for strong shear ( $U_s=35 \text{ m s}^{-1}$ ) control run with  $qv=17 \text{ g kg}^{-1}$ .**

cell to the north of the main cell. This divergence alters the surface flow in the region where strong low-level vorticity would be expected to develop based on the other control simulations. (Indeed, in a serendipitous simulation of this same case in a domain which was slightly insufficient in size, development of the cell to the north was inhibited by the boundary, and the main cell *did* develop large values of low-level vorticity.)

Thus, I do not believe that the lack of low-level vertical vorticity is due directly to the increased moisture, but is due instead to changes in the details of cell redevelopment and interaction. It is of interest to note that when several cells are present, the generation of a strong supercell with significant low level rotation from re-developments depends on the ability of one cell to become dominant and/or isolated. In both the 14 g/kg and 17 g/kg cases, this occurs through cell merger. On the other hand, when the cells all have equal intensity and are fairly close together, as in the 16 g/kg case, their interference prevents one cell from becoming dominant. As a result, the outflow from one cell may disrupt the production of low-level vorticity by its neighbor.

#### 4.3.3.c Inhomogeneous Run Starting with $q_{vmix}=14$ g/kg

We now examine the inhomogeneous case with  $q_v=14$  g kg<sup>-1</sup> at the initial bubble location and a gradient of  $q_v$  toward the south across the domain. The original cell in the inhomogeneous run evolves and moves in a manner similar to the 14 g/kg control run for the first 2 hours of its lifetime, as expected. After two hours, the original right-mover is located in an environment corresponding to a mixed-layer  $q_v$

of approximately  $15.5 \text{ g kg}^{-1}$ . A cell similar to cell B in the control run develops, splits, and merges with a new cell in a manner very similar to the control run. It does not have the cell interaction difficulties which plagued the  $16 \text{ g kg}^{-1}$  control simulation, but *it does* contain additional redevelopments on the southern side, one of which results in the demise of the original right-moving cell. The cell formed via merger becomes the dominant cell, moving well to the right of the mean wind with a deviate motion greater than any of the control simulations, suggesting that its motion is being influenced by the gradient of CAPE. It remains fairly isolated despite the redevelopments occurring on the flanks.

Figure 4.56 shows the maximum vertical vorticity for this simulation. We see that the cell develops strong low-level vorticity at approximately the same time as the control simulations. The magnitude of the low-level vorticity lies between those for the control runs corresponding to the  $q_v$  values at the initial and current positions. Thus, the increase in moisture over the storm system's lifetime has amplified the low-level vorticity well beyond that which it would have had in its original location. Although the cell has evolved in a manner similar to the  $17 \text{ g/kg}$  control run from 2 to 3 hours and has vertical velocity values equaling those found in that control run, it does not develop equally large values of vertical vorticity. This is not surprising, given that it has not been in the  $17 \text{ g kg}^{-1}$  region for a large amount of time. We might expect that some time will be required for the updraft and cold pool to adjust to the increased moisture.

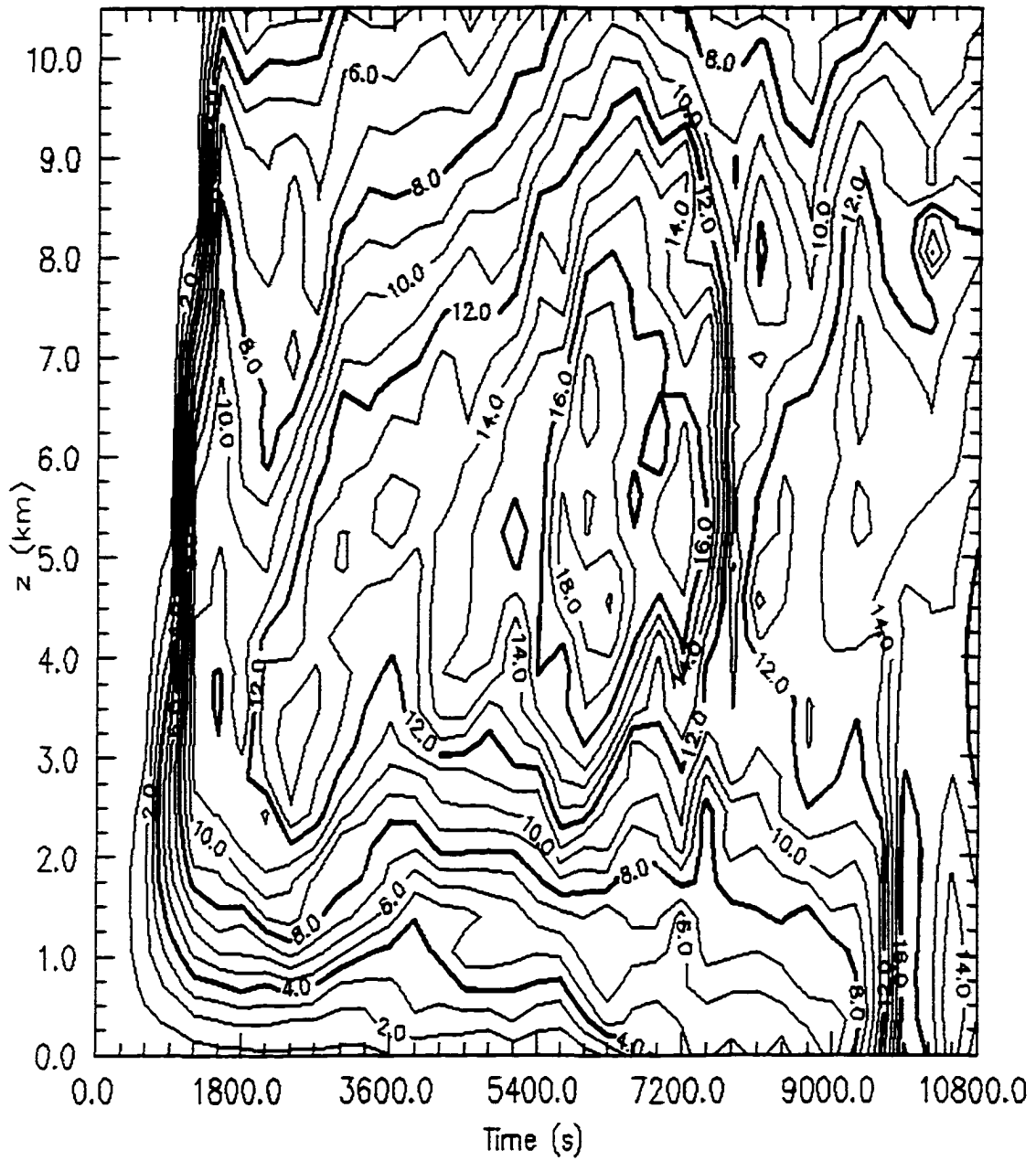


**Figure 4.56: Time-height diagram of maximum vertical vorticity ( $s^{-1}$ ) multiplied by 1000 for strong shear ( $U_x=35 \text{ m s}^{-1}$ ) inhomogeneous simulation with initial  $qv=14 \text{ g kg}^{-1}$ .**

Thus, a cell moving into greater moisture might be expected to experience an increase in low-level vorticity, as long as this is not prevented by detrimental cell interactions.

#### **4.3.4 Low-Level Rotation: Supercell with $U_s=30 \text{ m s}^{-1}$**

In the supercell simulations described above, development of low-level vertical vorticity is delayed until the second major cell forms. This muddies the interpretation of the results, as they become highly dependent on the details of the redevelopments. In an effort to aid in this interpretation, we now perform an experiment with a slightly lower shear value ( $U_s=30 \text{ m s}^{-1}$ ) in the hope of achieving significant low-level vorticity in the original split pair, making it easier to perform cell-to-cell comparisons between the inhomogeneous environment and associated control runs.

##### **4.3.4.a Control Simulation for $q_{\text{vmix}}=12 \text{ g/kg}$ with $U_s=30 \text{ m s}^{-1}$**

With  $q_{\text{vmix}} = 12 \text{ g/kg}$ , the initial storm splits into right and left-moving cells that remain dominant throughout the simulation (Figure 4.31). These cells never develop significant low level vorticity (Figure 4.57), presumably due to both the diminished gradients in the cold pool as a result of decreased rainfall as well as diminished low level vertical velocities due to a higher LFC. The low-level vorticity never exceeds  $.005 \text{ s}^{-1}$  throughout the 3 hour simulation.

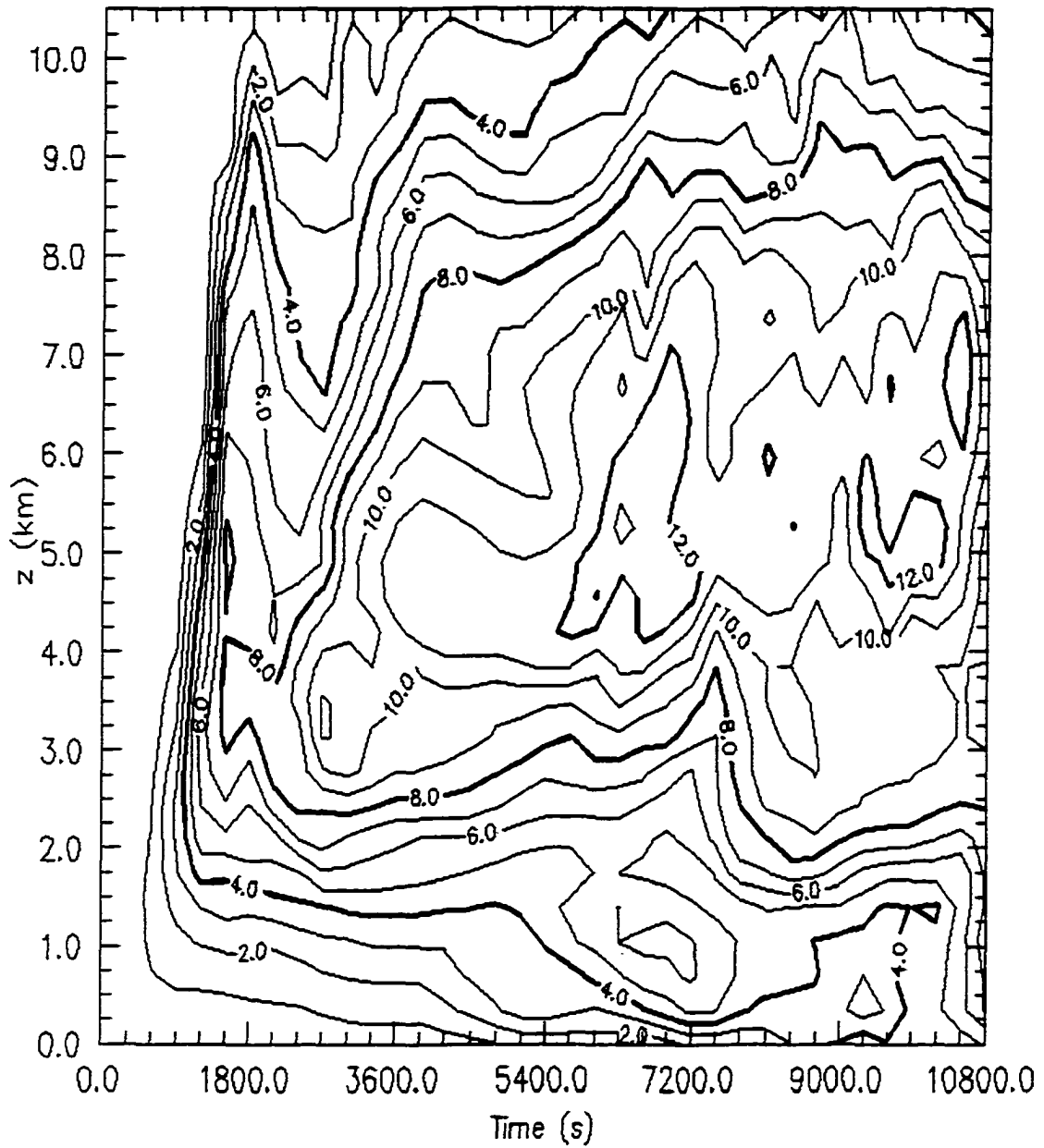


**Figure 4.57: Time-height diagram of maximum vertical vorticity ( $\text{s}^{-1}$ , multiplied by 1000) for strong shear ( $U_x=30 \text{ m s}^{-1}$ ) control simulation with mixed layer  $qv = 12 \text{ g kg}^{-1}$ .**

#### **4.3.4.b Control Simulation for $q_{vmix}=14 \text{ g/kg}$ with $U_s=30 \text{ m s}^{-1}$**

When a control simulation is performed using  $q_{vmix} = 14 \text{ g kg}^{-1}$ , the initial storm splits into right and left-moving cells that remain the dominant cells throughout the simulation. These cells develop significant low level rotation after nearly two hours and maintain it for over 30 minutes (Figure 4.58). Smaller cells develop to the west of the main cells but do not appear to significantly influence them.

#### **4.3.4.c Inhomogeneous Run starting with $q_{vmix}=12 \text{ g kg}^{-1}$ with $U_s=30 \text{ m s}^{-1}$**

When a cell is initiated in the inhomogeneous domain with an initial mixing ratio of  $12 \text{ g kg}^{-1}$ , the southern cell moves into moisture values that were associated with greater low-level vorticity in the control simulations. The environment at the initiation location in the inhomogeneous run does not support low-level rotation in the control run; it is unclear whether a storm beginning there will develop low level rotation as it moves into better moisture.

The right-moving cell in this simulation was considered in section 4.3.2.a with regard to updraft strength and we noted a departure from anticipated results due to cell interference. This cell interference also plays a role in the establishment of low-level vorticity. Even though the cell ingests water vapor of greater than  $13 \text{ g kg}^{-1}$  from 1.5 hours on, it does not produce low-level rotation of equal value to the  $13$  (Figure 4.59) or  $14$  (Figure 4.58)  $\text{g kg}^{-1}$  control runs. A detailed analysis of low-level circulation is planned for the future but has not been performed. However, we believe the cell interactions are again responsible for the lack of vorticity. This supposition is supported by the fact that low-level vorticity is greatly enhanced from

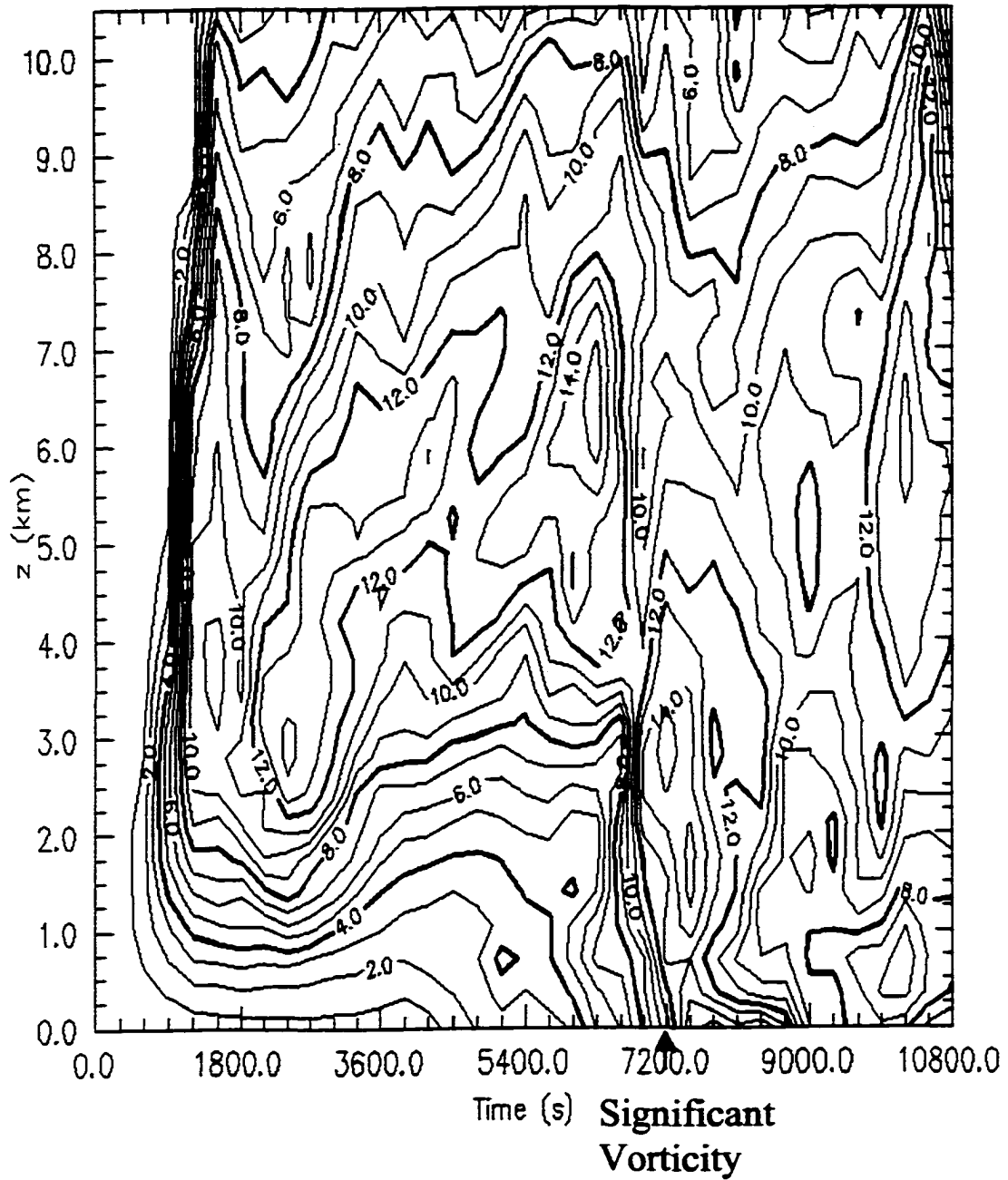


**Figure 4.58: Time-height diagram of maximum vertical vorticity ( $s^{-1}$ , multiplied by 1000) for strong shear ( $U_s=30m/s$ ) control run with  $q_{vmix}=14 g kg^{-1}$ .**

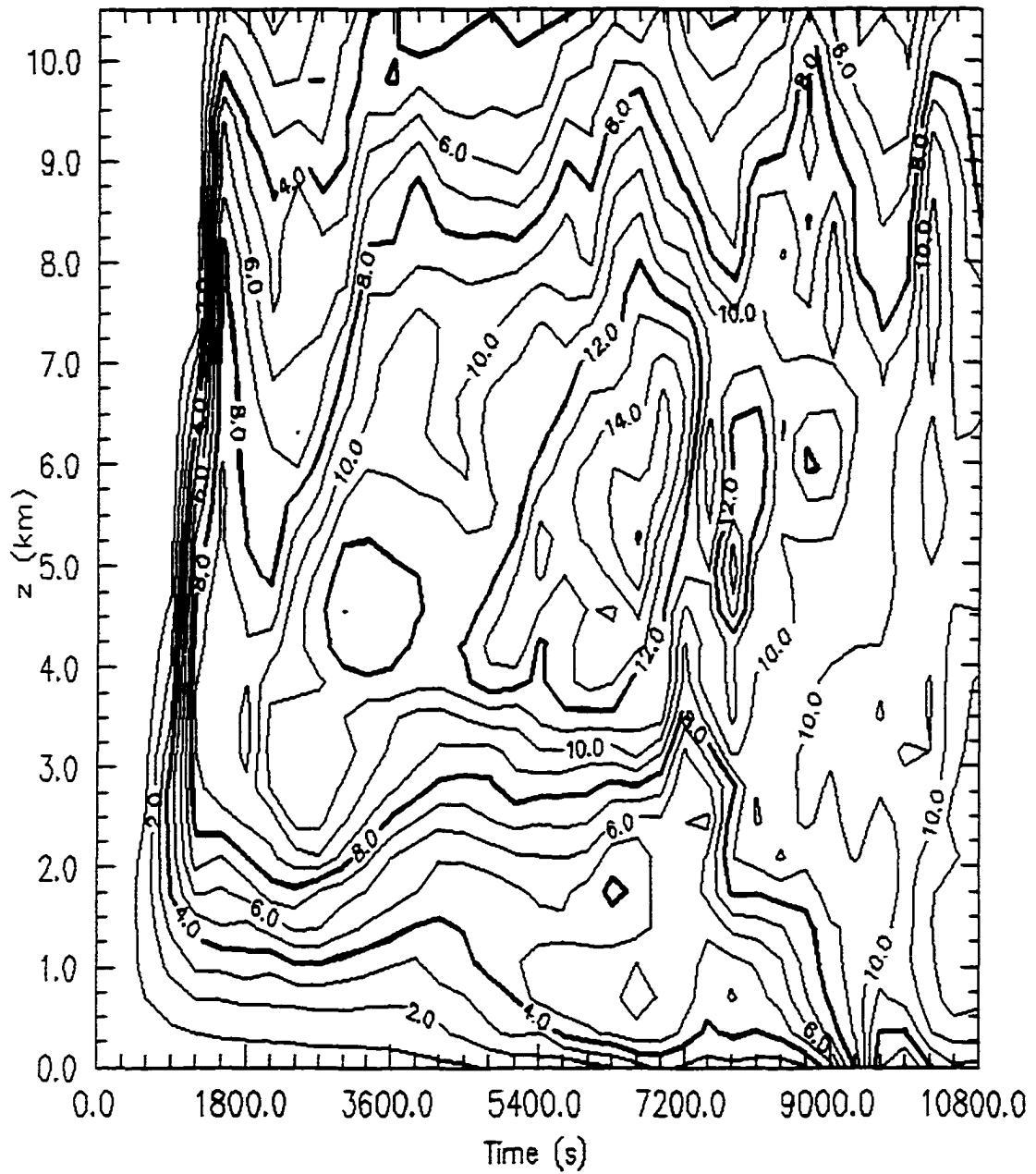


**Figure 4.59: Time-height diagram of maximum vertical vorticity ( $s^{-1}$ ) times 1000 for strong shear ( $U_x=30 \text{ m s}^{-1}$ ) control run with mixed layer  $qv=13 \text{ g kg}^{-1}$ .**

2.5 hours on and *does* reach significant values, at least for a short period of time, when the cell becomes more isolated and intensifies after 3 hours.

#### **4.4 Summary**

In a weak shear environment, inhomogeneous moisture skews the storm system toward the higher moisture region in time. This is explained through a feedback process in which preferred cell development due to a lower LFC leads to even greater preferential development as the cold pool also becomes skewed toward the high moisture region. This provides additional convergence to enhance the production of new cells. System motion is determined in part by individual cell motion along the mean wind and in part by new cell development on the high moisture flank, resulting in a motion at an angle to the shear vector, directed toward higher moisture.

In a strong shear environment, a storm can continue to survive when it moves into a region that could not produce a storm from inception. While the reasons for this have not been fully explored, we suspect this behavior is due in part to the lifting pressure gradient force on the flank of a rotating cell, which helps lift air to its LFC, and possibly due to the ability of the inflow low to draw in air from a higher moisture region.

Increased moisture also is found to increase updraft speed in a supercell, particularly when a cell is isolated. The influence of increased buoyancy in the updraft may not be directly apparent if cells are close together such that an adverse pressure gradient due to cell interference compensates for the increased buoyancy.

Low-level rotation is also found to have a response that depends on whether the cell is isolated. For a cell that does remain isolated, increased water vapor appears to amplify the low-level vorticity beyond that produced in the control run using the sounding from the initial location.

## **Chapter 5 Experiments with Inhomogeneous Environmental Shear**

There are many ways in which the shear can vary in a given observed environment, often as the result of specific mesoscale features present. However, this is often an intractable problem to analyze theoretically given the complexity of real environments and the concomitant variability of several environmental variables. Thus, it is often the case that no general conclusion is reached concerning, for example, the role of changes in environmental vertical shear over a storm's lifetime.

In this study, the focus is not on replicating observed features using real data, but instead on understanding the influence on storm structure of spatially-varying environments, the configuration of which is specified analytically in order to facilitate interpretation. Results are shown for both weak and strong shear environments, and for a case in which the vertical shear varies along the mean wind.

### **5.1 Analytic Environment Setup**

Many factors must be considered when attempting to specify an analytic environment with varying wind shear for use in a computer simulation. First of all, proper boundary conditions must be specified, and this is difficult if the environment evolves in a manner that does not permit an analytic solution in time. Even with an analytic solution in time, interpretation of changes following storm motion is more difficult if the environment is also changing in time. Real environments, of course,

do exhibit changes in time, and this can have a profound influence on storm development (e.g., Burgess and Curran, 1985).

Early in this study, simulations in which the shear was forced to vary temporally, rather than spatially, were examined (Richardson and Droegemeier, 1996). While the results were promising, there are a number of interesting questions that simulations of that nature cannot address even though changes in various quantities as the storm moves through an inhomogeneous environment could just as easily be cast as changes in time in the storm's reference frame. One of the most interesting questions concerns the alteration of storm propagation due to the inhomogeneities present. Specifying a change in time across the entire storm precludes study of this important question. Thus, we decided to pursue a steady-state solution with horizontally-variable shear instead. In the future, the two methods of investigation could be combined to produce even more comprehensive results.

The next consideration is the Coriolis force. When the Coriolis force is included, very few steady-state environments with horizontally varying wind shear are possible due to the concomitant variations in temperature and pressure across the domain. An unsteady, inhomogeneous environment initially in thermal wind balance, (i.e., with the Coriolis force included) was also attempted early in this study. However, although the results were interesting, they were also difficult to interpret because both vertical shear and CAPE were varying in a complex manner. The environment was also evolving slightly in time due to the advection of thermal

perturbations necessary for thermal wind balance, causing us to question the validity of our prescribed boundary conditions.

For all of these reasons, it became evident that more readily interpretable results were likely if the Coriolis force was neglected in our simulations. Its exclusion is justifiable for relatively short-lived phenomena (i.e., less than or equal to 4 hours) such that the perturbation winds are not significantly altered. In terms of the vorticity dynamics of the problem, the Coriolis force may be excluded if the tilting term is significantly larger than the stretching term associated with planetary vorticity (Davies-Jones, 1984). This will be true if

$$\left[ \frac{\partial w}{\partial z} f \right] / \left[ \frac{\partial w}{\partial y} \frac{\partial U}{\partial z} \right] \ll 1 \quad (5.1)$$

or, using scale analysis,

$$\frac{fD}{HS} \ll 1 \quad (5.2)$$

where S represents the shear of the environment (normally  $dU/dz$ ), D represents the horizontal scale of the storm, and H represents the vertical scale. For a severe storm,  $D/H=1$ , so the Coriolis force may be excluded as long as it is much smaller in magnitude than the shear. For the simulations to be presented, this condition is always satisfied and, thus, the Coriolis force is not included. Note that this scale analysis is not appropriate near the ground where  $w$  is zero but  $\partial w/\partial z$  is nonzero. Thus, conclusions regarding changes in very low-level vorticity will be made with caution.

Given that we desire an environment that remains steady without the Coriolis force, we must examine the momentum equations for an inviscid fluid in a non-rotating reference frame, given by

$$\frac{\partial \bar{v}}{\partial t} + \bar{v} \cdot \nabla \bar{v} = -\frac{1}{\rho} \nabla p - g \hat{k} \quad (5.3)$$

from which it is clear that a hydrostatic environment with no horizontal pressure gradients will be steady state if the advection terms are zero. The simplest environment satisfying this condition consists of the superposition of a horizontally-homogeneous base-state wind that is unidirectional with height, and a perturbation environmental wind that is parallel to it. The magnitude of this perturbation varies in the direction perpendicular to the wind direction (see Figure 5.1). (A setup somewhat similar to this was used by Skamarock et al. (1994b) to study the effect of environmental variability along a squall line. However, both the shear and CAPE varied in their study.)

The setup in Figure 5.1 is relatively easy to simulate and is completely flexible in the allowed magnitudes of the perturbations. However, it has the inherent drawback of allowing shear variations only in a direction perpendicular to the mean wind. Thus, a cell moving with the mean wind will not experience changes in the environmental shear over its lifetime. Despite this limitation, the configuration may be used to study the effect of changes in shear for storms that do not move with the mean wind, namely supercells. It can also be used to study the initiation of cells as a cold outflow boundary spreads laterally and encounters changing shear conditions.

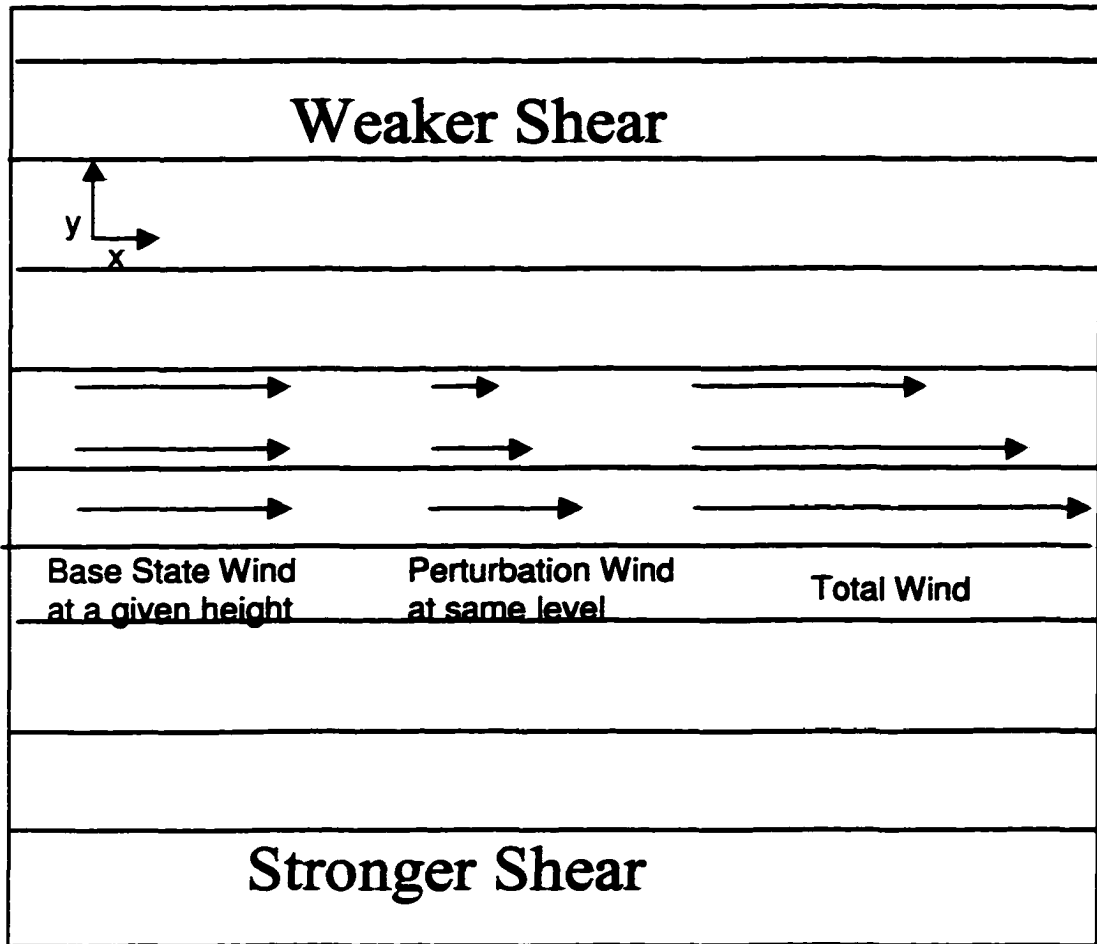


**Figure 5.1: Setup for inhomogeneous environment for unidirectional shear simulations. Thin lines indicate shear contours on an x-y cross section of the domain.**

Simulations for both of these situations are presented and an understanding of them is essential to the understanding of more complicated setups that follow.

An initial condition producing steady-state horizontal winds may be found in which the shear *does* vary in the direction of the mean wind over the cloud layer, thus allowing the shear to vary along the storm's motion vector. To determine this initial condition, we assume a linear variation of the winds so that we may write their horizontal components as

$$U = \bar{U} + ax + (e - q)y \quad (5.4)$$

and

$$V = \bar{V} + (e + q)x - ay \quad (5.5)$$

where '2a' and '2e' are stretching and shearing deformation, and '2q' represents the vertical vorticity. Each of these ('a', 'e', and 'q') can be functions of z but not x or y.

The variables U and V represent the total environmental winds, while  $\bar{U}$  and  $\bar{V}$  represent the horizontally-homogeneous base state component of the environmental winds. Note that this solution yields a non-divergent wind field. Although we recognize that convergence is present in most severe storm environments and may alter storm behavior significantly (Crook and Moncrieff, 1988), this is not the phenomenon of interest in this study. Including convergence in the environment is not necessary to achieve our goal of understanding of the influence of variable vertical shear on storm morphology.

Using (5.4) and (5.5), the equations of motion may be expressed

$$\frac{\partial U}{\partial t} = -U \frac{\partial U}{\partial x} - V \frac{\partial U}{\partial y} = -(\bar{U} + ax + (e - q)y)a - (\bar{V} + (e + q)x - ay)(e - q) \quad (5.6)$$

and

$$\frac{\partial V}{\partial t} = -U \frac{\partial V}{\partial x} - V \frac{\partial V}{\partial y} = -(\bar{U} + ax + (e - q)y)(e + q) - (\bar{V} + (e + q)x - ay)(-a) \quad (5.7)$$

which can be simplified to yield

$$\frac{\partial U}{\partial t} = [-\bar{U}a - \bar{V}(e - q)] + (a^2 + e^2 - q^2)x \quad (5.8)$$

and

$$\frac{\partial V}{\partial t} = [-\bar{U}(e + q) + \bar{V}a] - (a^2 + e^2 - q^2)y. \quad (5.9)$$

In order to obtain a steady-state solution, 'a', 'e', and 'q' must be chosen such that the right hand side sums to zero for both equations. Because x and y vary, and we are enforcing a steady state everywhere, we can set the terms in brackets to zero individually. Determining 'a' and 'e' requires the simultaneous solution of the two equations of motion, so that

$$a\bar{U} + \bar{V}(e - q) = 0 \quad (5.10)$$

$$(e + q)\bar{U} - \bar{V}a = 0 \quad (5.11)$$

yielding the condition,

$$\bar{V}^2(e - q) + \bar{U}^2(e + q) = 0 \quad (5.12)$$

from which e and q are related by

$$e = \frac{\bar{V}^2 - \bar{U}^2}{\bar{V}^2 + \bar{U}^2} q \quad (5.13)$$

The deformation 'a' is then given by

$$a = q \frac{2\bar{U}\bar{V}}{\bar{U}^2 + \bar{V}^2} \quad (5.14)$$

and 'q' is left as a free parameter. It can easily be shown that these values for 'e' and 'a' satisfy  $a^2 + e^2 - q^2 = 0$  so that the spatially dependent term is also zero for both wind components. Thus, a steady-state solution can be obtained for an arbitrary hodograph by specifying 'q' as a function of height and using the above relations for 'e' and 'a'.

Given a function for 'q', the horizontal wind components are determined by

$$U = \frac{2q\bar{U}}{(\bar{U}^2 + \bar{V}^2)} (\bar{V}_x - \bar{U}_y) + \bar{U} \quad (5.15)$$

and

$$V = \frac{2q\bar{V}}{(\bar{U}^2 + \bar{V}^2)} (\bar{V}_x - \bar{U}_y) + \bar{V} \quad (5.16)$$

where U and V represent the horizontal components of the base state wind field.

In effect, this solution represents patterns of wind perturbations such that the gradient of the wind is perpendicular to the wind direction at each level. Thus, the perturbation environmental winds are in the same direction as the base state winds.

In fact, the above result (5.15-5.16) can be derived based on this premise. For example, the north-south component of the wind must satisfy

$$V' = \frac{\bar{V}}{\bar{U}} U' \quad (5.17)$$

at each level to give the correct direction for the perturbations (in the same direction as the base state winds). Assuming that the perturbations vary linearly in  $x$  and  $y$  and do not vary along the wind direction (i.e., contour lines of  $U'$  and  $V'$  are straight and have a slope  $\bar{V}/\bar{U}$ ), the total wind must satisfy

$$\begin{aligned} U &= \bar{U} + g(\bar{V}_x - \bar{U}_y) \\ V &= \bar{V} + g\frac{\bar{V}}{\bar{U}}(\bar{V}_x - \bar{U}_y) \end{aligned} \quad (5.18)$$

where  $g$  is an arbitrary function of height. The vertical vorticity of this wind field is

$$\zeta = \frac{\partial V}{\partial x} - \frac{\partial U}{\partial y} = g\frac{\bar{V}^2}{\bar{U}} - g\bar{U} = 2g \quad (5.19)$$

If we solve for  $g$  in terms of  $q$  and substitute into (5.18), we obtain the same result as (5.15) and (5.16). Thus, at each level we are simply adding perturbation winds in the same direction as the base state winds and do not allow their magnitude to vary along the wind direction. The levels are then superimposed, with the largest gradients occurring at the level where  $q$  is a maximum. The simplified cases presented for straight hodographs are a subset of this solution.

## 5.2 Variable Vertical Shear in a Weak Shear Environment

We first examine shear variations in an environment where the base state shear is weak, such that storm evolution is dominated by redevelopments along the outflow from the original storm. In this case, a homogeneous environment would produce a redevelopment downshear from the initial storm, where the inflow and outflow winds most strongly oppose one another. With an inhomogeneous environment, the cold pool spreads into stronger shear on one side and weaker shear

on the other. We seek to discover if the shear variability will bias the redevelopments toward the strong shear flank of the storm rather than the downshear direction.

The analytic sounding devised by Weisman and Klemp (1982) is used to produce the base state thermodynamic and moisture profiles (Figure 5.2) with a mixed layer mixing ratio of  $14 \text{ g kg}^{-1}$ . The base state winds for this case are given by:

$$\bar{U} = 12 \tanh(z/z_s) \text{ m s}^{-1} \quad (5.20)$$

and the variations are given by

$$U' = \frac{10y}{y_s} (1 - \tanh(z/z_s)) \text{ ms}^{-1} \quad (5.21)$$

where  $y_s$  is 100 km and  $z_s$  is 3000 m. The domain used is  $90 \times 192 \times 20 \text{ km}^3$ , so  $U$  varies from  $2.4 \tanh(z/z_s) \text{ m s}^{-1}$  to  $21.6 \tanh(z/z_s) \text{ m s}^{-1}$  from the northern boundary to the southern boundary (Figure 5.3). (The multicell actually occupies less than half the domain, so the variations in shear across it are much smaller than those implied for the entire domain.) The domain translation is toward the east at  $8 \text{ m s}^{-1}$ .

This shear variation is associated with negative vertical vorticity in the environment. While we would prefer not to include vertical vorticity, it is unavoidable because we require a steady environment. However, in the present configuration, the shear is strongest on the right side, where we expect the cyclonic member of the original vortex couplet, while the environmental vorticity is anticyclonic. Thus, if anything, the environmental vorticity is acting to suppress the feature we are trying to observe. If we observe a favoring of the right side, it is likely to be *in spite of* the environmental vorticity rather than because of it.

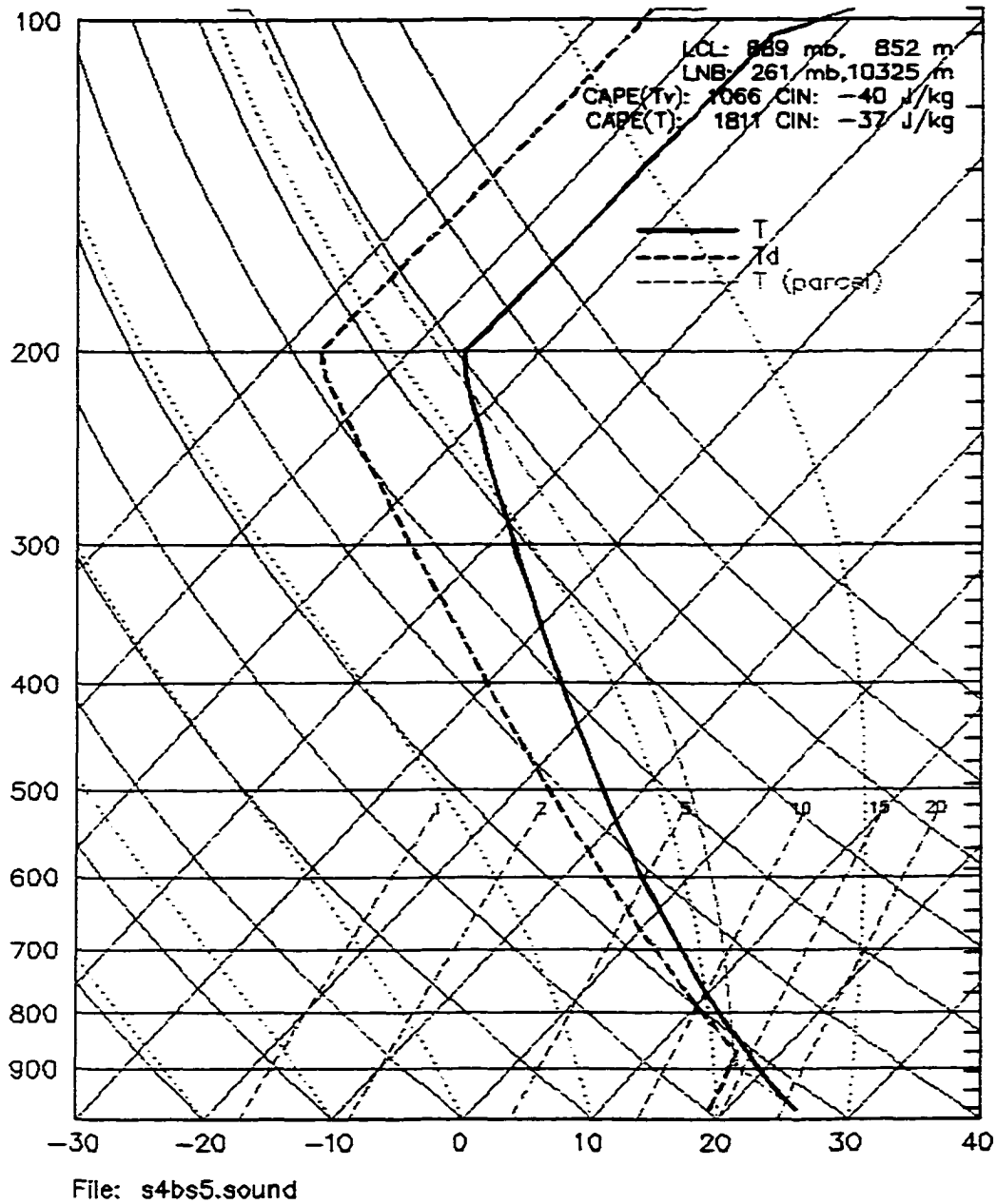


**Figure 5.2: Sounding used in inhomogeneous shear simulations. (based on Weisman and Klemp 1982)**

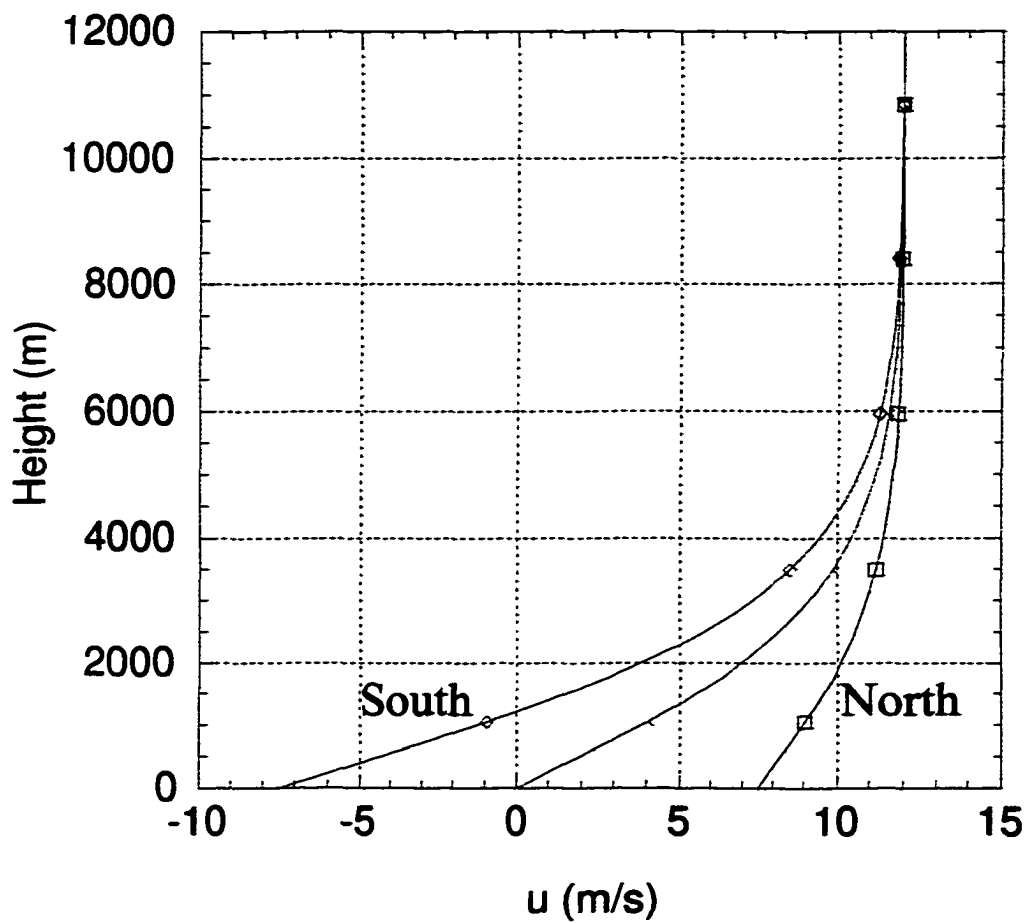
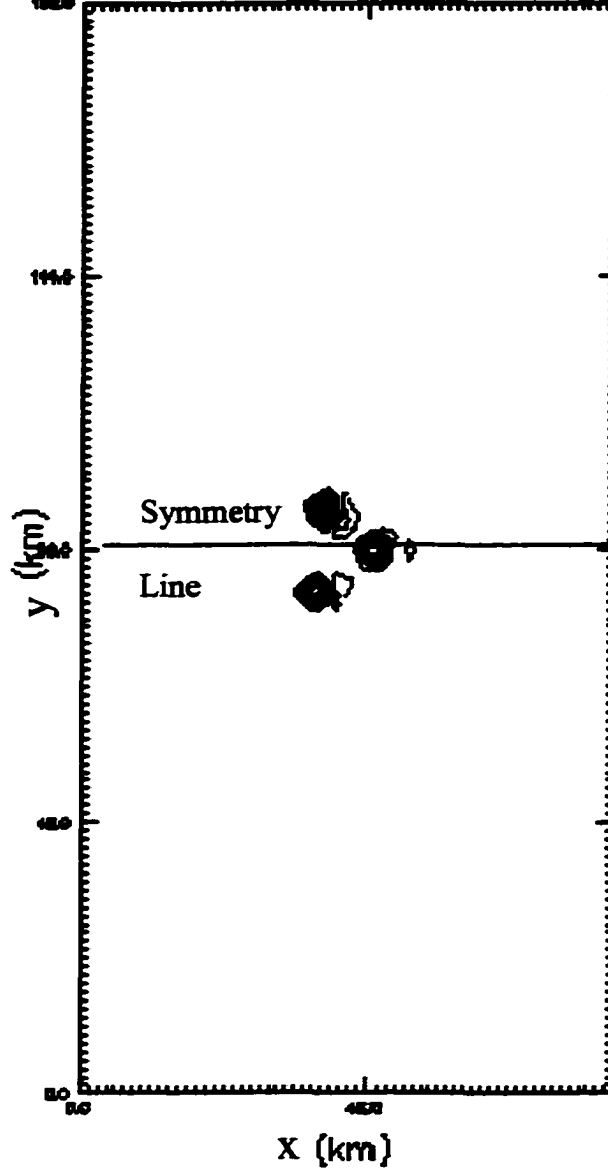


**Figure 5.3: Profile of east-west velocity component for inhomogeneous, unidirectional, weak shear experiments. The middle line represents the profile at the domain center, while the other two lines represent profiles at a distance 75 km to the north and south of the domain center.**

*Because everything else in the simulation is symmetric, any asymmetries that develop can be attributed to differences in the magnitude of the shear across the domain.*

When a storm is initiated in the center of the domain, Figure 5.4 shows that the resulting system remains quite symmetric for the first hour. By two hours, however, the system has developed noticeable asymmetries (Figure 5.5). At 2.5 hours (Figure 5.6), even more cells are present south of the original symmetry line. Figure 5.7 shows the surface divergence at the surface; the maximum convergence is clearly biased toward the southern flank where the shear, and thus the storm-relative winds, is greater and the cold pool is stronger and deeper (Figure 5.8). This increased convergence is presumably aiding in the development of new cells on this flank. However, the strongest updraft at any particular time is not necessarily on this flank. Thus, although cell development is enhanced, updraft strength is not. *A multicell system may become biased toward the higher shear region in terms of number of cells, with the strength of the updrafts remaining fairly uniform. This is in contrast to the variable CAPE experiments where both cell generation and cell strength were clearly biased to the high moisture flank.*

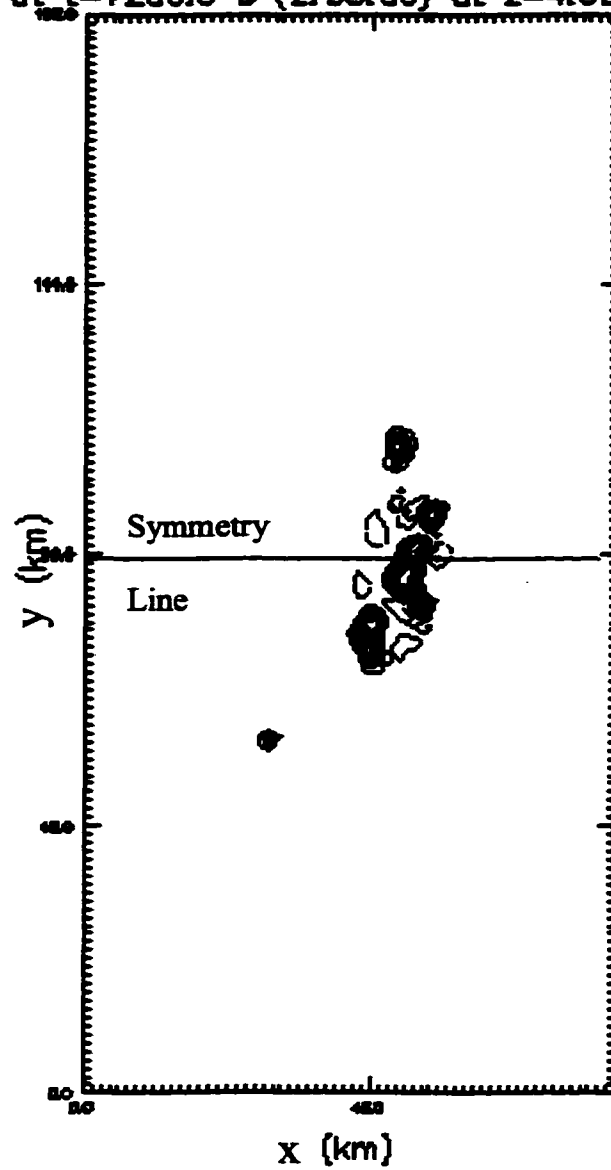
wprt (m/s) at t=4200.0 s (1:10:00) at z=4.600 km (contour)



Min=-5.19 Max=16.8 Inc=2.00 (contour)

Figure 5.4: Horizontal cross section of vertical velocity ( $\text{m s}^{-1}$ ) at  $z=4.6$  km at  $t=4200$  s for weak, unidirectional, inhomogeneous shear as in Figure 5.3.

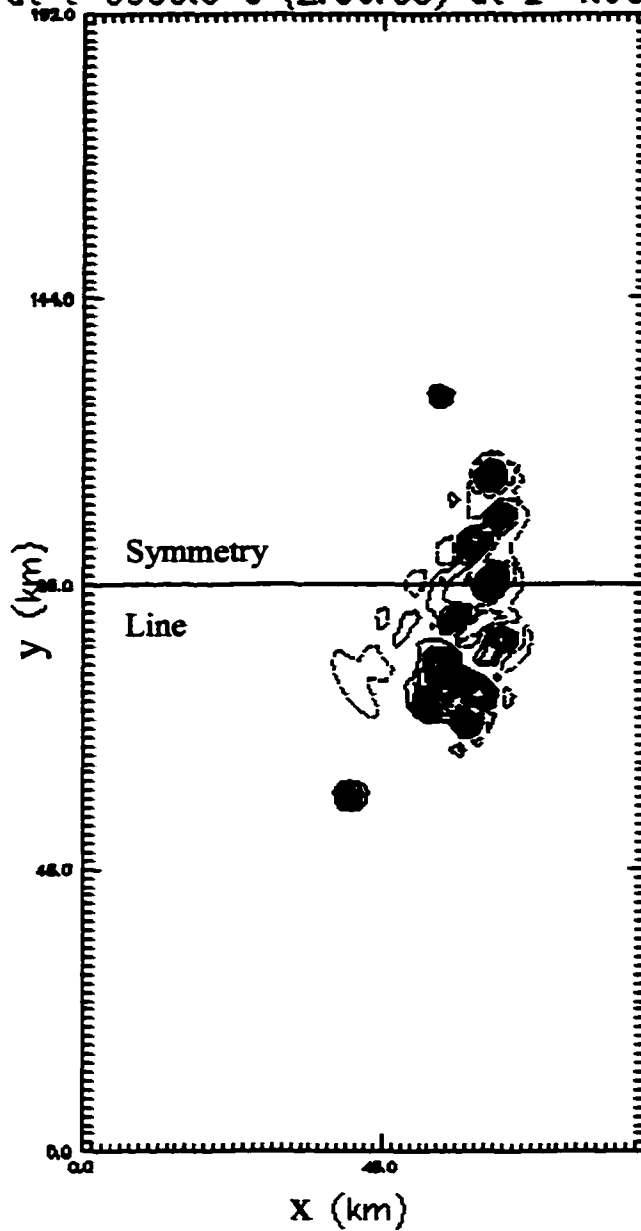
wprt (m/s) at t=7200.0 s (2:00:00) at z=4.600 km (contour)



Min=-4.67 Max=14.4 Inc=2.00 (contour)

**Figure 5.5: Horizontal cross section of vertical velocity at  $z=4.6$  km at  $t=7200$  s for weak ( $U_s=12$  m  $s^{-1}$ ), unidirectional, inhomogeneous shear as in Figure 5.3.**

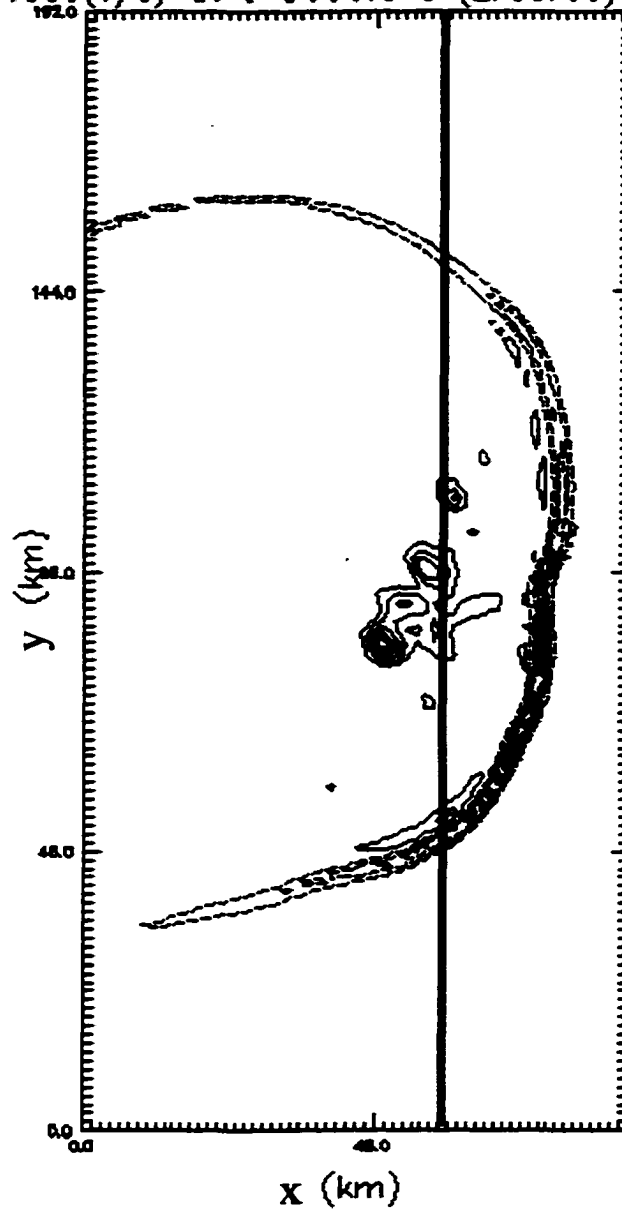
wprt (m/s) at t=9000.0 s (2:30:00) at z=4.600 km (contour)



Min=-7.40 Max=20.7 Inc=2.00 (contour)

**Figure 5.6: Horizontal cross section of vertical velocity at z=4.6 km at t=9000 s for weak, unidirectional, inhomogeneous shear as in Figure 5.3.**

Div.\*1000(1/s) at t=9000.0 s (2:30:00) at surface



Min=-11.4 Max=10.5 Inc=2.00 (contour)

**Figure 5.7: Surface divergence (negative values dashed) at 9000 for weak, unidirectional, inhomogeneous shear as in Figure 5.3. Thick solid line indicates location of cross section shown in the following figure.**

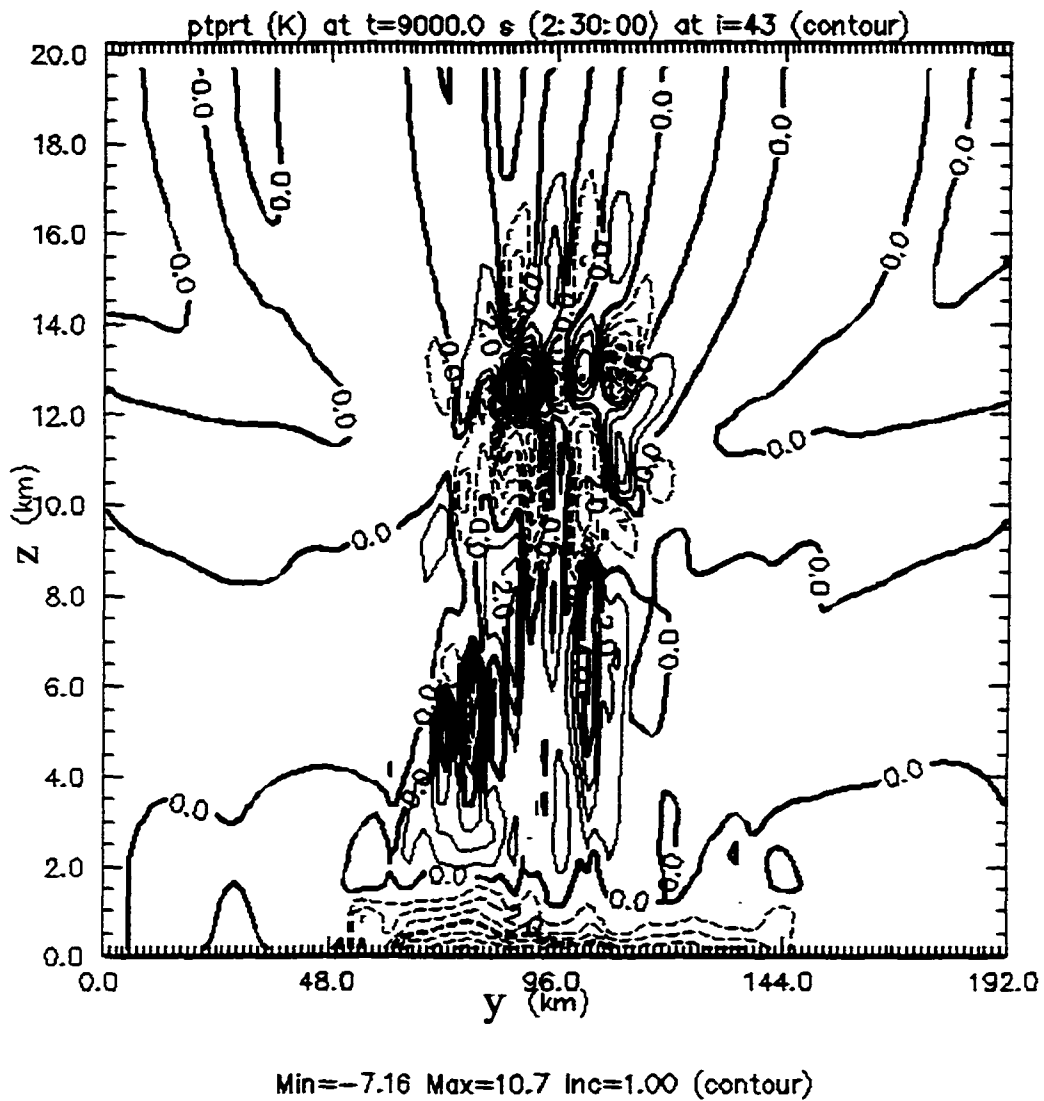


**Figure 5.8: Vertical (y-z) cross section of potential temperature for weak, unidirectional, inhomogeneous shear as in Figure 5.3.**

### 5.3 Variable Vertical Shear in a Strong Shear Environment

We now examine a similar configuration, but with a stronger base state vertical shear. The base state hodograph used in this simulation is given by

$$\bar{U} = 22 \tanh(z/z_s) \text{ ms}^{-1} \quad (5.22)$$

and the variations are given by

$$U' = \frac{10y}{y_s}(1 - \tanh(z/z_s)) \text{ ms}^{-1} \quad (5.23)$$

The environmental perturbation wind magnitude varies by  $10 \text{ m s}^{-1}$  over  $y_s = 100 \text{ km}$  at the ground and falls to zero aloft, with  $z_s = 3000 \text{ m}$ . This corresponds to an environmental vorticity value of  $-\partial U / \partial y = -10^{-4} \text{ s}^{-1}$  at the ground. The profile of  $U$  at the domain center, as well as  $\pm 75 \text{ km}$ , is shown in Figure 5.9. The domain translation is toward the east at a speed of  $17 \text{ m s}^{-1}$ .

The analytic sounding devised by Weisman and Klemp (1982) is again used to produce the base state thermodynamic and moisture profiles (Figure 5.2), with a mixed layer mixing ratio of  $14 \text{ g kg}^{-1}$ . The base state, therefore, corresponds to the Weisman and Klemp (1982)  $U_s=22 \text{ m s}^{-1}$  case and produces a split pair of storms as well as a secondary redevelopment along the symmetry axis in the downshear direction. This value of shear is purposely somewhat marginal for producing a supercell storm so that, given the variation prescribed by (5.23) and the expected cell motion, the left moving cell will reach the vertical shear values normally associated with multicells. Conversely, the right cell will encounter vertical shear that is increasingly favorable to supercell development over its lifetime. If the initial storm

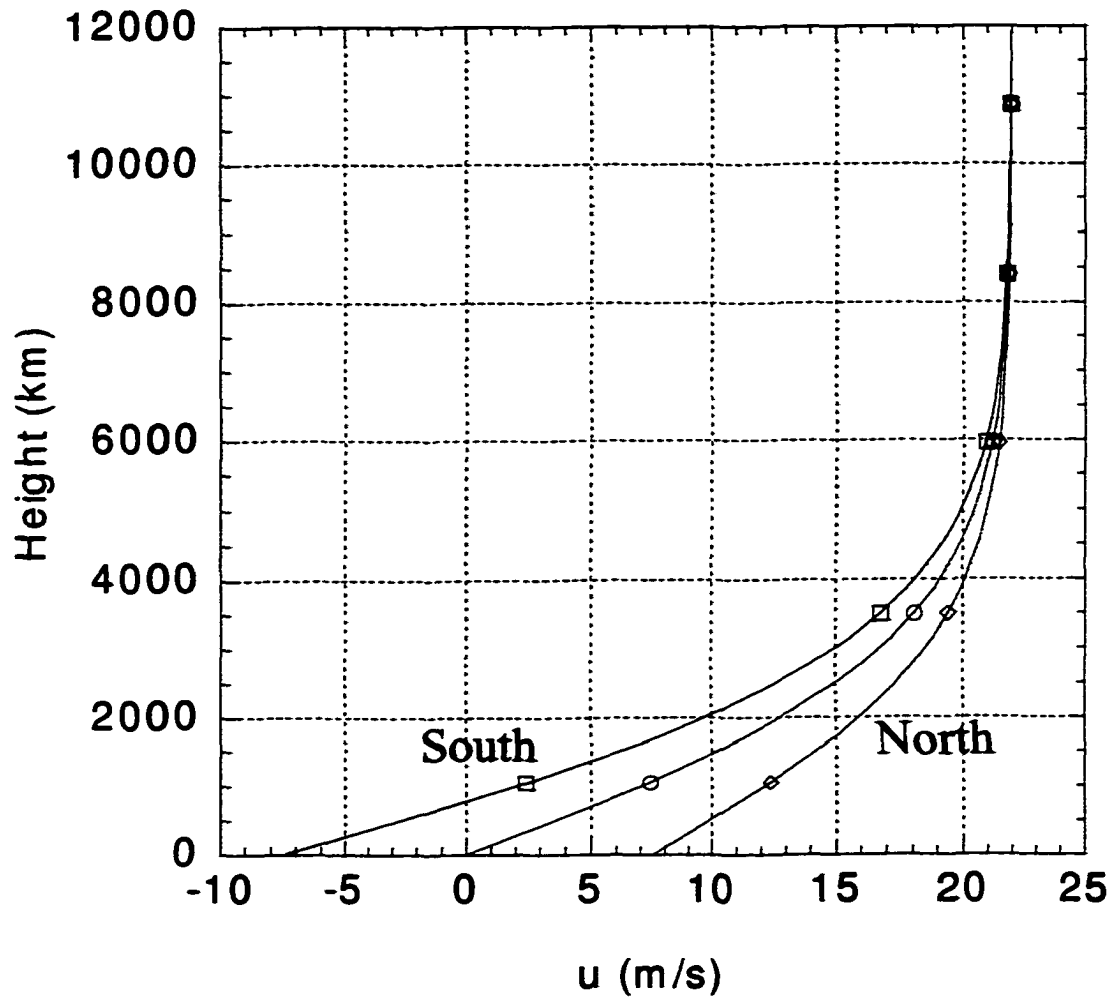


**Figure 5.9: Profile of east-west velocity component for inhomogeneous, unidirectional, strong shear experiments. Middle line corresponds to the profile at the domain center, while the other two lines represent profiles at locations 75 km to the north and south of the domain center.**

were started in a strongly sheared environment, the variability in the environment would not be great enough to cause significant changes in expected storm type as the cells move apart.

Figure 5.10 shows the vertical velocity at  $z=4.6$  km for the inhomogeneous simulation at 2 hours. The system has remained fairly symmetric in lateral extent, but the updraft furthest to the south has the greatest degree of organization and is highly correlated with vertical vorticity (Figure 5.11). At three hours, this cell has become a bow echo (Figure 5.12) while the northern flank exhibits multicell behavior. The lateral extent of the system is greater to the north, where the shear is weaker, but the shear is still sufficient for new cell generation. Thus, in this case, the effect of the shear variation is to bias new cell development toward the *weaker* shear flank while increasing the *organization* of cells to the south.

wprt (m/s) at t=7200.0 s (2:00:00) at z=4.600 km

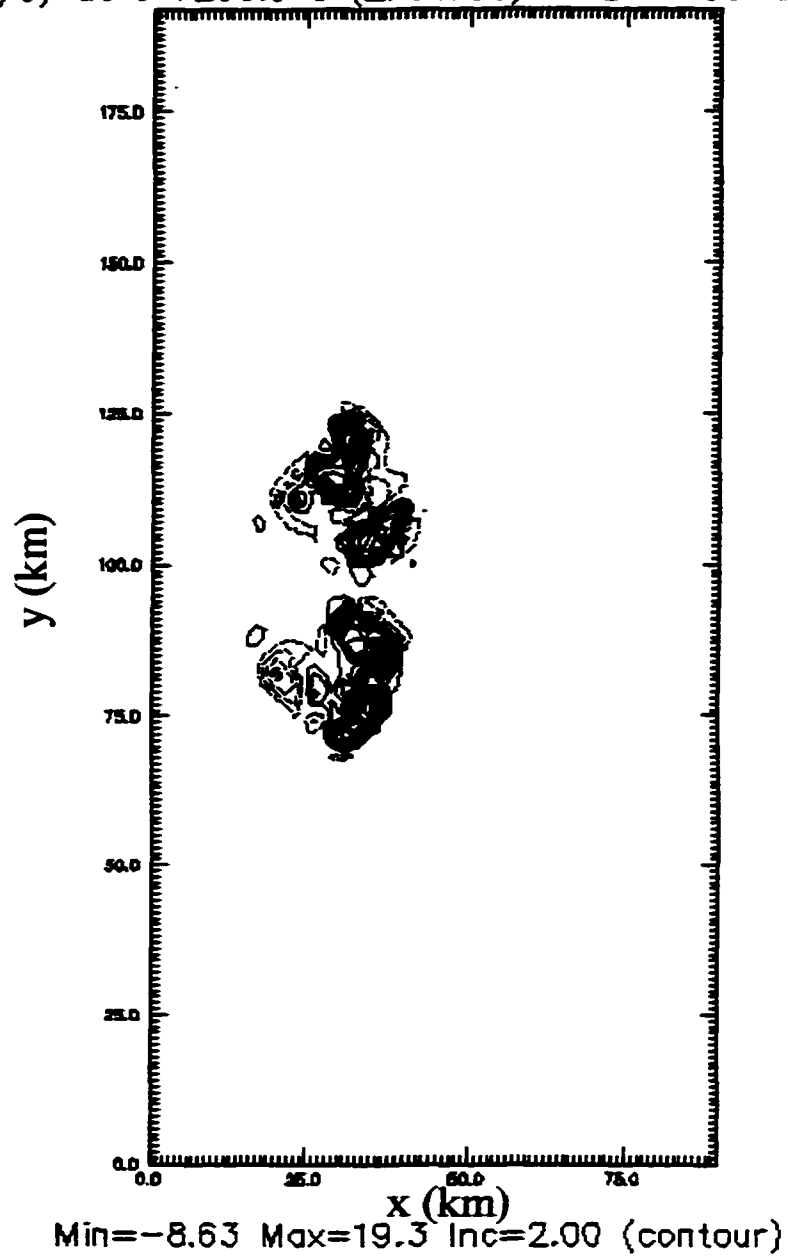


**Figure 5.10: : Vertical velocity at  $z=4.6$  km and  $t=2$  hours for strong shear ( $U_s=22$  m s<sup>-1</sup>), unidirectional shear case as in Figure 5.9.**

Vort\*10<sup>5</sup>(1/s) at t=7200.0 s (2:00:00) at z=4.600 km

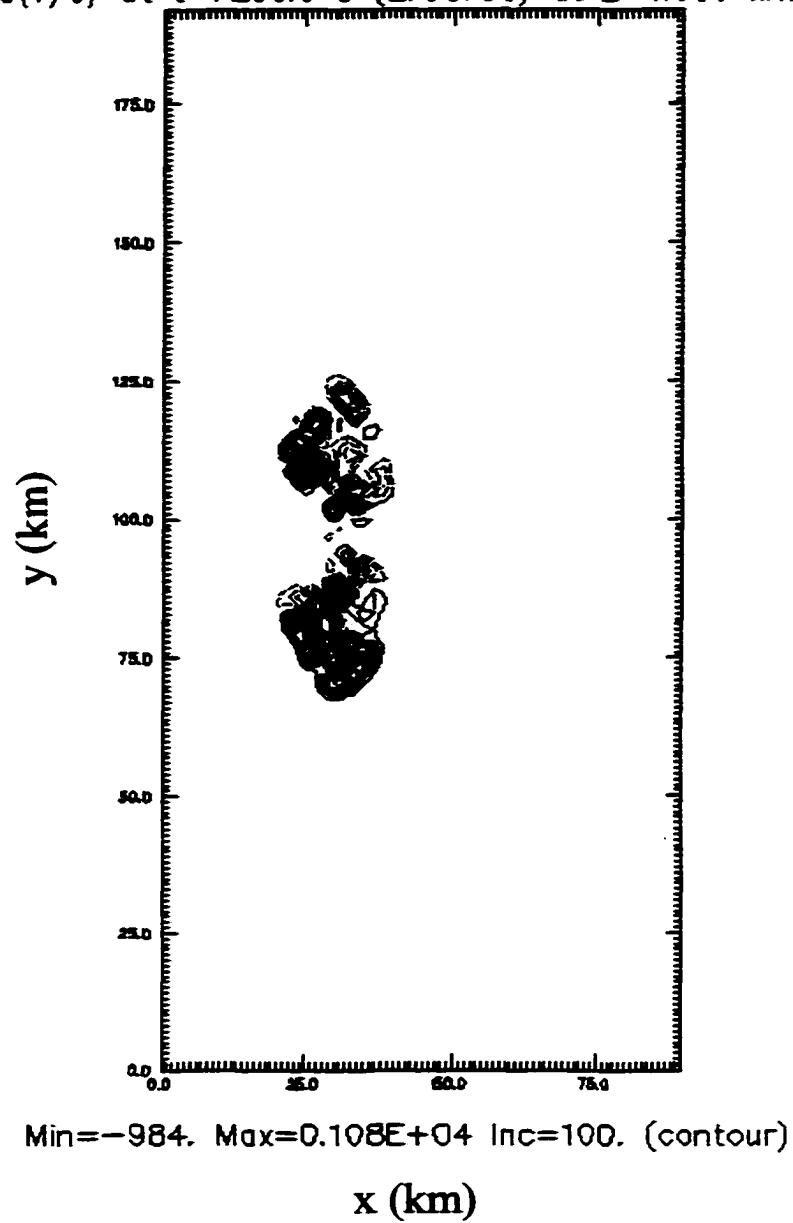


**Figure 5.11 Vertical vorticity ( $s^{-1}$ ) multiplied by  $10^5$  at  $z=4.6$  km and  $t=2$  hours for strong ( $U_s=22$  m  $s^{-1}$ ), inhomogeneous, unidirectional shear case as in Figure 5.9.**

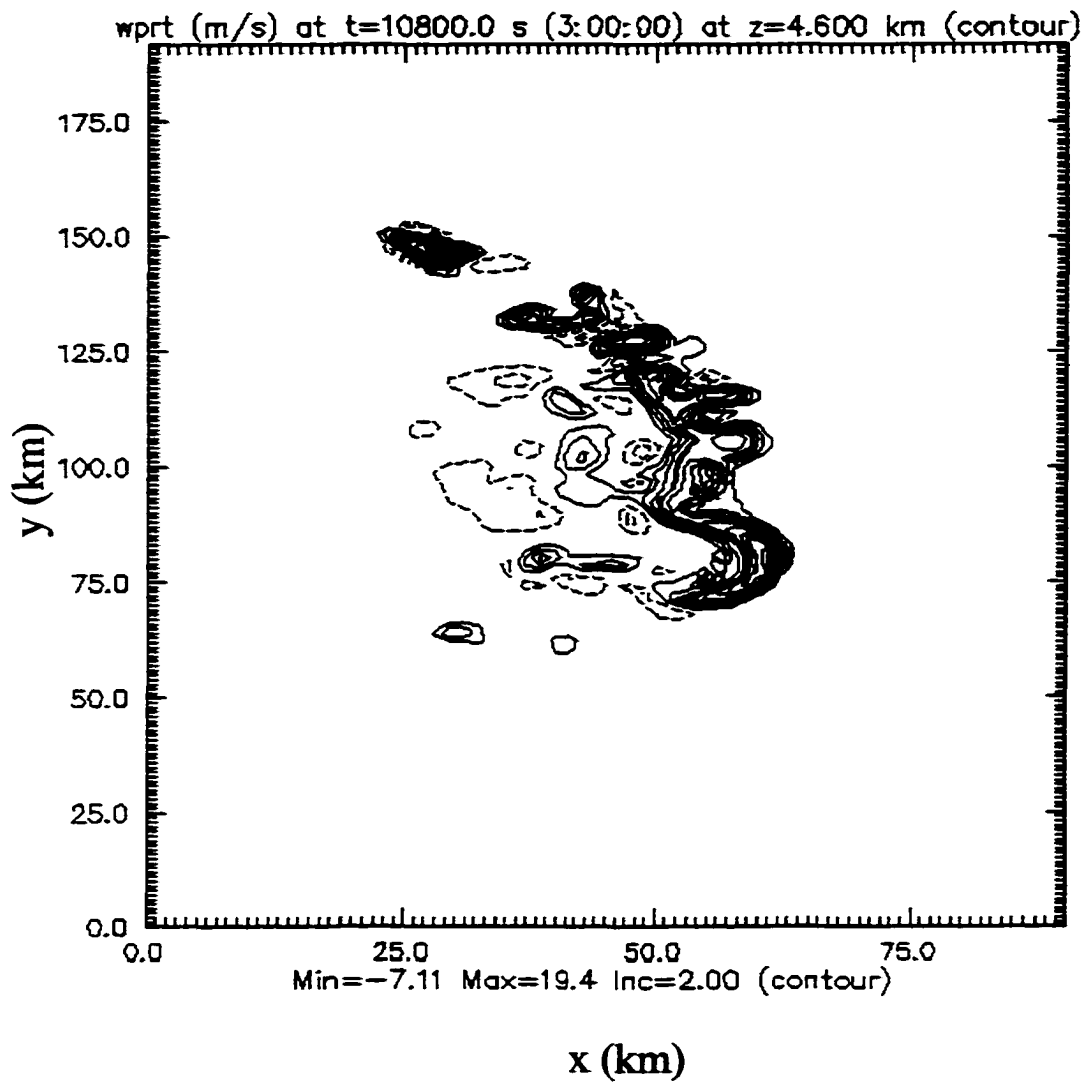


**Figure 5.12 Vertical velocity at  $z=4.6$  km and  $t=3$  hours for strong ( $U_s=22$  m s<sup>-1</sup>), unidirectional shear case as in Figure 5.9. (Note the aspect ratio is exaggerated in this plot).**

#### **5.4 Variable Vertical Shear Along the Mean Wind**

The previous shear configurations, though enlightening, have an important limitation: the shear can vary only in the direction perpendicular to the wind. This prevents study of storm system behavior when the entire system moves into stronger shear. To overcome this limitation, we now configure the environment such that the shear changes along the mean wind. We use it to examine a multicell storm system that encounters increasing shear over its lifetime.

We accomplish this using (5.15) and (5.16) with carefully determined profiles for  $U$ ,  $V$ , and  $q$ . In order to achieve changes in the shear along the direction of the mean wind, the perturbations to the homogeneous base state wind must be maximized at a level where the wind direction is different than that of the mean wind. We wish to examine the influence of variations in low to mid level shear, and these can be achieved using wind perturbations maximized at either low or middle levels. If they are maximized at middle levels, however, the expected storm motion is nearly parallel to the shear contours and a storm moving with the mean wind experiences little change in shear over its lifetime. Thus, we place the maximum wind variation near the ground and use a hodograph in which the surface and mean wind have different orientations.

Although it is true that a steady state solution can be devised for an arbitrary hodograph and arbitrary specification of vertical vorticity with height, care must be taken to ensure that the resulting hodographs across the domain are at least fairly realistic. For example, certain choices of 'q' profiles and hodographs will result in

undesirable jet structures in the wind field. While these features can certainly appear in nature, their influence in a simulation is unclear and peculiar hodograph shapes often result in unexpected results. Thus, it is desirable to limit the hodographs to fairly smooth shapes throughout the simulation domain.

This can be achieved by specifying the *desired* vertical profile for one wind component at a particular point in the domain and then solving ‘backward’ for the necessary ‘q’ profile. This vertical wind profile can only be specified for one of the velocity components; the other will then be determined by the base state hodograph together with (5.15) or (5.16). Because the variations in U and V are linear, at some distance from the origin the shear will become great enough that the environment will be dynamically unstable. For this reason, it is very important to prevent the computational domain from extending into these regions.

After much trial and error a viable environment for our purposes was determined by specifying

$$V' = \frac{2q\bar{V}}{\bar{V}^2 + \bar{U}^2} (\bar{V}x_s - \bar{U}y_s) = \Delta V(1 - \tanh(z/z_s)) \quad (5.24)$$

where  $\Delta V$  is chosen to produce the desired change in shear at some point  $(x_s, y_s)$ .

The solution specified in this manner will have a reasonable vertical profiles for V where  $(x,y) < (x_s,y_s)$ . The profile can still be unreasonable for U, however, if  $\bar{U}$  and  $\bar{V}$  have vastly different values. Thus, the hodograph used must have similar values for the two velocity components in order to avoid generation of unrealistic profiles across the domain, but must also have a significant change in wind direction with

height in order to generate shear perturbations that are along the mean wind. It also must have a sufficiently large mean wind so that a storm traverses a significant distance over its lifetime. Very few wind profiles satisfy all of these constraints. The hodograph chosen is thus a compromise in which the relatively small angle between shear variations and the mean wind is compensated by a large mean wind speed, reasonable hodograph variations, and stability of the environment.

The base state wind components are given by

$$\bar{U} = 18 \tanh(z/z_s) + 5 \text{ m s}^{-1} \quad (5.25)$$

$$\bar{V} = \bar{U} + 6 \text{ m s}^{-1} \quad (5.26)$$

where  $z_s$  is set to 3000 m. By specifying a change in shear of  $45 \text{ m s}^{-1}$  at  $x_s=300 \text{ km}$  and  $y_s=-300 \text{ km}$ , the profile for  $q$  is given by

$$q = \frac{-45(1 - \tanh(z/z_{\text{def}}))(\bar{V}^2 + \bar{U}^2)}{2\bar{V}(\bar{V}x_s - \bar{U}y_s)} \quad (5.27)$$

where  $z_{\text{def}}$  is 3000 m. This produces a change in shear, as measured by the 'u' term in the BRN, shown in Figure 5.13. This figure also shows the computational domain ( $150 \times 150 \times 20 \text{ km}^3$ ) and its position within this larger environment over the four-hour integration. Hodographs valid in the computational domain at three times are shown in Figure 5.14. The domain translation ( $u_{\text{grid}}, v_{\text{grid}}$ ) is (17,23) from 0 to 2.5 hours, (23,29) from 2.5 to 3.5 hours, and (23,19) from 3.5 to 4 hours.

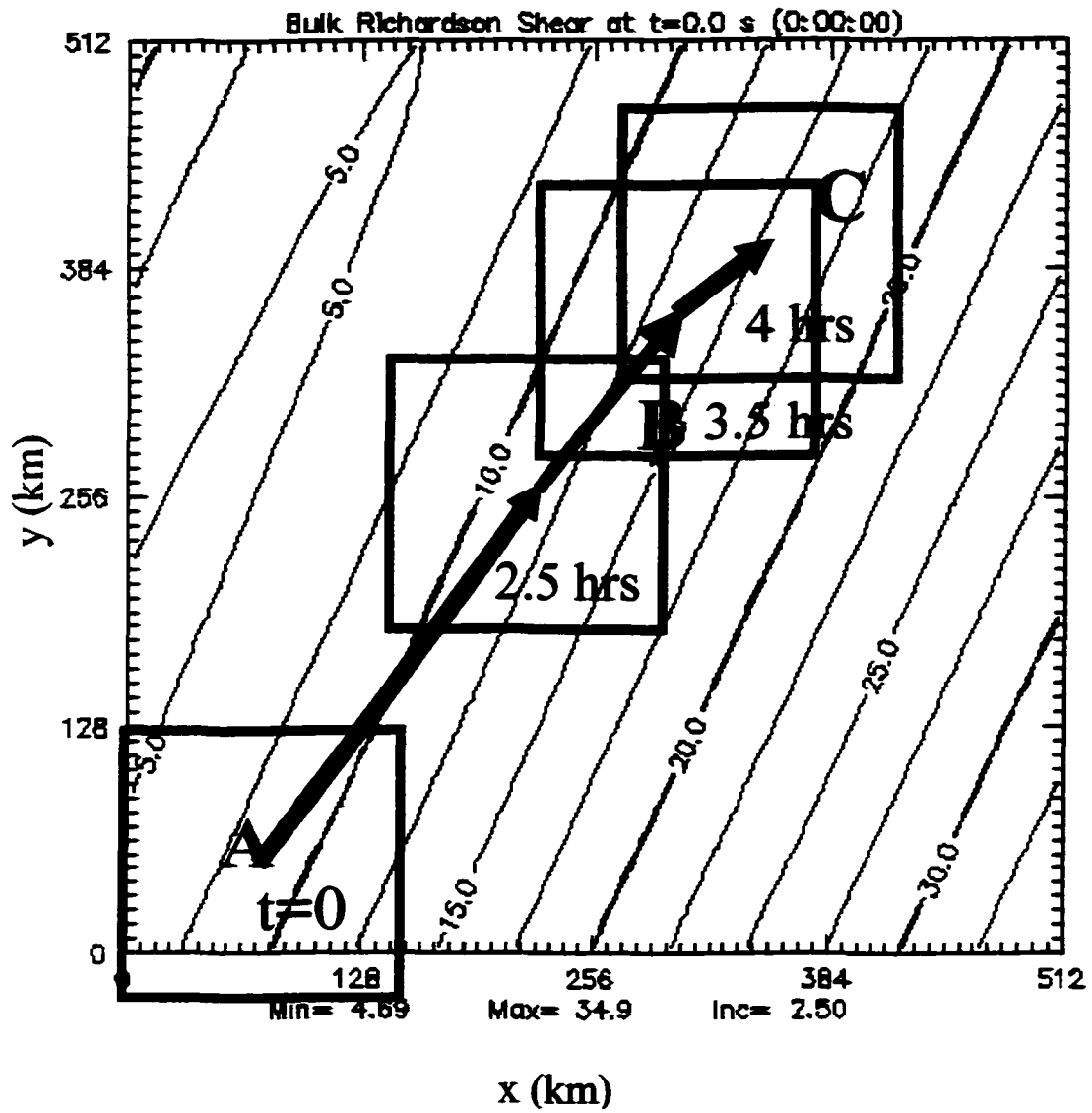


**Figure 5.13: Variation of the  $u$  term in the Bulk Richardson Number for the environment in which shear varies along the mean wind. Computational domain location at 0, 2.5, 3.5, and 4 hours is shown.**

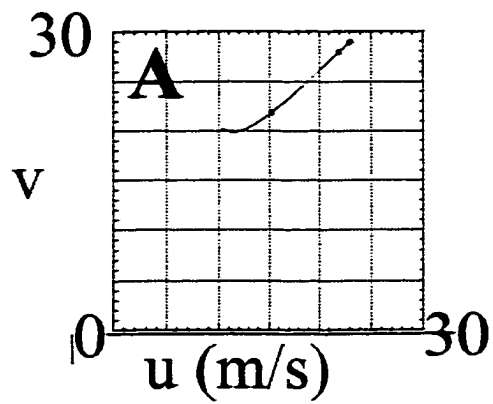
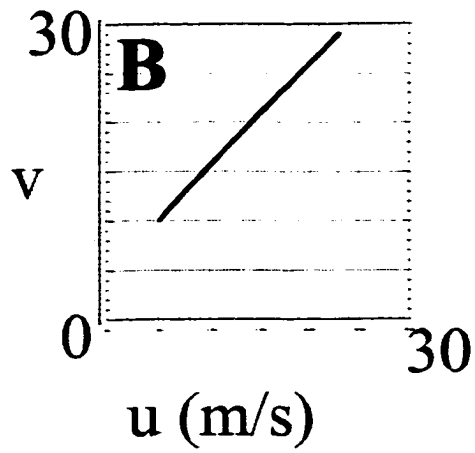
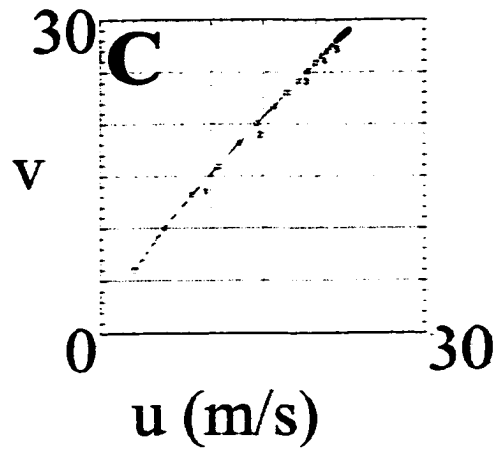


**Figure 5.14: Hodographs for domain locations as shown in Figure 5.13.**

To aid our interpretation of the change in storm behavior due to the change in shear, we first perform a *homogeneous* simulation using the sounding valid at the storm initiation location. In this simulation, the initial cell splits, with slight favoring of the left-moving cell as expected given the counterclockwise curvature in the hodograph. New cells develop quickly along the gust front so that, by 2.5 hours, the system is very multicellular (Figure 5.15). This behavior continues in a classic pattern for the duration of the simulation, as shown in Figure 5.16 at  $t=4$  hours. The domain motion is the same as the inhomogeneous simulation.

We compare this experiment with another homogeneous simulation using a sounding corresponding to the  $t=3$  hour position of cells in the inhomogeneous domain (profile B in Figure 5.14). The domain motion for this control run is (17,23) from 0 to 3 hours and (23,19) from 3 to 4 hours. The behavior using this sounding is quite different, with the original right-mover transforming to a bow echo by 2.5 hours (Figure 5.17). The storms in this simulation show a great deal of organization compared with those in the first control run. The compelling question is whether a storm initiated in the original weak shear environment and moving into the new strong shear environment will also become organized, or if it will continue to exhibit a disorganized, multicellular structure.

The answer is shown in Figure 5.18 for the inhomogeneous environment simulation at 2.5 hours. The cell to the south is in stronger shear than the cell to the north and is much better organized. This is very similar to the idealized simulation with a straight hodograph and a shear variation across the storm. The shear has a

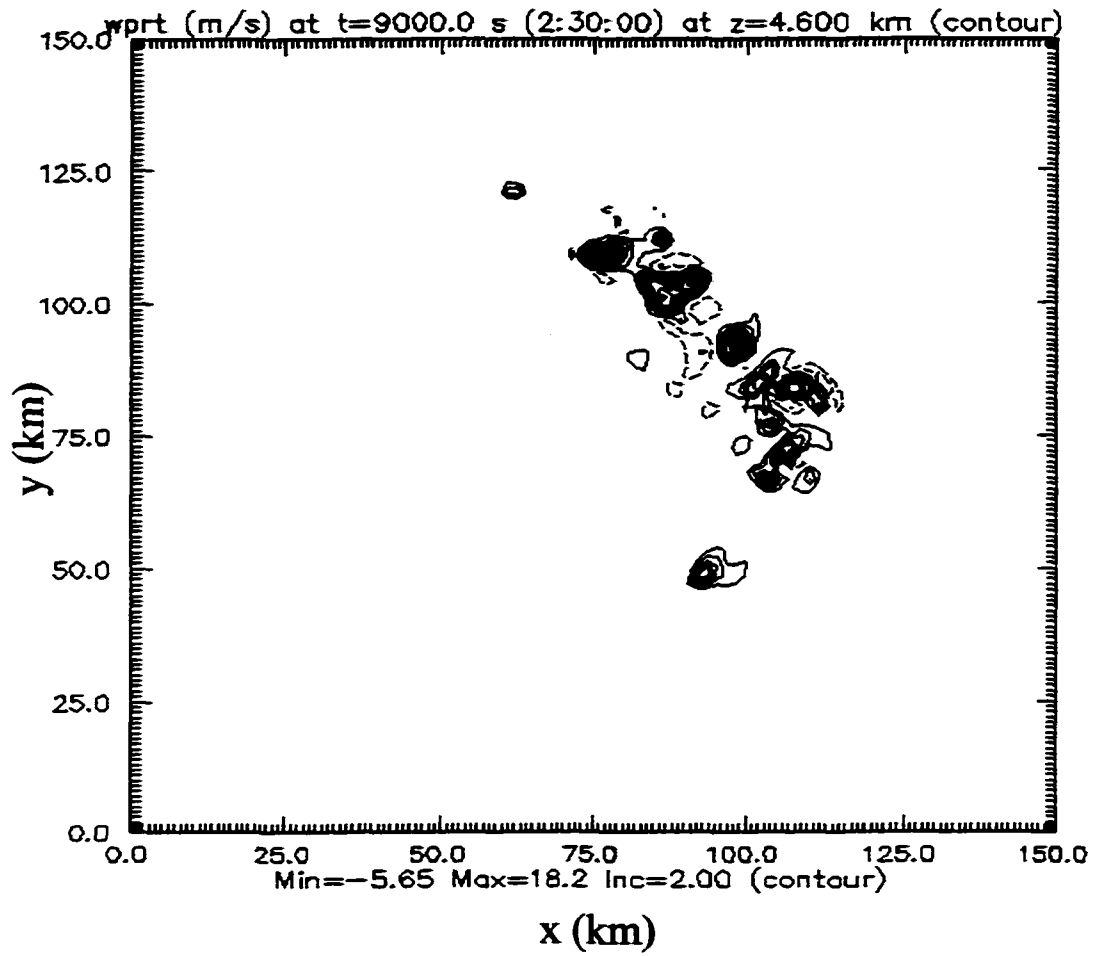


**Figure 5.15: Horizontal cross-section of vertical velocity at  $z=4.6$  km for weak shear (profile A in Figure 5.14) homogeneous control run at  $t = 2.5$  hours.**

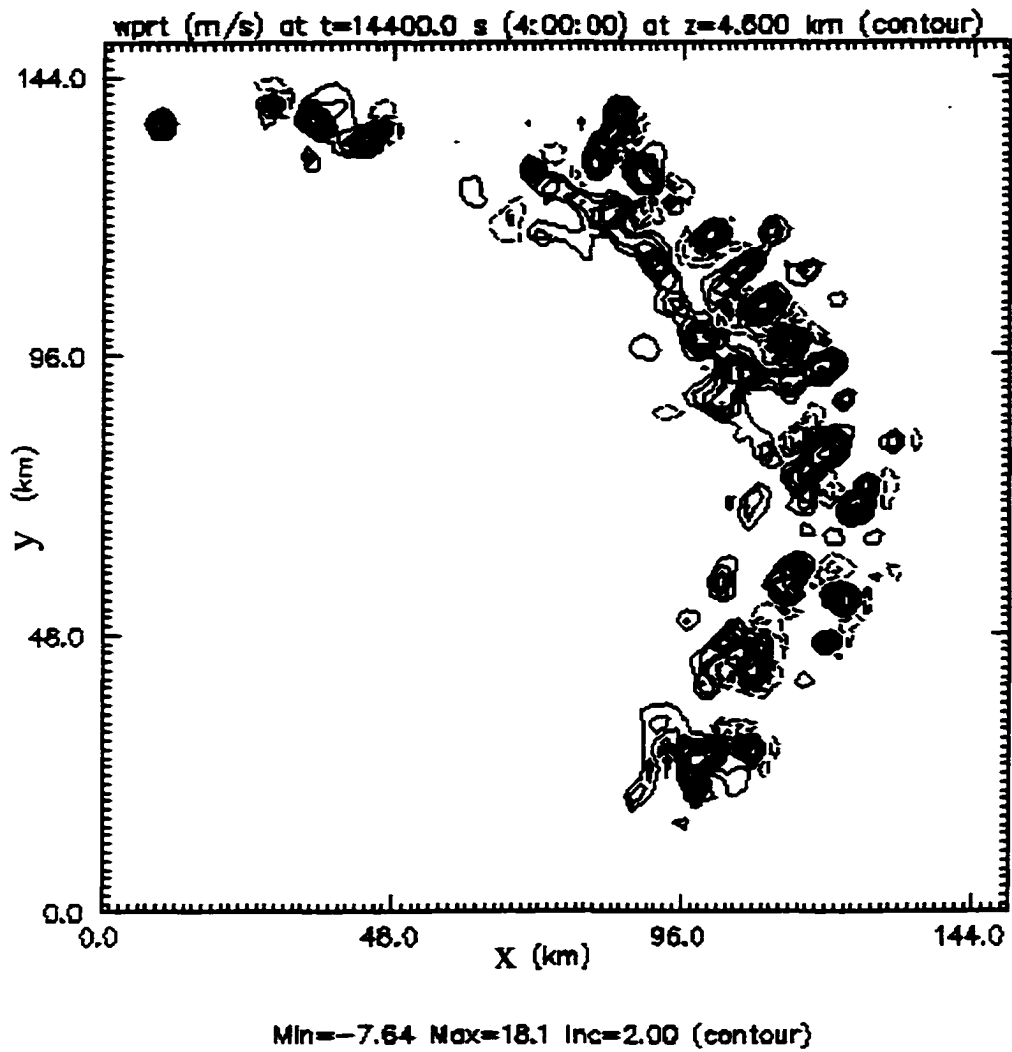
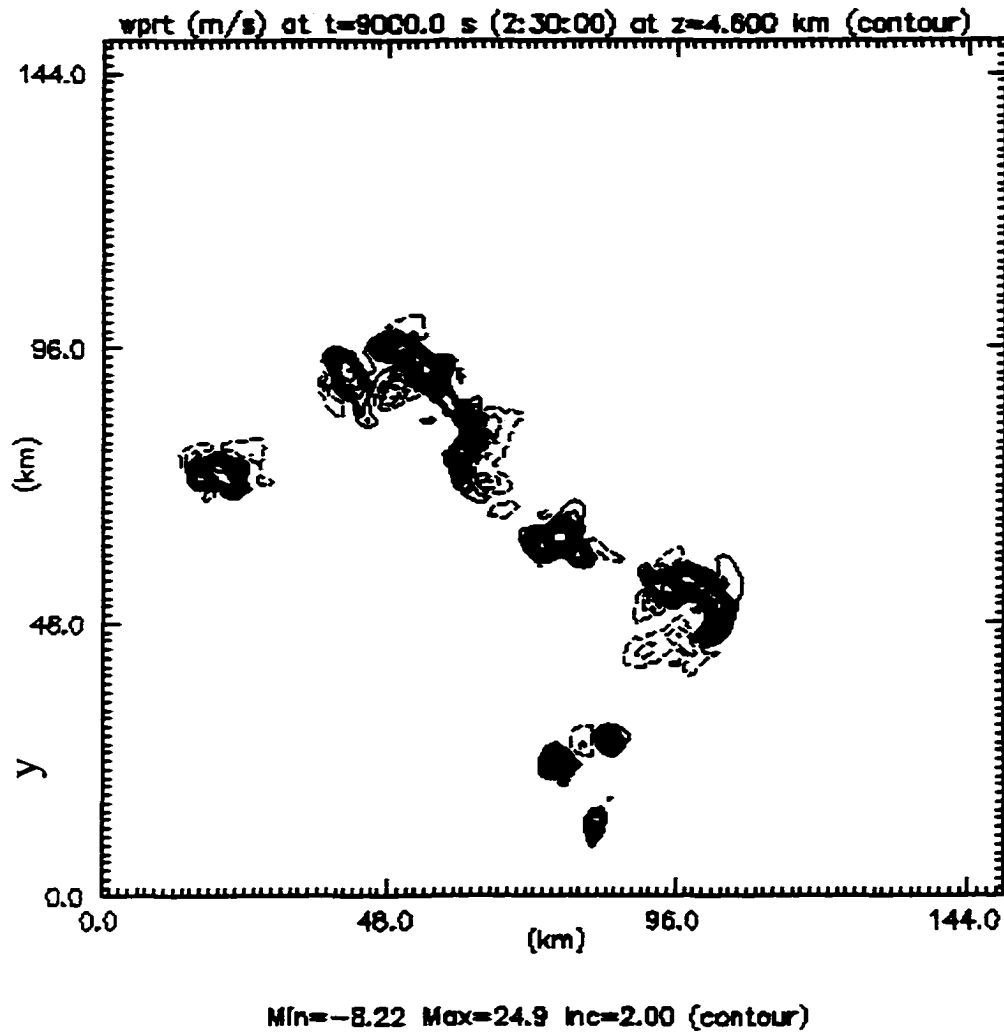


**Figure 5.16: Horizontal cross-section of vertical velocity at  $z=4.6$  km at  $t=4$  hours for homogeneous control run using sounding from initiation location in inhomogeneous domain (profile A in Figure 5.14.).**



X

**Figure 5.17: Horizontal cross section of vertical velocity ( $\text{m s}^{-1}$ ) at  $z=4.6$  km at  $t=2.5$  hours for homogeneous control run using sounding from the location B (297.6, 296.4) in the inhomogeneous environment shown in Figure 5.13.**

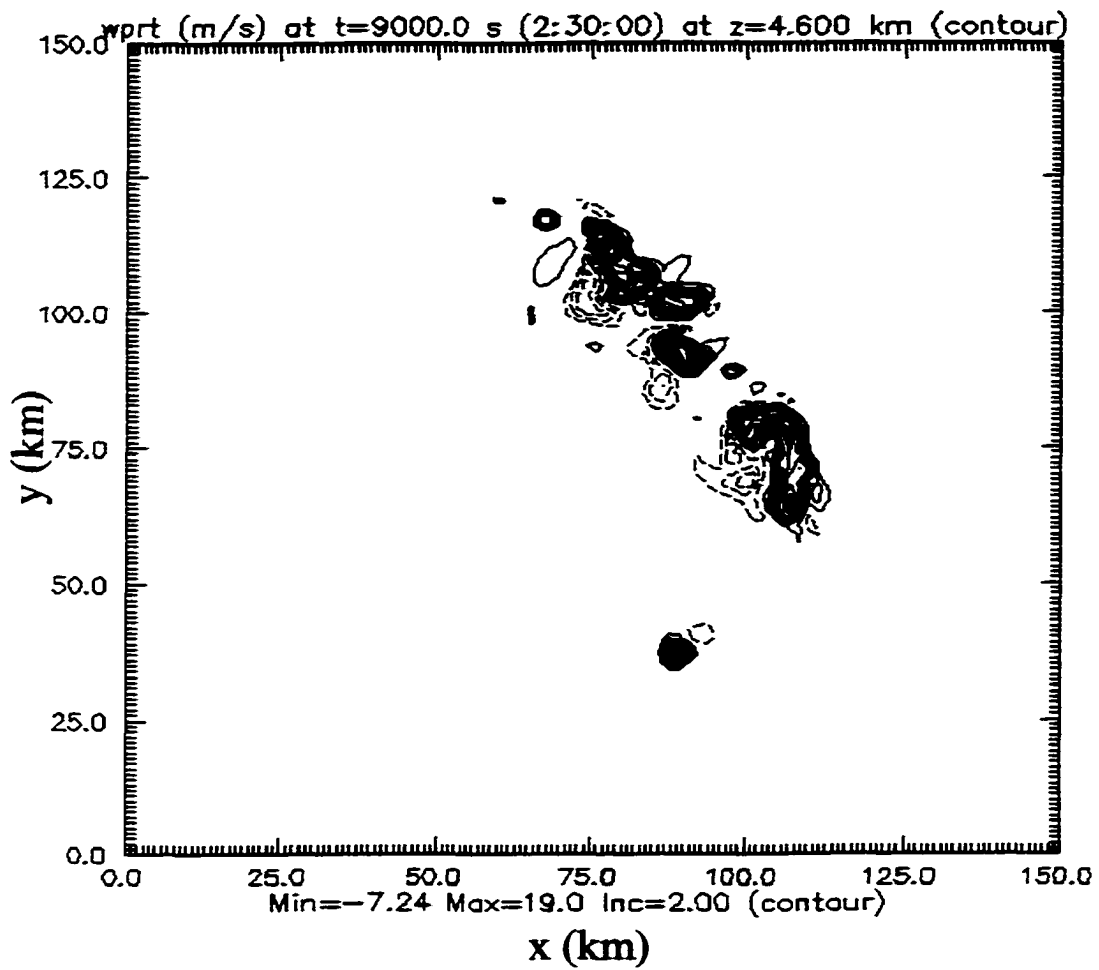


**Figure 5.18: Horizontal cross-section of vertical velocity at  $z=4.6$  km at  $t=2.5$  hours for inhomogeneous simulation with shear varying along the mean wind as in Figure 5.13.**

similar organizing influence in this simulation. In this case, the increased shear allows the original right-moving cell to maintain its position along the gust front much longer than in the weak shear control run, and with much larger vertical vorticity (compare Figure 5.20 and Figure 5.19).

The right-most cell then splits into a bow echo and a strongly rotating cell at approximately 3 hours (Figure 5.21), while the left side of the system continues to exhibit a more disorganized, multicellular pattern. As the entire system continues to move into increasing shear, the disorganized cells at the nose of the gust front combine to form another bow echo (Figure 5.22). Comparing this to the control run from the original location (Figure 5.16), we must conclude that *the change in shear over the lifetime of the storm system has had a profound impact on the storm structure*. The dynamics governing this transition in storm structure will be the subject of much future research.

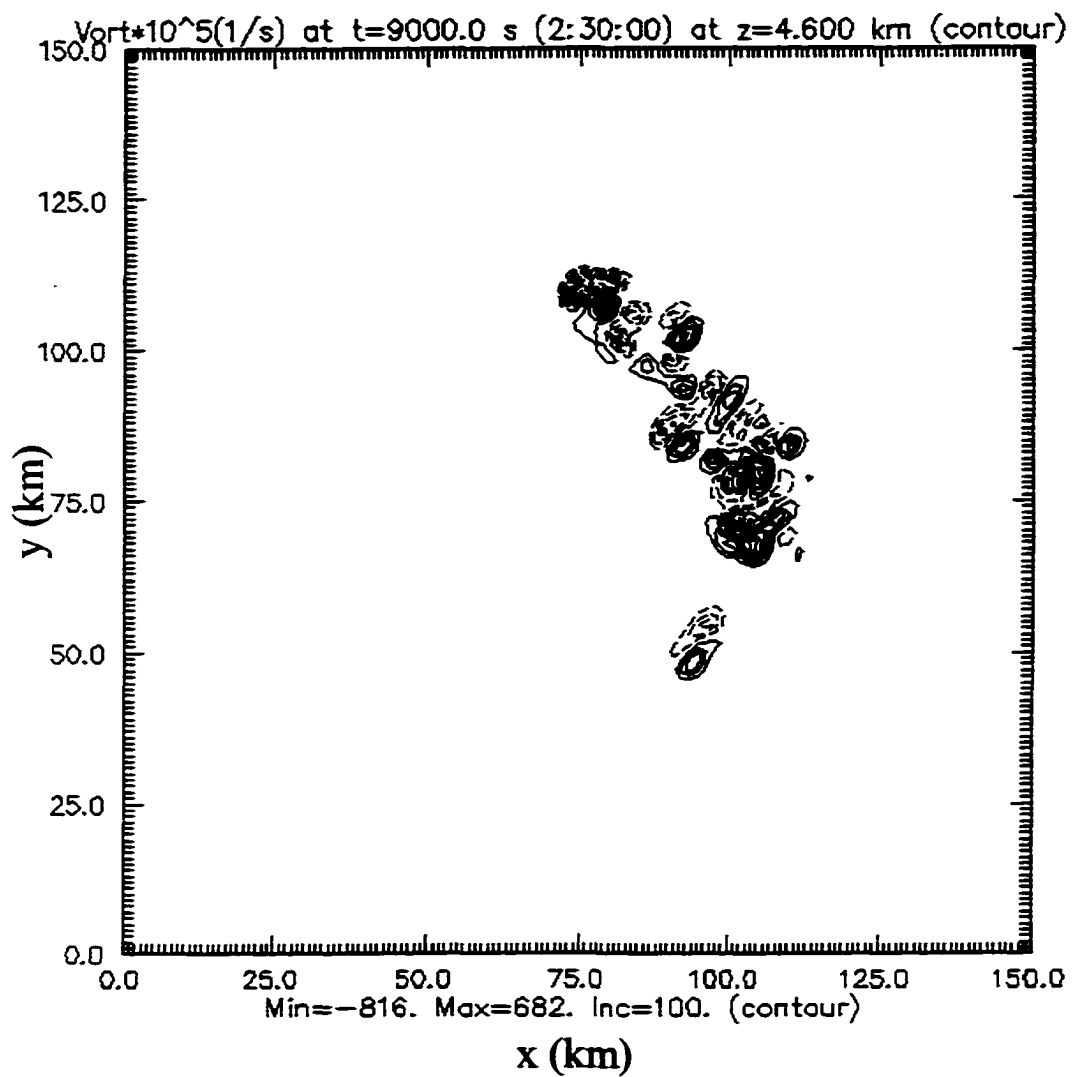


**Figure 5.19: Horizontal cross-section of vertical vorticity multiplied by  $10^5$  at  $z=4.6$  km at  $t \approx 2.5$  hours for homogeneous control run using profile A in Figure 5.14.**

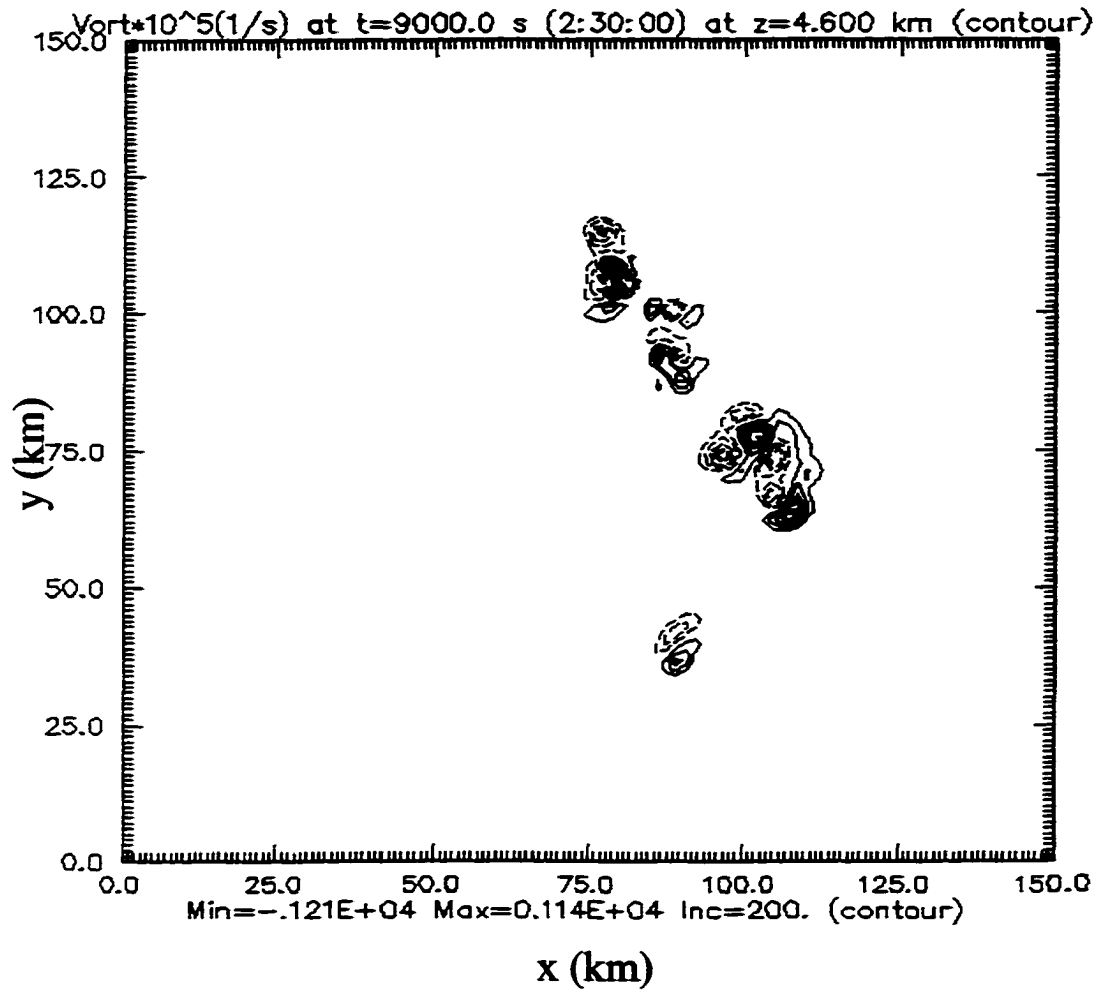


**Figure 5.20: Horizontal cross-section of vertical vorticity at  $z=4.6$  km at  $t=2.5$  hours for inhomogeneous shear simulation with shear varying along the mean wind as in Figure 5.13. (Note the change in contour interval).**

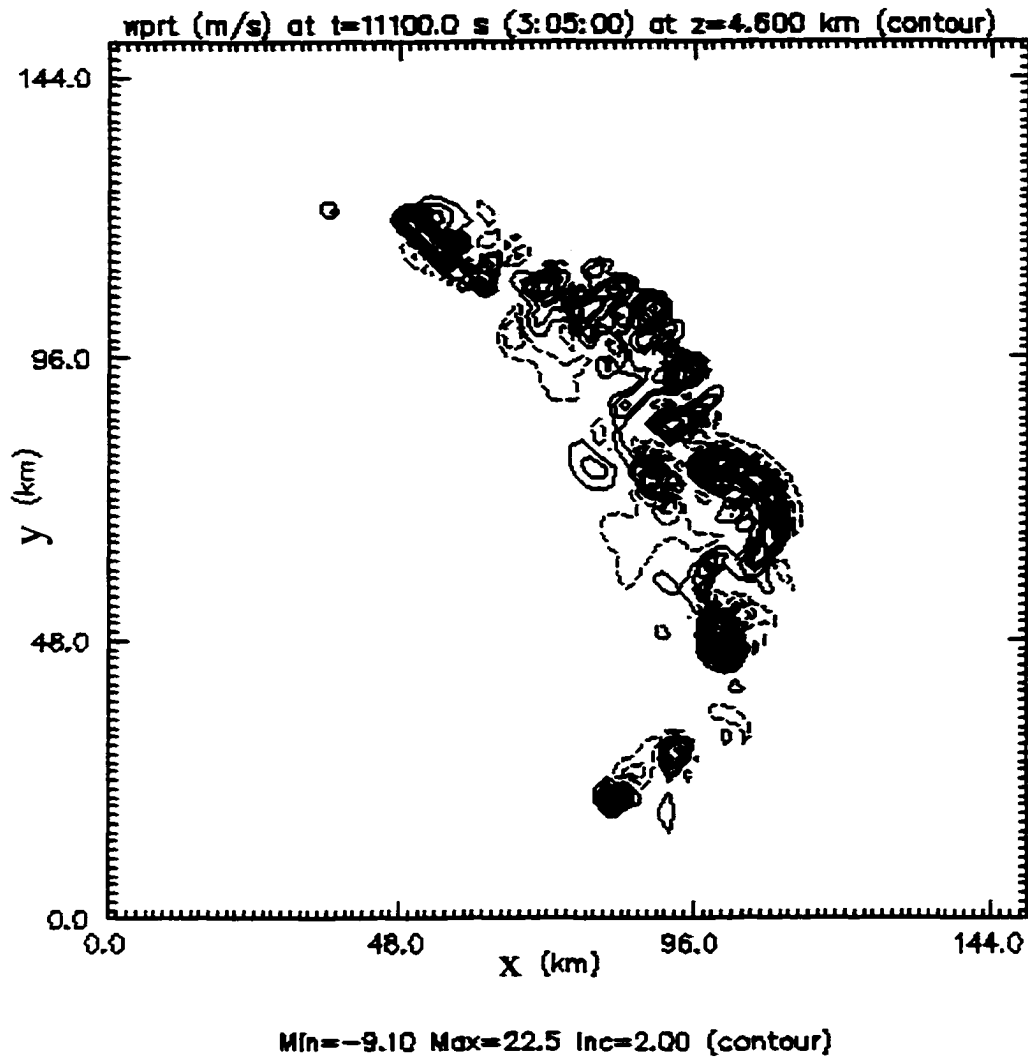


**Figure 5.21: : Horizontal cross-section of vertical velocity at  $z=4.6$  km at  $t=11100$  s (3:05 hours) for inhomogeneous shear simulation with shear varying along the mean wind as in Figure 5.13.**

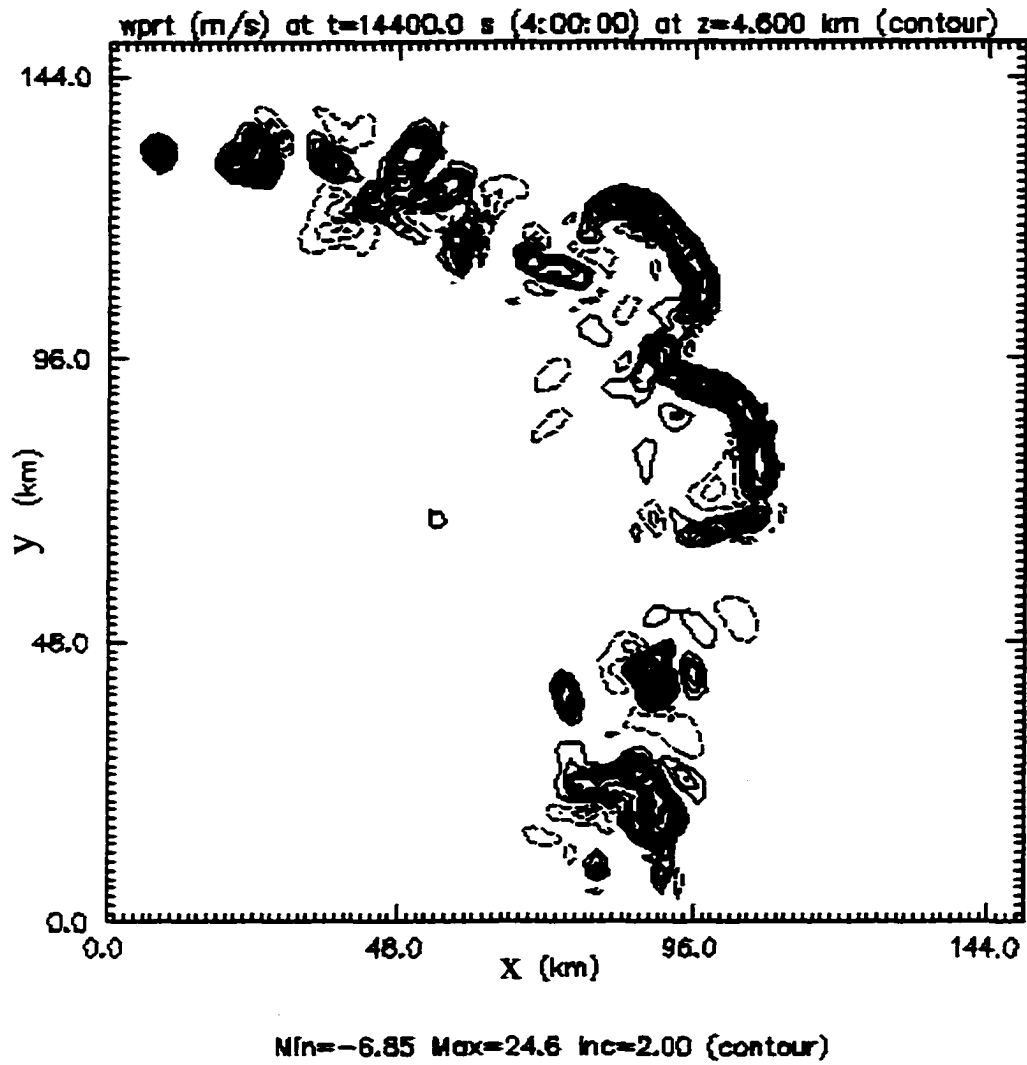


**Figure 5.22: Horizontal cross-section of vertical velocity at  $z=4.6$  km at 4 hours for inhomogeneous shear simulation with shear varying along the mean wind as in Figure 5.13.**

## **Chapter 6 Summary, Conclusions, and Outlook**

The purpose of this study was to bridge the gap in understanding between simulations of storms in highly idealized homogeneous environments and real data predictions in highly complex environments. To do this, we performed simulations of storms in analytically-specified, horizontally inhomogeneous environments that were carefully chosen to produce clear responses in convection to variations in vertical shear and low-level moisture.

Model alteration to accommodate the inhomogeneous environment proved to be a considerable task, predominantly due to the absence of other such studies to lead the way. After revising the lateral boundary conditions, Rayleigh damping, computational mixing, lateral boundary advection, and grid translation, the model proved to be quite amenable to the specified environmental inhomogeneities and did not generate spurious disturbances at the boundaries. This allowed for the use of a computational domain of an affordable size that could be moved through the inhomogeneous environment.

The first attempts, in which the environment was allowed to evolve slightly in time, required a stationary domain of considerable size. These early attempts also included the Coriolis force such that it balanced the pressure gradient force and advection. The result was an environment in which vertical shear and low-level moisture varied simultaneously. The results were nearly as complicated as real data

**predictions in terms of their ability to contribute to our fundamental understanding of storm behavior.**

**The transition to a steady-state environment and the exclusion of the Coriolis force improved the interpretability of the results tremendously, as vertical shear and low-level moisture variations could be studied separately.**

**In order to study the effects on storm morphology of steady-state horizontal variations in low-level moisture, the key was to recognize that no perturbation in pressure could be allowed (i.e., to cause horizontal accelerations), and that the atmosphere had to remain in hydrostatic balance. This can be accomplished if both density and pressure remain horizontally homogeneous. The easiest way to satisfy this constraint is to keep virtual temperature constant by prescribing a very small change in temperature for a given change in water vapor mixing ratio. It is a fortuitous property of the virtual temperature that only a very small temperature perturbation is required for a sizeable change in water vapor. This allowed us to devise a steady-state environment where the results can be interpreted in terms of variations in moisture almost exclusively.**

**Several interesting conclusions can be made regarding the variable moisture simulations. First, it is clear that a storm comprised of ordinary cells will develop a component of motion toward regions of larger low-level mixing ratio. This has been a part of forecaster terminology through oft-heard statements such as 'a storm will seek out the better moisture'. It is clear in the simulations that individual cells do not possess such a "mindset", as they continue to move largely with the mean wind, but**

the storm system as a whole *does* develop a mechanism for promoting new cell growth predominantly on the high moisture side. New cell development is, of course, initially preferred on this flank due to the lower LFC and decreased CIN. Once storms form, they contribute toward a preferential evolution of the cold pool toward the high moisture side, resulting in increased convergence that further favors development on this flank. Eventually, the system may have fewer cells on the low moisture flank than predicted by corresponding control runs in homogeneous environments having the same thermodynamic properties.

In high shear environments, variable moisture can also have profound influences. Perhaps most interestingly, we found that a rotating storm can continue to exist when it moves into a region of low-level moisture that would not support a sustained storm from inception. This suggests that the storm has mechanisms for lifting parcels to their LFC, such as favorable upward pressure gradient forces on the flanks due to rotation, or a mechanism, that does not exist during the formative stages, for transporting moisture to the updraft. The exact mechanism for continued cell existence is a subject for future research.

Development of cells along the gust front is heavily influenced by moisture variations in both strong and weak shear regimes as the overall storm system becomes skewed toward the higher moisture flank due to preferred cell growth. The feedback mechanism discussed above, however, is not as apparent for high shear environments. This is to be expected since supercells, once spawned, are forced not primarily by

gust front processes, but rather by dynamic pressure gradients associated with their rotational properties.

Vertical velocity and mid-level vertical vorticity are influenced by variations in moisture in two distinct ways. First, a direct influence occurs owing to the increase in parcel buoyancy (CAPE) associated with increasing low-level moisture. This leads to an increase in updraft speed. Second, an indirect influence occurs via the modification of the timing and location of neighboring cells forming along the gust front. This can result in either cell merger or cell interference, with seemingly opposite effects on storm intensity and rotational characteristics.

Variations in shear are also found to profoundly influence storm morphology. When a storm is initiated in weak shear, with varying shear across the storm, the development of new cells tends to be favored on the higher shear flank of the gust front where convergence is enhanced. The updraft strength, however, is not necessarily larger on this flank, presumably because of the competing influence of increased entrainment. Thus, we might expect a storm system to appear to propagate toward higher shear.

When a storm is initiated in higher shear with varying shear across the storm, new cell growth is preferred on the weaker shear side, but storms on the strong shear side show greater organization and longevity. Redevelopment cells are eliminated as the shear exceeds a threshold value on one side of the storm, in agreement with Weisman and Klemp (1982). Thus, we might expect a storm system to appear to

propagate toward lower shear, where redevelopment cells are likely, while it maintains the most organized cells on the higher shear side.

When an entire storm system moves into increasing shear over its lifetime, overall system structure is affected as disorganized multicells form coherent structures of greater vorticity and intensity. This represents a new way to develop a feature such as a bow echo from *existing* cells which were not originally supercells as opposed to those formed in Weisman (1993) in which 'cases that eventually evolve into bow echoes all originate with splitting cells earlier in the lifetime of the system'.

This study represents only the first step toward understanding the response of storms to inhomogeneous environments. Additional analysis is needed in order to explain the dynamics governing many of the responses noted. Detailed trajectory analyses are planned for the future along with diagnostic techniques to elucidate various forcings. A comparison of these results with those based on varying the environmental properties temporally might provide the best method of analysis, particularly for the shear experiments, since this would remove the need for environmental vorticity.

## **References Cited**

- Adlerman, E.J., K.K. Droegemeier, and R.P. Davies-Jones, 1999: A numerical simulation of cyclic mesocyclogenesis. . *J. Atmos. Sci.*, **56**, 2045-2069.
- Asselin, R., 1972: Frequency filter for time integrations. *Mon. Wea. Rev.*, **100**, 487-490.
- Bluestein, H.B., E.W. McCaul, Jr., G.P. Byrd, and G. R. Woodall, 1988: Mobile sounding observations of a tornadic storm near the dryline: The Canadian, Texas storm of 7 May 1986. *Mon. Wea. Rev.*, **116**, 1790-1804.
- \_\_\_\_\_, and M.L. Weisman, 1998: The interactions of numerically simulated supercells initiated along lines. Preprints, *19th Conf. on Severe Local Storms*, Minneapolis, Amer. Meteor. Soc., 265-268.
- Brooks, H.E., and R. B. Wilhelmson, 1993: Hodograph curvature and updraft intensity in numerically modeled supercells. *J. Atmos. Sci.*, **50**, 1824-1833.
- \_\_\_\_\_, C.A. Doswell III, and R.P. Davies-Jones, 1993a: Environmental helicity and the maintenance and evolution of low-level mesocyclones. *The Tornado: Its Structure, Dynamics, Prediction and Hazards, Geophys. Monogr.*, No. 79, Amer. Geophys. Union, 97-114.
- \_\_\_\_\_, \_\_\_\_\_, and L.J. Wicker, 1993b: STORMTIPE: A forecasting experiment using a three-dimensional cloud model. *Wea. Forecasting*, **8**, 352-362.
- \_\_\_\_\_, \_\_\_\_\_, and R.B. Wilhelmson, 1994a: The role of midtropospheric winds in the evolution and maintenance of low-level mesocyclones. *Mon. Wea. Rev.*, **122**, 126-136.
- \_\_\_\_\_, \_\_\_\_\_, and J. Cooper, 1994b: On the environments of tornadic and nontornadic mesocyclones. *Wea. Forecasting*, **9**, 606-618.
- Browning, K.A., 1962: Cellular structure of convective storms. *Meteor. Mag.*, **91**, 341-350.
- \_\_\_\_\_, and F.H. Ludlam, 1962: Airflow in convective storms. *Quart. J. Roy. Meteor. Soc.*, **88**, 117-135.
- \_\_\_\_\_, and R.J. Donaldson, Jr., 1963: Airflow and structure of a tornadic storm. *J. Atmos. Sci.*, **20**, 533-545.

- \_\_\_\_\_, 1964: Airflow and precipitation trajectories within severe local storms which travel to the right of the winds. *J. Atmos. Sci.*, **21**, 634-639.
- \_\_\_\_\_, 1968: The organization of severe local storms. *Weather*, **23**, 429-434.
- Burgess, D.W., and E.B. Curran, 1985: The relationship of storm type to environment in Oklahoma on 26 April 1984. Preprints, *15th Conf. on Severe Local Storms, Location*, Amer. Meteor. Soc., 208-211.
- Carpenter, K.M., 1982: Note on the paper 'Radiation conditions for the lateral boundaries of limited-area numerical models' by M.J. Miller and A.J. Thorpe. *Quart. J. Roy. Meteor. Soc.*, **108**, 717-719.
- Clark, T.L., 1979: Numerical simulations with a three-dimensional cloud model: Lateral boundary condition experiments and multicellular severe storm simulations. *J. Atmos. Sci.*, **36**, 2191-2215.
- Cotton, W.R., and G.J. Tripoli, 1978: Cumulus convection in shear flow - Three-dimensional numerical experiments. *J. Atmos. Sci.*, **35**, 1503-1521.
- Crook, N.A., and M.W. Moncrieff, 1988: The effect of large-scale convergence on the generation and maintenance of deep moist convection. *J. Atmos. Sci.*, **45**, 3606-3624.
- \_\_\_\_\_, 1996: Sensitivity of moist convection forced by boundary layer processes to low-level thermodynamic fields. *Mon. Wea. Rev.*, **124**, 1767-1785.
- Davies-Jones, R.P., 1974: Discussion of measurements inside high-speed thunderstorm updrafts. *J. Appl. Meteor.*, **13**, 710-717.
- \_\_\_\_\_, 1984: Streamwise vorticity: The origin of updraft rotation in supercell storms. *J. Atmos. Sci.*, **41**, 2991-3006.
- \_\_\_\_\_, 1985: Dynamical interaction between an isolated convective cell and a veering environmental wind. Preprints, *14th Conf. on Severe Local Storms*, Boston, Mass., Amer. Meteor. Soc., pp. 216-219.
- \_\_\_\_\_, D. Burgess, and M. Foster, 1990: Test of helicity as a tornado forecast parameter. Preprints, *16th Conf. on Severe Local Storms*, Kananaskis Park, Amer. Meteor. Soc., pp. 588-592.

- \_\_\_\_\_, and H.E. Brooks, 1993: Mesocyclogenesis from a theoretical perspective. *The Tornado: Its Structure, Dynamics, Prediction and Hazards, Geophys. Monogr.*, No. 79, Amer. Geophys. Union, 105-114.
- \_\_\_\_\_, 1996a: Inclusion of boundary conditions on pressure in conceptual models of updraft-environment interaction. Preprints, *18th Conf. Severe Local Storms*, San Francisco, Amer. Meteor. Soc., 713-717.
- \_\_\_\_\_, 1996b: Formulas for the barotropic and baroclinic components of vorticity with applications to vortex formation near the ground. Preprints, *7th Conf. Mesoscale Processes*, Reading, United Kingdom, Amer. Meteor. Soc., 14-16.
- Deardorff, J.W., 1980: Stratocumulus-capped mixed layers derived from a three-dimensional model. *Boundary Layer Meteorology*, Reidel, Boston, 495-527.
- Doswell, C.A. III, and D.W. Burgess, 1993: Tornadoes and tornadic storms: A review of conceptual models. *The Tornado: Its Structure, Dynamics, Prediction and Hazards, Geophys. Monogr.*, No. 79, Amer. Geophys. Union, 161-172.
- \_\_\_\_\_, and E.N. Rasmussen, 1994: The effect of neglecting the virtual temperature correction on CAPE calculations. *Wea. Forecasting*, **9**, 625-629.
- \_\_\_\_\_, 1996: What is a supercell? Preprints, *18th Conf. on Severe Local Storms*, San Francisco, CA, Amer. Meteor. Soc., 641.
- Droegemeier, K.K., S.M. Lazarus, and R. Davies-Jones, 1993: The influence of helicity on numerically simulated convective storms. *Mon. Wea. Rev.*, **121**, 2005-2029.
- \_\_\_\_\_, 1997: The numerical prediction of thunderstorms: Challenges, potential benefits, and results from realtime operational tests. *WMO Bull.*, **46**, 324-336.
- Foote, G.B., and H.W. Frank, 1983: Case study of a hailstorm in Colorado. Part III: Airflow from triple-Doppler measurements. *J. Atmos. Sci.*, **40**, 686-707.
- Fujita, T., and H. Grandoso, 1968: Split of a thunderstorm into anticyclonic and cyclonic storms and their motion as determined from numerical model experiments. *J. Atmos. Sci.*, **25**, 416-439.
- Hitschfeld, W., 1960: The motion and erosion of convective storms in severe vertical wind shear. *J. Meteor.*, **17**, 270-282.

- Jahn, D.E., 1995: *Simulation of convective storms in environments with independently varying Bulk Richardson Number and storm-relative helicity*. Masters Thesis, Dept. of Meteorology, Univ. of Oklahoma-Norman, 124 pp.
- Klemp, J.B., and R.B. Wilhelmson, 1978a: The simulation of three-dimensional convective storm dynamics. *J. Atmos. Sci.*, **35**, 1070-1096.
- \_\_\_\_\_, and \_\_\_\_\_, 1978b: Simulations of right- and left-moving storms produced through storm splitting. *J. Atmos. Sci.*, **35**, 1097-1110.
- \_\_\_\_\_, R.B. Wilhelmson, and P.S. Ray, 1981: Observed and numerically simulated structure of a mature supercell thunderstorm. *J. Atmos. Sci.*, **38**, 1558-1580.
- \_\_\_\_\_, and R. Rotunno, 1983: A study of the tornadic region within a supercell thunderstorm. *J. Atmos. Sci.*, **40**, 359-377.
- \_\_\_\_\_, 1987: Dynamics of tornadic thunderstorms. *Ann. Rev. Fluid Mech.*, **19**, 369-402.
- Lemon, L.R., 1976: The flanking line, a severe thunderstorm intensification source. *J. Atmos. Sci.*, **33**, 686-694.
- Lilly, D.K., 1982: The development and maintenance of rotation in convective storms. *Intense Atmospheric Vortices*, L. Bengtsson and J. Lighthill, Eds., Springer-Verlag, 149-160.
- \_\_\_\_\_, 1986a: The structure, energetics and propagation of rotating convective storms. Part I: Energy exchange with the mean flow. *J. Atmos. Sci.*, **43**, 113-125.
- \_\_\_\_\_, 1986b: The structure, energetics and propagation of rotating convective storms. Part II: Helicity and storm stabilization. *J. Atmos. Sci.*, **43**, 126-140.
- Marwitz, J.D., 1972a: The structure and motion of severe hailstorms. Part I: Supercell storms. *J. Appl. Meteor.*, **11**, 166-179.
- \_\_\_\_\_, 1972b: The structure and motion of severe hailstorms. Part II: Multi-cell storms. *J. Appl. Meteor.*, **11**, 180-188.
- \_\_\_\_\_, 1972c: The structure and motion of severe hailstorms. Part III: Severely sheared storms. *J. Appl. Meteor.*, **11**, 189-201.
- Miller, L.J., and R.P. Pearce, 1974: A three-dimensional primitive equation model of cumulonimbus convection. *Quart. J. Roy. Meteor. Soc.*, **100**, 133-154.

- \_\_\_\_\_, 1977: Updraft intensification and hail production after cell merger. Preprints, *10th Conf. on Severe Local Storms*, Omaha, NE, Amer. Meteor. Soc., 110-115.
- \_\_\_\_\_, and J.C. Fankhauser, 1983: Radar echo structure, air motion and hail formation in a large stationary multicellular thunderstorm. *J. Atmos. Sci.*, **40**, 2399-2418.
- Moeng, C.H., 1984: A large-eddy simulation model for the study of planetary boundary-layer turbulence. *J. Atmos. Sci.*, **41**, 2052-2062.
- \_\_\_\_\_, and J.C. Wyngaard, 1988: Spectral analysis of large-eddy simulations of the convective boundary layer. *J. Atmos. Sci.*, **45**, 3573-3587.
- Moncrieff, M.W., and J.S.A. Green, 1972: The propagation and transfer properties of steady convective overturning in shear. *Quart. J. Roy. Meteor. Soc.*, **98**, 336-352.
- Nelson, S.P., and N.C. Knight, 1987: The hybrid multicellular-supercellular storm - an efficient hail producer. Part I: An archetypal example. *J. Atmos. Sci.*, **44**, 2042-2059.
- \_\_\_\_\_, and N.C. Knight, 1987: The hybrid multicellular-supercellular storm - an efficient hail producer. Part II: General characteristics and implications for hail growth. *J. Atmos. Sci.*, **44**, 2060-2073.
- Newton, C.W., and H.R. Newton, 1959: Dynamical interactions between large convective clouds and environment with vertical shear. *J. Meteor.*, **16**, 483-496.
- \_\_\_\_\_, and J.C. Fankhauser, 1975: Movement and propagation of multicellular convective storms. *Pure Appl. Geophys.*, **113**, 747-764.
- Orville, H.D., Y.H. Kuo, R.D. Farley, and C.S. Hwang, 1980: Numerical simulation of cloud interactions. *J. Rech. Atmos.*, **14**, 499-516.
- Richardson, Y.P., and K.K. Droegemeier, 1996: An investigation of the dynamics governing organized multicell rotation and transition. Preprints, *18th Conf. on Severe Local Storms*, San Francisco, CA, Amer. Meteor. Soc., 195-199.
- Rotunno, R., 1981: On the evolution of thunderstorm rotation. *Mon. Wea. Rev.*, **109**, 577-586.

- \_\_\_\_\_, and J.B. Klemp, 1982: The influence of the shear-induced pressure gradient on thunderstorm motion. *Mon. Wea. Rev.*, **110**, 136-151.
- \_\_\_\_\_, and \_\_\_\_\_, 1985: On the rotation and propagation of simulated supercell thunderstorms. *J. Atmos. Sci.*, **42**, 271-292.
- \_\_\_\_\_, \_\_\_\_\_, and M.L. Weisman, 1988: A theory for strong, long-lived squall lines. *J. Atmos. Sci.*, **45**, 463-485.
- \_\_\_\_\_, 1993: Supercell thunderstorm modeling and theory. *The Tornado: Its Structure, Dynamics, Prediction and Hazards, Geophys. Monogr.*, No. 79, Amer. Geophys. Union, 57-73.
- Schlesinger, R.E., 1980: A three-dimensional numerical model of an isolated thunderstorm. Part II: Dynamics of updraft splitting and mesovortex couplet evolution. *J. Atmos. Sci.*, **37**, 395-420.
- \_\_\_\_\_, 1984: Effects of the pressure perturbation field in numerical models of unidirectionally sheared thunderstorm convection: Two versus three dimensions. *J. Atmos. Sci.*, **41**, 1571-1586.
- Shapiro, A., 1993: The use of an exact solution of the Navier-Stokes equations in a validation test of a three-dimensional nonhydrostatic numerical model. *Mon. Wea. Rev.*, **121**, 2420-2425.
- \_\_\_\_\_, and Y.L. Kogan, 1994: On vortex formation in multicell convective clouds in a shear-free environment. *Atmos. Res.*, **33**, 125-136.
- Skamarock, W.C., and J.B. Klemp, 1992: The stability of time-split numerical methods for the hydrostatic and the nonhydrostatic elastic equations. *Mon. Wea. Rev.*, **120**, 2109-2127.
- \_\_\_\_\_, M.L. Weisman, and J.B. Klemp, 1994a: Three-dimensional evolution of simulated long-lived squall lines. *J. Atmos. Sci.*, **51**, 2563-2584.
- \_\_\_\_\_, \_\_\_\_\_, C.A. Davis, and J.B. Klemp, 1994b: The evolution of simulated mesoscale convective systems in idealized environments. Preprints, *6th Conf. Mesoscale Processes*, AMS, 407-410.
- Soong, S., and Y. Ogura, 1973: A comparison between axi-symmetric and slab-symmetric cumulus cloud models. *J. Atmos. Sci.*, **30**, 879-893.

- Tapp, M.C., and P.W. White, 1976: A non-hydrostatic mesoscale model. *Quart. J. Roy. Meteor. Soc.*, **102**, 277-296.
- Thorpe, A.J., and M.J. Miller, 1978: Numerical simulations showing the role of the downdraught in cumulonimbus motion and splitting. *Quart. J. Roy. Meteor. Soc.*, **104**, 873-893.
- Turpeinen, O., 1982: Cloud interactions and merging on day 261 of GATE. *Mon. Wea. Rev.*, **110**, 1238-1254.
- Weisman, M.L., and J.B. Klemp, 1982: The dependence of numerically simulated convective storms on vertical wind shear and buoyancy. *Mon. Wea. Rev.*, **110**, 504-520.
- \_\_\_\_\_, and \_\_\_\_\_, 1984: The structure and classification of numerically simulated convective storms in directionally varying wind shears. *Mon. Wea. Rev.*, **112**, 2479-2498.
- \_\_\_\_\_, 1993: The genesis of severe, long-lived bow echoes. *J. Atmos. Sci.*, **50**, 645-670.
- \_\_\_\_\_, M.S. Gilmore, and L.J. Wicker, 1998: The impact of convective storms on their local environment: What is an appropriate ambient sounding? Preprints, *19th Conf. on Severe Local Storms*, Minneapolis, Minnesota, Amer. Meteor. Soc., 238-241.
- Westcott, N.E., 1984: A historical perspective on cloud mergers. *Bull. Amer. Meteor. Soc.*, **65**, 219-226.
- Wilhelmson, R.B., and Y. Ogura, 1972: The pressure perturbation and the numerical modeling of a cloud. *J. Atmos. Sci.*, **29**, 1295-1307.
- \_\_\_\_\_, 1974: The life cycle of a thunderstorm in three dimensions. *J. Atmos. Sci.*, **31**, 1629-1651.
- \_\_\_\_\_, and J.B. Klemp, 1978: A numerical study of storm splitting that leads to long-lived storms. *J. Atmos. Sci.*, **35**, 1974-1986.
- \_\_\_\_\_, and \_\_\_\_\_, 1981: A three-dimensional numerical simulation of splitting severe storms on 3 April 1964. *J. Atmos. Sci.*, **38**, 1581-1600.
- \_\_\_\_\_, and C. Chen, 1982: A simulation of the development of successive cells along a cold outflow boundary. *J. Atmos. Sci.*, **39**, 1466-1483.

Xue, M., K.K. Droegemeier, V. Wong, A. Shapiro, and K. Brewster, 1995: *ARPS Version 4.0 User's Guide*, Center for Analysis and Prediction of Storms, Univ. of Oklahoma, pp. 380

Zalesak, S.T., 1979: Fully multidimensional flux-corrected transport algorithms for fluids. *J. Comput. Phys.*, **31**, 335-362.

### **Additional Reading**

- Acheson, D.J., 1990: *Elementary Fluid Dynamics*. Oxford Press, 397pp.
- Achtemeier, G.L., 1994: Contrasts in objective analysis philosophy: Comments on "The theoretical, discrete, and actual response of the Barnes objective analysis scheme for one- and two-dimensional fields". *Mon. Wea. Rev.*, **122**, 397-401.
- Agee, E.M., J.T. Snow, and P.R. Clare, 1976: Multiple vortex features in the tornado cyclone and the occurrence of tornado families. *Mon. Wea. Rev.*, **104**, 552-563.
- Anthes, R.A., Y.H. Kuo, S.G. Benjamin, and Y.F. Li, 1982: The evolution of the mesoscale environment of severe local storms: Preliminary modeling results. *Mon. Wea. Rev.*, **110**, 1187-1213.
- Asai, T., and A. Kasahara, 1967: A theoretical study of the compensating downward motions associated with cumulus clouds. *J. Atmos. Sci.*, **24**, 487-496.
- \_\_\_\_\_, 1970: Stability of a plane parallel flow with variable vertical shear and unstable stratification. *J. Met. Soc. Japan*, **48**, 129-138.
- \_\_\_\_\_, 1970: Three-dimensional features of thermal convection in a plane Couette flow. *Met. Soc. Japan*, **48**, 18-29.
- \_\_\_\_\_, and I. Nakasuji, 1971: Thermal instability in a parallel flow with vertical and horizontal shears. *Met. Soc. Japan*, **49**, 757-765.
- Balaji, V., and T.L. Clark, 1988: Scale selection in locally forced convective fields and the initiation of deep cumulus. *J. Atmos. Sci.*, **45**, 3188-3211.
- Barnes, S.L., 1970: Some aspects of a severe, right-moving thunderstorm deduced from mesonet rawinsonde observations. *J. Atmos. Sci.*, **27**, 634-648.
- \_\_\_\_\_, 1978: Oklahoma thunderstorms on 29-30 April 1970. Part I: Morphology of a tornadic storm. *Mon. Wea. Rev.*, **106**, 673-684.
- \_\_\_\_\_, 1978: Oklahoma thunderstorms on 29-30 April 1970. Part II: Radar-observed merger of twin hook echoes. *Mon. Wea. Rev.*, **106**, 685-696.
- \_\_\_\_\_, 1978: Oklahoma thunderstorms on 29-30 April 1970. Part III: Tornado characteristics inferred from damage tracks. *Mon. Wea. Rev.*, **106**, 697-703.

- \_\_\_\_\_, and S.P. Nelson, 1978: Oklahoma thunderstorms on 29-30 April 1970. Part IV: Study of a dissipating severe storm. *Mon. Wea. Rev.*, **106**, 704-712.
- Beebe, R.G., and F.C. Bates, 1955: A mechanism for assisting in the release of convective instability. *Mon. Wea. Rev.*, **83**, 1-10.
- Bell, G.D., and D. Keyser, 1993: Shear and curvature vorticity and potential-vorticity interchanges: Interpretation and application to a cutoff cyclone event. *Mon. Wea. Rev.*, **121**, 76-102.
- Bluestein, H.B., and C.R. Parks, 1983: A synoptic and photographic climatology of low-precipitation severe thunderstorms in the southern plains. *Mon. Wea. Rev.*, **111**, 2034-2046.
- \_\_\_\_\_, and M.H. Jain, 1985: Formation of mesoscale lines of precipitation: Severe squall lines in Oklahoma during the Spring. *J. Atmos. Sci.*, **42**, 1711-1732.
- \_\_\_\_\_, and S.S. Parker, 1993: Modes of isolated, severe convective storm formation along the dryline. *Mon. Wea. Rev.*, **121**, 1354-1372.
- Boer, G.J., 1994: Predictability regimes in atmospheric flow. *Mon. Wea. Rev.*, **122**, 2285-2295.
- Bonesteel, R.G., and Y.J. Lin, 1978: A study of updraft-downdraft interaction based on perturbation pressure and single-Doppler radar data. *Mon. Wea. Rev.*, **106**, 62-68.
- Bonner, W.D., 1966: Case study of thunderstorm activity in relation to the low-level jet. *Mon. Wea. Rev.*, **94**, 167-178.
- \_\_\_\_\_, S. Esbensen, and R. Greenberg, 1968: Kinematics of the low-level jet. *J. Appl. Met.*, **7**, 339-347.
- Brandes, E.A., 1984: Vertical vorticity generation and mesocyclone sustenance in tornadic thunderstorms: The observational evidence. *Mon. Wea. Rev.*, **112**, 2253-2269.
- \_\_\_\_\_, R.P. Davies-Jones, and B.C. Johnson, 1988: Streamwise vorticity effects on supercell morphology and persistence. *J. Atmos. Sci.*, **45**, 947-963.
- \_\_\_\_\_, and C.L. Ziegler, 1993: Mesoscale downdraft influences on vertical vorticity in a mature mesoscale convective system. *Mon. Wea. Rev.*, **121**, 1337-1353.

- \_\_\_\_\_, 1993: Tornadic thunderstorm characteristics determined with Doppler radar. *The Tornado: Its Structure, Dynamics, Prediction and Hazards, Geophys. Monogr.*, No. 79, Amer. Geophys. Union, 143-159.
- Brewster, K.A., 1986: Photographs of a funnel-producing indented cloud-base swirl. *Mon. Wea. Rev.*, **114**, 1771-1774.
- Brill, K.F., L.W. Uccellini, R.P. Burkhart, T.T. Warner, and R.A. Anthes, 1985: Numerical simulation of a transverse indirect circulation and low-level jet in the exit region of an upper-level jet. *J. Atmos. Sci.*, **42**, 1306-1320.
- Brown, J.M., and K.R. Knupp, 1980: The Iowa cyclonic-anticyclonic tornado pair and its parent thunderstorm. *Mon. Wea. Rev.*, **108**, 1626-1646.
- Brown, R.A., 1992: Initiation and evolution of updraft rotation within an incipient supercell thunderstorm. *J. Atmos. Sci.*, **49**, 1997-2014.
- \_\_\_\_\_, 1993: A compositing approach for preserving significant features in atmospheric profiles. *Mon. Wea. Rev.*, **121**, 874-880.
- Browning, G.L., and H.O. Kreiss, 1994: Splitting methods for problems with different timescales. *Mon. Wea. Rev.*, **122**, 2614-2630.
- Byers, H.R., and R.R. Braham, Jr., 1949: *The Thunderstorm*. U.S. Government Printing Office, Washington, DC, 287 pp.
- CAPS, 1995: *ARPS Version 4.0 User's Guide*. Center for the Analysis and Prediction of Storms, Univ. of Okla., Norman, 381 pp.
- Carbone, R.E., 1982: A severe frontal rainband. Part I: Stormwide hydrodynamic structure. *J. Atmos. Sci.*, **39**, 258-279.
- Carbone, R.E., 1982: A severe frontal rainband. Part II: Tornado parent vortex circulation. *J. Atmos. Sci.*, **40**, 2639-2654.
- Carpenter, R.L., 1994: *Entrainment and Detrainment in Numerically Simulated Cumulus Congestus Clouds*. Ph.D. Dissertation, Dept. of Meteorology, Univ. of Oklahoma-Norman, 256 pp.
- Chang, S.W., and H.D. Orville, 1973: Large-scale convergence in a numerical cloud model. *J. Atmos. Sci.*, **30**, 947-950.
- Chen, C.H., and H.D. Orville, 1980: Effects of mesoscale convergence on cloud convection. *J. Appl. Meteor.*, **19**, 256-274.

- Clark, T.L., 1973: Numerical modeling of the dynamics and microphysics of warm cumulus convection. *J. Atmos. Sci.*, **30**, 857-878.
- \_\_\_\_\_, T. Hauf, and J.P. Kuttner, 1986: Convectively forced internal gravity waves: Results from two-dimensional numerical experiments. *Quart. J. Roy. Meteor. Soc.*, **112**, 899-925.
- Cohen, C., 1989: Numerical experiments showing the response of parameterized convection to large-scale forcing. *J. Atmos. Sci.*, **46**, 132-149.
- Colquhoun, J.R., and P.A. Riley, 1996: Relationships between tornado intensity and various wind and thermodynamic variables. *Wea. Forecasting*, **11**, 360-371.
- Conway, J.W., H.E. Brooks, and K.D. Hondl, 1996: The 17 August 1994 Lahoma, OK supercell: Issues of tornadogenesis and bow echo formation. Preprints, *18th Conf. Severe Local Storms*, San Francisco, Amer. Meteor. Soc., 52-56.
- Crook, N.A., and J.D. Tuttle, 1994: Numerical simulations initialized with radar-derived winds. Part II: Forecasts of three gust-front cases. *Mon. Wea. Rev.*, **122**, 1204-1217.
- Darkow, G.L., and O.E. Thompson, 1968: Diurnal oscillation of the tropospheric wind field above a low-level jet. *J. Atmos. Sci.*, 39-46.
- David, C.L., 1976: A study of upper air parameters at the time of tornadoes. *Mon. Wea. Rev.*, **104**, 546-551.
- Davies-Jones, R.P., 1982: Observational and theoretical aspects of tornadogenesis. *Intense Atmospheric Vortices*, L. Bengtsson and J. Lighthill, Eds., Springer-Verlag, 175-189.
- \_\_\_\_\_, 1993: Useful formulas for computing divergence, vorticity, and their errors from three or more stations. *Mon. Wea. Rev.*, **121**, 713-725.
- \_\_\_\_\_, C.A. Doswell III, and H.E. Brooks, 1994: Comments on "Initiation and evolution of updraft rotation within an incipient supercell thunderstorm". *J. Atmos. Sci.*, **51**, 326-331.
- Davis, C.A., and M.L. Weisman, 1994: Balanced dynamics of mesoscale vortices produced in simulated convective systems. *J. Atmos. Sci.*, **51**, 2005-2030.
- Donaldson, R.J., 1959: Analysis of severe convective storms observed by radar - II. *J. Meteor.*, **16**, 281-287.

- Droegemeier, K.K., and R.B. Wilhelmson, 1985: Three-dimensional numerical modeling of convection produced by interacting thunderstorm outflows. Part I: Control simulation and low-level moisture variations. *J. Atmos. Sci.*, **42**, 2381-2403.
- \_\_\_\_\_, and \_\_\_\_\_, 1985: Three-dimensional numerical modeling of convection produced by interacting thunderstorm outflows. Part II: Variations in vertical wind shear. *J. Atmos. Sci.*, **42**, 2404-2414.
- \_\_\_\_\_, M. Xue, A. Sathye, K. Brewster, G. Bassett, J. Zhang, Y. Liu, M. Zou, A. Crook, V. Wong, R. Carpenter, and C. Mattocks, 1996: Realtime numerical prediction of storm-scale weather during VORTEX '95: Goals and methodology. Preprints, *18th Conf. on Severe Local Storms*, San Francisco, CA, Amer. Meteor. Soc., pp. 6-10.
- \_\_\_\_\_, Y.P. Richardson, G.M. Bassett, and A. Marroquin, 1997: Three-dimensional numerical simulations of turbulence generated in the near-environment of deep convective storms. Preprints, *7th Conf. on Aviation, Range, and Aerospace Meteorology*, Long Beach, AMS, 169-174.
- Dudhia, J., and M.W. Moncrieff, 1987: A numerical simulation of quasi-stationary tropical convective bands. *Quart. J. Roy. Meteor. Soc.*, **113**, 929-967.
- \_\_\_\_\_, and \_\_\_\_\_, 1989: A three-dimensional numerical study of an Oklahoma squall line containing right-flank supercells. *J. Atmos. Sci.*, **46**, 3363-3391.
- Durrant, D.R., 1989: Improving the anelastic approximation. *J. Atmos. Sci.*, **46**, 1453-1820.
- Emanuel, K.A., 1994: *Atmospheric Convection*. Oxford University Press, 580 pp.
- Fankhauser, J.C., 1971: Thunderstorm-environment interactions determined from aircraft and radar observations. *Mon. Wea. Rev.*, **99**, 171-192.
- Fiedler, B.H., 1994: The thermodynamic speed limit and its violation in axisymmetric numerical simulations of tornado-like vortices. *Atmosphere-Ocean*, **32**, 335-359.
- Fitzjarrald, D.E., 1973: A laboratory simulation of convective vortices. *J. Atmos. Sci.*, **30**, 894-902.
- Foot, G.B., and C.G. Wade, 1982: Case study of a hailstorm in Colorado. Part I: Radar echo structure and evolution. *J. Atmos. Sci.*, **39**, 2828-2846.

- Frisch, U., and S.A. Orszag, 1990: Turbulence: Challenges for theory and experiment. *Physics Today*, 24-32.
- Fuelberg, H.E., and J.R. Scoggins, 1978: Kinetic energy budgets during the life cycle of intense convective activity. *Mon. Wea. Rev.*, **106**, 637-653.
- Fujita, T., 1959: Precipitation and cold air production in mesoscale thunderstorm systems. *J. Meteor.*, **16**, 454-466.
- Gilmore, M.S., and L.J. Wicker, 1996: The influence of DCAPE on supercell dynamics. Preprints, *18th Conf. on Severe Local Storms*, San Francisco, CA, Amer. Meteor. Soc., 723-727.
- Grasso, L.D., and W.R. Cotton, 1995: Numerical simulation of a tornado vortex. *J. Atmos. Sci.*, **52**, 1192-1203.
- Heymsfield, G.M., and R. Fulton, 1994: Passive microwave structure of severe tornadic storms on 16 November 1987. *Mon. Wea. Rev.*, **122**, 2587-2595.
- Hide, R., 1977: Experiments with rotating fluids. *Quart. J. Roy. Meteor. Soc.*, **103**, 1-28.
- \_\_\_\_\_, 1982: High vorticity regions in rotating thermally driven flows. *Intense Atmospheric Vortices*, L. Bengtsson and J. Lighthill, Eds., Springer-Verlag, 313-326.
- Hill, G.E., 1974: Factors controlling the size and spacing of cumulus clouds as revealed by numerical experiments. *J. Atmos. Sci.*, **31**, 646-673.
- Holler, H., V.N. Bringi, J. Hubbert, M. Hagen, and P.F. Meischner, 1994: Life cycle and precipitation formation in a hybrid-type hailstorm revealed by polarimetric and Doppler radar measurements. *J. Atmos. Sci.*, **51**, 2500-2522.
- Hoskins, B.J., and F.P. Bretherton, 1972: Atmospheric frontogenesis models: Mathematical formulation and solution. *J. Atmos. Sci.*, **29**, 11-37.
- Janish, P.R., R.H. Johns, and K.C. Crawford, 1996: An evaluation of the 17 August 1994 - Lahoma, Oklahoma supercell/MCS event using conventional and non-conventional analysis and forecasting techniques. Preprints, *18th Conf. Severe Local Storms*, San Francisco, Amer. Meteor. Soc., 76-80.
- Johns, R.H., and C.A. Doswell III, 1992: Severe local storms forecasting. *Wea. Forecasting*, **9**, 588-612.

- Johnson, K.W., P.S. Ray, B.C. Johnson, and R.P. Davies-Jones, 1987: Observations related to the rotational dynamics of the 20 May 1977 tornadic storms. *Mon. Wea. Rev.*, **115**, 2463-2478.
- Kaiser, J.A.C., 1973: Laboratory vortices in rotating, sheared flow. *J. Atmos. Sci.*, **30**, 950-953.
- Kanak, K.M., and D.K. Lilly, 1996: The linear stability and structure of convection in a circular mean shear. *J. Atmos. Sci.*, **53**, 2578-2593.
- Kay, M.P., and L.J. Wicker, 1998: Numerical simulations of supercell interactions with thermal boundaries. Preprints, *18th Conf. on Severe Local Storms*, Minneapolis, Amer. Meteor. Soc., 246-248.
- Kelly, D.L., J.T. Schaefer, R.P. McNulty, C.A. Doswell III, and R.F. Abbey, Jr., 1978: An augmented tornado climatology. *Mon. Wea. Rev.*, **106**, 1172-1183.
- Kennedy, P.C., N.E. Westcott, and R.W. Scott, 1993: Single-Doppler radar observations of a mini-supercell tornadic thunderstorm. *Mon. Wea. Rev.*, **121**, 1860-1870.
- Kessler, E., 1970: Thunderstorms over Oklahoma - 22 June 1969. *Weatherwise*, 56-69.
- Keyser, D., and M.J. Pecnick, 1985: A two-dimensional primitive equation model of frontogenesis forced by confluence and horizontal shear. *J. Atmos. Sci.*, **42**, 1259-1282.
- \_\_\_\_\_, and \_\_\_\_\_, 1985: Diagnosis of ageostrophic circulations in a two-dimensional primitive equation model of frontogenesis. *J. Atmos. Sci.*, **42**, 1283-1305.
- Klaassen, G.P., and T.L. Clark, 1985: Dynamics of the cloud-environment interface and entrainment in small cumuli: Two-dimensional simulations in the absence of ambient shear. *J. Atmos. Sci.*, **42**, 2621-2642.
- Klemp, J.B., and D.K. Lilly, 1978: Numerical simulations of hydrostatic mountain waves. *J. Atmos. Sci.*, **35**, 78-107.
- Knupp, K.R., R.L. George, and W.R. Cotton, 1982: An intense, quasi-steady thunderstorm over mountainous terrain. Part I: Evolution of the storm-initiating mesoscale circulation. *J. Atmos. Sci.*, **39**, 343-358.

- \_\_\_\_\_, and W.R. Cotton, 1982: An intense, quasi-steady thunderstorm over mountainous terrain. Part II: Doppler radar observations of the storm morphological structure. *J. Atmos. Sci.*, **39**, 343-358.
- \_\_\_\_\_, and \_\_\_\_\_, 1982: An intense, quasi-steady thunderstorm over mountainous terrain. Part III: Doppler radar observations of the turbulent structure. *J. Atmos. Sci.*, **39**, 359-368.
- Koch, S.E., and J. McCarthy, 1982: The evolution of an Oklahoma dryline. Part II: Boundary-layer forcing of mesoconvective systems. *J. Atmos. Sci.*, **39**, 237-257.
- Kogan, Y.L., and W.J. Martin: Parameterization of microphysical processes in convective storm models: Evaluation of the applicability limits based on a three-dimensional model with explicit microphysics. Preprints, 316-319.
- Korotky, W., R.W. Przybylinski, and J.A. Hart, 1993: The Plainfield, Illinois, tornado of August 28, 1990: The evolution of synoptic and mesoscale environments. *The Tornado: Its Structure, Dynamics, Prediction and Hazards, Geophys. Monogr.*, No. 79, Amer. Geophys. Union, 611-624.
- Kropfli, R.A., and L.J. Miller, 1976: Kinematic structure and flux quantities in a convective storm from Dual-Doppler radar observations. *J. Atmos. Sci.*, **33**, 520-529.
- Lemon, L.R., D.W. Burgess, and R.A. Brown, 1978: Tornadic storm airflow and morphology derived from single-Doppler radar measurements. *Mon. Wea. Rev.*, **106**, 48-61.
- \_\_\_\_\_, and C.A. Doswell III, 1979: Severe thunderstorm evolution and mesocyclone structure as related to tornadogenesis. *Mon. Wea. Rev.*, **107**, 1184-1197.
- Leslie, L.M., K. Fraedrich, and T.J. Glowacki, 1989: Forecasting the skill of a regional numerical weather prediction model. *Mon. Wea. Rev.*, **117**, 550-557.
- Lilly, D.K., 1979: The dynamical structure and evolution of thunderstorms and squall lines. *Ann. Rev. Earth Planet Sci.*, **7**, 117-161.
- \_\_\_\_\_, 1981: Wave-permeable lateral boundary conditions for convective cloud and storm simulations. *J. Atmos. Sci.*, **38**, 1313-1316.
- \_\_\_\_\_, 1983: Dynamics of rotating thunderstorms. *Mesoscale Meteorology - Theories, Observations and Models*, D.K. Lilly and T. Gal-Chen, Eds., Reidel, 531-543.

- \_\_\_\_\_, 1983: Linear theory of internal gravity waves and mountain waves. *Mesoscale Meteorology - Theories, Observations and Models*, D.K. Lilly and T. Gal-Chen, Eds., Reidel, 293-312.
- \_\_\_\_\_, 1988: Cirrus outflow dynamics. *J. Atmos. Sci.*, **45**, 1594-1605.
- \_\_\_\_\_, 1989: Two-dimensional turbulence generated by energy sources at two scales. *J. Atmos. Sci.*, **46**, 2026-2030.
- \_\_\_\_\_, and B.F. Jewett, 1990: Momentum and kinetic energy budgets of simulated supercell thunderstorms. *J. Atmos. Sci.*, **47**, 707-726.
- \_\_\_\_\_, 1990: Numerical prediction of thunderstorms - has its time come? *Quart. J. Roy. Meteor. Soc.*, **116**, 779-797.
- \_\_\_\_\_, and T. Gal-Chen, 1990: Can dryline mixing create buoyancy? *J. Atmos. Sci.*, **47**, 1170-1171.
- \_\_\_\_\_, 1996: A comparison of incompressible, anelastic and Boussinesq dynamics. *Atmospheric Research*, **40**, 143-151.
- Lorenz, E.N., 1965: A study of the predictability of a 28-variable atmospheric model. *Tellus*, **17**, 321-333.
- Maddox, R.A., 1976: An evaluation of tornado proximity wind and stability data. *Mon. Wea. Rev.*, **104**, 133-142.
- \_\_\_\_\_, L.R. Hoxit, and C.F. Chappell, 1980: A study of tornadic thunderstorm interactions with thermal boundaries. *Mon. Wea. Rev.*, **108**, 322-336.
- \_\_\_\_\_, D.J. Perkey, and J.M. Fritsch, 1981: Evolution of upper tropospheric features during the development of a mesoscale convective complex. *J. Atmos. Sci.*, **38**, 1664-1674.
- Magor, B.W., 1959: Mesoanalysis: Some operational analysis techniques utilized in tornado forecasting. *Bull. Amer. Meteor. Soc.*, **40**, 499-511.
- Marroquin, A., and D.J. Raymond, 1982: A linearized convective overturning model for prediction of thunderstorm movement. *J. Atmos. Sci.*, **39**, 146-151.
- Marwitz, J.D., 1972: Locating the organized updraft on severe thunderstorms. *J. Appl. Meteor.*, **11**, 236-238.

- \_\_\_\_\_, and D.W. Burgess, 1994: The observed inflow structure of a thunderstorm with a mesocyclone. *Mon. Wea. Rev.*, **122**, 393-396.
- Matthews, D.A., and J.F. Henz, 1975: Verification of numerical model simulations of cumulus-environmental interaction in the high plains. *Pageoph*, **113**, 803-823.
- \_\_\_\_\_, and B.A. Silverman, 1980: Sensitivity of convective cloud growth to mesoscale lifting: A numerical analysis of mesoscale convective triggering. *Mon. Wea. Rev.*, **108**, 1056-1064.
- May, P.T., and J.M. Wilczak, 1993: Diurnal and seasonal variations of boundary-layer structure observed with a radar wind profiler and RASS. *Mon. Wea. Rev.*, **121**, 673-682.
- McCann, D.W., 1994: WINDEX - A new index for forecasting microburst potential. *Wea. Forecasting*, **9**, 532-541.
- McCarthy, J., and S.E. Koch, 1982: The evolution of an Oklahoma dryline. Part I: A Meso- and subsynoptic-scale analysis. *J. Atmos. Sci.*, **39**, 225-236.
- McCaul, E.W., H.B. Bluestein, and R.J. Doviak, 1987: Airborne Doppler lidar observations of convective phenomena in Oklahoma. *J. Atmos. Ocean. Technol.*, **4**, 479-497.
- \_\_\_\_\_, 1991: Buoyancy and shear characteristics of hurricane-tornado environments. *Mon. Wea. Rev.*, **119**, 1954-1978.
- \_\_\_\_\_, and M.L. Weisman, 1996: Simulations of shallow supercell storms in landfalling hurricane environments. *Mon. Wea. Rev.*, **124**, 408-429.
- McNulty, R.P., 1978: On upper tropospheric kinematics and severe weather occurrence. *Mon. Wea. Rev.*, **106**, 662-672.
- McWilliams, J.C., 1985: A uniformly valid model spanning the regimes of geostrophic and isotropic, stratified turbulence: Balanced turbulence. *J. Atmos. Sci.*, **42**, 1773-1774.
- Moller, A.R., C.A. Doswell III, M.P. Foster, and G.R. Woodall, 1994: The operational recognition of supercell thunderstorm environments and storm structures. *Wea. Forecasting*, **9**, 327-347.
- Morris, D.A., and P.R. Janish, 1996: The utility of mesoscale versus synoptic scale surface observations during the Lahoma hail and windstorm of 17 August

1994. Preprints, *18th Conf. on Severe Local Storms*, San Francisco, CA, Amer. Meteor. Soc., 60-64.
- Morton, B.R., 1984: The generation and decay of vorticity. *Geophys. Astrophys. Fluid Dynamics*, **28**, 277-308.
- Murphy, A.H., and E.S. Epstein, 1989: Skill scores and correlation coefficients in model verification. *Mon. Wea. Rev.*, **117**, 572-581.
- Nelson, S.P., 1977: Rear flank downdraft: A hailstorm intensification mechanism. Preprints, *10th Conf. on Severe Local Storms*, Omaha, NE, Amer. Meteor. Soc., 521-525.
- Noilhan, J., and S. Planton, 1989: A simple parameterization of land surface processes for meteorological models. *Mon. Wea. Rev.*, **117**, 536-549.
- Orlanski, I., 1976: A simple boundary condition for unbounded hyperbolic flows. *J. Comp. Physics*, **21**, 251-269.
- Park, S.K., and K.K. Droegemeier, 1997: Validity of the tangent linear approximation in a moist convective cloud model. *Mon. Wea. Rev.*, **125**, 3320-3340.
- Pauley, R.L., C.R. Church, and J.T. Snow, 1982: Measurements of maximum surface pressure deficits in modeled atmospheric vortices. *J. Atmos. Sci.*, **39**, 369-377.
- Peterson, R.E., Jr., 1984: A triple-Doppler radar analysis of a discretely propagating multicell convective storm. *J. Atmos. Sci.*, **41**, 2973-2990.
- Purdom, J.F.W., 1976: Some uses of high-resolution GOES imagery in the mesoscale forecasting of convection and its behavior. *Mon. Wea. Rev.*, **104**, 1474-1483.
- \_\_\_\_\_, 1993: Satellite observations of tornadic thunderstorms. *The Tornado: Its Structure, Dynamics, Prediction and Hazards*, Geophys. Monogr., No. 79, Amer. Geophys. Union, 265-274.
- Rasmussen, E.N., and R.B. Wilhelmson, 1983: Relationships between storm characteristics and 1200 GMT hodographs, low-level shear, and stability. Preprints, *13th Conf. on Severe Local Storms*, Tulsa, OK, Amer. Meteor. Soc., J5-J8.

- Ray, P.S., 1976: Vorticity and divergence fields within tornadic storms from Dual-Doppler observations. *J. Appl. Meteor.*, **15**, 879-890.
- \_\_\_\_\_, B.C. Johnson, K.W. Johnson, J.S. Bradberry, J.J. Stephens, K.K. Wagner, R.B. Wilhelmson, and J.B. Klemp, 1981: The morphology of several tornadic storms on 20 May 1977. *J. Atmos. Sci.*, **38**, 1643-1663.
- Raymond, D.J., 1975: A model for predicting the movement of continuously propagating convective storms. *J. Atmos. Sci.*, **32**, 1308-1317.
- Richardson, Y.P., K.K. Droegemeier, and R.P. Davies-Jones, 1998: A study of the influence of horizontally-varying vertical shear and CAPE on numerically simulated convective storms. Preprints, *19th Conf. on Severe Local Storms*, Minneapolis, MN, Amer. Meteor. Soc., 249-252.
- Rothfus, L.P., and D.K. Lilly, 1989: Quantitative and theoretical analyses of an experimental helical vortex. *J. Atmos. Sci.*, **46**, 2265-2279.
- Sanders, F. and D.O. Blanchard, 1993: The origin of a severe thunderstorm in Kansas on 10 May 1985. *Mon. Wea. Rev.*, **121**, 133-149.
- Savijarvi, H., 1995: Error growth in a large numerical forecast system. *Mon. Wea. Rev.*, **123**, 212-221.
- Schlesinger, R.E., 1973: A numerical model of deep moist convection: Part I. Comparative experiments for variable ambient moisture and wind shear. *J. Atmos. Sci.*, **30**, 835-856.
- \_\_\_\_\_, 1984: Mature thunderstorm cloud-top structure and dynamics: A three-dimensional numerical simulation study. *J. Atmos. Sci.*, **41**, 1551-1570.
- Schreiber, W.E., 1986: Case studies of thunderstorms initiated by radar-observed convergence lines. *Mon. Wea. Rev.*, **114**, 2256-2266.
- Seitter, K.L., and J.L. Kuo, 1983: The dynamical structure of squall-line type thunderstorms. *J. Atmos. Sci.*, **40**, 2831-2854.
- Shapiro, A., 1994: Annular downdraft formation in an elevated vortex at high swirl ratios. Preprints, *6th Conf. on Mesoscale Processes*, Portland, Oregon, AMS, 636-639.
- \_\_\_\_\_, 1996: Nonlinear shallow-water oscillations in a parabolic channel: Exact solutions and trajectory analyses. *J. Fluid Mech.*, **318**, 49-76.

- Simpson, J., and V. Wiggert, 1969: Models of precipitating cumulus towers. *Mon. Wea. Rev.*, **97**, 471-489.
- \_\_\_\_\_, N.E. Westcott, R.J. Clerman, and R.A. Pielke, 1980: On cumulus mergers. *Arch. Met. Geoph. Biokl.*, **29**, 1-40.
- \_\_\_\_\_, 1980: Downdrafts as linkages in dynamic cumulus seeding effects. *J. Appl. Meteor.*, **19**, 477-487.
- \_\_\_\_\_, and G. van Helvoirt, 1980: GATE cloud - subcloud layer interactions examined using a three-dimensional cumulus model. *Cont. Atmos. Phys.*, **53**, 106-134.
- Skamarock, W.C., and J.B. Klemp, 1993: Adaptive grid refinement for two-dimensional and three-dimensional nonhydrostatic atmospheric flow. *Mon. Wea. Rev.*, **121**, 788-804.
- Straka, J.M., and E.N. Rasmussen, 1997: Toward improving microphysical parameterizations of conversion processes. *J. Appl. Met.*, **36**, 896-902.
- Sun, J., D.W. Flicker, and D.K. Lilly, 1991: Recovery of three-dimensional wind and temperature fields from simulated single-Doppler radar data. *J. Atmos. Sci.*, **48**, 876-890.
- Szeto, K.K., and H.R. Cho, 1994: A numerical investigation of squall lines. Part I: The control experiment. *J. Atmos. Sci.*, **51**, 414-424.
- \_\_\_\_\_, K.K., and H.R. Cho, 1994: A numerical investigation of squall lines. Part II: The mechanics of evolution. *J. Atmos. Sci.*, **51**, 414-424.
- Tao, W.K., and J. Simpson, 1974: A further study of cumulus interactions and mergers: Three-dimensional simulations with trajectory analyses. *J. Atmos. Sci.*, **46**, 2974-3004.
- Thompson, P.D., 1982: A generalized class of exact time-dependent solutions of the vorticity equation for nondivergent barotropic flow. *Mon. Wea. Rev.*, **110**, 1321-1324.
- Trapp, R.J., and R.P. Davies-Jones, 1997: Tornadogenesis with and without a dynamic pipe effect. *J. Atmos. Sci.*, **54**, 113-133.

- Tremback, C.J., J. Powell, W.R. Cotton, and R.A. Pielke, 1987: The forward-in-time upstream advection scheme: Extension to higher orders. *Mon. Wea. Rev.*, **115**, 540-555.
- Tripoli, G.J., and W.R. Cotton, 1980: A numerical investigation of several factors contributing to the observed variable intensity of deep convection over south Florida. *J. Appl. Meteor.*, **19**, 1037-1063.
- Ulanski, S.L., and M. Garstang, 1978: The role of surface divergence and vorticity in the life cycle of convective rainfall. Part I: Observation and analysis. *J. Atmos. Sci.*, **35**, 1047-1062.
- \_\_\_\_\_, and \_\_\_\_\_, 1978: The role of surface divergence and vorticity in the life cycle of convective rainfall. Part II: Descriptive model. *J. Atmos. Sci.*, **35**, 1063-1069.
- Vasiloff, S.V., E.A. Brandes, and R.P. Davies-Jones, 1986: An investigation of the transition from multicell to supercell storms. *J. Climate Appl. Meteor.*, **25**, 1922-1036.
- Wakimoto, R.M., 1983: The West Bend, Wisconsin storm of 4 April 1981: A problem in operational meteorology. *J. Climate Appl. Meteor.*, **22**, 181-189.
- \_\_\_\_\_, and N.T. Atkins, 1996: Observations on the origins of rotation: The Newcastle tornado during VORTEX 94. *Mon. Wea. Rev.*, **124**, 384-407.
- Weaver, J.F., and S.P. Nelson, 1982: Multiscale aspects of thunderstorm gust fronts and their effects on subsequent storm development. *Mon. Wea. Rev.*, **110**, 707-718.
- Weckwerth, T.M., J.W. Wilson, and R.M. Wakimoto, 1996: Thermodynamic variability within the convective boundary layer due to horizontal convective rolls. *Mon. Wea. Rev.*, **124**, 769-784.
- Weinstein, A.I., 1970: A numerical model of cumulus dynamics and microphysics. *J. Atmos. Sci.*, **27**, 246-255.
- Weisman, M.L., and H.B. Bluestein, 1985: Dynamics of numerically simulated LP storms. Preprints, *14th Conf. on Severe Local Storms*, Boston, Mass., Amer. Meteor. Soc., 167-170.

- \_\_\_\_\_, and J.B. Klemp, 1986: Characteristics of isolated convective storms. *Mesoscale Meteorology and Forecasting*, Peter S. Ray, Ed., Amer. Meteor. Soc., 331-358.
- \_\_\_\_\_, \_\_\_\_\_, and R. Rotunno, 1988: Structure and evolution of numerically simulated squall lines. *J. Atmos. Sci.*, **45**, 1990-2013.
- \_\_\_\_\_, 1996: On the use of vertical wind shear versus helicity in interpreting supercell dynamics. Preprints, *18th Conf. on Severe Local Storms*, San Francisco, CA, Amer. Meteor. Soc., 200-204.
- Westcott, N.E., and P.C. Kennedy, 1989: Cell development and merger in an Illinois thunderstorm observed by Doppler radar. *J. Atmos. Sci.*, **46**, 117-131.
- \_\_\_\_\_, 1994: Merging of convective clouds: Cloud initiation, bridging, and subsequent growth. *Mon. Wea. Rev.*, **122**, 780-790.
- Wexler, R., R.H. Blackmer, Jr., 1982: Radar reflectivities and satellite imagery of severe storms 20 May 1977. *Mon. Wea. Rev.*, **110**, 719-724.
- Wicker, L.J., and R.B. Wilhelmson, 1995: Simulation and analysis of tornado development and decay within a three-dimensional supercell thunderstorm. *J. Atmos. Sci.*, **52**, 2675-2703.
- Wilkins, E.M., Y.K. Sasaki, G.E. Gerber, and W.H. Chaplin, Jr., 1976: Numerical simulation of the lateral interactions between buoyant clouds. *J. Atmos. Sci.*, **33**, 1321-1329.
- Wilson, J.W., and W.E. Schreiber, 1986: Initiation of convective storms at radar-observed boundary-layer convergence lines. *Mon. Wea. Rev.*, **114**, 2516-2536.
- \_\_\_\_\_, G.B. Foote, N.A. Crook, J.C. Fankhauser, C.G. Wade, J.D. Tuttle, C.K. Mueller, and S.K. Krueger, 1992: The role of boundary-layer convergence zones and horizontal rolls in the initiation of thunderstorms: A case study. *Mon. Wea. Rev.*, **120**, 1785-1815.
- Wong, V.C., and X. Song, 1995: A dynamic closure method for anisotropic subgrid-scale stresses. Proceedings, *10th Symposium on Turbulent Shear Flows*, University Park, PA.
- Wood, V.T., R.A. Brown, and D.W. Burgess, 1996: Duration and movement of mesocyclones associated with southern great plains thunderstorms. *Mon. Wea. Rev.*, **124**, 97-101.

- Wu, W., D.K. Lilly, and R.M. Kerr, 1992: Helicity and thermal convection with shear. *J. Atmos. Sci.*, **49**, 1800-1809.
- Xu, Q., M. Xue, and K.K. Droegemeier, 1996: Numerical simulations of density currents in sheared environments within a vertically confined channel. *J. Atmos. Sci.*, **53**, 770-786.
- Xue, M., Q. Xu, and K. K. Droegemeier, 1996: A theoretical and numerical study of density currents in non-constant shear flows. Preprints, *7th Conf. on Mesoscale Processes*, Reading, U.K., Amer. Meteor. Soc.
- Zamora, R.J., B.L. Weber, and D.C. Welsh, 1994: The accuracy of divergence estimates calculated using the linear vector point function method and three profilers. *Mon. Wea. Rev.*, **122**, 2603-2630.
- Ziegler, C.L., and C.E. Hane, 1993: An observational study of the dryline. *Mon. Wea. Rev.*, **121**, 1134-1151.
- Zipser, E.J., and K.R. Lutz, 1994: The vertical profile of radar reflectivity of convective cells: A strong indicator of storm intensity and lightning probability. *Mon. Wea. Rev.*, **122**, 1751-1759.

## **Appendix A**

The following model settings were used in the numerical simulations presented:

Potential temperature perturbation	2 K Amplitude
Horizontal Radius	10 km
Vertical Radius	1.4 km
Height of maximum	1.4 km
No terrain	
Horizontal Resolution	1500 m
Vertical Resolution	350 m from 0-11900 m Stretching based on $z^3$ applied from 11.9-20 km Average vertical resolution from 0-20 km is 450 m
Large time step	5 s
Small time step	1 s
Lateral boundary conditions	Radiation condition for normal wind component as in Klemp and Wilhelmson (1978a) (with modifications as described in Chapter 3), phase speed = $45 \text{ m s}^{-1}$ ; relaxation to base state also applied with relaxation coefficient = 0.5
Top boundary condition	Rigid lid with a Rayleigh damping layer from 12-20 km; Rayleigh damping coefficient = $0.0067 \text{ s}^{-1}$
Bottom boundary condition	Rigid; no surface physics
Coriolis parameter	0
Turbulence Parameterization	1.5-order closure based on predicted turbulent kinetic energy $K_m = 0.1 E^{1/2} l$ ; where $l$ is a stability- dependent length scale following Deardorff (1980) and length scales are assumed to be anisotropic
Dissipation coefficient ( $C_e$ )	3.9 at lowest level 0.93 otherwise
Computational Mixing	2 <sup>nd</sup> -order in vertical, coefficient (scaled by vertical grid spacing) = $8.1 \times 10^{-4} \text{ s}^{-1}$ 4 <sup>th</sup> -order in horizontal, coefficient (scaled

Nondimensional divergence damping coeff. 0.05  
Nondimensional time filter coeff. 0.1  
Kessler warm rain microphysics  
Vertically implicit integration for w and p  
Advection of perturbation potential temperature, and all mixing ratios done with flux-corrected transport  
Advection of momentum variables, pressure and turbulent kinetic energy done with a fourth order scheme in the horizontal and a second order scheme in the vertical

by horizontal grid spacing) =  $5 \times 10^{-4} \text{ s}^{-1}$